University of Exeter
Department of Physics and Astronomy

2D nanocrystal heterostructures – novel production methods and device applications

Darren Nutting

Submitted by Darren Nutting, to the University of Exeter as a thesis for the degree of Doctor of Philosophy in Physics, May 2021.

Signed:

Abstract

This thesis primarily investigates an approach to realise a variety of functional heterostructures based on van der Waals (vdW) nanocrystalline films produced through the mechanical abrasion of bulk powders. This novel production technique represents the next step in the evolution of scalable production routes which can take advantage of vdW materials and their heterostructures whilst preserving the high electronic and optical quality of the individual crystals. To demonstrate the efficacy of this method, a slew of different device architectures are developed, including photovoltaics, triboelectric nanogenerators, strain sensors, capacitive pressure sensors and thermistors. All exhibit either superior or comparable performance to analogous systems within the literature, and show great potential for future optimised vdW heterostructure devices.

The secondary focus of this thesis is the incorporation of talc dielectrics as a potentially clean and atomically flat alternative substrate to hexagonal boron nitride (hBN) for few-layer transition metal dichalcogenide (TMDC) field-effect transistors (FETs) and for excitonic TMDC monolayers. It is found that talc-based TMDC FETs show small hysteresis which does not strongly depend on back gate sweep rate as well as have negligible leakage current for the dielectric thicknesses studied. Furthermore, it is found that photoluminescent (PL) emission from monolayer TMDC materials using talc as a substrate have narrow linewidths reduced to as little as 10 meV which, in addition to the high intensity PL emission, suggests that talc can be used to preserve the intrinsic excitonic properties of the TMDC. Additionally, the spontaneous doping properties of talc allow for the room-temperature observation of trions in all of the TMDC/talc devices studied.

Acknowledgements

I would like to begin by thanking my two primary supervisors, Dr. Freddie Withers and Dr. Eros Mariani. Freddie has proven to be a veritable fount of knowledge and has consistently guided me through the difficulties of device manufacture and experimental procedure. Thank you for always being available for fruitful conversation, whether it be about physics or otherwise. Eros always had a way of bringing out the beauty in my topic, your enthusiasm is infectious and I always valued our meetings together.

I also thank my family for their patience and support throughout my undergraduate and postgraduate studies, you were always there for me and I am forever grateful. In particular I thank my Mother, Davida, who sparked my initial interest in science as a child, and my Father, Darren, for always reminding me of what truly matters. I am fortunate to be blessed with the wonderful, enormous and sometimes chaotic family that I have. I appreciate every one of you.

Most of all I would like to thank Ciara Whateley, my best friend. Without your love and guidance I would not be the man that I am today.

Lastly, I thank God for giving me life, so that I may live for even one second.

Publications

1. **Darren Nutting**, Jorlandio F Felix, Evan Tillotson, Dong-Wook Shin, Adolfo De Sanctis, Hong Chang, Nick Cole, Saverio Russo, Adam Woodgate, Ioannis Leontis, Henry A. Fernández, Monica F. Craciun, Sarah J. Haigh and Freddie Withers. Heterostructures formed through abraded van der Waals materials. *Nature Communications*, 11(1):1-10, 2020.

2. **Darren Nutting** and Freddie Withers. Flux pinning in $NbSe_2$ - $CrGeTe_3$ heterostructures. *Physica C: Superconductivity and its Applications*, 1353803, 2020.

3. Namphung Peimyoo, Thorsten Deilmann, Freddie Withers, Janire Escolar, **Darren Nutting**, Takashi Taniguchi, Kenji Watanabe, Kristian S. Thygesen, Monica F. Craciun and Saverio Russo. Electrical tuning of optically active interlayer excitons in bilayer MoS_2. *Nature Nanotechnology*, 16, 888-893, 2021.

4. **Darren Nutting**, Gabi Prando, Marion Severijnen, Ingrid D. Barcelos, Peter C. M. Christianen, Uli Zeitler, Yara Galvão and Freddie Withers. Electrical and optical properties of transition metal dichalcogenides on talc dielectrics. *Nanoscale*, 2021.

5. **Darren Nutting**, Emily Fellingham, Emily Morrison and Freddie Withers. Flexible pressure and temperature sensors using abraded van der Waals materials. (In preparation).

Contents

List of Figures

List of Tables

1. Introduction

1.1 Introduction

Graphene is a two dimensional (2D) layer of carbon atoms arranged in a honeycomb lattice structure. Although theoretically predicted since the 1940's [1] it took until 2004 before it was first successfully isolated [2], whereby its unique electronic and mechanical properties were soon revealed to be quite unlike any previously identified material. This inevitably triggered an explosion of interest in the scientific community not just within condensed matter research groups but from many different fields, ranging from biomedical [3] through to environmental science [4].

As experimental techniques and an understanding of the necessary conditions for clean isolation improved, a slew of new 2D materials were discovered such as TMDCs [5], hBN [6] and many others [7, 8, 9, 10, 11]. The development of stacking technologies [12] subsequently allowed for the creation of high-quality vdW heterostructures [13, 14] with customisable properties depending on the choice of constituent materials and layer sequence, opening up an entirely new domain of 2D physics for exploration. Compared to conventional semiconductor compound heterostructure devices, these new vdW structures have the potential to offer many advantages such as being lightweight, semi-transparent and flexible, all whilst maintaining competitive performance.

In fact, the highest quality vdW heterostructures even out-perform conventional materials, such as those incorporating TMDC monolayers into FET architecture in an attempt to continue Moore's Law [15, 16, 17, 18, 19, 20], although these devices consistently underperform when compared to their maximum theoretical potential as a result of both extrinsic and intrinsic scattering centres [15, 21], which in turn serve to lower the channel carrier mobility and reduce FET performance [22]. Despite this, the majority of research into 2D FET development continues to be skewed towards optimisation of the channel material, with relatively little being done on identifying the optimal dielectric outside of, for example, hBN [23, 24], Al_2O_3 [25], HfO_2 [26, 27] or conventional SiO_2 [28, 29]. Investigation of the entire dielectric parameter space is therefore required, and it is for this reason that in this work secondary focus is placed on the material known as talc which, like hBN, can be exfoliated into atomically flat monolayers in addition to possessing a number of other useful properties such as having a large band gap and high dielectric constant [10, 30]. These properties also give talc the potential to act as a clean substrate to isolate TMDC monolayers from the environment and thus preserve their intrinsic optoelectronic qualities, and so an investigation into the photoluminescent properties of a mechanicaly exfoliated WS_2/talc heterostructure is also completed.

The aforementioned devices all rely on mechanical exfoliation of bulk single crystals which are then stacked on top of one another by mechanical transfer procedures. However, this precise yet time-consuming method is not scalable and alternative device manufacturing routes are urgently required to achieve widespread uptake of these materials and the subsequent unique heterostructures that they offer. There have been many attempts at achieving this, such as chemical vapour deposition (CVD) [31], which relies on the growth of vdW heterostructures layer-by-layer at high temperatures, and liquid phase exfoliation (LPE) [32, 33, 34], in which vdW dispersions are created by ultra-sonication of material within suitable solvents before printing onto pre-treated substrates. Unfortunately, the initial investment required and energy cost of CVD growth is high for a given amount of monolayer material produced, and the growth of multilayer systems are confined to a limited number of 2D material combinations. Furthermore, CVD growth requires the use of catalyst substrates and subsequent transfer of the heterostructure films onto suitable substrates for device fabrication, which introduces contamination, tears and cracks which prevent the formation of high quality heterostructure devices [31]. Likewise, LPE heterostructures often exhibit strong disorder within the films as a result of material oxidation, small crystallite sizes and poor interface quality between subsequent layers of the heterostructure [35], once again limiting the performance of the final device.

The issue of finding a high-quality and scalable vdW heterostructure production method is the therefore the primary focus of this thesis. Here, the simplest possible approach is used, that is the mechanical abrasion of bulk powders to produce, layer-by-layer, a heterostructure of abritrary size whilst maintaining high electronic and optoelectronic quality. In this work, it is demonstrated that this process not only produces clearly defined nanocrystalline films with little-to-no material intermixing across the interface, but also that it has the potential to produce a myriad of different devices with comparable or superior performance to analogous systems created via other means. Specific attention is placed on various materials including graphite, MoS_2, $MoSe_2$, WS_2 and hBN, as these are often the focus of devices produced via CVD and LPE and therefore allows for accurate comparison between different scalable production methods. The simplicity of the abrasive process allows for almost complete autonomisation by simple modification of a computer numerical control (CNC) micro engraver system, expanding the scope of potential applications to devices using exotic and volatile materials which require isolation from the atmosphere in addition to encouraging large-scale uptake by industry. The applicability of this novel process is increased further by the vast array of substrates that abrasive deposition is compatible with, all of which require no pre-treatment to ensure strong adhesion of the films.

1.2 Thesis overview

Chapter 1 provides a broad introduction of the subject matter as well as an overview of the contents of the other sections within this work.

Chapter 2 includes a discussion on the structure and properties of each material used within this study, and relates this to their individual mechanical, electronic and thermal qualities in order to provide a comparison between them. In particular, a description of graphene (and graphite), monolayer hBN, TMDCs (from monolayer to bulk) and talc are given in the first four sections. This chapter also provides details of the various interfacial phenomena which occur when said materials are stacked into heterostructures and discusses how these alter the electrical performance of the final device, how they determine the set and order of material combinations which can be combined during the abrasive process and how they can be utilised to create entirely unique devices.

Chapter 3 covers the various measurement techniques used to collect data during the study. This includes Raman and photoluminescence spectroscopy, and how these can be used to gather characteristic information such as the thickness and degree of doping present for each individual material. This chapter then concludes with a discussion on the fundamental working principles of atomic force and scanning electron microscopy.

Chapter 4 is split into two main sections, each covering one of the two focal points of this thesis. The first and primary focus is that of abraded films and their use in a selection of device types, whilst the second covers the incorporation of talc into FETs. This chapter therefore describes the manufacturing and design processes employed to create both manually and automatically abraded vdW films and heterostructures, mechanically exfoliated and assembled heterostructures and then the various device architectures which were created from both.

Chapter 5 is also split into two sections in the same manner. The first includes a comprehensive characterisation of the films produced via the abrasive method and then a discussion of how, when incorporated into various devices, they compare to other analogous systems present within the literature. The second section includes a full electronic characterisation of FETs utilising talc as the dielectric barrier material, and then compares the results to the literature on comparable devices using other, well established dielectric materials. Within this section is also a discussion on the photoluminescent behaviour of TMDCs bound to talc, along with an assessment of the suitability of talc to act as an isolating substrate.

2. Theoretical concepts

2.1 Graphene

2.1.1 Lattice and band structure

Carbon contains six electrons in the $1s^22s^22p^2$ configuration, meaning that two of its six electrons exist within the low energy $1s$ orbital close to the nucleus while the remaining four occupy the outer $2s$ and $2p$ orbitals. This is true for a solitary carbon atom, but in the presence of others it becomes energetically favorable to have one electron be excited from the $2s$ orbital into the $2p$ orbital in order to form covalent bonds [36]. This corresponds to four equivalent excited states given by $|2s\rangle$, $|2p_x\rangle$, $|2p_y\rangle$ and $|2p_z\rangle$ which can interact with each other through quantum-mechanical superposition to form new hybrid states, such that the superpositon of the $|2s\rangle$ state with $n\,|2p_i\rangle$ states is known as sp^n hybridization [36]. Graphene consists of the planar sp^2 hybridization, which is the superposition of the $|2s\rangle$ orbital with the $|2p_x\rangle$ and $|2p_y\rangle$ orbitals. This results in the formation of three in-plane σ-bonds at angles of 120° to each other which can be tiled to form the familiar hexagonal graphene lattice (lattice constant, $a_{\text{graphene}} \approx 2.46$ Å[36]) shown in Figure 2.1.

The remaining $|2p_z\rangle$ orbital is orientated perpendicular to the plane of the σ-bonds. These hybridise with the $|2p_z\rangle$ orbitals on neighbouring carbon atoms and form the delocalised, conducting π-bonds above and below the carbon sheet which are responsible for conduction throughout the lattice as well as the weak vdW forces which bind the planes of multilayer graphene and graphite together [37]. The hexagonal structure is itself composed of two in-equivalent, triangular sublattices, denoted A and B in Figure 2.1, which arise due to the differing possible orientations

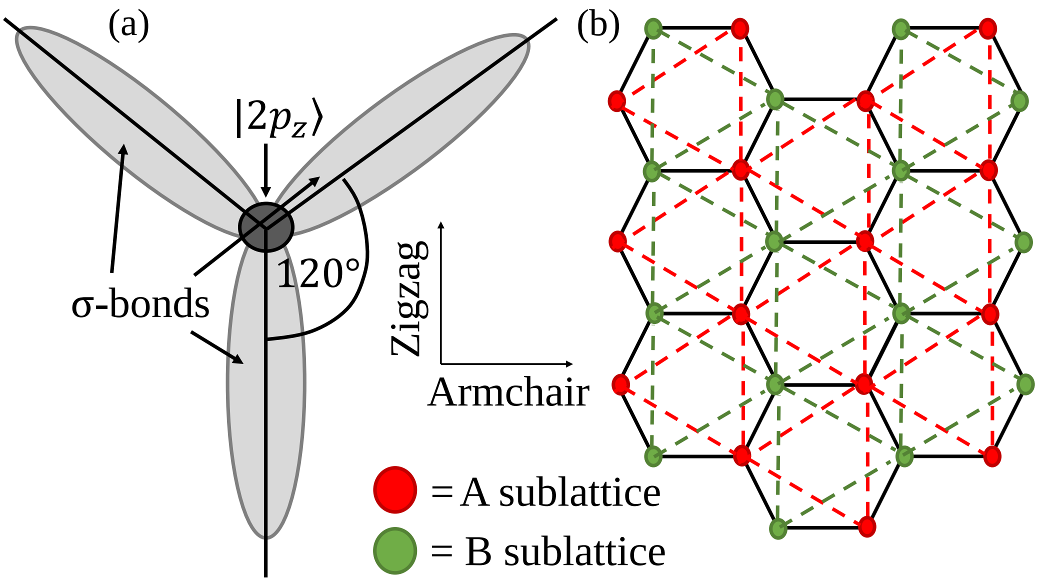

Figure 2.1: *The orientation of the in-plane σ-bonds between the carbon atoms (a) and how it relates to the overall hexagonal structure of graphene (b). The $|2p_z\rangle$ orbital is shown orientated perpendicular to the plane of the σ-bonds, while the two triangular sublattices are indicated by the red (A) and green (B) filled circles and dotted lines.*

of the σ-bonds between carbon atoms on each sublattice. The zigzag and armchair directions [38] are also indicated in Figure 2.1. The carbon sheet can be modelled as a triangular lattice with two atoms per unit cell [36, 38]. This, and the fact that only electrons within the delocalised π-bonds contribute towards the unusual electronic properties [39], means that graphene can be accurately modelled using the tight-binding approximation with a two-atom basis and with only one type of contributing orbital.

Tight-binding calculation of graphene's electronic structure

In a system with N lattice sites the resultant Bloch state at position $\mathbf{r}$ due to atoms of type j centered at atomic sites $\mathbf{R_j}$, each contributing a $|2p_z\rangle$ orbital, ϕ_{p_z}, is [40]

$$\Phi_j(\mathbf{r}) = \frac{1}{\sqrt{N}} \sum_{\mathbf{R_j}} e^{i\mathbf{k}\cdot\mathbf{R_j}} \phi_{p_z}(\mathbf{r} - \mathbf{R_j}). \tag{2.1}$$

Hence the Bloch states due to the two inequivalent sublattices, which can be thought of as composed of "type A" and "type B" atoms, are

$$\Phi_A(\mathbf{r}) = \frac{1}{\sqrt{N}} \sum_{\mathbf{R_A}} e^{i\mathbf{k}\cdot\mathbf{R_A}} \phi_{p_z}(\mathbf{r} - \mathbf{R_A}) \tag{2.2}$$

and

$$\Phi_B(\mathbf{r}) = \frac{1}{\sqrt{N}} \sum_{\mathbf{R_B}} e^{i\mathbf{k}\cdot\mathbf{R_B}} \phi_{p_z}(\mathbf{r} - \mathbf{R_B}), \tag{2.3}$$

respectively. Returning back to the general two-atom basis (eqn. 2.1), the overall crystal wave function, Ψ_j, can be expressed as a linear combination of Bloch states such that [40, 41]

$$\Psi_j(\mathbf{r}) = \sum_j c_j \Phi_j(\mathbf{r}), \tag{2.4}$$

where c_j is just a coefficient used to keep track of the contributing Bloch states. The variational principle states that the Ψ_j which most accurately describes the real crystal wave function, Ψ, will be the one with the lowest energy [42]. Therefore in order to accurately model Ψ, the energy of the system with Hamiltonian $\hat{H}$, $\langle\Psi_{j'}|\,\hat{H}\,|\Psi_j\rangle$, should be minimised with respect to one such tracking coefficient. One way to do this is through the use of Lagrange multipliers [43] with the constraint $\langle\Psi_j|\Psi_j\rangle = 1$, giving

$$\langle E\rangle = \langle\Psi_{j'}|\,\hat{H}\,|\Psi_j\rangle - \lambda(\langle\Phi_{j'}|\Phi_j\rangle - 1), \tag{2.5}$$

where λ is the Langrange multiplier, which in this case represents an energy E [43]. Given that

$$\begin{aligned} \langle\Psi_{j'}|\,\hat{H}\,|\Psi_j\rangle &= \int \sum_{j'} c_{j'}^* \Phi_{j'}^* \hat{H} \sum_j c_j \Phi_j d\mathbf{r} \\ &= \sum_{j'} \sum_j c_{j'}^* c_j \langle\Phi_{j'}|\,\hat{H}\,|\Phi_j\rangle\,, \end{aligned} \tag{2.6}$$

and

$$\begin{aligned}\lambda(\langle\Phi_{j'}|\Phi_j\rangle - 1) &= \lambda(\int \sum_{j'} c^*_{j'}\Phi^*_{j'} \sum_j c_j \Phi_j d\mathbf{r} - 1) \\ &= \lambda(\sum_{j'}\sum_j c^*_{j'} c_j \langle\Phi_{j'}|\Phi_j\rangle - 1),\end{aligned} \tag{2.7}$$

then

$$\langle E\rangle = \sum_{j'}\sum_j c^*_{j'} c_j \langle\Phi_{j'}|\hat{H}|\Phi_j\rangle - \lambda(\sum_{j'}\sum_j c^*_{j'} c_j \langle\Phi_{j'}|\Phi_j\rangle - 1). \tag{2.8}$$

To minimise eqn. 2.8 it should be differentiated with respect to a single coefficient, say c^*_m, such that $\frac{\partial\langle E\rangle}{\partial c^*_{j'}}$ is only finite when $j' = m$. Therefore,

$$\frac{\partial\langle E_j\rangle}{\partial c^*_m} = \sum_j c_j \langle\Phi_m|\hat{H}|\Phi_j\rangle - \lambda\sum_j c_j \langle\Phi_m|\Phi_j\rangle = 0. \tag{2.9}$$

This can be simplified by re-labeling $\langle\Phi_m|\hat{H}|\Phi_j\rangle$ to H_{mj} and recognising that

$$\langle\Phi_m|\Phi_j\rangle = \begin{cases} 1 & \text{if m=j} \\ 0 & \text{if m}\neq\text{j}, \end{cases}$$

which acts just like a Kronecka delta function, δ_{mj}. Hence we have

$$\frac{\partial\langle E_i\rangle}{\partial c^*_m} = \sum_j c_j(H_{mj} - \lambda\delta_{mj}) = 0. \tag{2.10}$$

By setting $m = A$ and $j = B$ to denote the two sublattices, it becomes clear that this is a 2x2 matrix equation, where δ_{mj} is analogous to I, the identity matrix. This matrix equation can be solved for the Langrange multiplier by taking its determinant as

$$|\mathbf{H} - \lambda\mathbf{I}| = \begin{vmatrix} H_{AA'} - \lambda & H_{AB} \\ H^*_{AB} & H_{BB'} - \lambda \end{vmatrix} = 0, \tag{2.11}$$

using $H_{BA} = H^*_{AB}$. Therefore, in order to solve for the Lagrange multiplier, and hence the energy, all one needs to do is to determine the values of $H_{AA'}$, $H_{BB'}$ and H_{AB}. Here, H_{AB} represents the Hamiltonian of the superimposed wavefunction of nearest neighbour sites on differing sublattices and $H_{AA'}$ ($H_{BB'}$) represents the

Hamiltonian between two nearest neighbour sites on the same A (B) sublattice.

Calculation of $\mathbf{H_{AA'}}$ and $\mathbf{H_{BB'}}$:

Recall that $H_{mj} = \langle \Phi_m | \hat{H} | \Phi_j \rangle$ and hence

$$H_{AA'} = \frac{1}{N} \sum_{\mathbf{R_A}} \sum_{\mathbf{R_{A'}}} e^{i\mathbf{k}\cdot(\mathbf{R_{A'}}-\mathbf{R_A})} \int \phi^*_{p_z}(\mathbf{r}-\mathbf{R_A}) \hat{H} \phi_{p_z}(\mathbf{r}-\mathbf{R_{A'}}) d\mathbf{r} \tag{2.12}$$

through the use of eqn. 2.1. Using $\mathbf{x} = \mathbf{r} - \mathbf{R_{A'}}$ and recognising that $\mathbf{R_{A'}} - \mathbf{R_A}$ is just another lattice site, $\mathbf{R_{A''}}$, gives

$$\begin{aligned} H_{AA'} &= \frac{1}{N} \sum_{\mathbf{R_A}} \sum_{\mathbf{R_{A''}}} e^{i\mathbf{k}\cdot\mathbf{R_{A''}}} \int \phi^*_{p_z}(\mathbf{x}) \hat{H} \phi_{p_z}(\mathbf{x}-\mathbf{R_{A''}}) d\mathbf{r} \\ &= \sum_{\mathbf{R_{A''}}} e^{i\mathbf{k}\cdot\mathbf{R_{A''}}} \langle \phi_{p_z}(\mathbf{x}) | \hat{H} | \phi_{p_z}(\mathbf{x}-\mathbf{R_{A''}}) \rangle \end{aligned} \tag{2.13}$$

where a factor of N appears and then cancels due to the new lack of dependency on $\mathbf{R_A}$ [40]. The different terms in the summation over $\mathbf{R_{A''}}$ can be separated by considering the actual range over which the conducting $|2p_z\rangle$ orbital is significant, i.e. by noting that it is large when $|\mathbf{r}|$ is small and decays rapidly as you move away from $\mathbf{r} = 0$ [1]. When $\mathbf{R_{A''}} = 0$, the integral in eqn. 2.13 becomes

$$\begin{aligned} \int \phi^*_{p_z}(\mathbf{x}) \hat{H} \phi_{p_z}(\mathbf{x}) d\mathbf{r} &= \int \phi^*_{p_z}(\mathbf{x}) \epsilon_{p_z} \phi_{p_z}(\mathbf{x}) d\mathbf{r} \\ &= \epsilon_{p_z}, \end{aligned} \tag{2.14}$$

the energy of an atomic $|2p_z\rangle$ orbital on an isolated atom, due to $H\phi_{p_z}(\mathbf{x}) = \epsilon_{p_z}\phi_{p_z}(\mathbf{x})$ and the fact that the orbitals are normalised. When $|\boldsymbol{R_{A''}}| \gg |\boldsymbol{\tau}|$, where $\boldsymbol{\tau}$ is the nearest neighbour vector between members of the A sublattice, then $H_{AA'}$ approaches zero as the wave functions on atoms separated by a large distance do not significantly overlap [1].

When $|\boldsymbol{R_{A''}}| \approx |\boldsymbol{\tau}|$,

$$\begin{aligned} H_{AA'} &= \sum_{\boldsymbol{\tau}} e^{i\boldsymbol{k}\cdot\boldsymbol{\tau}} \langle \phi_{pz}(\boldsymbol{x}) | \hat{H} | \phi_{pz}(\boldsymbol{x}-\boldsymbol{\tau}) \rangle \\ &= \sum_{\boldsymbol{\tau}} e^{i\boldsymbol{k}\cdot\boldsymbol{\tau}} \gamma(|\boldsymbol{\tau}|), \end{aligned} \tag{2.15}$$

where $\gamma(|\boldsymbol{\tau}|)$ represents the hopping energy required to move between nearest neighbour sites on each sublattice (i.e. $A \rightarrow A'$). Therefore, as a whole, the hopping between members on the A sublattice can be represented by

$$H_{AA} = \epsilon_{p_z} + \sum_{\boldsymbol{\tau}} e^{i\boldsymbol{k}\cdot\boldsymbol{\tau}} \gamma(|\boldsymbol{\tau}|) = H_{BB}, \tag{2.16}$$

as can be seen by repeating the calculation over the B sublattice. In this calculation only nearest neighbours (the A and B lattice sites) are considered to significantly interact with each other, meaning that no single A-site can interact with another (see Figure 2.1). Therefore the contribution from either sublattice, H_{AA} and H_{BB}, can simply be approximated by the on-site energy ϵ_{p_z}.

Calculation of $\mathbf{H_{AB}}$:

Similar to before, we begin with

$$H_{AB} = \frac{1}{N} \sum_{\boldsymbol{R_A}} \sum_{\boldsymbol{R_B}} e^{i\boldsymbol{k}\cdot(\boldsymbol{R_B}-\boldsymbol{R_A})} \left\langle \phi_{pz}(\boldsymbol{r} - \boldsymbol{R_A}) \right| \hat{H} \left| \phi_{pz}(\boldsymbol{r} - \boldsymbol{R_B}) \right\rangle . \tag{2.17}$$

The contribution to H_{AB} only comes from nearest neighbours, meaning that if an A-site is taken as the centre then only the three nearest B-sites would need to be considered, simplifying the summation over B-sites to $\sum_{\boldsymbol{R_B}=1}^{3}$. The implied integral in eqn. 2.17 represents the hopping energy between nearest neighbours, $-\gamma_0$, which, in the case of neutral graphene, is independant of direction and has the same value between each neighbouring pair of ≈ 2.8 eV [38]. Therefore

$$H_{AB} = -\frac{\gamma_0}{N} \sum_{\boldsymbol{R_A}} \sum_{j=1}^{3} e^{i\boldsymbol{k}\cdot\boldsymbol{t}_j}, \tag{2.18}$$

where $\boldsymbol{R_B} - \boldsymbol{R_A} = \boldsymbol{t}$, the nearest neighbour vector (i.e. $A \rightarrow B$). This can be simplified further by defining $f(\boldsymbol{k}) = \sum_{j=1}^{3} e^{i\boldsymbol{k}\cdot\boldsymbol{t}_j}$ and noting that the $\sum_{\boldsymbol{R_A}}$ just contributes another factor of N [40], giving

$$H_{AB} = -\gamma_0 f(\boldsymbol{k}). \tag{2.19}$$

In order to evaluate H_{AB}, first $f(\boldsymbol{k})$ needs to be solved explicitly. Electrons within the carbon sheet are confined to two dimensions, meaning that their momenta can be represented by $\boldsymbol{k} = (k_x, k_y)$, while the nearest neighbour vectors are $\boldsymbol{t_1} = \left(0, \frac{a}{\sqrt{3}}\right)$, $\boldsymbol{t_2} = \left(\frac{a}{2}, \frac{-a}{2\sqrt{3}}\right)$ and $\boldsymbol{t_3} = \left(\frac{-a}{2}, \frac{-a}{2\sqrt{3}}\right)$, where $a \approx 1.42$Å [36, 38]. Expanding $f(\boldsymbol{k})$ using these vectors now gives

$$f(\boldsymbol{k}) = \exp\left(\frac{ik_y a}{\sqrt{3}}\right) + 2\cos\left(\frac{k_x a}{2}\right)\exp\left(\frac{-ik_y a}{2\sqrt{3}}\right). \tag{2.20}$$

Energy dispersion of graphene

Substitution of $H_{AA'}$, $H_{BB'}$ and H_{AB} into eqn. 2.11 gives

$$|\boldsymbol{H} - \lambda\boldsymbol{I}| = \begin{vmatrix} \epsilon_{p_z} - \lambda & -\gamma_0 f(\boldsymbol{k}) \\ -\gamma_0 f(\boldsymbol{k})^* & \epsilon_{p_z} - \lambda \end{vmatrix} = 0. \tag{2.21}$$

The on-site energy can then be chosen as the origin, allowing the value of λ, and hence the energy distribution, E, to be calculated as

$$E = \pm\gamma_0 |f(\boldsymbol{k})|. \tag{2.22}$$

This is the electronic dispersion of graphene under the influence of nearest neighbours only, where the positive (negative) solution represents the conduction (valence) band. In neutral graphene, the conduction band is completely empty while the valence band is completely full [38]. A plot of eqn. 2.22 shows certain points of interest within the Brillouin zone where the conduction and valence band touch, as is depicted in Figure 2.2.

As E is a linear function of $|f(\boldsymbol{k})|$, it is possible to find these touching points at $E = 0$ by looking for the value of $\boldsymbol{k}$ which satisfies $f(\boldsymbol{k}) = 0$. In doing so it can be shown that within graphene the two touching points, known as the Dirac points, coincide with the in-equivalent reciprocal lattice points at

$$\boldsymbol{K} = \left(0, \frac{4\pi}{3a}\right) \text{ and } \boldsymbol{K'} = \left(0, -\frac{4\pi}{3a}\right) \tag{2.23}$$

at the edge of the first Brillouin zone as is shown in Figure 2.2. The electronic

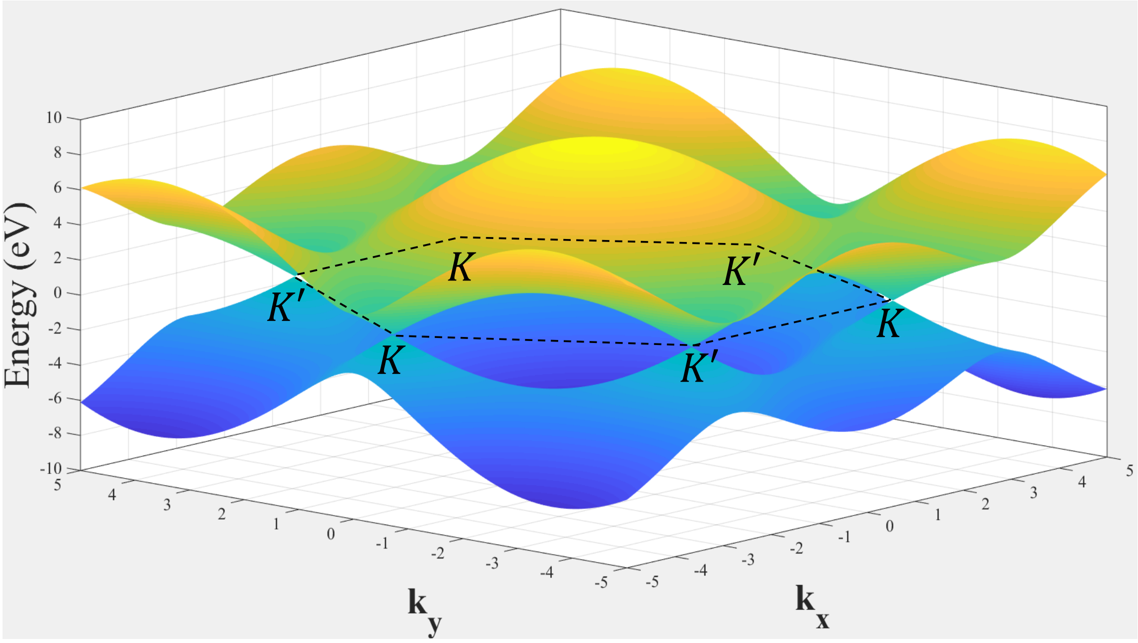

Figure 2.2: *The electronic dispersion of graphene calculated using the tight-binding model with nearest neighbours only. The yellow and blue sections represent the conduction and valence bands respectively.*

dispersion passes through $E = 0$ at these points. In order to find the low-energy dispersion relation here, we simply need to know how E and hence $f(\boldsymbol{k})$ behaves around these $\boldsymbol{K}$ or $\boldsymbol{K'}$ points. A simple way to do this is via a Taylor expansion [1]. Consider the function $f(\boldsymbol{k}) = f(\boldsymbol{k_x}, \boldsymbol{k_y})$ at a small displacement $\delta\boldsymbol{k} = (\delta k_x, \delta k_y)$ away from the K/K'-points. Applying the expansion to first order gives

$$f(k_x + \delta k_x, k_y + \delta k_y) = f(\boldsymbol{K}) + \delta k_x \frac{\delta f(\boldsymbol{K})}{\delta k_x} + \delta k_y \frac{\delta f(\boldsymbol{K})}{\delta k_y} + ... \tag{2.24}$$

Evaluating this at the K-point gives the low energy form of $f(\boldsymbol{k})$ as

$$\begin{aligned} f(k_x + \delta k_x, k_y + \delta k_y) &= \frac{\sqrt{3}a}{2} \left(i\delta k_x - \delta k_y \right) \\ &= \frac{v_F}{\gamma_0} \left(i\delta p_x - \delta p_y \right) \end{aligned} \tag{2.25}$$

by using the Fermi velocity, $v_F = \sqrt{3}a\gamma_0/2\hbar$ [44] and $\boldsymbol{p} = \hbar\boldsymbol{k}$, the momentum as measured from the K-point. Substituting this into eqn. 2.21, with $\lambda = E$ and $\epsilon_{p_z} = 0$, gives

$$|\mathbf{H} - \lambda\mathbf{I}| = \begin{vmatrix} -E & v_F \left(-i\delta p_x + \delta p_y \right) \\ v_F \left(i\delta p_x + \delta p_y \right) & -E \end{vmatrix} = 0, \tag{2.26}$$

where the modified low-energy Hamiltonian is

$$\mathbf{H} = v_F \begin{pmatrix} 0 & -i\delta p_x + \delta p_y \\ i\delta p_x + \delta p_y & 0 \end{pmatrix}. \tag{2.27}$$

Therefore, the low-energy dispersion becomes

$$E = \pm v_F \sqrt{\delta p_x^2 + \delta p_y^2}, \tag{2.28}$$

which can be simplified further using $|\mathbf{p}| = \sqrt{\delta p_x^2 + \delta p_y^2}$. Doing this gives the well known form for the low energy, linear electronic dispersion of graphene as [45]

$$E = \pm v_F |\mathbf{p}|. \tag{2.29}$$

This shows that for low energies near the Dirac points the energy dispersion becomes linear (see Figure 2.3), a characteristic which is indicative of massless particles such as photons. It should be noted that these low energy particles at the Dirac point are not ordinary electrons, but are in fact quasiparticles made from electron contributions from both in-equivalent sublattices [46]. Although these quasiparticles move at a Fermi velocity of $v_F \approx 10^6$ ms^{-1} [47, 48] rather than the speed of light, $c \approx 3\text{x}10^8$ ms^{-1}, they can still be described by the relativistic Dirac equation rather than the usual Schrödinger equation. These entities are therefore known as massless Dirac fermions [2, 36, 38]. The conduction and valence bands of the electronic dispersion shown in Figure 2.2 are symmetrical about $E = 0$ as a result of exclusion of next-nearest neighbours from the tight-binding calculation. When next-nearest neighbours are taken into account, they serve to shift the energy of the Dirac point such that the electron-hole symmetry of the system is broken and the dispersion becomes asymmetric as can be seen in Figure 2.3 [38, 41, 49].

It is important to note that this linear dispersion ultimately arises due to two things: the existence of the two in-equivalent sublattices and the fact that the atoms of each sublattice are identical [38, 50]. For example, consider a square array of atoms related by two nearest-neighbour vectors. The reciprocal of these real lattice vectors

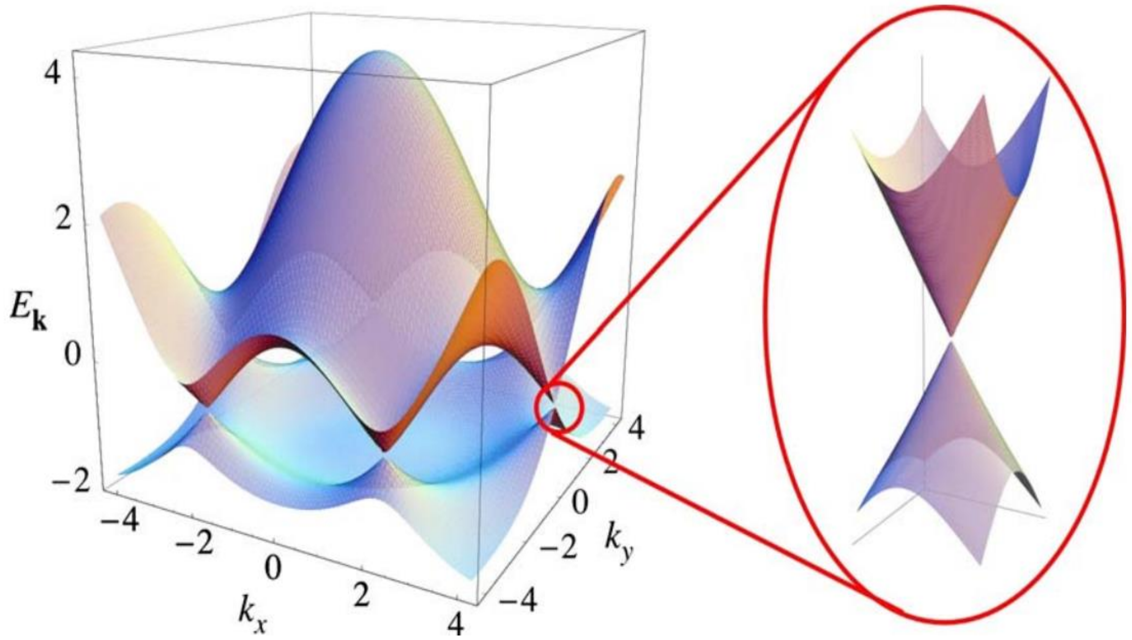

Figure 2.3: *Electronic dispersion of graphene with next-nearest neighbour interaction included and the linear dispersion around the Dirac points highlighted [38].*

still translates between lattice sites, which is not the case for the reciprocal of $\boldsymbol{t_j}$ in graphene. This results in $f(\boldsymbol{k})$ of eqn. 2.20, and hence the resultant low-energy Hamiltonian (eqn. 2.27) off-diagonals becoming complex, consequently making the dispersion linear at certain momenta [46]. While it is possible to produce 2D systems which also exist within a hexagonal lattice structure, such as hBN [51], the atoms are non-identical and thus the sublattice symmetry is broken, inducing diagonal terms into the eqn. 2.27 and thus forcing a band gap into the electronic dispersion [38]. Knowledge of this allows for many possible avenues for the induction of a band gap within graphene by sublattice symmetry breaking through methods such as charge doping [52], physical confinement of charge carriers [53, 54] and straining of the atomic lattice [44, 55].

2.1.2 Physical properties

Electronic properties

In order to understand the origin of graphene's unique electronic characteristics, one must first grasp the concept of pseudospin and chirality. As mentioned in Section 2.1.1, charge carriers within graphene exists on one of two in-equivalent sublattices.

Just as the spin degree of freedom allows an electron pair to be distinguished from one another, so to does the sublattice to which they belong. It is for this reason that the electrons within graphene are said to inherit a pseudospin, $\boldsymbol{\sigma}$, which is determined by the sublattice that they occupy and serves as an additional degree of freedom [50]. Dirac particles of each psuedospin state contribute one arm of the linear energy dispersion each [46], allowing the electrons and holes within each band to be characterised depending on their momenta as is shown in Figure 2.4.

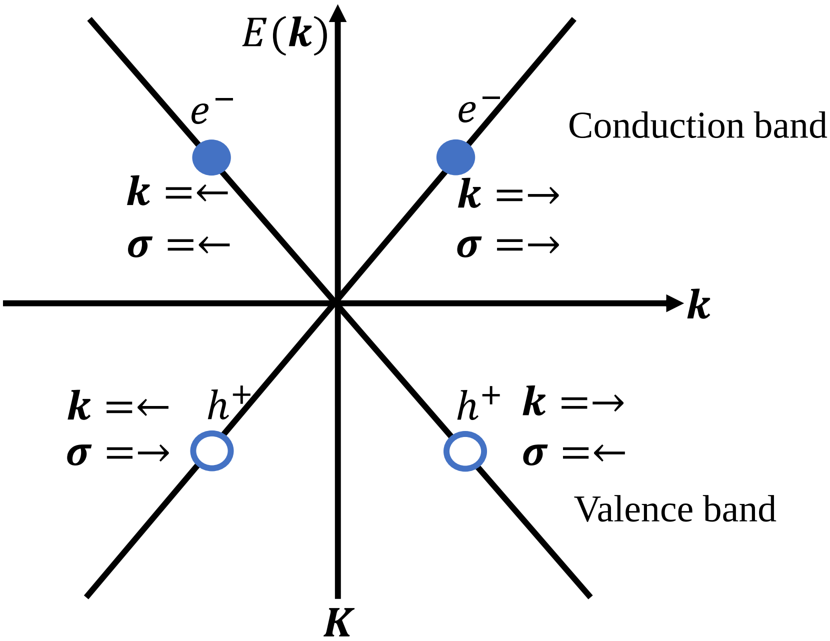

Figure 2.4: *The relative orientations of the electron (e^-) and hole (h^+) momenta,* $\mathbf{k}$*, with respect to the pseudospin,* $\boldsymbol{\sigma}$*, in each arm of the linear dispersion around the* $\boldsymbol{K}$ *point in graphene.*

The existence of this pseudospin degree of freedom facilitates Klein tunneling [56] within graphene when the charge carriers are incident upon a potential barrier. To understand this, consider a free electron with energy E incident on a potential barrier V such that $E < V$, as shown in Figure 2.5.

As is well known, quantum mechanics predicts that the electron has a non-zero probability of existing on the other side of the barrier, with the probability decreasing with increasing potential barrier thickness and height [42]. Therefore, for a sufficiently high barrier the transmission probability effectively goes to zero. Now consider a Dirac particle normally incident upon a potential barrier where the potential is high, so that $E \ll V$, and is smooth on the scale of the lattice parameter, such that

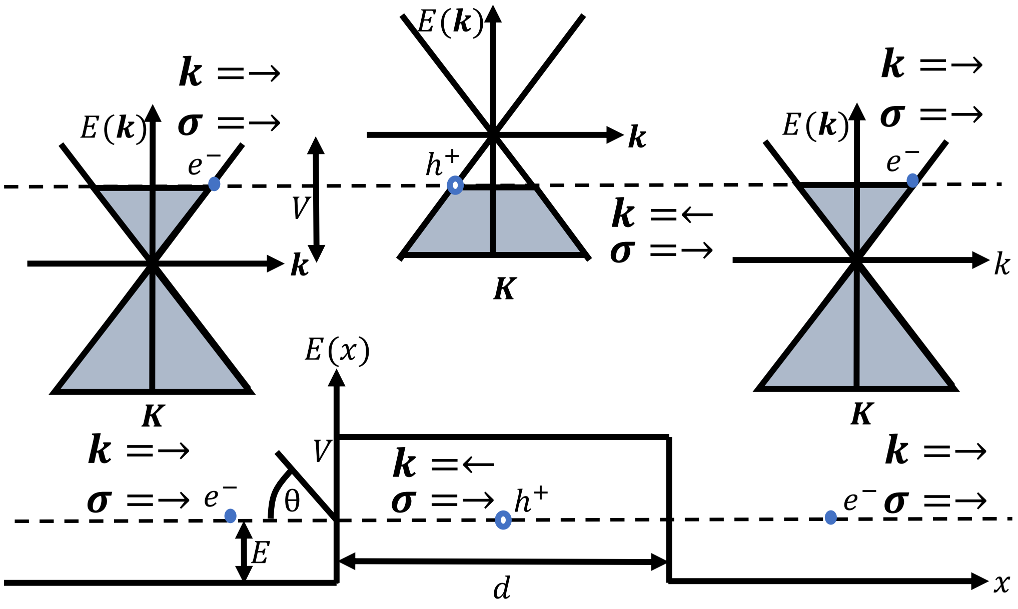

Figure 2.5: *Diagram showing the change in Fermi level position within the potential barrier and how it facilitates pseudospin-based Klein tunneling.*

neighbouring Dirac cones are decoupled during the interaction [57]. Upon reaching the potential barrier the electron will attempt to backscatter and hence reverse its momentum, $\boldsymbol{k} \rightarrow -\boldsymbol{k}$, which, as can be seen from Figure 2.4, would result in it transferring to the opposite arm of the Dirac cone, requiring $\boldsymbol{\sigma} \rightarrow -\boldsymbol{\sigma}$. However, the potential is not coupled to the psuedospin, which only exists within sublattice space [57], meaning that pseudospin must be conserved throughout this interaction and thus backscattering is prohibited [46, 57].

In order to understand what happens instead, one needs to consider that the Fermi level can shift as the particle enters the potential barrier (Figure 2.5). The linear energy dispersion offered by graphene ensures that regardless of the initial energy of the particle there is always a state with a matching energy inside of the potential barrier, which, for a conduction band electron incident on the potential barrier, will correspond to a valence band state due to the shift in Fermi level. Therefore, in order to conserve pseudospin during the scattering process, the electron shifts along its own arm of the Dirac cone into the valence band and propagates forward unimpeded by the barrier [57]. This is pseudospin facilitated Klein tunneling [46, 56, 57, 58, 59], although the word “tunneling” is a misnomer as it doesn’t tunnel in the usual sense. This phenomenon, along with the observation of unitary transmission at certain critical angles due to quantum interference within the barrier [58, 59], are partially responsible for the high mobility of the charge carriers in graphene even at room temperature by means of ballistic transport [60]. It may also be responsible for the minimum in the conductivity observed experimentally even in the limit of vanishing charge density [46, 57].

Mechanical properties

Graphene has an extremely high Young's modulus of ~ 1 TPa along with an intrinsic, defect-free tensile strength of 42 Nm^{-1} [61], making it one of the stiffest, strongest materials known. It is the σ-bonds within the lattice of graphene which are directly responsible for this mechanical robustness [38]. Exploitation of the high intrinsic breaking strength of graphene has already begun via incorporation of monolayers into various materials to improve their mechanical properties [62], whilst at the same time graphene's superior Young's modulus enables the production of high performance nanoelectromechanical systems (NEMS) [63].

NEMS are a class of device which integrate electrical and mechanical functionality on the nano-scale, and include devices such as force, mass and charge sensors which are designed around a central resonating component. Previously, ultra-thin Si cantilevers have been investigated as a potential NEMS, but have inferior Young's moduli ($\sim 50 - 170$ GPa) and deteriorate with decreasing thickness [61, 64]. Graphene, being a 2D membrane of high surface area and stiffness, along with having low mass, naturally represents the ultimate limit for nanoresonators [63]. As a result, it has already been shown to exhibit superior responsivity to external stimuli with force and charge sensitivities of ~ 1 $\text{fN/Hz}^{\frac{1}{2}}$ and $\sim 1 \times 10^{-3}$ $\text{electrons/Hz}^{\frac{1}{2}}$ [61], respectively, outperforming other NEMS within the literature [64, 65]. Graphene resonators also exhibit a quality factor of ~ 210 [63].

Furthermore, graphene monolayers only absorb 2.3% of incident light [66]. In conjunction with the aforementioned electrical and mechanical properties, this allows graphene to function as transparent, flexible electrodes in the next generation of nanoelectronic devices [67, 68]

Thermal properties

Efficient removal of heat (in particular at hot spots generated in regions of high power density) from modern electronic devices and systems has become a critical limiting factor in their performance and reliability [69]. Usually, a micro or nano-scale semi-conducting heat spreader would be used to dissipate energy away from these hot spots, but as the scale of these devices decrease this becomes less effective as the thermal conductivity of semiconductor nanostructures diminishes with decreasing lateral dimensions [70].

Graphene is a nanoscale material which has a room temperature thermal conductivity of $\kappa \approx 3000 - 5000$ WmK^{-1} in suspended samples (it is known that κ varies with the purity, grain size and sample size of the graphene flake [71], hence the large variation), although this value decreases for graphene adhered to a substrate due to enhanced phonon scattering by the inevitable defects and impurities present on the substrate surface [72, 73]. The thermal properties of graphene are analogous to that of graphite in that thermal conductivity is extremely high in the direction parallel to the plane as a result of the strong sigma bonds between atoms and low atomic mass whilst at the same time it is reduced in the direction of the c-axis due to weak van der Waal coupling between layerszcitepop2012thermal. The difference between graphite and graphene however arises due to enhanced phonon mean free path (itself due to the uniquie phonon dispersion of graphene) allowing for near-ballistic phonon transport for typical exfoliated sample sizes, leading to an increase in thermal conductivity. Therefore, graphene offers not only high thermal conductivity for a material of this length scale, but one of the highest known thermal conducivities in general, making graphene a potential candidate for heat control in future nano-scale electronic devices [69, 74].

2.1.3 Multilayer graphene and graphite

Band structure of multilayer graphene and graphite

As the number of graphene layers within the crystal increases the electronic dispersion changes. Rather than simply being similar to that which is found in monolayer graphene, each type of few-layer graphene system has its own characteristic dispersion. The band structure evolves from linear in monolayer, to parabolic in bilayer and then to overlapping parabola in trilayer graphene [45]. This evolution continues as the number of layers increases into the limit of bulk graphite, as is shown in Figure 2.6.

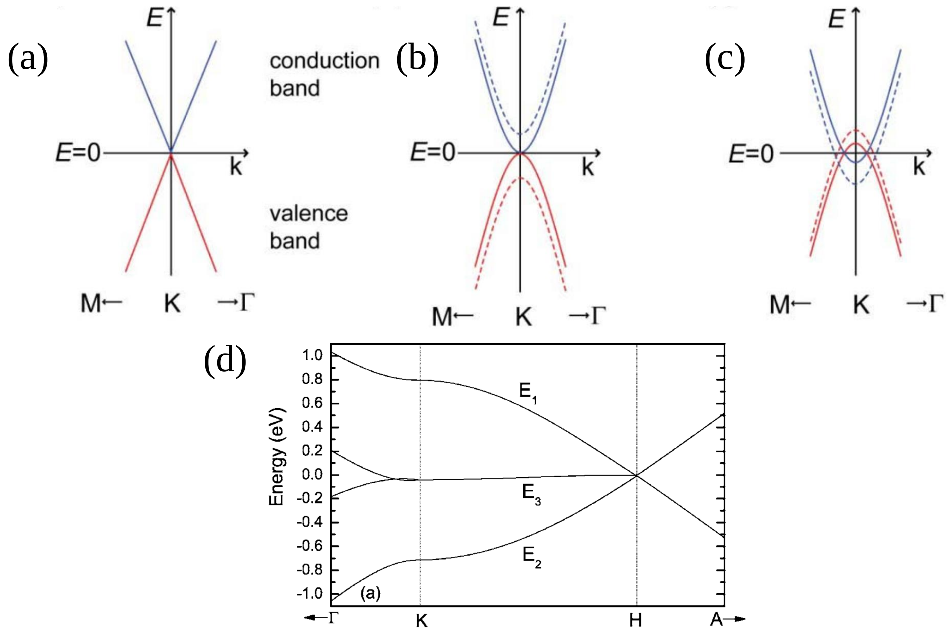

Figure 2.6: *Evolution of the electronic dispersion of (a) monolayer, (b) bilayer and (c) trilayer graphene along with (d) that of bulk graphite. The dotted lines in (a-c) represent the band structure during application of a perpendicular electric field. (a-c) Adapted from [45], while (d) was taken from [75].*

The different layers can be stacked in two main different ways: Bernal stacking, where all the atoms in one sublattice, say A, in the upper graphene sheet lie above atoms from sublattice A in the lower sheet, while atoms in sublattice B of the upper sheet lie directly above the hexagonal spaces in the underlying graphene sheet (in an ABAB.. sequence), and rhombohedral stacking, which would have sublattice B atoms in a third layer lying above atoms within sublattice A of the second (in an ABCABC.. sequence) [76].

The addition of a second layer of graphene allows for inter-layer hopping of charge carriers in addition to the inter/intra-sublattice hopping discussed within Section 2.1.1, transforming the low-energy Hamiltonian (eqn. 2.27) into a 4×4 matrix and adding diagonal terms corresponding to the shift in chemical potential between the two layers [38] (if such a potential change exists, for example by independant electrical gating of the two layers [77], otherwise the dispersion of pristine bilayer graphene remains gapless [38]). This alters the electronic dispersion in two ways: firstly, the introduction of diagonal terms into the low-energy Hamiltonian of impure bilayer graphene forces a band gap into the electronic dispersion (similar to other materials like hBN [51], see Section 2.2.1), and secondly, the additional off-diagonal terms transform the low-energy dispersion from linear to quadratic, resulting in charge carriers with a non-zero effective mass [38].

The addition of a third graphene layer similarly alters the system Hamiltonian, in this case causing the top of the valence band and bottom of the conduction band to overlap at the $\boldsymbol{K}$-points thus leading to a finite density of states at the Fermi level [45]. The electronic dispersion continues to change as the number of layers increases until ~ 10 layers are reached, at which point it has approached the dispersion of bulk graphite [78].

2.2 Hexagonal boron nitride

2.2.1 Lattice and band structure

Bulk hexagonal boron nitride is composed of atomically thin monolayers of boron and nitrogen in a hexagonal lattice formation. Similar to graphene, the two species undergo sp^2 orbital hybridization to form strong σ-bonds while the individual monolayers are attracted to their neighbours via weak vdW bonding, allowing for mechanical exfoliation of monolayers in the same manner as graphene [51]. hBN is therefore an isomorpth of Bernal-stacked graphite with the A and B sublattices being occupied by equal numbers of boron and nitrogen atoms arranged in a honeycomb configuration [79, 80], see Figure 2.7, with a comparable lattice constant to that of graphene, $a_{\mathrm{hBN}} \approx 2.5$ Å[81] (~ 1.7 % mismatch to graphene [79]).

Following Section 2.1.1, we can use the tight-binding approach to model the band-structure of hBN. Unlike graphene, the sites of the two sublattices are occupied by different species of atom which have their own on-site energies of E_B and E_N for boron and nitrogen, respectively. The sublattice symmetry is therefore broken and

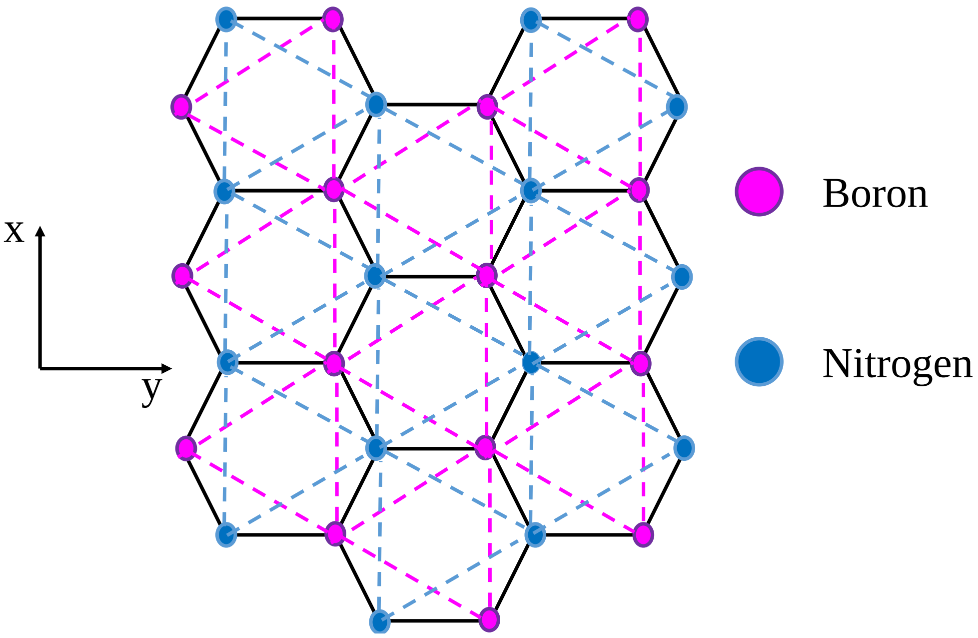

Figure 2.7: *The hexagonal lattice structure of monolayer hBN. The individual triangular sublattices are indicated by the dashed pink (blue) lines corresponding to occupation of lattice sites by boron (nitrogen) atoms.*

the resultant Hamiltonian becomes

$$\mathbf{H} = \begin{pmatrix} E_B & \Phi \\ \Phi^* & E_N \end{pmatrix}, \tag{2.30}$$

where

$$\frac{\Phi}{t} = 1 + \exp\left(ia\left(\frac{-k_x}{2} + \frac{\sqrt{3}k_y}{2}\right)\right) + \exp\left(ia\left(\frac{k_x}{2} + \frac{\sqrt{3}k_y}{2}\right)\right) \tag{2.31}$$

and t is the hopping parameter for charge carriers moving between nearest neighbours only [82].

Following the same derivation method discussed in Section 2.1.1, one can see that the dispersion relation for monolayer hBN is

$$E = E_0 \pm \frac{1}{2}\sqrt{E_g^2 + 4|\Phi|^2}, \tag{2.32}$$

where $E_0 = (E_B + E_N)/2$ is the energy in the middle of the band gap and $E_g = E_B + E_N$ is the width of the band gap [83]. This is a clear example of how breaking sublattice symmetry can induce band gaps within these materials, along with how the magnitude of these band gaps are related to the on-site energies of the constituent species of the lattice [79]. In reality, this corresponds to a direct band gap of $E_g \sim 5.97$ eV in pristine hBN crystals at the K-points of the Brillouin zone [51], thus making hBN an insulator. A comparison between the bandstructures of graphene and hBN is given in Figure 2.8. It is clear that the bandstructure of hBN is very similar to graphene throughout most of the Brillouin zone, only markedly differing at the K/K'-points.

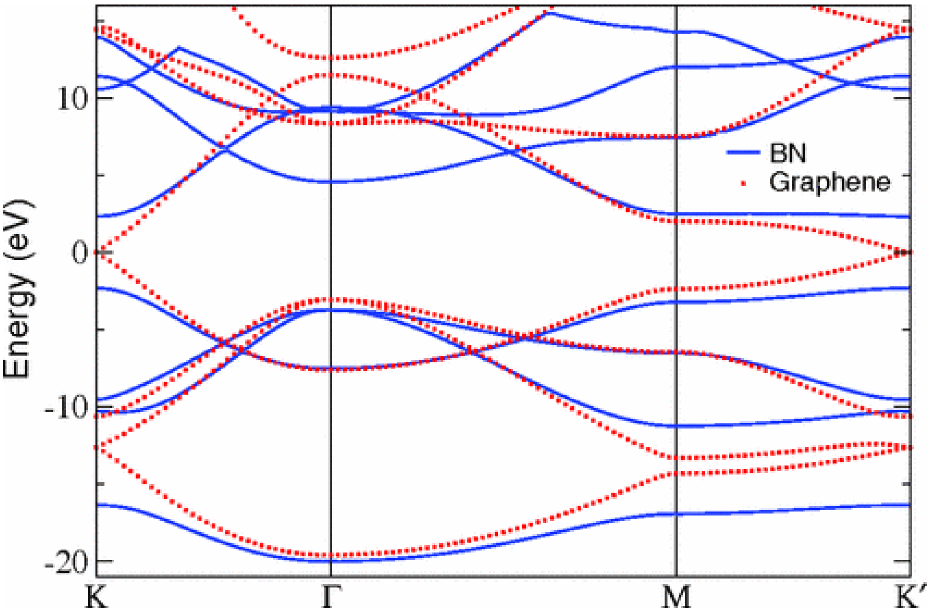

Figure 2.8: *A comparison between the bandstructure of monolayer hBN (blue solid curves) and graphene (red dotted curves). Taken from [82].*

2.2.2 Physical properties

The strong in-plane ionic bonding between the boron and nitrogen ions and lack of surface dangling bonds or charge traps causes hBN to be both relatively inert [51, 79] and atomically flat [84]. This, in addition to having insulating behaviour and resistance to oxidation and corrosion [80, 85], allows hBN to be used as an ideal gate dielectric for the study of not just graphene but many other 2D materials as well [79, 86, 87, 88]. This is due to suppression of scattering events by the substrate (e.g. from interfacial charge traps and surface impurities/phonons from the substrate) and adsorbates from the environment (e.g. from contamination, oxidation and thermally/electrically induced degredation) when used to encapsulate samples, which in turn serves to improve device performance by increasing charge carrier mobility [80]. Figure 2.9 compares the surface topography and charge density of hBN and SiO_2, a commonly used dielectric substrate in 2D materials research, and clearly highlights the relative performance of each. Furthermore, hBN is also optically transparent [80] and so does not impede optical probing measurements when used as encapsulation.

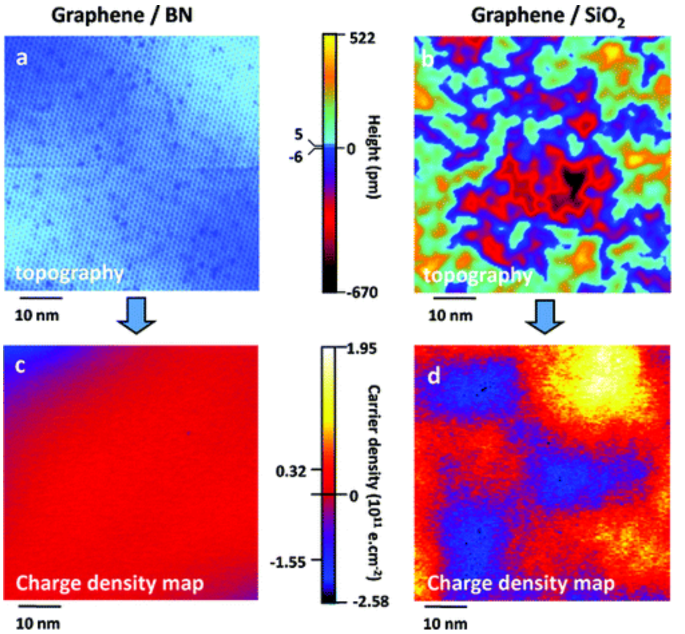

Figure 2.9: *A comparison of the surface topography and charge density for (a) a graphene/hBN and (b) a graphene/*SiO_2 *heterostructure. Taken from [89].*

It has been shown that incorporation of hBN crystals into graphene-based devices, either as a substrate [79] and/or as encapsulation [90, 91] significantly improves carrier mobility and overall device performance and is even comparable to suspended graphene samples [91]. Moreover, hBN has an optical phonon mode energy two times that of SiO_2, a high breakdown field $V_{\text{breakdown}} = 0.7$ Vnm^{-1} and high dielectric constant of $\epsilon \sim 3-4$, allowing general 2D devices utilising hBN as a substrate to have improved performance at higher temperatures and applied electric field strengths compared to their contemporaries utilising SiO_2 [51, 80].

Lastly, the high thermal stability of monolayer hBN (oxidation begins at 850 °C in ambient conditions [92], compared to $\sim$ 300 °C for graphene [93]), high thermal conductivity ($\kappa = 243$ WmK^{-1} [94]), along with excellent mechanical strength (Young's modulus $\approx$ 0.865 TPa and tensile strength of 8.8 Nm^{-1} [95]) serves to drastically increase the scope of potential applications for this material in 2D device design [80] .

2.3 Transition metal dichalcogenides

2.3.1 Lattice and band structures

Transition metal dichalcogenides (TMDCs) are group-VI semiconducting crystals of the form MX_2, where M are transition metals (e.g. Mo, W) and X are chalcogens (e.g. S, Se). Bulk TMDC crystals have a layered structure where each TMDC monolayer consists of a 2D hexagonal lattice of M atoms sandwiched between two hexagonal lattices of X atoms (X-M-X) [11, 96, 97] in two main polytypes of interest, see Figure 2.10 (a, b), respectively. These refer to the octahedral (1T) and thermodynamically stable trigonal prismatic (2H) co-ordination geometries for describing the bulk crystal, in specific reference to the vertical arrangement of layers within the unit cell [96]. In the case of an MX_2 monolayer however, the nomenclature is such that a 2H-MX_2 (1T-MX_2) monolayer refers to one which is isolated from a 2H (1T) bulk crystal [96]. Either way, each TMDC monolayer is bound together by covalent intralayer bonds whilst being attracted to adjacent monolayers (when in a bulk crystal) by weak vdW forces of attraction, allowing for easy exfoliation into individual monolayers. For example, it has been shown that monolayer TMDCs can be extracted using mechanical exfoliation [98], CVD [99] and liquid phase exfoliation [34].

The electronic band structure of pristine TMDCs are determined by the lattice polytype and the nature of the orbital hybridization between the d-orbitals of the transition metal atoms and the p-orbitals of the chalcogen atoms [96, 97]. The valence and conduction bands of the 2H (1T) polytype are made by hybridization of the d_{xy}, $d_{x^2-y^2}$ and d_{z^2} [97, 100] (d_{xy}, d_{xz} and d_{yz} [96, 101]) orbitals of the M atoms with the p_x, p_y and p_z orbitals of the chalcogen atoms [97], resulting in semiconducting (metallic) behaviour as is shown in Figure 2.10 (c, d). The ability to be either metallic or semiconducting at room temperature is true of most MX_2 materials [11, 102], with the stable phase at room temperature being the 2H phase [102], although the 1T phase can be obtained by Li-intercalation [103] or electron beam irradiation [104] of the 2H phase as well. Stable 1T phases can also be formed by plasma induced phase change from the 2H phase [105] as well.

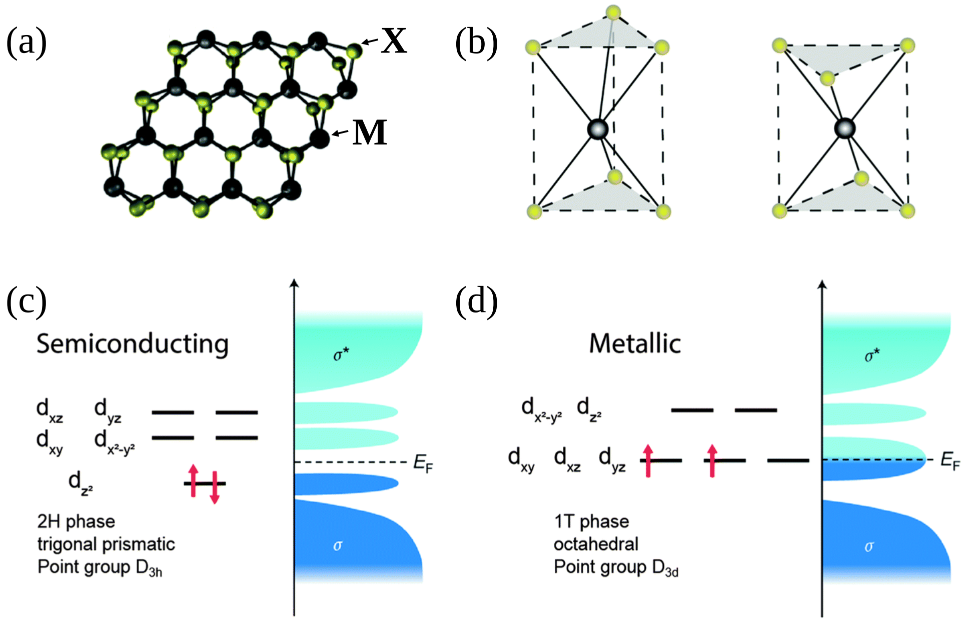

Figure 2.10: *Atomic and electronic structure of MX_2 TMDCs. (a) Top-down view of monolayer MX_2. (b) Trigonal prismatic (left) and octahedral (right) co-ordination geometries. (c) Filling of the non-bonding d-orbitals, band structure and Fermi energy, E_F, for trigonal prismatic (2H) phase and (d) octahedral (1T) phase. Adapted from [96].*

Another key aspect of group-VI TMDCs is the effect of the number of layers on the electronic band structure. As can be seen in Figure 2.11, 2H-MX_2 materials transition between indirect semiconductors in the bulk to direct semiconductors when in monolayer form [96, 97, 106, 107, 108, 109]. Therefore 2H-MX_2 materials have a band gap in the visible to near infrared (1-2 eV) [96] depending on the material and number of layers which, as will be discussed in Section 2.7.3, is responsible for a number of interesting and useful optoelectronic properties [5, 107, 110]. The transition from indirect to direct is a result of quantum confinement of charge carriers in the direction perpendicular to the plane of the monolayer as the thickness decreases [109, 111] and the resultant absence of interlayer interactions [112], causing the indirect band gap width to increase at a faster rate than the direct gap until eventually the material transitions into a direct band gap semiconductor [111]. This, along with a change in the orbital hybridization between the M and X atoms [109], is ultimately responsible for this peculiar behaviour within MX_2 materials. Furthermore, spin-orbit interactions in monolayer TMDCs split the valence band maximum at the K-points of the Brillouin zone [112], see Figure 2.11 (c), resulting in the formation of two separate excitonic features within the photoluminescence spectrum [97] as will also be discussed in Section 2.7.3. It should also be noted that the magnitude of the spin-orbit splitting is greater in MX_2 materials when X=Se than when X=S, and when M=W than when M=Mo, due to the greater atomic mass [97].

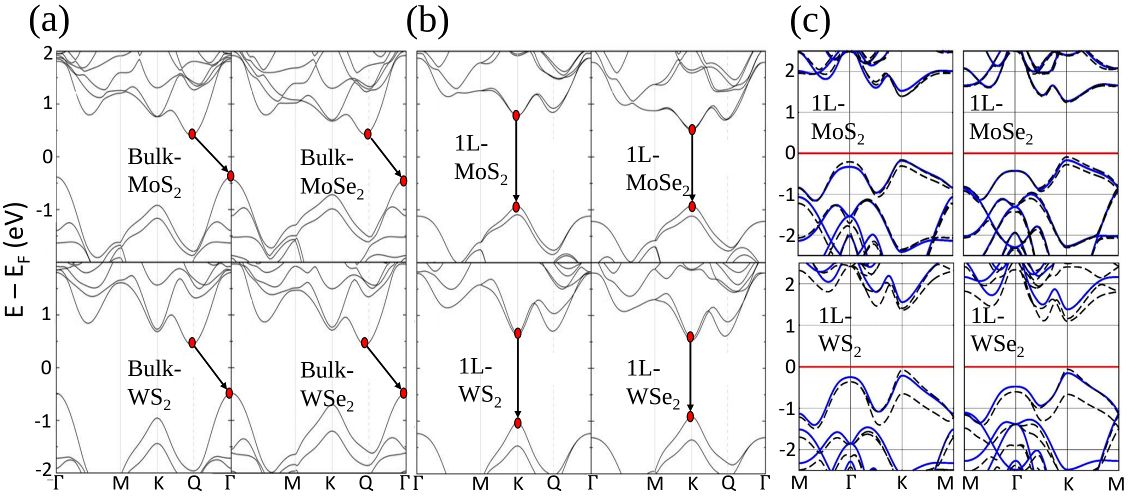

Figure 2.11: *Bandstructures of various TMDC (a) monolayers (1L) and (b) bulk crystals as calculated using density functional theory (DFT). The transition between states at the top of the valence band and bottom of the conduction bands (red circles) are indicated. Adapted from [97]. (c) Electronic band structure of monolayer TMDCs with the effect of spin-orbit coupling included (dashed-black) compared to when it is neglected (solid blue), calculated using DFT. Adapted from [113].*

2.3.2 Physical properties

Electronic properties

The presence of a band gap in 2H-MX_2 materials, along with atomic scale thickness and lack of dangling bonds (negating the need for lattice-matching, e.g. as is needed for graphene/hBN heterostructures) [109] is a distinct advantage compared to graphene with regards to incorporation into vdW heterostructure devices, particularly in the production of high performance FETs. The next generation of ultra-compact FETs require both decreased device length scales and an increase in electrical performance, such as having increased switching speeds, reduced energy cost per switch and improved sub-threshold swings [114]. To meet these requirements, there has been significant research efforts into replacement FET channel materials which have a large band gap (to reduce current on/off ratios), atomic scale thickness (mitigating scaling issues such as source-drain tunneling) and have high carrier mobility (for improved switching behaviour).

In addition to having a large band gap and atomic thickness, pristine TMDCs can also have high field-effect carrier mobilities, with values of $30-60$ cm^{2}V^{-1}s^{-1}, ~ 50 cm^{2}V^{-1}s^{-1}, 50 cm^{2}V^{-1}s^{-1} and ~ 80 cm^{2}V^{-1}s^{-1} in MoS$_2$, MoSe$_2$, WS$_2$ and WSe$_2$ FETs (using mono/few-layer channels, SiO$_2$ dielectrics of similar thickness and measured at room temperature), respectively [115, 116, 117, 118]. Compared to other 2D materials such as graphene, these values of mobility pale in comparison ($\mu \sim 10,000$ cm^{2}V^{-1}s^{-1} for graphene on SiO$_2$ [119]). However, pristine graphene does not possess a band gap and can only be modified to have one under specific circumstances [77, 120, 121], and so cannot be used to produce competitive FETs thus preventing a meaningful comparison to TMDCs in this case.

The fundamental mobility of TMDC monolayers is limited by the high effective mass of the charge carriers [96], although in real devices the mobility is often less than this due to short range scattering by surface adsorbants (e.g. charged impurities, such as water), interfacial phonons/charged defects from the substrate and TMDC lattice defects/vacancies, as well as the amount of dielectric screening from the environment [22, 23, 97, 122]. Furthermore, the mobility is dependant on the method used to fabricate the monolayers. For example, in CVD-grown monolayers the charge carriers can scatter on grain boundaries which lie perpendicular to their movement, lowering their mobility, although if the domains are large enough then the mobility in these devices can be even higher than in exfoliated flakes [96, 123]. These factors explain why there is such a large variation of TMDC monolayer mobilities reported in the literature, with values typically ranging between $1-1000$ cm^{2}V^{-1}s^{-1} [96]. Understanding this, one can therefore improve TMDC mobilities by encapsulation (to quench phonon modes, protect from adsorbants and electrically screen the channel) [109, 122], careful device fabrication to limit defects and through careful selection of the dielectric substrate to one which preferably has a large band gap and band offset to the TMDC to prevent leakage current, as well as having a lack of dangling bonds and being atomically flat.

The electronic band structures of monolayer TMDCs are also highly sensitive to external pertubations such as strain, pressure and doping as a result of their atomic thickness [97, 109]. Strain lowers the band gap within monolayer TMDCs until a semiconductor-metal transition occurs at around 10 % strain in addition to shifting it back to indirect [124, 125], with similiar effects occuring for mono and few-layer TMDCs under high pressure as well [126, 127]. Metallic behaviour can also be induced via application of an external electric field or doping, even allowing for a superconducting transition in MoS_2 [97, 128, 129], see Figure 2.12 (a). This extreme electrical sensitivity to the local environment allows for TMDCs to be used in a variety of NEMS and sensing applications [130, 131, 132, 133], along with having the potential to fine-tune the electrical properties of the material in a highly controllable manner [102].

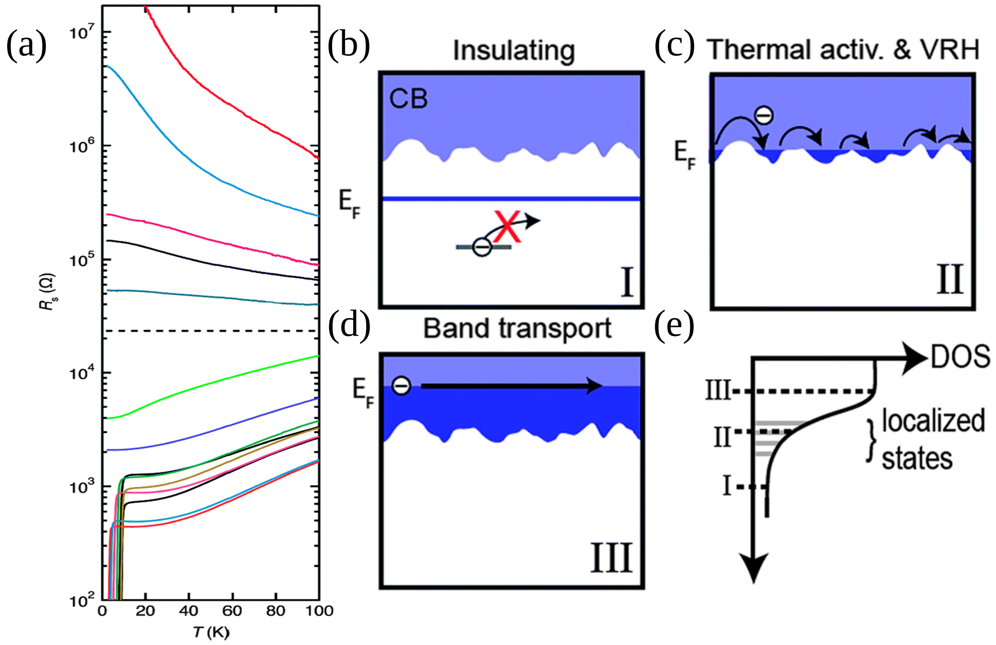

Figure 2.12: *(a) Temperature dependant resistivity of ionically gated few-layer* MoS_2*. (b-d) Schematic energy diagram representing different charge transport regimes: (b) insulating; (c) conduction by thermal activation and hopping; and (d) band transport. (e) Density of states diagram showing the disorder-derived band tails states (I and II), along with that of the conduction band (III). All panels adapted from [96].*

The conduction mechanism in monolayer TMDCs depends on the Fermi energy. At low doping (low Fermi energy), there are no mobile charge carriers and so the monolayer TMDC is insulating (Figure 2.12 (b)). At intermediate doping levels, the Fermi energy is shifted towards the conduction band edge and thermal activation of charge carriers allows for hopping conduction between impurity-induced localised edge states (Figure 2.12. (c)). Eventually, at very high doping levels, the Fermi energy is shifted entirely into the conduction band and the TMDC has metallic behaviour (Figure 2.12. (d)) [96].

Mechanical properties

TMDC monolayers are almost as thin, transparent and flexible as graphene [102]. MoS_2 has a Young's modulus of ~ 270 GPa and an average tensile strength of ~ 15 Nm^{-1} [134], making ultrathin MoS_2 the strongest known semiconducting material [109]. Similar behaviour can be expected of other group-VI monolayers because of their analogous lattice structures [109], with $MoSe_2$, WS_2 and WSe_2 predicted to have Young's moduli of $\sim 100 - 120$ Nm^{-1}, $\sim 140 - 160$ Nm^{-1} and $\sim 110 - 130$ Nm^{-1}, respectively [135]. Moreover, MoS_2 NEMS exhibit a quality factor, Q, between $\sim 100 - 700$ depending on its thickness [136, 137, 138], surpassing that of graphene, whilst $Q_{WSe_2} \sim 160$ [139]. Unfortunately, the field of TMDC NEMS is not as developed as graphene NEMS, and so a proper comparison cannot be completed. Despite this, the combination of high field-effect mobility, atomic thickness, flexibility and transparency will no doubt allow for the incorporation of ultra-thin TMDC materials into a variety of transparent and flexible electronics.

Thermal properties

The thermal conductivity of monolayer MoS_2, $MoSe_2$, WS_2 and WSe_2 are $\sim 30 - 90$ $Wm^{-1}K^{-1}$ [140, 141], 59 $Wm^{-1}K^{-1}$ [141], 32 $Wm^{-1}K^{-1}$ [142] and 0.05 $Wm^{-1}K^{-1}$ (the lowest thermal conductivity known for a dense solid) [143], respectively. These low thermal conductivities and, in MoS_2, large and tunable Seebeck coefficient (from -4×10^2 to -1×10^5 μVK^{-1} [144]), make monolayer TMDCs promising candidates for future thermoelectronic applications [145].

2.4 Talc

2.4.1 Lattice and band structure

Talc is a crystalline hydrated magnesium silicate with the general unit cell chemical formula $Mg_3Si_4O_{10}(OH)_2$ [10], although some deviation may be present due to substitution by small amounts of Al, Ti, Fe and Mn. Depending on the concentration of these impurities, talc is usually green, white, grey, brown or colourless in its bulk form, however many people would be more familiar with the material in its white powdered state where it is known as talcum powder ("baby powder"). It is a phylosilicate mineral with a monoclinic crystal symmetry [146], meaning it possesses a layered structure held together by vdW forces of attraction [147]. It has a small interlayer binding energy per unit area ($\sim 0.1 - 0.3$ Jm^{-2}) and tensile strength ($\sim 29 - 33$ Nm^{-1} for uniaxial deformation of monolayers), both of which make it amenable to mechanical exfoliation into monolayer sheets [10] in the same manner as other layered materials [2]. The crystal structure of monolayer talc is illustrated in Figure 2.13, while a comparison between the bulk and monolayer band structures is given in Figure 2.14.

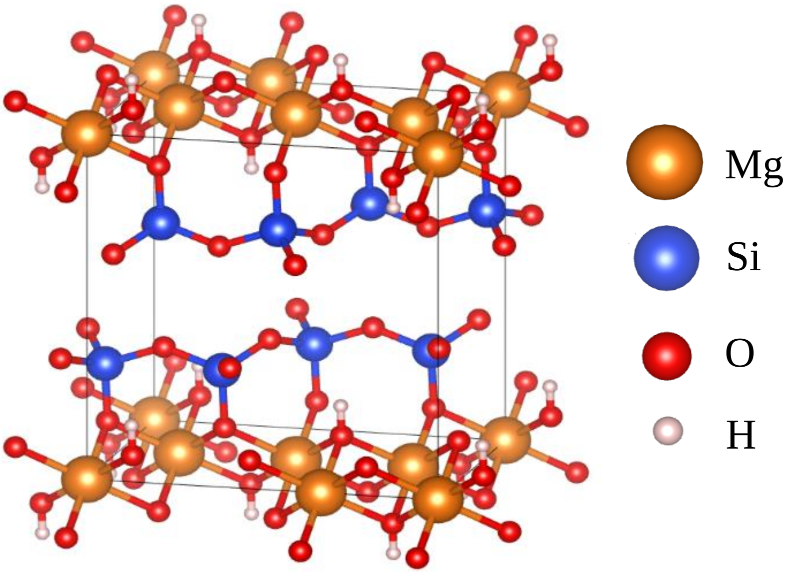

Figure 2.13: *The crystal structure of monolayer talc.*

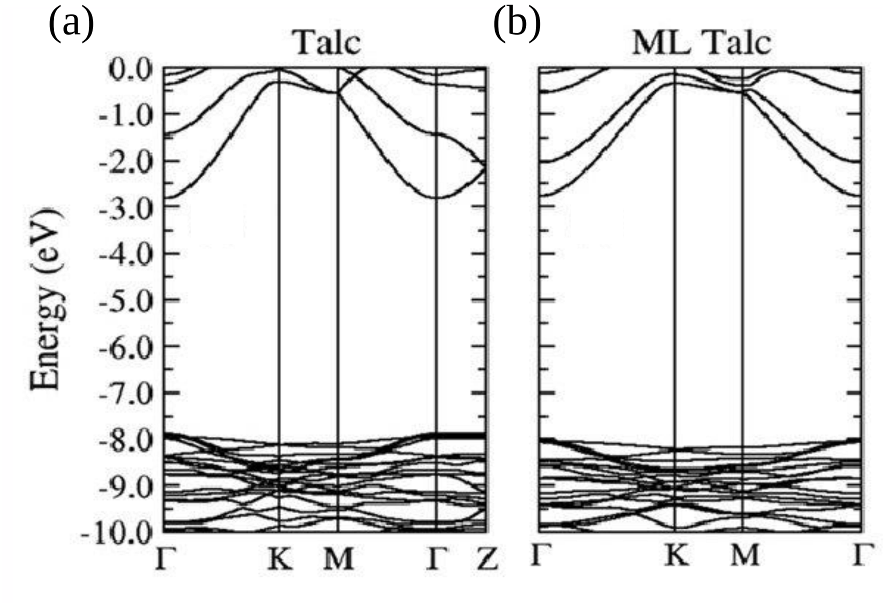

Figure 2.14: *Electronic band structures of (a) bulk and (b) monolayer (ML) talc calculated using density functional theory. Adapted from [10].*

As can be seen in Figure 2.14, both monolayer and bulk talc are insulators with a band gap $E_g \approx 5.3$ eV, with conduction band minima and valence band maxima located at the Γ-point of the Brillouin zone [10]. Furthermore, in addition to having a sizeable band gap, monolayer talc is also atomically flat like hBN [30], and so offers an interesting alternative substrate for fabrication of high quality 2D devices.

2.4.2 Physical properties

Bulk talc is the softest material known with a rating of 1 on the Mohs hardness scale, and has a number of interesting properties such as high electrical and thermal shock resistance, chemical inactivity, heat resistance, hydrophobicity [148] and oil absorption properties [149], all of which have resulted in its use in many industrial applications such as cosmetics, pharmaceuticals, paints, papers, ceramics and as a solid lubricant [150].

So far, hBN stands out as the ultimate substrate material for investigating the intrinsic properties of 2D materials such as the quantum properties of graphene near the charge neutrality point [151]. However, this begs the question of whether any interesting phenomena occur in graphene at Fermi energies away from the neutrality point, such as the expected phase transition to superconducting behaviour at high doping levels in graphene [152]. Furthermore, the presence of high doping concentrations in other 2D materials is also sometimes desired, for example as in high-performance lateral MoS_2 p-n junctions [153]. It has recently been shown that monolayer talc can be used as a substrate to spontaneously induce p-doping in graphene whilst maintaining high carrier mobility [30], therefore circumventing the need for other doping methods (such as ionic gating [154]) which considerably deteriorate device performance [30]. Therefore it is within this niche, that of a substrate which allows for controlled doping of 2D materials whilst preserving their electronic qualities, which monolayer talc crystals occupy. Also, in addition to being an insulator, having monolayer thickness and being chemically inert, talc is also orders of magnitude cheaper than hBN [10].

Important for incorporation within electronic devices, especially in FETs, is the dielectric constant, ϵ_r, which in talc is $\epsilon_r \approx 2.5$ [30]. This, in conjunction with its sizeable band gap, allows talc to compete with SiO_2 as an insulating substrate especially in the formation of ultra-compact FETs [148].

Finally, mono and few-layer talc has also been shown to possess some surprising mechanical properties such as negative compressibility, meaning it expands when subject to external pressure, and flexural rigidity, D, which is the stiffness of the monolayer to flexural deformations. It has been calculated that $D_{\text{talc}} = 68 \times 10^{-19}$ J while $D_{\text{graphene}} = 2.2 \times 10^{-19}$ J, and thus talc is $\sim$ 30 times stiffer than graphene [10]. It is also surprisingly resilient to uniaxial deformations with a theoretical defect-free intrinsic tensile strength between 29 Nm^{-1} - 33 Nm^{-1} [10], which is comparable to that of graphene (42 Nm^{-1} [61]), one of the strongest known materials. Therefore, to summarise the mechanical properties, talc is almost as strong as graphene for uniaxial deformations, but significantly stiffer to flexural deformations.

2.5 Interfacial physics

The very nature of 2D materials inevitably results in most, if not all in the case of graphene and its isomorphs, of their constituent atoms being located on the surface. As a result, their physical properties are uniquely sensitive to external pertubations such as strain and doping from the substrate to which they are mounted. Therefore, it is for this reason that gaining an understanding of the interfacial physics between a sample and its mount is of crucial importance when it comes to device design and experimental repeatablility.

2.5.1 Self-cleaning

Direct stacking of vdW materials to create a heterostructure inevitably leads to the presence of residues such as water and hydrocarbons between the individual layers [155, 156, 157]. Even after thermal annealing in high vacuum samples often remain densely covered in residue, and as a result one cannot be said to have a true vdW heterostructure but rather two loosely coupled layers glued together by contamination [155]. However, it has been found that certain combinations of materials lead to a "self-cleaning" phenomena, whereby the contaminants diffuse along the interface and become concentrated into pockets, leaving large areas of clean, strongly coupled heterostructure available for measurement [155, 156]. In order for this to occur the vdW materials to be stacked must have a degree of hydrophobicity – if one or both of them are hydrophillic, or they do not experience strong vdW coupling, then self-cleansing cannot happen [157].

This useful property is a result of dewetting induced hydrophobic collapse of the material/residue/material structure [157]. It has been found that confinement of water between two nanometre scale hydrophobic planes leads to the liquid becoming metastable at its vapour state under certain conditions [158]. The energy barrier for this dewetting (i.e. evaporation) transition depends upon temperature and the hydrophobicity of, and gap size between, the two planes. An increase in temperature and hydrophobicity, or a decrease in gap size, lowers the transition energy barrier and encourages dewetting. Therefore, under certain conditions, evaporation of residual water occurs leading to hydrophobic collapse and vdW stacking of the two planes of material, expelling the residue at this point of contact. The area in transition between the point of contact and the fully separated layers forms an ascending slope in the upper material plane. The gap size is therefore reduced here, leading to dewetting once again and thus the process repeats, creating a front of hydrophobic collapse which propagates away from the initial point of contact and forces the water, plus any other residue, along the interface and into confined pockets [157]. Another way of picturing this process is that if the affinity between the two 2D crystals is larger than between the crystals and the contaminants, then the energetically favourable situation is when the two crystals have the largest possible common interface. This condition is thus achieved when contaminants are pushed along the interface into pockets [14].

However, in particularly contaminated samples residue can remain between the planes. This can be removed by either: thermal annealing [155], where the increase in temperature facilitates dewetting; or through the "squeegee" method [157, 159], which involves using an atomic force microscope (AFM) tip to compress the planes together, reducing the gap size and hence initiate the self-cleaning process. The latter of these is illustrated in Figure 2.15.

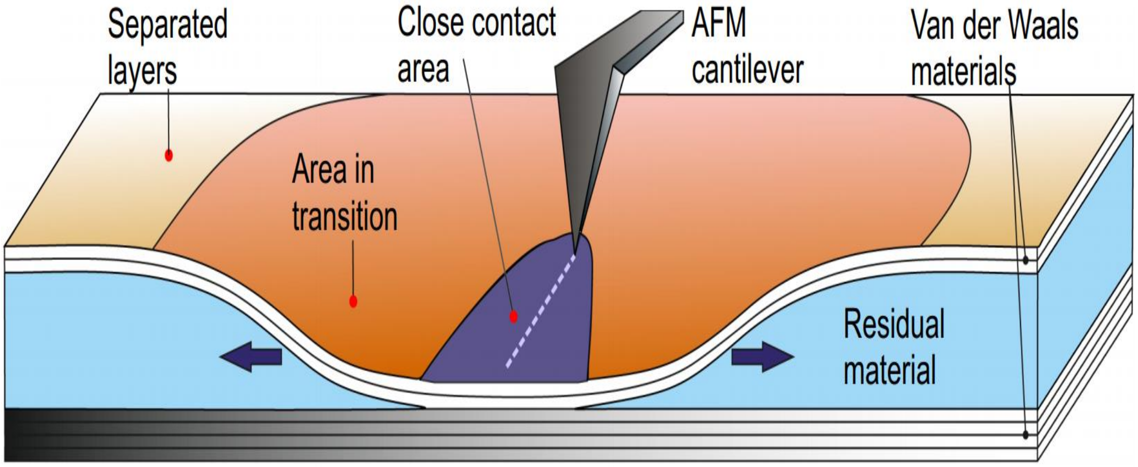

Figure 2.15: *Schematic of the squeegee interface cleaning method using an atomic force microscope (AFM) tip to expel residual contaminants. Adapated from [157]*

The self-cleaning process results in the formation of residual pockets which can lead to charge inhomogeneity and thus scattering [156], degrading sample-wide device performance. The squeegee method allows for the removal of these although, as the AFM must be used in contact mode, unwanted sample damage may occur (see Section 3.4.1). Likewise, thermal annealing of the sample can induce strain and a change in the relative rotation of the two vdW planes [157]. It is therefore apparent that one must decide whether investigation of a self-cleaned domain is sufficient or if further treatment is needed using the above processes in an attempt to achieve sample-wide cleanliness.

2.5.2 Surface roughness

The use of SiO_2/Si-based substrates for the manufacture of 2D devices has been popular since the discovery of graphene due to the ease with which suitable flakes can be identified as well as the high dielectric constant of the SiO_2 overlayer [2]. Unfortunately it was soon discovered that graphene devices produced in this manner were highly disordered and exhibited electronic qualities far inferior to that which was theoretically predicted [79]. As mentioned in Section 2.2.2, this reduction is largely due to carrier scattering from charged surface states and impurities, but it is also due to the roughness of the underlying SiO_2. Being a flexible membrane, graphene partially conforms to the SiO_2 and thus its surface morphology is determined by that of the substrate [160]. This manifests in the formation of corrugations within the graphene sheet which, in turn, act as scattering centres and lower the charge carrier mobility [161]. In fact, this phenomena extends beyond graphene and it has been observed that many thin films deposited onto any rough surface, not just SiO_2, also undergo wrinkling [161, 162, 163].

It is for this reason that atomically flat substrates such as hBN [79] and mica [162] have been increasingly used to produce high quality devices, as conformation to these results in a significant reduction of surface roughness of the 2D material, see Figure 2.16 (a-c) and Figure 2.9 (a, c). As can clearly be seen, in each case the 2D material partially conforms to the underlying substrate, resulting in a reduction in surface

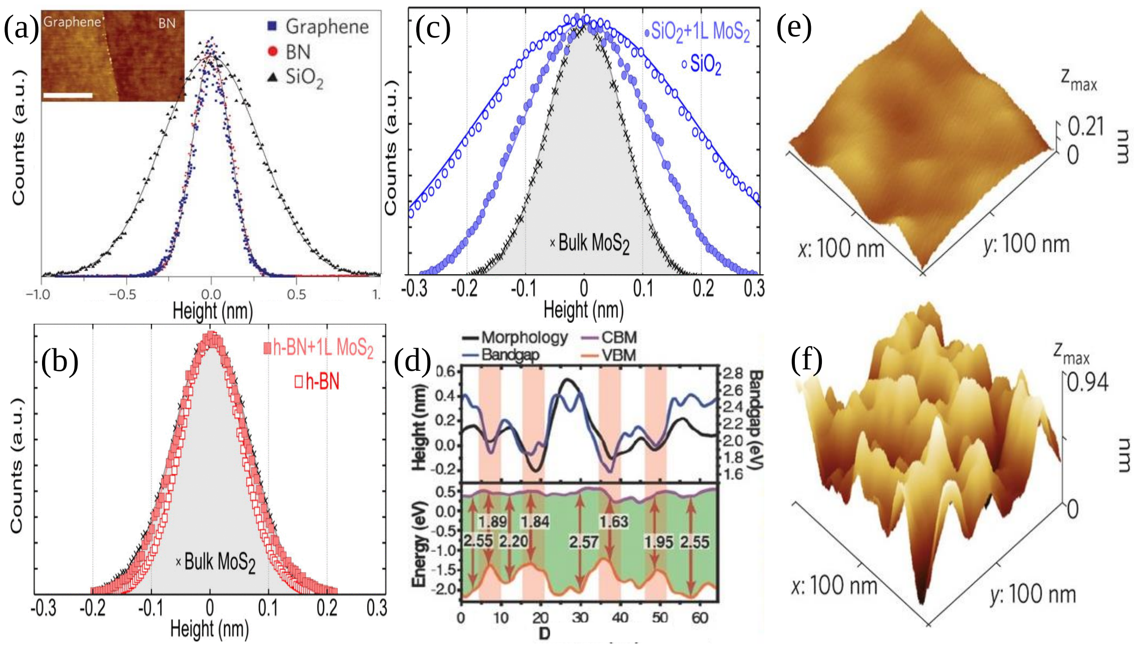

Figure 2.16: *Histograms of the height distribution (surface roughness) measured by AFM for (a) graphene/hBN, bare hBN and bare* SiO_2*. Inset: high-resolution AFM image showing comparison of graphene and hBN surfaces, (b) monolayer* MoS_2*/hBN and bare hBN and (c) monolayer* MoS_2/SiO_2 *and bare* SiO_2*. Solid lines are Gaussian fits to the distributions. (d) Line profiles of the height, band gap, valence band maximum (VBM) and conduction band minimum (CBM) for an area of monolayer* MoS_2/SiO_2*. (e, f) STM topographic image of graphene/hBN and graphene/*SiO_2*, respectively. (a) was adapted from [79], (b, c) were adapated from [162], (d) was adapted from [164] and (e, f) were adapted from [165].*

roughness. This reduction is most evident in the STM topographs illustrated in Figure 2.16 (e, f). In graphene, conformation to a rough surface introduces strain into the lattice [165]. This local curvature can, in turn, lead to inadvertant doping of the lattice [165, 166] and pseudo-magnetic fields [167], both of which can be detrimental to device performance. In monolayer TMDCs this locally induced strain results in variation in the electronic band gap with position via a change in lattice constant, even leading to a direct-indirect transition across much of the sample [164]. Figure 2.16 (d) illustrates the effect of surface roughness on the band gap of monolayer MoS_2, and clearly demonstrates the importance of a suitable choice of substrate in order to accurately measure the intrinsic properties of TMDCs.

Although rough substrates should be avoided, it has been noted that the use of atomically flat substrates which lack the ability to self-clean does not always correspond to an increase in device quality, indicating that having an atomically clean and sharp interface should be a greater priority than minimising substrate roughness [156].

2.5.3 Charge transfer and band alignment

As discussed previously, mounting onto a substrate can alter the electronic properties of a 2D material via interfacial roughness and cleanliness. This section is devoted to the discussion of another process, that is the intrinsic charge transfer across the interface either into or out of the system.

Graphene/metal interface: Electronic transport measurements through graphene require contacts to metal electrodes, and so it is essential to have a full understanding of the physics of the metal/graphene interface [168]. For instance, it is now known that when graphene is bound to Co, Ni or Pd, the graphene band structure is significantly perturbed as a result of the strong bonding which could potentially result in the removal of the conical structure at the K/K'-points of the Brillouin zone [168, 169], whilst bonding to metals such as Al, Ag, and Cu is significantly weaker and thus the intrinsic properties of graphene are preserved [168]. In both cases the difference in Fermi level between the metal and graphene drives charge carriers between the two in order to equilibriate their Fermi levels, resulting in either n or p-type doping within the graphene depending on whether its Fermi level is shifted to higher or lower energies, respectively, see Figure 2.17 (b). More precisely, the charge transfer is driven by the disparity in average energy between carriers occupying states at the Fermi level in each material - those occupying a higher Fermi level have a higher average energy, and so they naturally migrate to the material with lower Fermi energy once contact is established [170]. As the density of states around the Dirac point in graphene is much lower than that of the metal conduction band, equilibrium is essentially achieved by shifting the Fermi level of the graphene alone. Once equilibrium has been achieved, the transfer of charge across the interface and the subsequent separation between the two charged sides results in the formation of an interfacial dipole layer with an associated potential step [168], leading to charge scattering at the interface and an increase in contact resistance [171]. Ideally, contact resistance should be minimised within an experiment in order to properly characterise a given device, and so an appropriate choice of contacting metal is required.

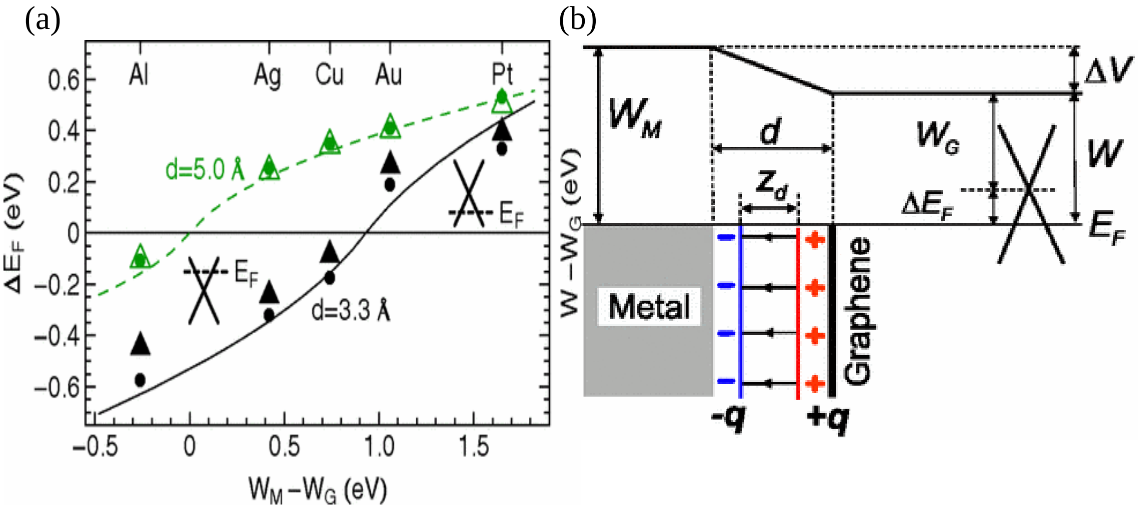

Figure 2.17: *(a) Calculated Fermi energy shift with respect to the Dirac point, ΔE_F (dots), and change in work function, $W - W_G$ (triangles), as a function of $W_M - W_G$, the difference between the metal and graphene work functions. The insets illustrate the position of the Fermi level with respect to the Dirac point of graphene. (b) Illustration of the interface dipole and potential step formation at a graphene-metal interface. Z_d is the effective charge separation distance, d is the metal-graphene separation distance and ΔV is the potential step height at the interface. Adapted from [168].*

Graphene/substrate interface: Similar to a graphene-metal interface, graphene also becomes doped when bound to an insulating substrate. It is known that graphene bound to SiO_2 promotes the formation of electron-hole "puddles" [172], which are regions which have a pronounced positive or negative charge as a result of extrinsic adsorbates present along the interface [173], see Figure 2.9. Furthermore, it has been predicted that graphene experiences a net gain in charge when placed onto SiO_2 due to the formation of a partially occupied state above the Dirac point. This pins the Fermi level above the Dirac point and thus the graphene becomes n-doped [174]. The magnitude and type of doping depends upon the substrate, which can force a positive or negative shift in the Fermi level of graphene and thus induce n or p-doping, respectively [175, 176]. This can be further tailored via the use of functional molecules/groups adhered to the substrate before exfoliation of the graphene, which can serve to increase carrier concentrations (up to $\sim 10^{12}$ cm^{-2}) or change the carrier type entirely [176].

Graphene/TMDC interface: Contact between graphene and a semiconducting 2H-MX_2 TMDC crystal results in the formation of a Schottky barrier at the interface [170], see Figure 2.18, with potential (approximately) equal to the energy difference between the conduction band minimum of the TMDC and the Fermi level of graphene, as is shown in Figure 2.18 (b) [177]. As a result, this barrier to charge transfer between the two layers also depends on the individual doping of the layers as well. This, in addition to temperature (via thermal excitation of carriers across the Schottky barrier), allows for a measure of control over the number of carriers which can move between the layers [177]. Upon initial contact, charge moves between the two materials in order to equilibriate the Fermi levels as previously described, leading to doping in both of the layers [170].

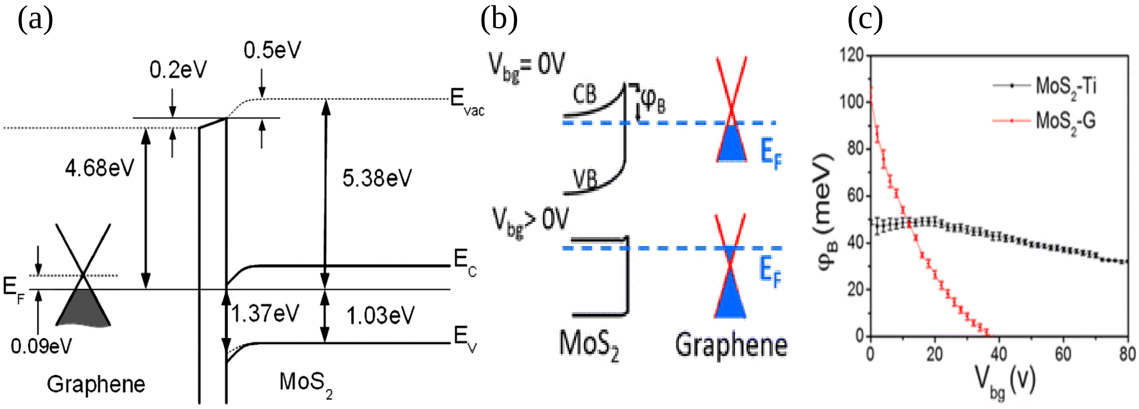

Figure 2.18: *(a) Illustration of the electronic band structure at a graphene/MoS_2 interface. E_C, E_V and E_{Vac} are the conduction, valence and vacuum energies, respectively. (b) Influence of an external bias voltage, V_g, on the graphene Fermi level and overall Schottky barrier height, Φ_B. (c) Schottky barrier height as a function of bias voltage for a MoS_2/graphene and MoS_2/Ti junction. Adapted from [178, 179].*

Rather than comprehensively considering each TMDC material in turn, a monolayer MoS_2/graphene heterostructure will be used as a representative example. In this case, the graphene becomes *p*-doped and the MoS_2 becomes n-doped [170]. It has been predicted that the small binding energy and large separation between the two layers corresponds to only a weak interlayer interaction, preserving the linear band structure of the graphene along with its unique properties [180]. As TMDCs have a large band gap, metal/TMDC contacts typically have a large Schottky barrier and thus high contact resistance. The highly tunable Fermi level of graphene allows for an excellent work function match between it and the MoS_2, lowering the Schottky barrier and consequently reducing the contact resistance by ~ 10 times compared to conventional metal/MoS_2 contacts, see Figure 2.18 (b, c) [170, 179]. As a result, graphene is often incorporated into TMDC devices as simply a transparent and flexible electrode if not for any higher purpose.

TMDC/metal interface: In the same manner as TMDC/graphene interfaces, metallic contacts to semiconducting TMDC materials results in the formation of a Schottky barrier at the interface [181]. The carrier type moving through the TMDC depends on the relative position of the Fermi level of the metallic contact to either the conduction or valence band of the TMDC. For example, a metal with a Fermi level aligned close to the TMDC conduction band (i.e. one with a low work function) facilitates electron injection whereas alignment close to the TMDC valence band (i.e. a metal with a high work function) facilitates hole injection [182]. In either case, the Schottky barrier limits the charge transfer into the TMDC and thus increases contact resistance, and so significant effort has been made to reduce the metal-TMDC Fermi level disparity in order to produce ohmic contacts. Other than using graphene as a mediation material between the metallic contacts and the TMDC, one can dope the TMDC material present beneath a metal contact in order to locally tune the Fermi level in this region [182]. This is usually done through the introduction of a surface dopant before the contacts are deposited, such as potassium (for n-type doping) or NO_2 (for p-type doping), although other, more damaging methods exist such as plasma doping of the contact area as well [182, 183, 184, 185].

It should be noted that, specifically, the Schottky barrier height, Φ_{SB}, is not precisely determined by the difference in metal work function, Φ_M, and semiconducting electron affinity, χ_S, such that the Schottky-Mott equations,

$$\Phi_{SB-n} = \Phi_M - \chi_S \text{ and } \Phi_{SB-p} = E_G + \chi_S - \Phi_M, \tag{2.33}$$

are erroneous [181]. Instead, the real Schottky barrier height lies between the Schottky and Bardeen limit, with the latter describing the pinning of the metal Fermi level at some interface state energy, Φ_{IS}, within the TMDC band gap [181, 182]. If these states are metal induced gap states (from superposition of metal and semiconducting surface atomic orbitals [181]) then the Fermi level is pinned at the semiconducting charge neutrality level (the Fermi level position which ensures no net surface charge). In this case, the Schottky barrier height is approximated as

$$\Phi_{SB-n} = (S \times \Phi_M - \chi_S) + (1 - S)\,\Phi_{IS}, \tag{2.34}$$

where the Schottky pinning factor, $S = \partial\Phi_{SB-n}/\partial\Phi_M$, modulates the strength of energy level pinning with $S = 0$ (1) indicating strong (weak) pinning [181, 182].

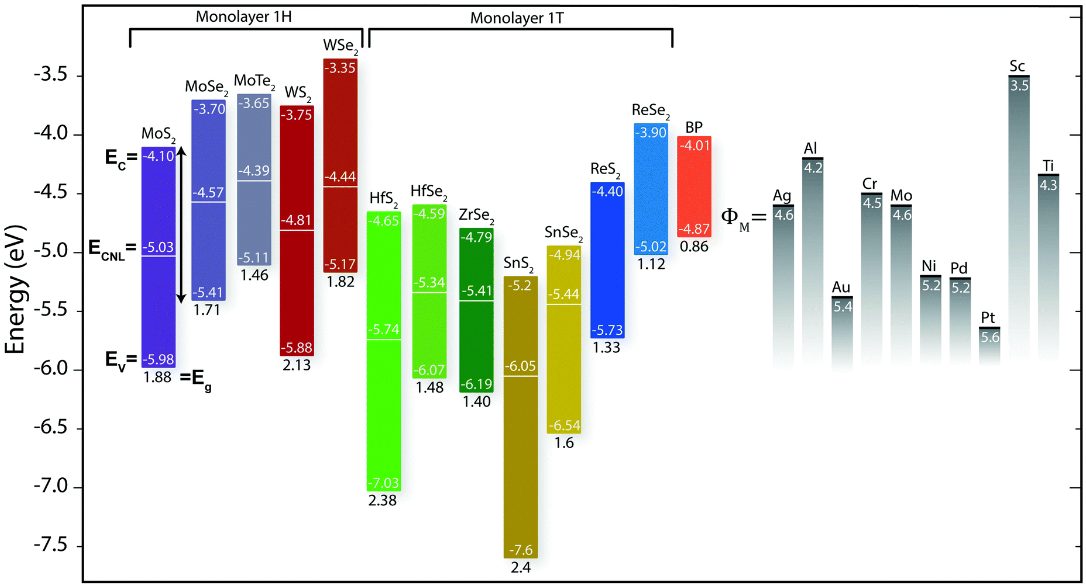

Figure 2.19: *Schematic of the band gap, electron affinity, ionisation potential and charge neutrality levels (CNL) for a selection of monolayer 2D materials along with the work functions of common contact metals. Adapted from [182].*

Figure 2.19 illustrates the calculated band alignments using density functional theory for a variety of 2D materials along with the work function of commonly used contact metals. Were the Schottky barrier height determined via eqn. 2.33, we would expect $\sim \Phi_{SB} = -0.7$ eV for MoS$_2$ with Sc contacts, although it is actually much closer to $\sim$ 30 meV due to Fermi level pinning, as is shown in Figure 2.20. Likewise, WSe$_2$

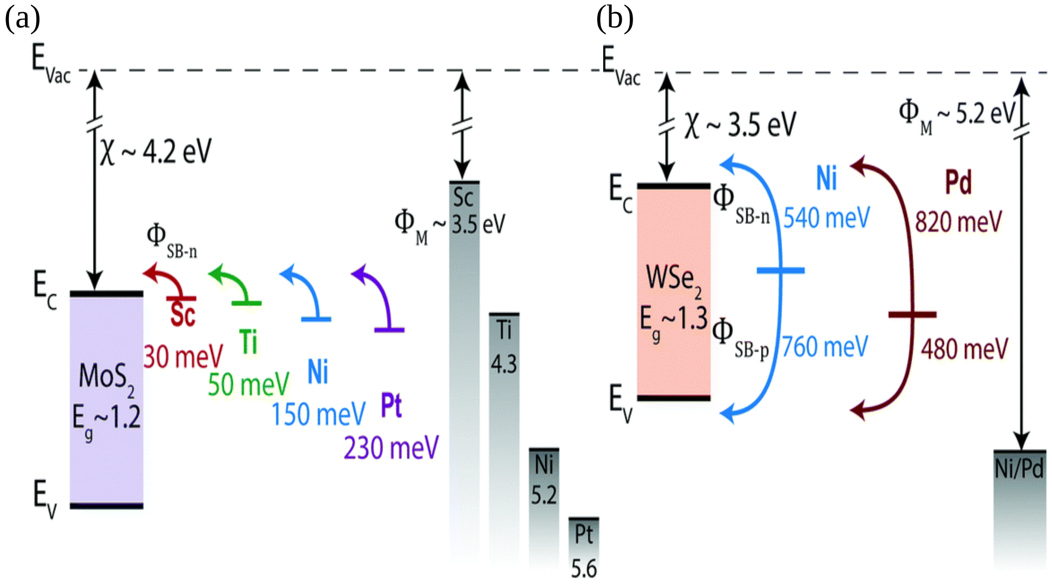

Figure 2.20: (a) The expected (top-right, grey bars) and actual (top-middle, coloured lines) metal/MoS_2 band alignment showing pinning near the TMDC conduction band. (b) The expected and actual band alignment for Ni and Pd with WSe_2 showing mid-gap Fermi level pinning. Adapted from [182].

should have a Schottky barrier height of $\sim$ 1.7 eV which is reduced to $\sim$ 540 meV due to Fermi level pinning towards the centre of the TMDC band gap. This also explains the FET behaviour of these TMDCs, as metals pin close to the conduction band of MoS_2 [186], leading to electron injection and n-type behaviour [187], and close to the middle of the band gap in WSe_2, allowing choice of either electron or hole injection and thus ambipolar behaviour [182]. It should be noted that the exact mechanism behind Fermi level pinning is unknown as of yet, although it has been shown that it is possible to de-pin the Fermi level via chemical doping [187]. Previously, Fermi level pinning severely restricted the choice of carrier type in FETs, and so it would appear that de-pinning via chemical doping would once again allow for control of the charge carrier type in traditionally unipolar TMDC FETs through careful choice of the contacting metal (and thus the metal work function).

TMDC/substrate interface: As will be discused in Section 3.3.1, the direct-gap semiconducting nature of 2H-MX_2 TMDC monolayers allows for the formation of neutral quasiparticles called excitons upon the absorption of a photon. In TMDCs, these have a binding energy $\sim$ 1-2 orders of magnitude greater than in conventional materials such as GaAs [188] which allows for strong light-matter coupling at room temperature. This, along with having high optical absorption ($\sim 5\%$) [25], makes monolayer TMDCs appealing candidates for the next generation of efficient optoelectronic devices.

Unfortunately, like graphene, it has been observed that placement of monolayer TMDCs onto substrates such as SiO_2 results in the loss of key properties of the material such as a stark reduction in photoluminescence [189, 190, 191]. Charge transfer into the TMDC alters the number of neutral (charged) excitons (trions) present, modulating the intensities of the corresponding PL emissions, as well as broadening their full-width half-maxima due to increased exciton-carrier scattering and subsequent reduction of excitonic recombination times [190], see Figures 2.21 and 2.22. It is thought that charge transfer from the substrate is due to the energy difference between the charge neutrality point of the substrate and the vacuum being less than the work function of the TMDC, thus driving electrons into the latter [190]. Fortunately, the PL emission intensity can be recovered through the use of substrates such as hBN and $SrTiO_3$ which minimise doping of the TMDC [189, 190].

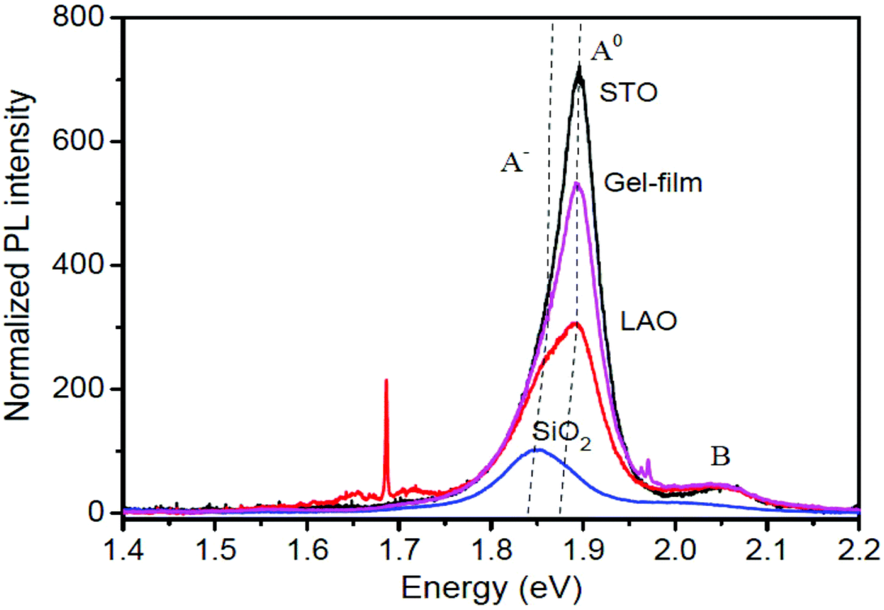

Figure 2.21: *Normalised PL spectra of monolayer MoS_2 on SiO_2, $LaAlO_3$ (LAO), Gel-film and $SrTiO_3$ (STO) substrates. Adapted from [190].*

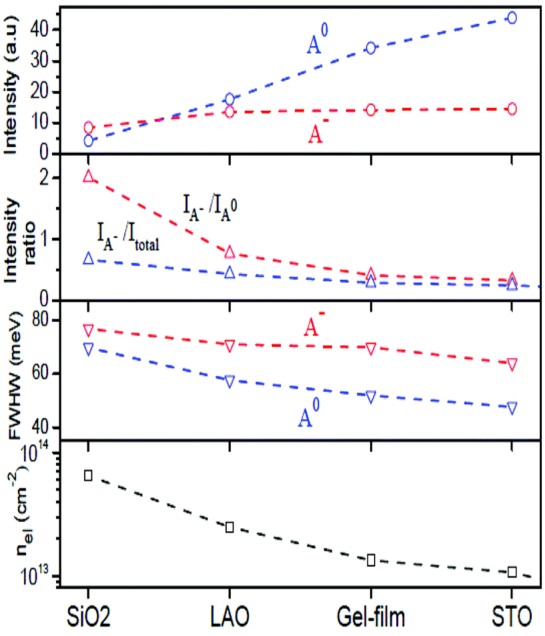

Figure 2.22: *For monolayer MoS_2 on different substrates: Top panel: Integrated intensity of neutral exciton emission (A^0) and trion emission (A^-). Second panel: The PL emission intensity ratios I_{A^-}/I_{A^0} and $I_{A^-}/(I_{A^0}+I_{A^-})$. Third panel: The FWHM of the neutral exciton and trion emission peaks. Bottom panel: Estimated electron density within the MoS_2 monolayer. Adapted from [190]*

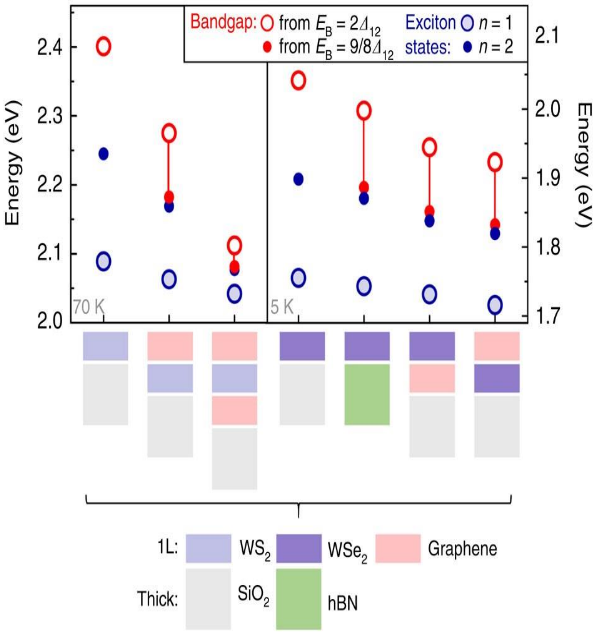

Figure 2.23: *Experimentally measured exciton ground state ($n = 1$) and first excited state ($n = 2$) transition energies, as well as estimated shifts in band gap energy for a variety of heterostructures. Adapted from [192].*

It has also been demonstrated that both the exciton binding energy and electronic band gap of monolayer TMDCs can be tuned by engineering the surrounding dielectric environment through proper substrate selection (see Figure 2.23 and Section 3.3)

[192, 193]. Therefore, careful substrate selection is required not just to prevent external doping but also to preserve the intrinsic electronic and optical properties of the monolayer TMDC.

TMDC/TMDC interface: Contact between two semiconducting TMDC crystals inevitably results in the exchange of charge between them due to the formation of a type-II band structure across the interface. Here, the energy offsets between the conduction and valence bands of the two TMDCs means that it becomes energetically favourable for electrons (holes) to move from the material with the higher (lower) conduction (valence) band into the material with the lower (higher) conduction (valence) band, see Figure 2.24 (a) [194].

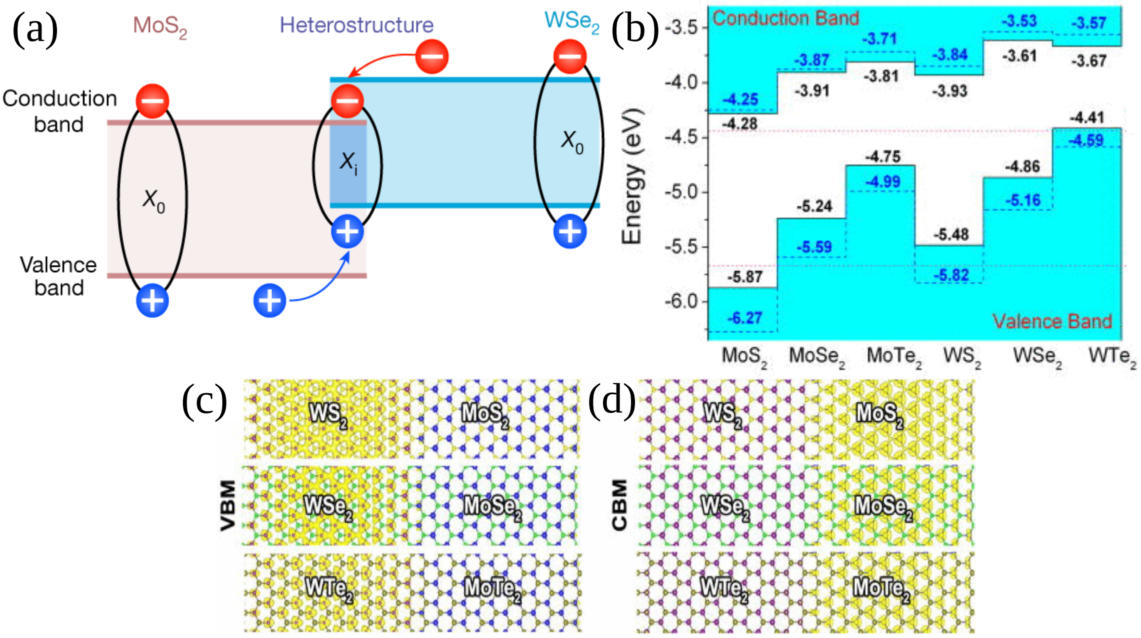

Figure 2.24: *(a) Representative type-II band alignment across a* MoS_2/WSe_2 *interface. (b) Calculated band alignment for* MX_2 *monolayers. (c) Charge density at the valence band maximum (VLM) and (d) conduction band minimum (CBM) for monolayer* WX_2/MoX_2 *heterostructures with common X. (a) was adapted from [195], whilst (b-d) was adapted from [194].*

This spontaneous separation of free electrons and holes proves to be a useful attribute of these 2D systems as it encourages the break up of neutral intralayer excitons which diffuse to the interface which can prove to be useful for photovoltaic applications such as solar cells [194]. Furthermore, interlayer, spatially separated excitons (where the electron and hole reside on opposite sides of the heterostructure interface, see

Figure (c, d), can form [194, 195], which manifests as the appearence of an additional peak in the PL spectra of the TMDC heterostructure [195]. Spatial (and momentum, when lattice mismatch between the layers is present as recombination is now indirect and requires the involvement of an external phonon) separation of the constituent electron and hole improves recombination times by an order of magnitude, from $\sim$ picoseconds in intralayer excitons to $\sim$ nanoseconds in interlayer excitons [195, 196]. Therefore, exploitation of these interlayer excitons facilitates exciton diffusion over micrometre length-scales [195] which, in addition to having high binding energies, bodes well for the use of monolayer TMDCs in the next generation of opto-electronic devices.

2.5.4 Triboelectric effect

The triboelectric effect is a type of contact-induced electrification, owing to which a material would become electrically charged after it comes into frictional contact with another dissimilar material, whereby the materials become oppositely charged after contact with the strength of the charges being different for different materials [197]. Despite being first observed over 2600 years ago [198], a conclusive model for explaining this phenomenon has not yet been reached. Until recently the general consensus was that electrification was due to either electron or ion transfer across the interface upon contact of two materials [199], although one can now tentatively assert the former [200]. Figure 2.25 illustrates a proposed electron cloud/potential well model which can be used to explain triboelectric charging between two dissimilar materials.

For two materials, A and B, the electrons within each atom occupy a potential well due to the Coloumb interaction between the electrons and the positively charged nucleus, see Figure 2.25 (a). When material A contacts material B, the electron clouds of the surface atoms (two, in this example) overlap and the initial two single potential wells become one asymmetric double-well. Electrons occupying states of higher energy in the potential well of one material, say A, can then hop into the lower energy states of material B, resulting in charge transfer across the interface

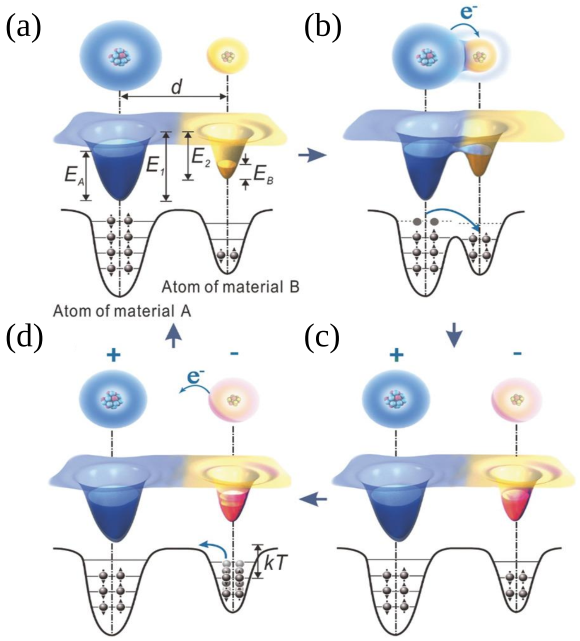

Figure 2.25: *An electron-cloud-potential-well model proposed for explaining the triboelectric effect via charge transfer between two materials. Shown is a schematic of the electron cloud and potential energy profile (2D and 3D) of two atoms belonging to two different materials, A and B, respectively, when they are: (a) initially separated, (b) in contact and (c) separated after contact, showing electron transfer between atoms after forced overlap of the corresponding electron clouds. (d) Charge release from an atom at an elevated temperature T once the thermal energy of the electrons, kT, approaches the barrier height. d is the nuclei separation distance, $E_{A,B}$ is the occupied energy levels, $E_{1,2}$ is the height of the potential well and k is the Boltzmann constant. Adapted from [200].*

as is shown in Figure 2.25 (b). This is why the two materials must be dissmilar to ensure that there is always a disparity between the energy levels of the two potential wells. Upon separation, Figure 2.25 (c), most of the electrons transferred to the atom within material B will remain bound to that site due to the potential barrier to escape, and so the two materials are left with a net surface charge (positive for A, negative for B). As the temperature, T, increases, the fluctuations in electron thermal energy, kT, where k is the Boltzmann constant, become larger and thus make it easier for electrons to hop out of the potential well and either move back to material A (if A and B are still in contact), or escape to the environment via thermionic emission, as is shown in Figure 2.25 (d) [200].

The total amount of charge transferred between two materials depends on a number of external factors such as the surface roughness, temperature, applied force and strain, as well as the intrinsic electron affinity of the two materials [197]. When considering just the intrinsic properties of a material it is possible to place it within the triboelectric series, which is a list of different materials ranked by their tendency to either gain or lose an electron when in contact with each other, with the maximum (minimum) total charge transfer occuring between materials far apart (close to) each other in the series [197]. Usually, the build up of static electricity is undesirable although, if controlled, can provide an efficient means of converting mechanical agitations into electrical signals using a triboelectric nanogenerator (TENG).

Triboelectric nanogenerator:

The operating principle of a TENG is illustrated in Figure 2.26.

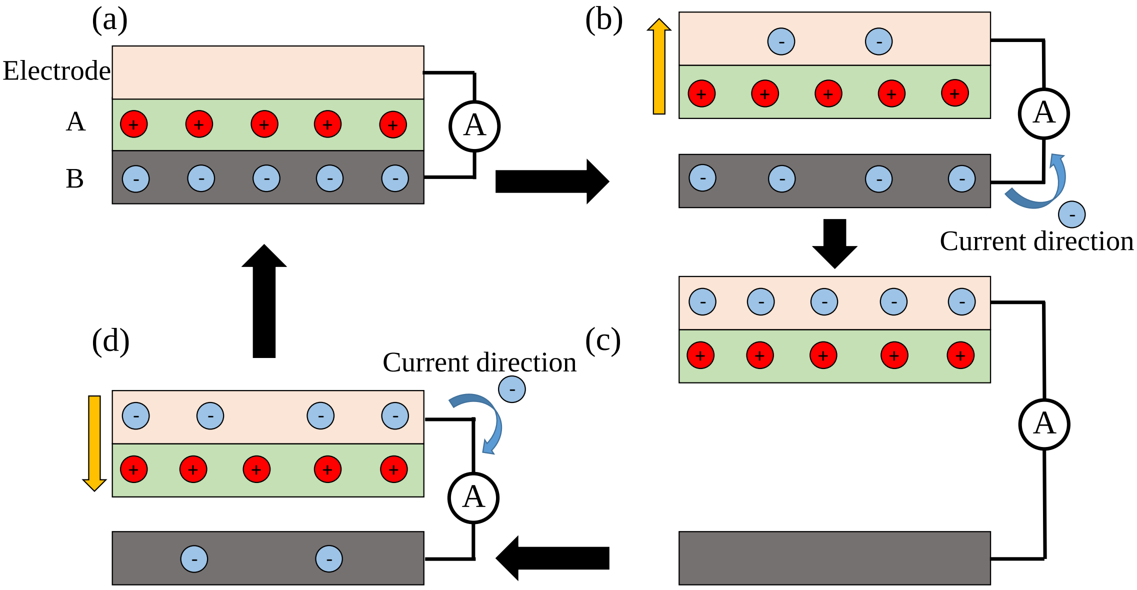

Figure 2.26: *Schematic showing the evolution of charge within a typical TENG charging/discharging cycle. (a) Material A and B are brought into contact before (b) separating, inducing current flow. (c) Material A and B are fully separated and the current reduces to zero, after which they are (d) brought into contact again, inducing current flow in the opposite direction. Black arrows indicate the progression direction, orange arrows indicate the movement of material and blue arrows indicate the direction of current flow.*

Upon contact, the surfaces of materials A and B become triboelectrically charged, with one becoming positively charged and the other negatively charged. As the charges are confined to the same plane, charges on opposite sides of the interface coincide with each other and there is no net electric field between the two materials [197]. When A and B are separated, the positive charge within material A electrostatically induces negative charge within an attached electrode, pulling charge from material

B and thus driving a current through the circuit. Eventually, the triboelectrically induced charge within material B is fully transferred into the electrode and the current reduces to zero. Moving material A and the electrode back towards material B similarly induces negative charge within B and current flows in the opposite direction. It is this conversion between mechanical movement and electricity which allows for energy to be harvested from the system by, for example, simply using the TENG to charge a capacitor.

Recently, it has been demonstrated that one strategy for enhancing the power output of a TENG devies relies on the use of multilayered structures [199]. For the devices studied here, this involves the introduction of charge trapping layers such as MoS_2 into the TENG which increases the magnitude of induced charge per unit area and leads to enhanced power output [199, 201].

2.5.5 Material hardness

The hardness of a material is used to describe its ability to withstand localised deformations induced by either mechanical indentation or abrasion. The key to understanding the mechanism behind hardness lies in understanding the structure and arrangement of atoms within the crystal lattice, or more specifically, the structure and arrangement of atoms within the many constituent grains of the material and in how these grains interact with their neighbours.

Each grain inevitably contains irregularities within its lattice which are classified as either point or line defects, with point defects including sites where atomic vacancies, substitution and interstitial defects occur, while line defects refer to irregularities throughout an entire crystal plane. From a macroscopic point of view, application of an external force allows for these planes of atoms to slip (i.e. become dislocated – a line defect) causing the material to undergo plastic deformation, with the material hardness controlling its resistance to said deformation.

However, in reality this force is first applied to one initial grain (the nucleus) of the specimen which results in a dislocation propagating out from the point of contact towards the grain boundary. The difference in lattice orientation between the nucleus and the neighbouring grains act as a potential barrier to the dislocation when propagating across the boundary due to the energy required to realign the dislocation, resulting in the “pile-up” of dislocations at the boundary of the nucleus [202, 203, 204]. The dislocations themselves generate repulsive stress fields [205], and so each successive dislocation arriving at the boundary applies a repulsive force to the first, increasing its potential energy until eventually it realigns to match the neighbouring grain and can propagate across the grain edge [202, 203]. This process repeats within each grain, resulting in a wave of plastic deformation (known as a Lüder wave) propagating outwards from the point of contact throughout the entire specimen.

The dislocations have a physical size associated with them [203], and so if the grains within the speciment are small then the number of dislocations which can pile-up at the boundary is reduced. Therefore, as the grain size is reduced the magnitude of external force which needs to be applied in order to give the dislocations enough energy to overcome the individual grain boundaries increases, which in turn is associated with an increase in material hardness as can be seen by the initial definition given. This is known as the Hall-Petcher effect [202], which can be mathematically described via

$$\sigma = \sigma_0 + \frac{k}{\sqrt{d}}, \tag{2.35}$$

where σ is the yield stress (the force needed to cause plastic deformation), σ_0 is the resistance to dislocation motion in the grain interior, k is a measure of the local stress needed to cause plastic deformation at the boundary and d is the grain size [203, 206].

The Hall-Petcher equation is an empirical fit to data collected from materials with micron-sized grains or larger [202], and implies that a material’s hardness will continue to increase as the grain size decreases. However, observations [207] indicate that grain sizes less than $\sim$ 1 µm yield values of hardness significantly less than that predicted by eqn. 2.35. This is known as the inverse Hall-Petcher effect due the hardness now being inversely proportional to grain size, and may be the result of either grain boundary sliding [208] or Coble creep [207]. Grain boundary sliding refers to the deformation of two grains along their interface as they pass across one another [209], whilst Coble creep refers to the diffusion of point and line defects within the grain towards the boundary when under tensile strain. Both of these represent a transition from dislocation controlled deformation to deformation by other means [203], and may be used to explain the inverse Hall-Petcher effect.

3. Measurement techniques

3.1 Raman spectroscopy

Raman scattering is the inelastic scattering of a photon through either the emission of an excitation of the system (Stokes) or through absorption of an excitation (anti-Stokes) [210], resulting in the scattered photon being red or blue-shifted accordingly, as is depicted in Figure 3.1. These excitations are typically lattice phonons of the material under investigation, and whilst the majority of incident laser light undergoes Rayleigh scattering, a small amount of the excited electrons couple to these phonons and lead to a shift in frequency of the light emitted upon de-excitation. The difference in energy between the incident and scattered light is known as the Raman shift. This directly corresponds to the energy of the emitted or absorbed excitation and, in the case of phonons, provides information on which vibrational modes are present within the sample. As phonons are sensitive to both the lattice structure and electronic characteristics of the material, Raman spectroscopy provides an excellent and non-destructive method for investigation of the structural and electronic properties of a given system.

Figure 3.1 illustrates resonant Raman scattering, although the process does not explicitly require a resonant transition into a real energy state in order to occur. In non-resonant Raman scattering, an electron within the valence band of a material can be excited into a transient "virtual" state before subsequent de-excitation and emission of the inelastically scattered photon, thus removing the need to tune the frequency of the incident light to match the band gap of each individual sample. These virtual states are not eigenstates of the system in that they do not correspond to a solution of the time-independant Schrödinger equation and thus a well-defined

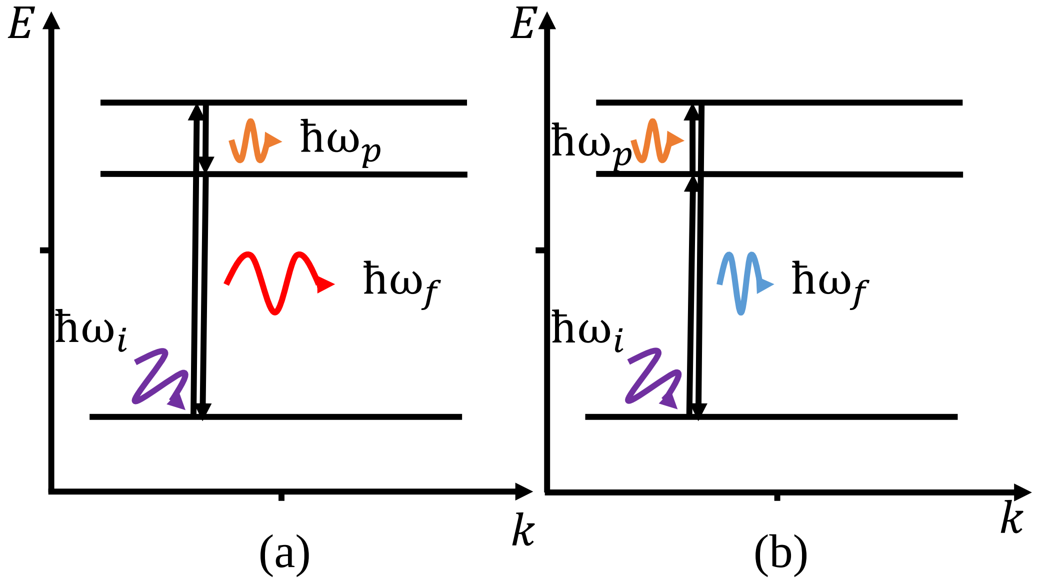

Figure 3.1: *Energy level diagrams showing resonant (a) Stokes and (b) anti-Stokes scattering, where* ω_i *and* ω_f *are the initial and final photon frequencies, and* ω_p *is the frequency of the lattice phonon.*

energy level [211]. Instead, the virtual states can be thought of as a superposition of the allowed excited states into which electrons can temporarily transition into. Eventually the virtual state collapses causing the electron to de-excite and emit the scattered radiation [212] such that one of the following processes occur: if the virtual state collapses back to the initial ground state, Rayleigh scattering occurs; if the virtual state collapses causing the electron to transition into an excited vibrational state before further emission of a phonon, then Stokes Raman scattering occurs; if the initial state occupied by the electron was a vibrationally excited state, and the virtual state then collapses into a state of lower energy than this, then anti-Stokes Raman scattering occurs. Non-resonant Raman spectroscopy therefore allows the use of incident light of a lower energy than the material band gap, as well as allow for measurement of multiple materials simultaneously. However, the probability of a transition into a real state is higher than transitions into a virtual one, meaning that the frequency of occurrence increases. As a result, the intensity of a resonant Raman peak can increase by up to a factor of 10^6 compared to that produced by non-resonant emission [213].

3.1.1 Graphene and graphite

Phonons are responsible for many of the properties of solids such as the heat capacity [214], the speed of sound throughout the material and for contributions towards the thermal conductivity [215]. They are divided into two types, labelled acoustic and optical, depending on whether the members of the unit cell oscillate in phase or out of phase, respectively. Although graphene is a 2D material, it exists within a three dimensional world and thus flexural phonon modes can also occur which oscillate perpendicular to the graphene plane [216]. A result of this three dimensionality is that the optical and acoustic arms of the phonon dispersion each split into three separate branches as is shown in Figure 3.2.

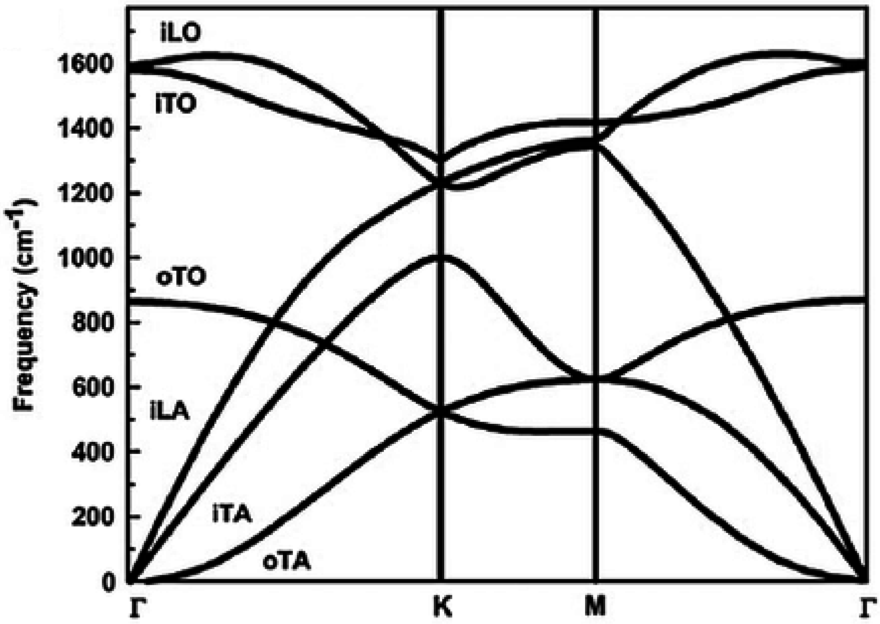

Figure 3.2: *Calculated phonon dispersion relation of graphene throughout the Brillouin zone showing the iLO, iTO, oTO, iLA, iTA and oTA phonon branches. Adapted from [217].*

This results in a total of 6 possible phonon modes, denoted by $x\mathrm{Y}Z$ within Figure 3.2, where x represents whether the mode is in-plane (i) or out-of-plane (o), Y represents whether the oscillations of the unit cell atoms are longitudinal (L) or transverse (T) to the line joining them and Z describes whether the mode is acoustic (A) or optical (O) [218]. When multiple phonon modes share the same frequency and momentum they are said to be degenerate, such as the iLO and iTO modes at the Γ-point of Figure 3.2.

Each material has its own unique phonon dispersion which, through the use of Raman spectroscopy, can be investigated to elicit information on both the phononic and electronic properties of that system. It should be noted that all low energy, inelastic light scattering events situated near the Dirac points within graphene are resonant in that they always involve transitions between real states (a result of the linear electronic dispersion at the K/K' points of the Brillouin zone), in contrast to the non-resonant Raman processes involving excitation into virtual states which often occur in other systems [218]. Raman scattering of phonons within graphene is largely dominated by the environment in which the electrons exist, meaning that any variation in the electronic properties due to the presence of defects, doping, stress/strain, temperature or the presence of external electromagnetic fields all also affect the position, width and/or intensity of the peaks within the Raman spectrum [218, 219, 220, 221, 222, 223, 224]. Figure 3.3 highlights a typical Raman spectrum of monolayer graphene.

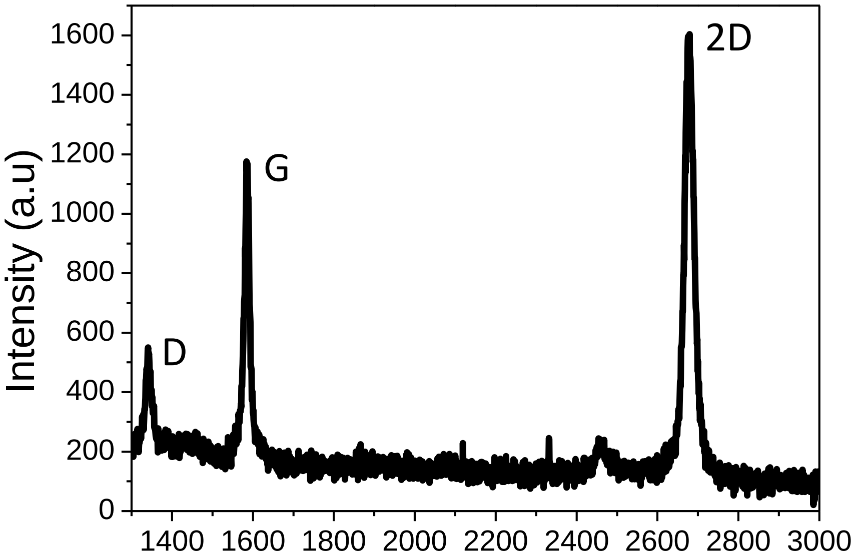

Figure 3.3: *A typical Raman spectrum of monolayer graphene.*

As can be seen, there are typically three main features of interest in the Raman spectrum of monolayer graphene, labelled the *D*, *G* and 2*D* peaks. The *G* peak occurs when a valence band electron near the Brillouin zone centre (Γ-point) absorbs a photon and is excited into the conduction band. Shortly afterwards, de-excitation occurs via emission of an iTO or iLO phonon of frequency $\sim 1582\ \mathrm{cm}^{-1}$ [218]. This is followed by further de-excitation of the electron back into the valence band and subsequent emission of the Raman-shifted photon, as is depicted in Figure 3.4. This is a first-order Raman scattering process (as it involves one phonon) and only includes phonons with momenta $q \approx 0$ in order to conserve momentum, hence why this transition occurs at the Γ-point of the Brillouin zone [225]. The degeneracy of the two contributing phonon modes results in a relatively intense G peak as two separate processes contribute towards the same Raman shift.

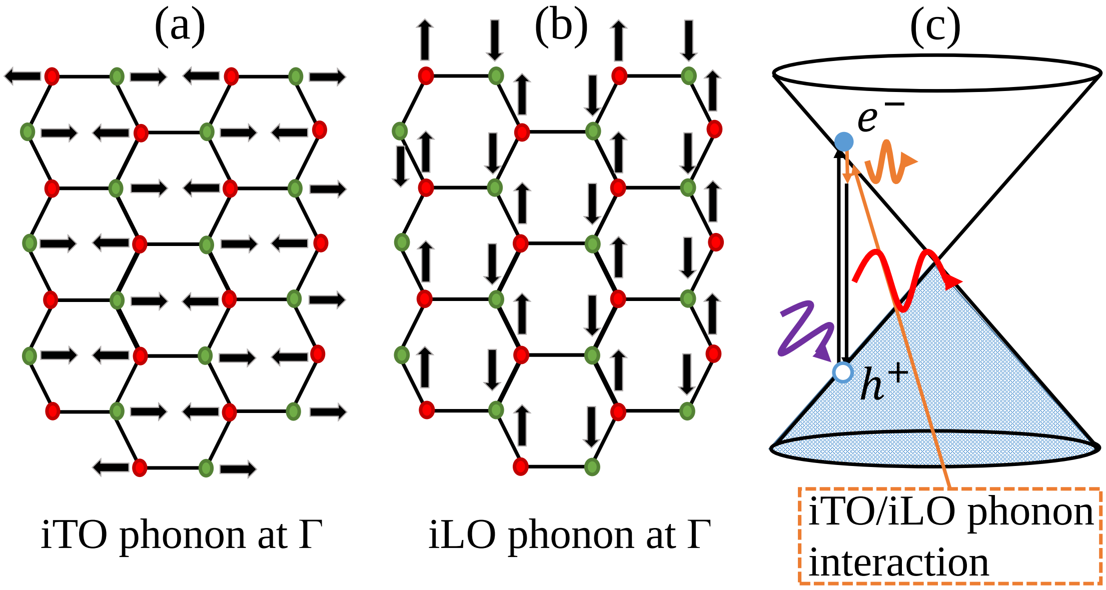

Figure 3.4: *Lattice vibrations associated with the (a) iTO and (b) iLO modes, along with the (c) G-peak Stokes Raman scattering process. The A and B sublattices are represented by the red and green circles, respectively.*

The D and D' (not shown) peaks both represent breathing modes within the lattice, and both involve an interaction with a defect within the system [218, 226]. They differ in that the D peak is due to an inter-valley scattering process whilst the D' peak is strictly an intra-valley process. Defect scattering allows the involvement of zone-edge phonons whilst maintaining conservation of momentum, and thus these events take place at the K/K' points of the Brillouin zone. They both occur when an electron in the vicinity of one of the Dirac points is excited by absorption of a photon into the conduction band before scattering off of a lattice defect into the conduction band of a neighbouring Dirac cone (e.g. K → K'). This is then followed by an emission of a Brillouin zone edge phonon ($\omega_D \approx 1350$ cm^{-1}, $\omega_{D'} \approx 1620$ cm^{-1} [218]), transferring the electron back to the initial Dirac cone, which then de-excites back into the valence band and emits the Raman-shifted photon. The D and D' processes are depicted in Figure 3.5. Both of these processes require a defect in order to occur, and thus the intensity of their associated Raman peaks can be used as a measure of how disordered a particular graphene sample is, with the Raman spectra of perfect, single crystal graphene lacking a D peak entirely [218, 226].

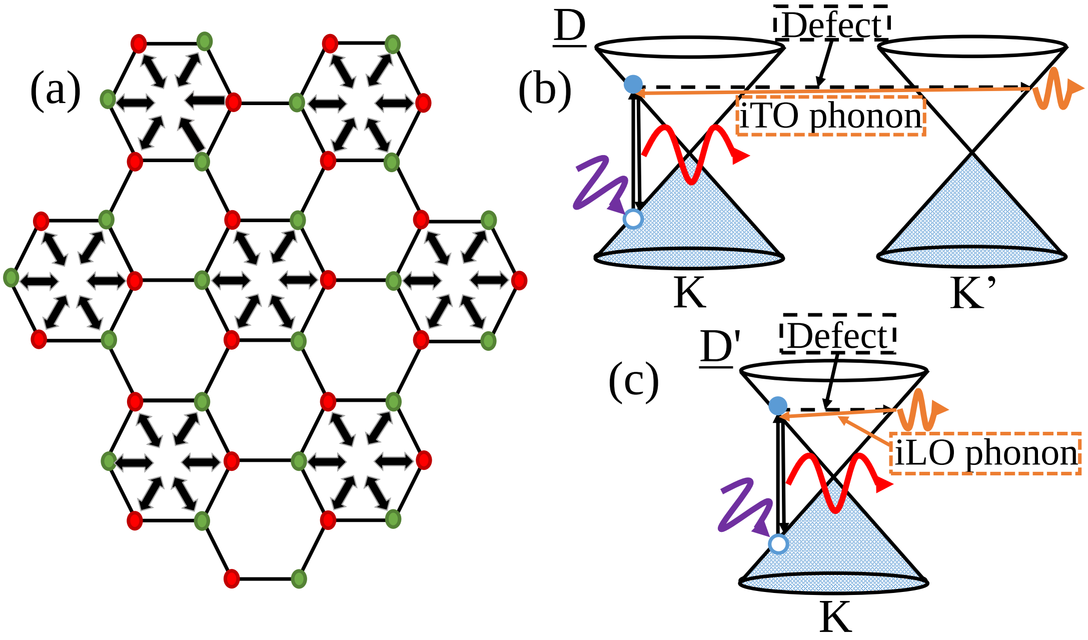

Figure 3.5: *Lattice vibrations associated with the (a) phonon breathing mode along with the Stokes Raman processes corresponding to the (b) D and (c) D' peaks.*

The $2D$ peak is an overtone of the D peak in that it no longer requires a defect in order to occur and is instead the result of two $\sim$ 1350 cm^{-1} zone-edge phonons inelastically scattering across the Brillouin zone between Dirac cones [221, 226]. It is therefore a second-order Raman scattering event as it involves two phonons [225]. The $2D$ peak within the Raman spectra of graphene is typically situated at $\sim$ 2700 cm^{-1} [218]. Since the $2D$ peak originates from a process where momentum conservation is obtained by the participation of two phonons with opposite wavevectors, it does not require the presence of defects for its activation and thus it is always present within the Raman spectra of graphene [221]. In this double-resonant inter-valley scattering process, shown in Figure 3.6, the photo-excited electron is scattered by an iTO phonon across the Brillouin zone before being scattered back by a second iTO phonon [218]. As both initial excitation and the second inter-valley scattering events both cause the electron to transition into a real state, the process is known as double-resonant. Furthermore, as both processes involve transitions into real states, the interaction probability increases and hence the $2D$ peak intensity is enhanced.

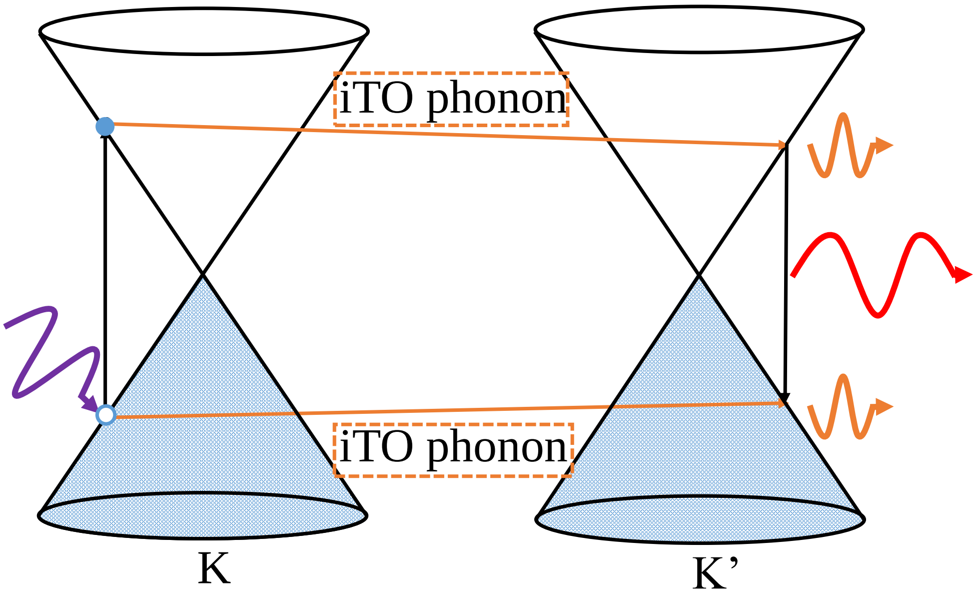

Figure 3.6: *Image showing the double-resonance process which produces the 2D Raman peak.*

It should be noted that there are variations in the D and $2D$ peak positions reported in the literature, even between comparable experiments. This is due to the peak positions being a function of the energy of the incident photons such that $\delta\omega_D/\delta E_{laser} \approx$ 50cm^{-1}eV^{-1} and $\delta\omega_{2D}/\delta E_{laser} \approx$ 100cm^{-1}eV^{-1} [218, 220]. This is because the iTO phonons associated with these two processes are known to preferentially couple to electronic states such that $k = 2q$ [218, 226], where k and q are the electron and phonon momenta when measured from the Dirac points, respectively. As the energy of the incident photon increases it has the potential to excite valence-band electrons situated further away from the Dirac points due to the linear nature of the energy dispersion. This changes the magnitude of k and hence which phonons take part in the process, changing the amount of Raman shift measured during the experiment. Another useful application of Raman spectroscopy is in determination of the number of monolayers present within a sample. As the number of graphene layers increases the electronic bandstructure evolves as a result (see Section 2.1.3). As the thickness increases, the number of possible avenues through which double-resonant $2D$ scattering can occur changes accordingly, resulting in the number of contributions (at different frequencies) towards the $2D$ peak of the Raman spectrum changing. For all multilayer systems this serves to broaden the $2D$ peak relative to that of monolayer graphene as well as alter its intensity and position, which allows one to differentiate between samples of different thicknesses by the number of Lorentzian curves required to fit the measured $2D$ peak lineshape [218]. The evolution of the $2D$ peak lineshape with increasing number of layers is shown in Figure 3.7. Another method to determine sample thickness is through the ratio of $2D/G$ peak intensities, as the G peak intensity scales almost linearly with the number of graphene layers [227]. However, the intensity of the $2D$ peak also scales with the amount of doping present [228], and so the ratio of $2D/G$ peak intensities should not be used as a definitive indicator of the number of layers present.

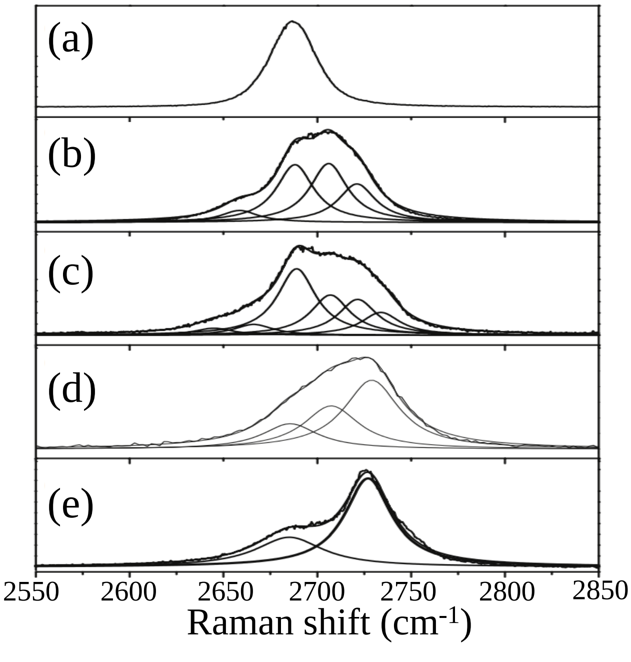

Figure 3.7: *Evolution of the* $2D$ *peak lineshape with increasing number of graphene layers for (a) monolayer, (b) bilayer, (c) trilayer, (d) 4-layer and (e) highly ordered pyrolitic graphite (HOPG). The inner, smooth curves are the Lorentizian fits and the outer curves represent the measured spectrum. Adapted from [218].*

Throughout the remainder of this section emphasis will be placed on the use of Raman spectroscopy to identify 2D material thickness as it is this variable which is most important to consider during device design.

3.1.2 Hexagonal boron nitride

As hBN has a large band gap it exhibits very little optical contrast, < 1.5 % [6], and so alternative methods of flake thickness identification must be used. Raman spectroscopy of bulk hBN reveals a prominent peak at a Raman shift of ~ 1366 cm^{-1} [229], attributed to the doubly-degenerate in-plane optical phonon mode where the boron and nitrogen atoms vibrate out of phase to each other (the E_{2g} mode) [230], see Figure 3.8 (b), left inset.

As the thickness decreases from bulk to monolayer, the intensity, position and FWHM of the E_{2g} Raman peak changes accordingly. The peak is blue-shifted by 3 - 7 cm^{-1} in monolayer samples comprared to bulk as a result of increased in-plane strain and reduced interlayer interaction [92], whilst at the same time a reduction towards monolayer thickness coincides with increased lattice straining from substrate interactions and stronger surface scattering of phonons, reducing the phonon lifetime and thus increasing the FWHM via the [92]. Furthermore, the intensity of the E_{2g} Raman peak increases linearly with an increasing number of layers present within the sample [6], see Figure 3.8 (b).

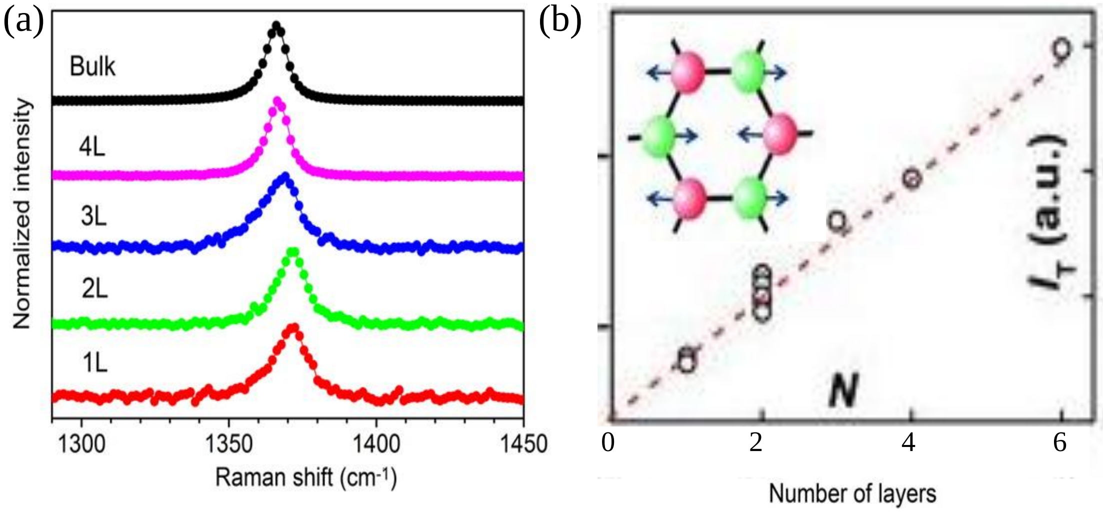

Figure 3.8: *(a) Raman spectra of hBN of different layer number, N, from monolayer (1L) to bulk. (b) The change in integrated intensity, I_T, with respect to the number of layers, N, for the E_{2g} Raman peak. Left inset: Illustration of the E_{2g} phonon mode. (a) Taken from [92], (b) adapted from [6].*

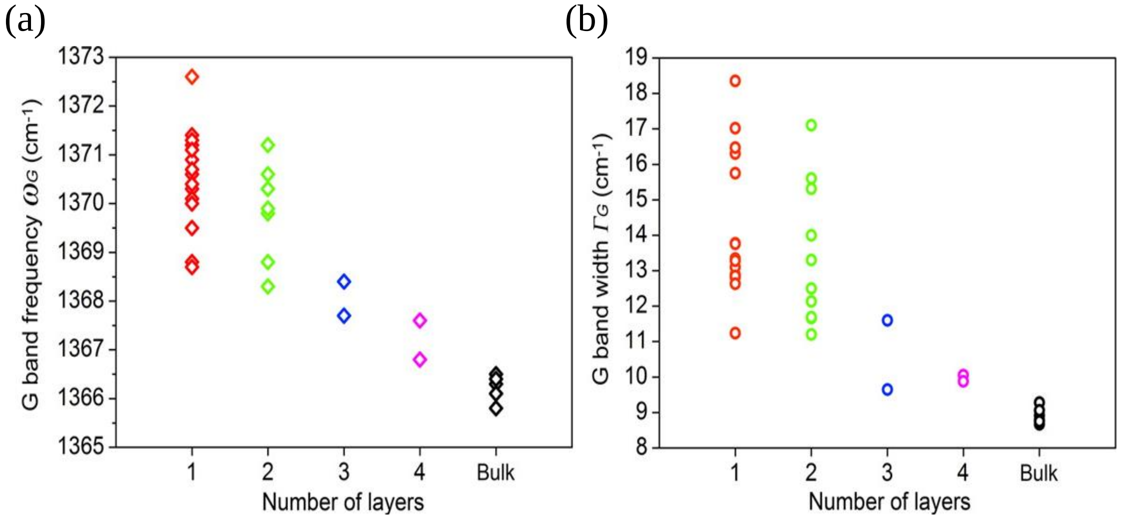

Figure 3.9: *(a) Position of the* E_{2g} *peak for different values of* N*. (b) FWHM of the* E_{2g} *peak for different values of* N*. Taken from [92].*

Overall, the E_{2g} Raman peak is blue-shifted in monolayers with respect to the bulk peak position, while the FWHM is inversely proportional to N. This, in combination with the peak intensity dependance on N, allows for accurate identification of the thickness of a given hBN sample.

3.1.3 Transition metal dichalcogenides

As discussed in Section 2.3, semiconducting TMDCs belong to the 2H polytype. In general, this corresponds to four possible Raman active modes of vibration (as can be seen in Figure 3.10), although only the E^1_{2g} and A_{1g} modes are usually experimentally accessible as the E^2_{2g} is at very low frequencies (at ~ 30 cm^{-1}, shifts less than 100 cm^{-1} are often filtered out) and the E_{1g} is forbidden during backscattering events which occur perpendicular to the c axis [231, 232].

The evolution of the Raman spectra for MoS_2, WS_2 and WSe_2 as a function of the number of layers is given in Figure 3.11. The E^1_{2g} and A_{1g} modes are clearly visible as two low-frequency Raman peaks, and upon closer inspection it can be seen that the positions of these depend upon the number of layers in the sample as is shown in Figures 3.12 and 3.13.

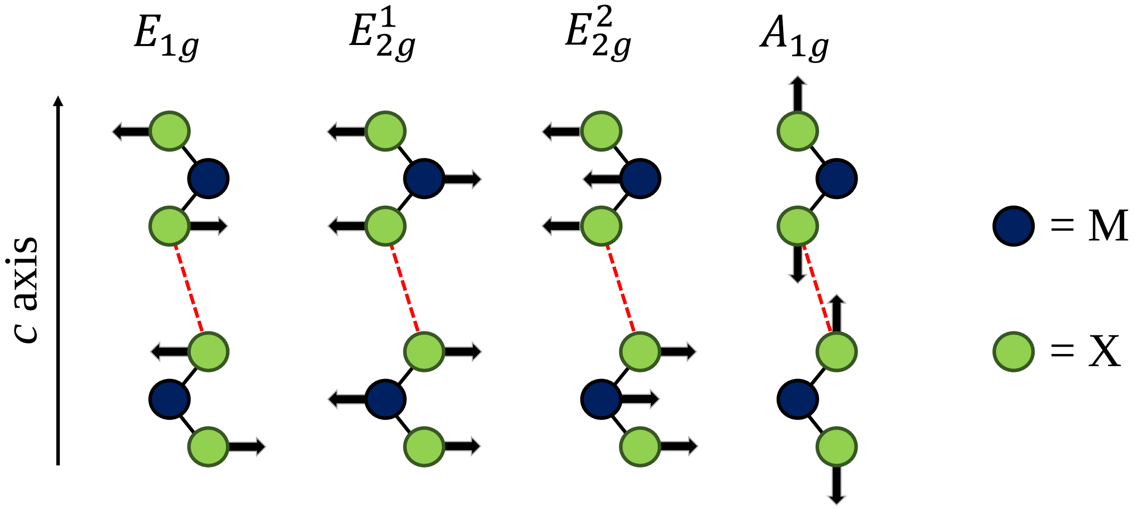

Figure 3.10: *Illustration of Raman active modes within TMDCs. The black (red dashed) lines represent covalent (vdW) bonding between the atoms. Adapted from [231].*

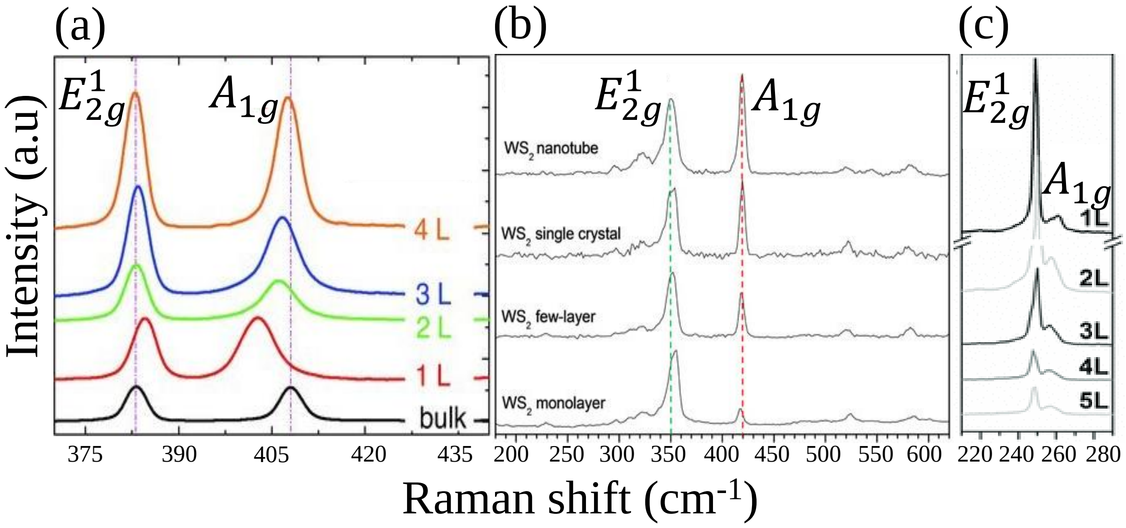

Figure 3.11: *Example Raman spectra for (a) MoS$_2$ ($\lambda = 488$ nm), (b) WS$_2$ ($\lambda = 514$ nm) and (c) WSe$_2$ ($\lambda = 532$ nm). Adapted from [233, 234, 235], respectively.*

Overall, as the number of layers increases, the $\mathrm{E}_{2\mathrm{g}}^1$ ($\mathrm{A}_{1\mathrm{g}}$) mode softens (hardens). The contrasting behaviour of these modes are thought to be due to the balance between increased vdW forces resulting in a blue-shift of the modes (due to increased restoring forces by adjacent layers), whilst at the same time they are red-shifted by a combination of long range Coloumb interactions and stacking induced changes in the

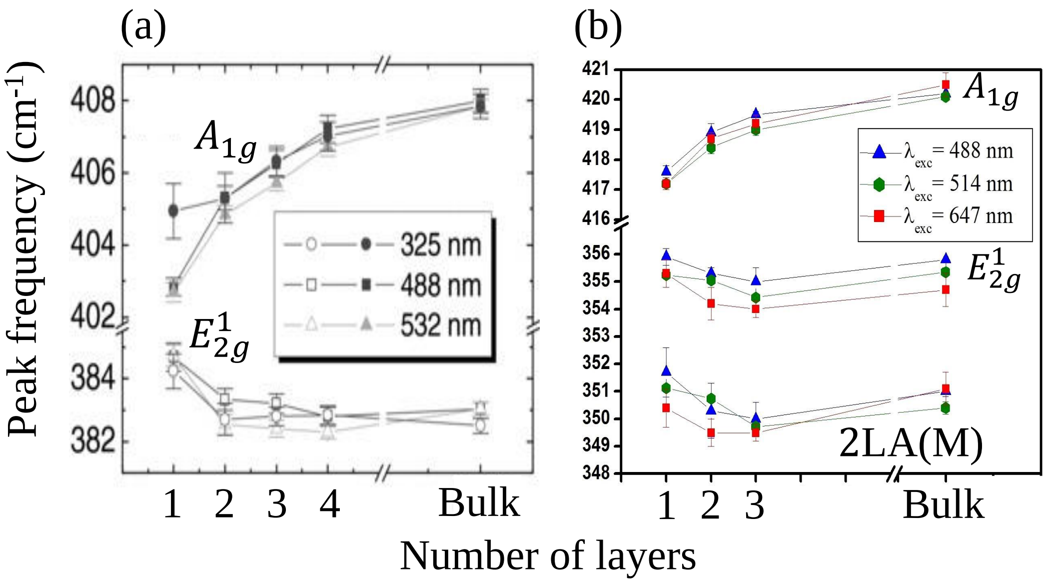

Figure 3.12: *Thickness-dependant peak position shifts for the* E^1_{2g} *and* A_{1g} *modes of (a)* MoS_2 *and (b)* WS_2*, The 2LA(M) peak within (b) is a second-order mode which can appear within* WS_2*. Adapted from [233] and [236], respectively.*

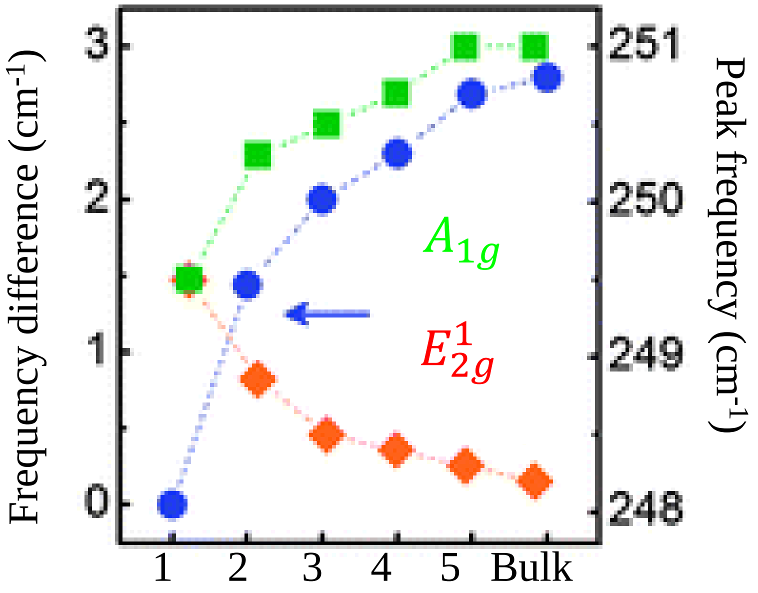

Figure 3.13: *Thickness-dependant peak position shifts for the* E^1_{2g} *and* A_{1g} *modes of* WSe_2*. The left axis represents the frequency difference between the bulk and sample* E^1_{2g} *and* A_{1g} *modes. Adapted from [237].*

lattice structure [238]. Therefore, in a similar manner to hBN, Raman spectroscopy can easily be used to identify the thickness of a given TMDC sample by comparison of the E^1_{2g} and A_{1g} peak positions in both the sample and in bulk.

3.1.4 Talc

Because of the large number of atoms and complex structure of this material, talc has an extremely rich Raman spectrum as is shown in Figure 3.14. [239].

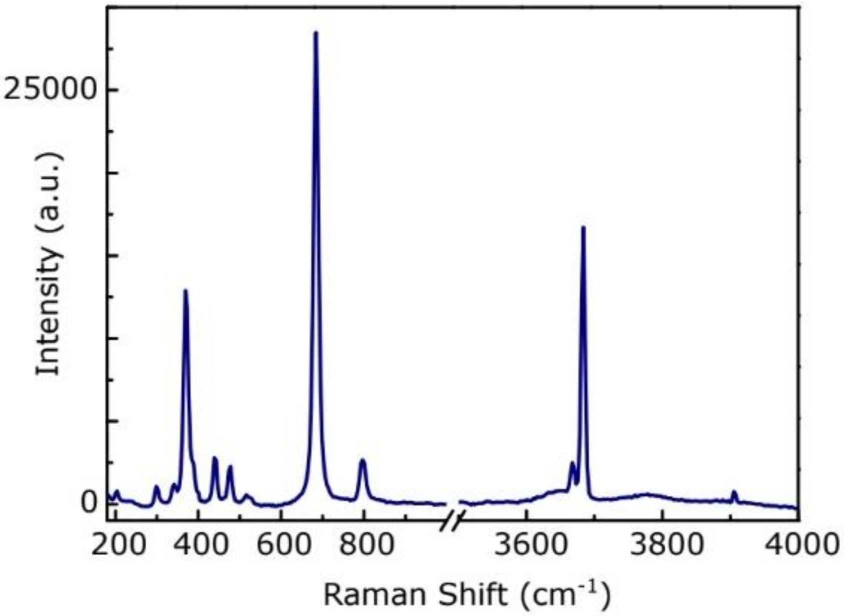

Figure 3.14: *Typical Raman spectrum for talc with* $\lambda = 457nm$. *Taken from [239].*

Table 3.1 details the myriad of peaks present within the spectrum.

Table 3.1: *Raman peak positions of talc and their relative intensities. The most intense peaks are highlighted in bold. Adapted from [239].*

Raman shift (cm^{-1})	**Intensity (a.u)**
204	Weak
298	Weak
342	Weak
369	Strong
388	Weak
440	Medium
475	Medium
516	Weak
528	Weak
684	Very strong
797	Medium
3667	Medium
3684	Strong

As can be seen, there are three prominent peaks at 369 cm^{-1}, 684 cm^{-1} and 3684 cm^{-1}. However, there is little literature regarding the interpretation of the Raman spectrum of talc and so clear identification of the responsible vibrational modes cannot be given here. Furthermore, as talc has only recently been considered a useful 2D material there have been no investigations into the use of Raman spectroscopy for the identification of sample thicknesses.

3.2 Photoluminescence spectroscopy

Photoluminescence (PL) is light emission from matter after the absorption of photons. In the case of semiconducting materials, an electron in the valence band absorbs a photon of energy equal to or greater than the band gap energy, E_g, and transitions into the conduction band, leaving behind a positively charged hole in the valence band. The excited electron and hole undergo energy and momentum relaxation towards the band gap edge (typically through either electron-electron or electron-phonon scattering), whereby they can then recombine and emit the scattered photon. Intra-band relaxation of carriers generally happens before inter-band radiative recombination can occur ($\sim$ picosecond compared to $\sim$ nanosecond timeframes, respectively) [240], meaning that radiative recombination always involves carriers at the band gap edge and thus the wavelength of the emitted photon is independant of the initial excitation energy. Therefore, in the simplest sense, PL spectroscopy can be used to determine the band gap width of a given material through analysis of the scattered photon wavelength. However, one often finds a number of other emission peaks unexpectedly correlating to states within the band gap itself, and it is these peaks which are a result of the interesting quasiparticles known as excitons.

3.2.1 Excitons

In materials with a sufficiently high (low) dielectric constant (effective carrier masses), the absorption of an external photon may result in the formation of a bound electron-hole pair known as an exciton, a neutral quasiparticle which can trasmit energy but not charge throughout the crystal [241, 242, 243]. The electron-hole pair are bound together via their attractive Coloumb interaction, and thus the total energy of the exciton is lower than its unbound counterpart by an amount equal to this binding energy, E_b, as is illustrated in Figure 3.13.

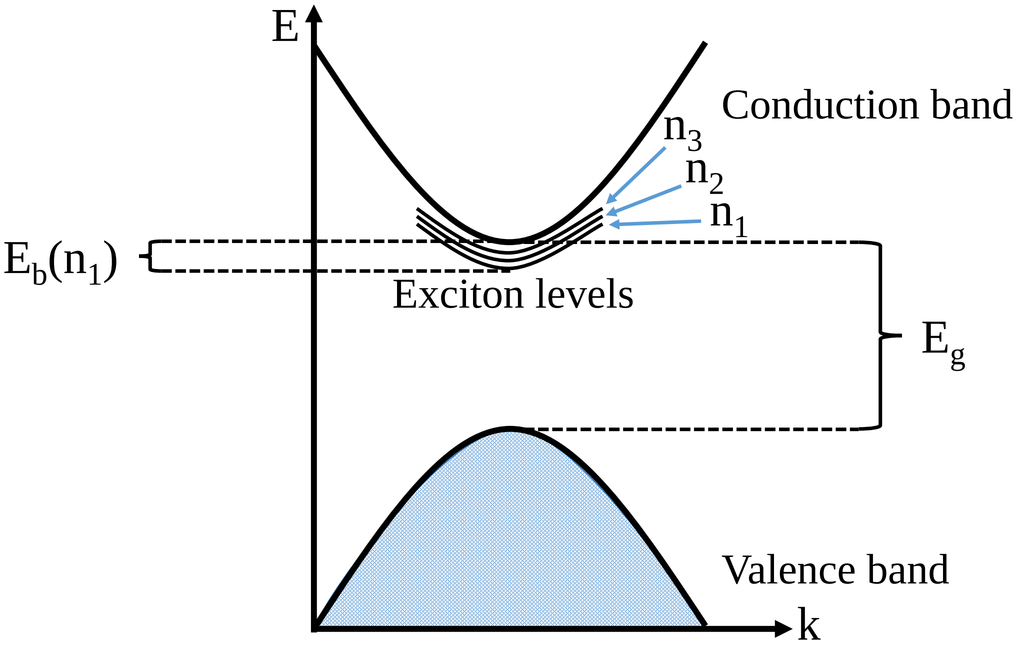

Figure 3.15: *An illustration of the exciton energy level positions within the bandstructure of an idealised semiconducting material.*

Excitons are usually considered under two limiting approximations, one where they are tightly bound together and are known as Frenkel excitons, and the other where the bond between the electron-hole pair is very weak and they are known as Mott-Wannier excitons.

Frenkel excitons: In a material with a relatively small dielectric constant, the Coloumb interaction between the electron and hole may be strong and thus the resultant exciton tends to be small. These excitons are tightly bound together and localized on or near a single atom due to the small orbital radius of the electron-hole pair [241]. Because of this, they are usually confined to a single unit cell of the crystal and can only propagate throughout the crystal by means of hopping between nearest-neighbours by virtue of the electronic coupling between them [241, 243]. Frenkel excitons are typically found in alkali halide crystals and molecular crystals, and do not appear in any of the devices covered within this thesis.

Mott-Wannier excitons: In semiconductors the dielectric constant is generally quite large. This screens the electron-hole Coloumb interaction and serves to increase the size of the overall exciton such that it has a radius many times larger than the lattice spacing of the material and, to a good approximation, allows the exciton to be modelled as hydrogen-like with the electron and hole orbiting their centre of mass [243]. This results in a Coloumb potential term of

$$U\left(r\right)=\frac{-e^2}{4\pi\epsilon_0 r}, \tag{3.1}$$

where r is the electron-hole separation and ϵ is the dielectric constant of the semiconductor [241]. For a simple parabolic band structure at the conduction (valence) band minima (maxima), this results in an excitonic energy dispersion, $E_b\left(n_i,\mathbf{K}\right)$, given by

$$E_b\left(n_i,\mathbf{K}\right)=E_g-Ry^*\frac{1}{n_i^2}+\frac{\hbar^2\mathbf{K}^2}{2M}, \tag{3.2}$$

where

$$n_i=1,\ 2,\ 3\ ... \tag{3.2a}$$

is the principle quantum number,

$$Ry^*=13.6\ \text{eV}\frac{\mu}{m_0}\frac{1}{\epsilon^2} \tag{3.2b}$$

is the Rydberg energy, with $\mu=\left(m_e m_h\right)/\left(m_e+m_h\right)$ being the reduced exciton mass and

$$M=m_e+m_h \text{ and } \mathbf{K}=\mathbf{k_r}+\mathbf{k_h} \tag{3.2c}$$

are the translational mass and wave vector of the exciton, respectively [243].

The value of n_i within eqn. 3.2a determines whether the exciton is found in the ground state or in an excited state, as depicted in Figure 3.13, with the excited states being situated closer to the conduction band edge. For $n_i=1$, eqn. 3.2 represents the ionisation energy of the excition - that is, the energy required to separate the electron-hole pair into free charges [241].

These equations represent the allowed energy levels of an exciton within a bulk semiconductor and accurately reproduce many of the observed excitonic features within the PL spectra of these materials [241]. However, it has also been observed that the basic excitonic properties of 3D semiconductors differ markedly from their 2D counterparts [193]. The real-space origin of this is shown in Figure 3.14.

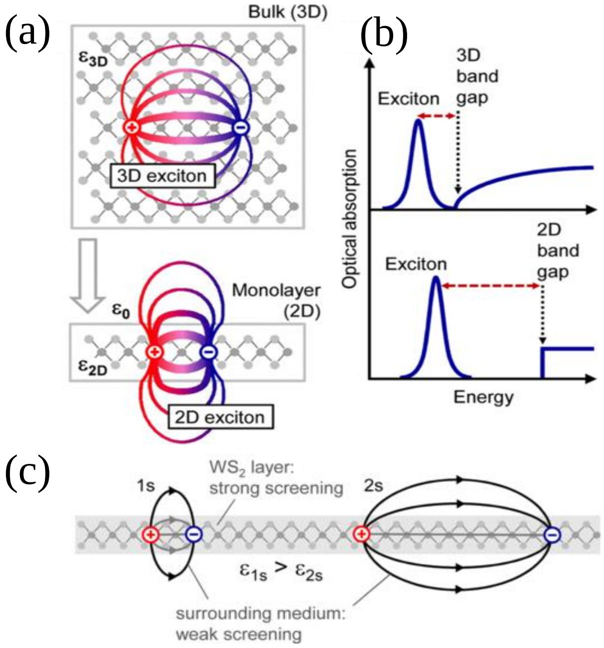

Figure 3.16: *(a) Real-space representation of electrons and holes bound into excitons within bulk and monolayer semiconductors. The dielectric constant of the environment for bulk, monolayer and vacuum are indicated by* ϵ_{3D}, ϵ_{2D} *and* ϵ_0, *respectively. (b) Schematic of the impact of the reduced dimensionality and dielectric screening on the electronic and excitonic properties manifested within optical absorption spectra. (c) Illustration of electron-hole pairs forming* $1s$ *and* $2s$ *excitonic states in a non-uniform dielectric envrionment. Adapted from [193].*

Confinement of the excitons to two dimensions increases the binding energy by a factor of four compared to the bulk [244], resulting in a 2D excitonic dispersion given by [193]

$$E_b\left(n_i\right) = \frac{\mu e^4}{2\hbar^2 e^2 \left(n_i - 1/2\right)^2}. \tag{3.3}$$

However, in addition to this confinement effect, the dielectric screening of excitons within 2D materials is significantly reduced compared to the bulk, which further warps the excitonic dispersion away from hydrogenic (eqn. 3.3) for small values of n_i. More specifically, the excitons in an excited state have a larger radius and thus a greater proportion of the electric field joining the electron-hole pair is situated outside of the atomic plane. Therefore, for large values of n_i the dielectric screening is effectively constant and the excitonic dispersion is represented by eqn. 3.3, see Figure. 3.14 (c), whilst at low values of n_i the dielectric screening is increased. This changes the electron-hole interaction potential from eqn. 3.1 to

$$U(r) = -\frac{\pi e^2}{2r_0}\left[H_0\left(\frac{r}{r_0}\right) - Y_0\left(\frac{r}{r_0}\right)\right], \tag{3.4}$$

where H_0 and Y_0 are Struve and Bessel functions, respectively, and r_0 is the screening length, which defines the crossover length scale between the the $1/r$ Coloumb interaction at large electron-hole separations and a $\log(r)$ interaction at small separations [193]. This modified interaction potential is responsible for the non-hydrogenic excitonic dispersions observed in the PL spectra of some 2D materials.

The manipulation of excitons in solid-state devices holds great promise for the realisation of efficient interconnects between optical data transmission and electrical processing systems [195]. Although proof-of-principle exciton-based optoelectronic devices have been demonstrated [245], they typically relied on the use of bulk materials and cryogenic temperatures in order to function, being limited by the small binding energy of the excitons present. In order to produce devices which can operate at room-temperature, materials exhibiting excitons with both high binding energies and long recombination lifetimes (i.e. diffusion lengths of the same order as the device scale) are needed. The use of 2D materials, with their strong geometric confinement and weak dielectric screening, has the potential to fill this niche [188].

3.2.2 Graphene and graphite

Graphene absorbs light in the near infrared to visible range, although the absence of a band gap in prinstine samples means that when light is absorbed electron-electron and electron-phonon interactions fully relax the system before exciton recombination can occur, preventing any meaningful information from being gathered by PL spectroscopy [246]. However, PL emission can be induced in graphene through the use of high intensity laser pulses, which excite the carriers enough to allow them to thermally stabilise amongst themselves, essentially becoming decoupled from phonons and thus allow radiative recombination to take place [246]. Other means of inducing PL from graphene involve the introduction of a band gap into the system through the methods mentioned in Section 2.1.1, with resultant PL quantum yields ranging from

0.5 – 28 % depending on the method used [247].

3.2.3 Hexagonal boron nitride

The band gap width and exciton binding energy of multilayer (monolayer) hBN was measured as 5.97 (6.1) eV and 0.7 (1.9) eV, respectively, using PL spectroscopy [248, 249, 250]. Although having a large band gap makes hBN suitable for devices such as high-efficiency ultraviolet emitters [251], excitonic excitation typically requires the use of wavelengths outside the spectral window of most readily available laser sources [250], limiting the practicality of hBN as an active medium in optoelectronic devices.

3.2.4 Transition metal dichalcogenides

As discussed in Section 2.3.1, 2H-MX_2 monolayers are semiconductors with a direct band gap at the K/K' points of the Brillouin zone. The valence band maximum here is split into two branches ($v1$ and $v2$) due to spin-orbit coupling, allowing for two primary optical excitations into the conduction band (c) to occur (i.e. $K_{v1} \rightarrow K_c$, $K_{v2} \rightarrow K_c$). These "valley" excitons, labelled the "A" and "B" excitons depending on which arm of the valence band maxima they originate from, eventually recombine and result in two emission features within the PL spectra of TMDCs [97, 107] as is illustrated in Figure 3.15.

It should be noted that the PL spectra of monolayer TMDCs within the literature is varied and contradictory, with some authors reporting only a single PL peak (corresponding to the transition between the highest valence band maximum and conduction band minimum - the A-exciton) [107, 231, 253, 254, 255], whilst others report two peaks [5, 252, 256, 257], with the relative intensities and subsequent interpretation [255, 257] of these also showing significant variation between experiments. This is due to two factors: firstly, the lowest energy transition channel, from the highest split valence band to the conduction band minimum, is dominant within the PL spectra and so the B-exciton peak is difficult to resolve; and secondly, both A- and B- emission intensities can vary wildly between samples as a result of differences

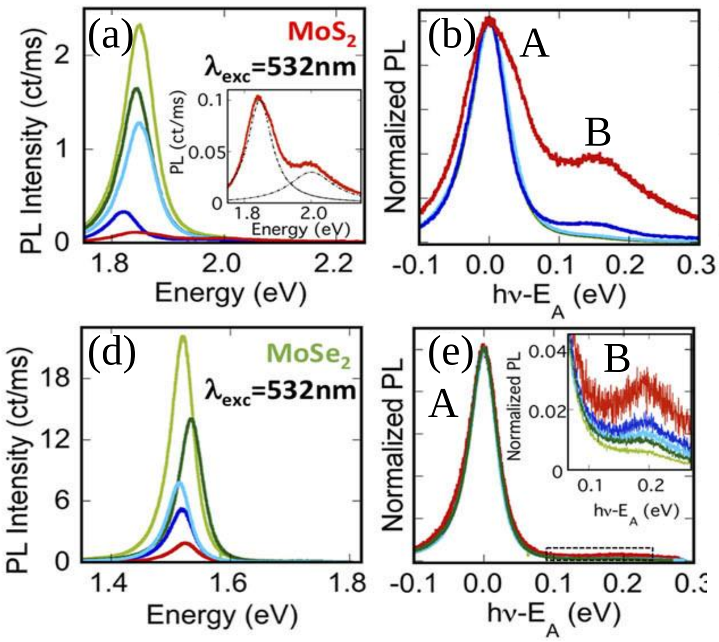

Figure 3.17: *(a, b) Photoluminescence (PL) from monolayer* MoS_2 *plotted in ct/ms and normalised to the maximum emission intensity, respectively. (c) PL from monolayer* WS_2 *where the inset shows emission from the B-exciton. (d, e) PL from monolayer* $MoSe_2$ *plotted in ct/ms and normalised to the maximum emission intensity, respectively. (f) PL from monolayer* WSe_2*, where the inset shows emission from the B-exciton. Adapted from [252].*

in non-radiative recombination associated with the density of defects present [252]. Specifically for the latter, the PL quantum yield is expected to be proportional to the ratio of radiative to nonradiative recombination times, where the second of these depends heavily on defect density and thus a significant sample-to-sample variation in the quantum yield is expected [252, 258]. Therefore, evaluation of the ratio of A- and B-exciton emission intensities, $I(A)$ and $I(B)$, respectively, allows one to qualitatively assess the sample quality, with low $I(B)/I(A)$ indicating a prolonged A-exciton lifetime and thus low (nonradiative) defect density [252]. Furthermore, the indirect-to-direct band gap transition when moving from multilayer to monolayer films facilitates a sudden enhancement of the PL quantum yield as phonon-mediated excitonic recombination is no longer required for emission, therefore also providing qualitative information on the number of layers within a given TMDC sample [107, 109].

To summarise the main features within the PL spectra of TMDCs, Table 3.2 highlights the calculated band gaps (E_g), exciton emissions (A, B) and binding energies (E_{bA},

E_{bB}) for monolayer MoS_2, $MoSe_2$, WS_2 and WSe_2.

Table 3.2: *The band gap, exciton emission and binding energies for monolayer MoS_2, $MoSe_2$, WS_2 and WSe_2. All energies are given in eV. Theoretical values are given here to provide a consistent comparison between materials. This is to compensate for absent data in the literature as well as to remove variation in results arising from experimental design. Data taken from [259].*

Material	$\boldsymbol{E_g}$	**A**	$\boldsymbol{E_{bA}}$	**B**	$\boldsymbol{E_{bB}}$
MoS_2	2.82	1.78	1.04	1.96	0.86
$MoSe_2$	2.41	1.50	0.91	1.75	0.66
WS_2	2.88	1.84	1.04	2.28	0.60
WSe_2	2.42	1.52	0.90	2.00	0.42

The high binding energy of excitons within monolayer TMDC materials, which is $\sim 1-2$ orders of magnitude greater than conventional materials such as GaAs [188], allow for strong light-matter coupling at room temperature and thus make TMDC monolayers appealing candidates for future optoelectronic devices.

Environmental effects on the properties of TMDC PL spectra:

A high (low) effective dielectric constant in the environment surrounding the excitons screens the Coloumb interaction between the constituent electron-hole pair and decreases (increases) the exciton binding energy. This manifests as a change in peak position for exciton emission within the PL spectra [260] as is shown in Figure 3.16 (a). Additionally, it has been observed that the direct band gap energy of TMDCs depends on both the sample thickness and dielectric constant of the surrounding medium [261], see Figure 3.16 (b).

Figure 3.16 (c) highlights the temperature dependance of the A-exciton and negatively charged trion PL peak positions in monolayer $MoSe_2$ [262]. As can be seen, both features are red-shifted with increasing temperature reflecting the standard semiconductor band gap dependance on temperature [265] (where thermal excitation of phonons influences the amount of electron-phonon coupling present, thus influencing the electronic dispersion). Furthermore, the relative intensities of these two features also depends on temperature, with the trion emission becoming negligible at moderate temperatures (> 50 K) due to electrons escaping the bound trion state via thermal excitation [262]. Figure 3.16 (d) presents the shift in monolayer MoS_2

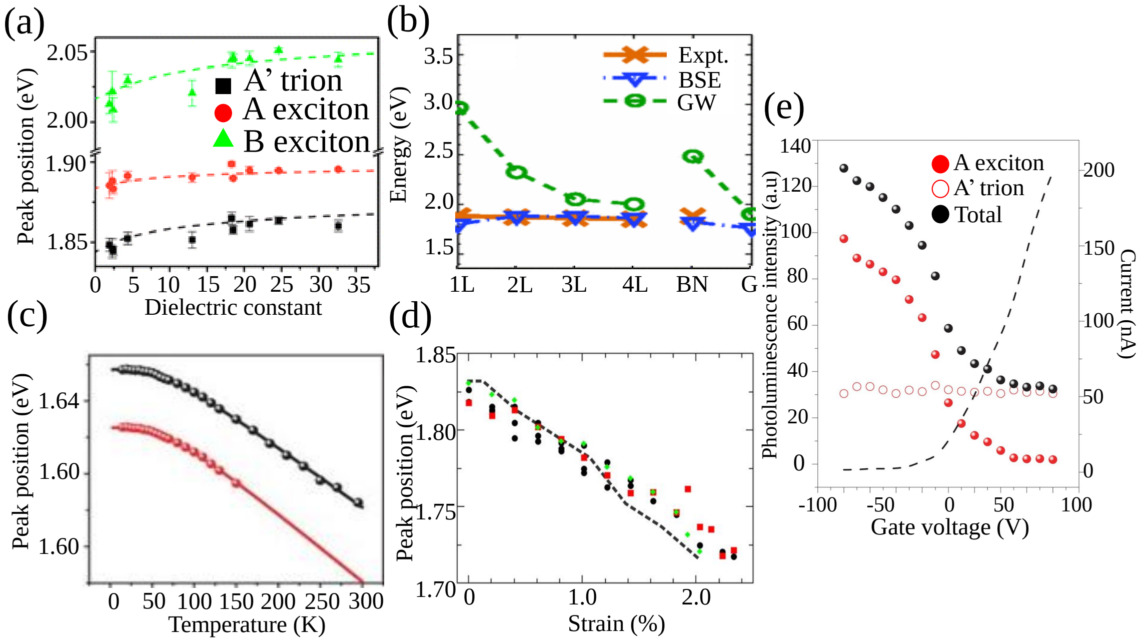

Figure 3.18: *(a) The effect of dielectric screening on exciton binding energy within monolayer* MoS_2*, where a trion is simply a positvely (negatively) charged exciton with an additional hole (electron). (b)* MoS_2 *theoretical direct band gap energy as a function of the number of layers (1-4L) and adjacent dielectric screening where BN and G represent monolayer hBN and graphene, respectively. BSE and GW represent two different theoretical methods used to produce the data, whilst Expt. represents measured data points. (c) Neutral A-exciton (black) and trion (red) peak positions versus temperature with fits (solid lines) for monolayer* $MoSe_2$*. (d) Evolution of the A-exciton peak position with uniaxial tensile strain for monolayer* MoS_2 *overlayed onto the expected theoretical shift (dashed line). (e) Dependance on gate voltage of the source-drain current (dashed) and PL intensity of the exciton and trion features for monolayer* MoS_2*. Adapted from [260, 261, 262, 263, 264].*

A-exciton peak position with applied uniaxial tensile strain. The feature undergoes a linear red-shift at a rate of $\sim 45 \pm 7$ meV/%, reflecting a strain-induced reduction of band gap width for this system [263]. Furthermore, the application of strain also leads to a reduction in both the indirect and direct band gap widths at a rate of 94 meV/% and 59 meV/%, respectively. This in turn leads to an eventual direct-indirect optical band gap transition at applied strains of $\sim 1.3 \pm 0.6\%$ and thus a subsequent reduction in the intensity of the PL features [263]. Finally, Figure 3.16 (e) presents the evolution of monolayer MoS_2 PL spectra as a function of doping. This can easily be achieved through the use of an applied back gate voltage and, as can be seen, depending on the doping concentration new PL features may emerge. Positive (negative) doping results in the formation of positively (negatively) charged trions, each with their own peaks within the PL spectra [264]. Furthermore, the relative intensities of these emissions depend upon the doping concentration, with trion emission only occuring at significant doping levels. Therefore, qualitative assessment of sample purity can be done by comparison of the peak intensities with that of an undoped flake [264].

Clearly, like Raman spectroscopy, the PL spectroscopy of TMDCs is affected by a wide variety of external factors. This can allow for further insight into these systems or simply be a detriment. In order to mitigate these variables and get insight into intrinsic system properties, careful experimental design such as the choice of substrate, device encapsulation and general purity controls must be used.

3.2.5 Talc

Talc is an insulating crystal with a large band gap of $E_g \sim 5$ eV. Although information regarding the PL spectra of both bulk and monolayer talc within the literature is scarce, it can be assumed that it offers similar behaviour to hBN. Despite this, it should be noted that the complex lattice structure of this material allows for easy substitution by impurity atoms, see Section 2.4.1, which in turn introduce mid-gap defect states into the electronic dispersion [239].

Subgap excitation, where the excitation energy is less than the band gap width, allows these defect states to be detected using PL spectroscopy. Unlike the aforementioned PL processes, where electrons are excited high into the conduction band before relaxing to the band edge to recombine, in this case the electrons are first excited into a virtual energy level (see Section 2.7.2) before subsequent decay into defect states and eventual recombination.

This atom-like PL emission differs from conventional crystal PL in two ways: firstly, the peak linewidth is reduced to reflect the discrete nature of the mid-gap states and secondly, the peak intensity has a sublinear dependance on excitation energy [239]. The former is a result of obedience to the uncertainty principle whilst the latter reflects saturation of the defect levels due to their limited density of states as opposed to the high density of states present in the crystal band structure (which leads to linear dependance) [239]. The subgap PL spectrum of bulk talc along with its sublinear peak intensity dependance is shown in Figure 3.17.

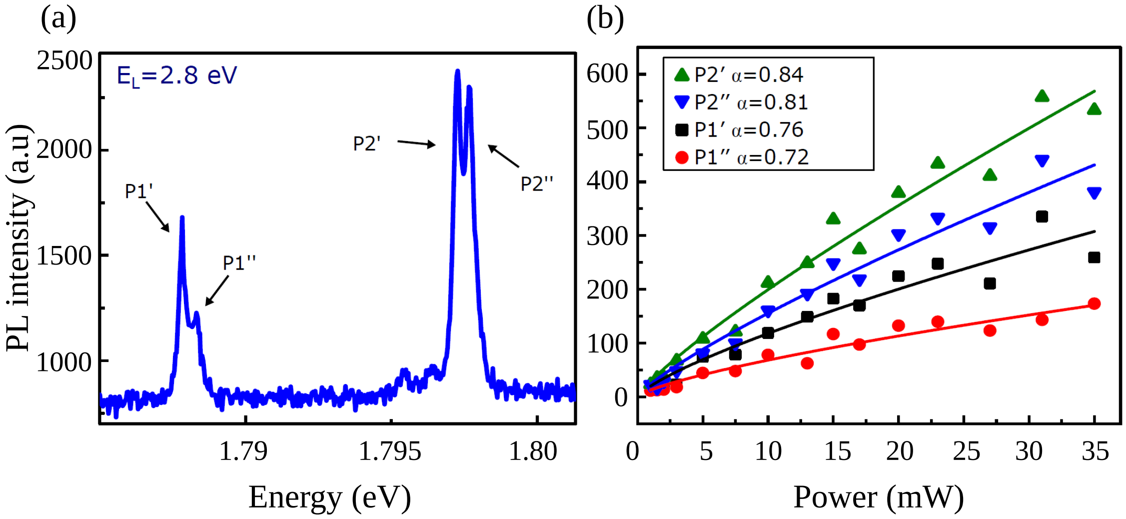

Figure 3.19: *(a) Subgap PL spectrum of bulk talc and (b) the sublinear peak intensity dependance on excitation energy. Solid lines represent a* $y = ax^{\alpha}$ *fit to the data, where* $\alpha < 1$ *indicates sublinear behaviour. Adapted from [239].*

3.3 Atomic force microscopy

Atomic force microscopy (AFM) is a type of scanning probe microscopy providing sub-nanometre resolution of a material surface allowing the optical diffraction limit to be bypassed without the need for expensive equipment or risk of damage to the sample [266]. The AFM probe consists of a sharpened tip (typically with a radius of curvature < 10 nm) mounted onto the free end of a Si or Si_3N_4 cantilever [267], while the fixed end is mounted onto a motorized stage. The sample to be measured is then fixed to the stage and positioned beneath the cantilever tip. When the probe is brought into close proximity with the sample surface, forces (vdW, electrostatic and magnetic dipole [268]) between the foremost atom of the tip and the surface lead to a deflection of the cantilever which can then easily be detected through the use of interferometry in conjunction with a laser focussed onto the free end of the cantilever. A schematic of a typical AFM set-up is shown in Figure 3.18.

This gives AFM three major applications: force measuremeant, topographic imaging

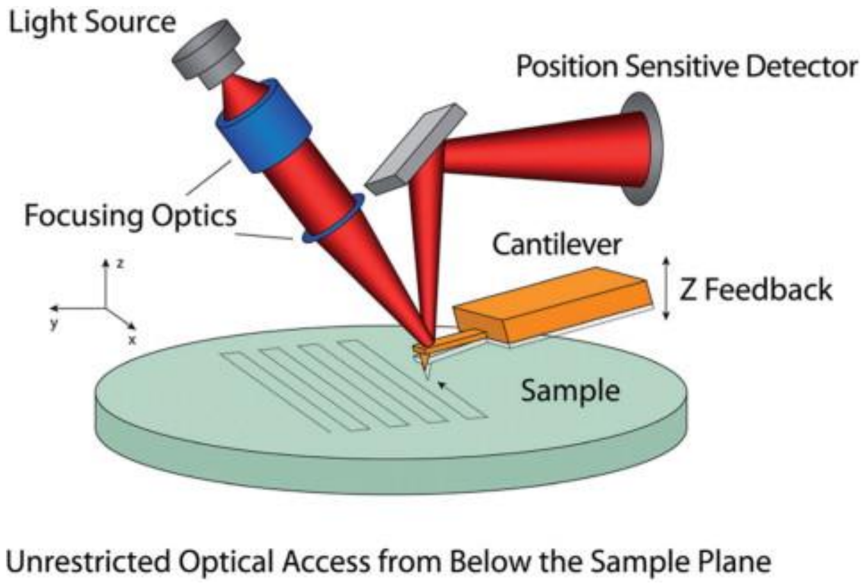

Figure 3.20: *Schematic depicting the optical level detection system used in AFMs. Light is reflected off of the cantilever and read on a detector as the probe is raster scanned across the surface. Taken from [267].*

and atomic manipulation. In force measurement, AFMs can be used to measure the forces between the probe and sample as a function of distance (force spectroscopy). This can be used to gather information about the mechanical properties of the sample such as the Young's modulus [61, 95, 134]. For topographic imaging, the probe can be raster scanned across the sample surface. The deflection of the probe as a function of its position can then be used to produce a three dimensional image of the sample surface. Finally, atomic manipulation can be achieved by exploiting the attractive forces between the tip and atom when they are in close proximity, allowing for control over individual atomic positions even at room temperature [269].

There are three main modes of AFM measurement: contact mode; non-contact mode and tapping mode.

3.3.1 Contact mode

In contact mode, the probe-tip is raster scanned across the sample surface whilst being in physical contact with it. The resulting deflection of the cantilever therefore directly corresponds to the surface topography. However, this method of measurement is usually avoided for 2D systems as both the tip and sample experience high compressive (due to tip-sample contact) and shear (due to lateral scan movement) forces which can damage the sample, blunt the AFM tip and distort the topographic image [270].

3.3.2 Non-contact mode

Both contact and tapping modes result in sample damage. If this must be avoided entirely then the non-contact mode of measurement should be used. This requires the cantilever to be driven at its resonant frequency through the use of a piezoelectric element in the cantilever holder. As the tip approaches the surface, attractive forces between the two begin to take effect. The gradient of the force between the tip and the sample modifies the compliance of the cantilever, inducing a change in resonance frequency and thus a shift in oscillation amplitude. Measurement of this vibration amplitude provides a feedback signal which can then be used to keep the tip-sample distance constant as it is scanned across the sample surface, therefore allowing topographic information about the surface to be extracted without contact with the tip and thus preventing sample damage [271]. However, the use of this technique in ambient conditions requires extremely responsive peizoelectric servos in order to track the changes in tip-sample distance and prevent the tip from contacting the sample accidentally, thus tapping mode is often chosen for ambient measurements instead.

3.3.3 Tapping mode

Samples often develop a thin liquid meniscus layer across their surface when kept in ambient conditions. If the performance of the peizoelectric servo is not sufficiently high, then the tip will accidentally stick to the surface due to these meniscus forces. To overcome this, the tip is vibrated at or near its resonant frequency and then deliberately *tapped* against the sample before detaching again on each oscillation cycle, provided that the oscillation amplitude is large enough to overcome the meniscus forces present on the sample surface [270]. This changes the oscillation amplitude of the cantilever, which can then be detected and used to modify the height of the cantilever above the stage in order to keep the amplitude constant. Therefore, topographic information is inferred from changes in oscillation amplitude and thus surface height with lateral position. As this is done with only periodic tip-sample contact, sample damage is minimised.

3.4 Scanning electron microscopy

The scanning electron microscope (SEM) utilises electron scattering to form an image of a sample surface and relies on the small de Broglie wavelength [272] (compared to the wavelength of optical light) of the electrons to surpass the diffraction limit of light and thus produce extremely high resolution micrographs. A schematic of an SEM is shown in Figure 3.19.

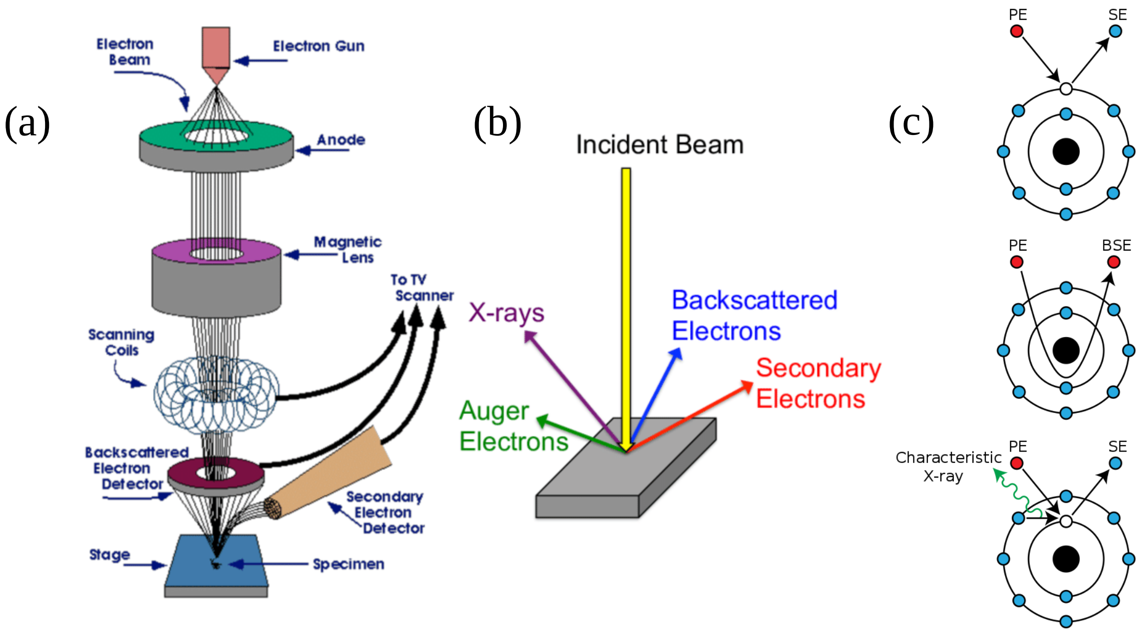

Figure 3.21: *Schematic of a typical (a) scanning electron microscope along with (b) the sample-beam interactions which take place within it. Taken from [273]. (c) The mechanisms for emission of secondary electrons (top), back-scattered electrons (middle) and x-rays (bottom).*

An electron gun (which is usually a W wire heated to ∼ 2500 °C [274]) undergoes thermionic emission and provides a source of electrons which are then accelerated towards the positively charged anode under high vacuum. A small proportion of these electrons will move through the anode and be focussed to a small point just a few nanometres in diameter on the sample surface by a series of magnetic lenses. In addition to magnetic lensing of the electron beam, they also pass through a set of scanning coils which provide lateral deflection and allow the beam to be raster scanned across the sample surface.

The electrons then penetrate the surface in a tear-drop shaped volume (known as the interaction volume) whose dimensions depend upon the energy of the incident electrons, the atomic masses of the elements within the sample surface and the angle of incidence [274]. These high-energy electrons lose energy through repeated scattering and absorption upon interaction with the sample, which in turn results in the production of secondary electrons, Auger electrons, x-rays, heat and back-scattered electrons, as is depicted in Figure 3.19 (c).

Of these emissions, secondary electrons are primarily used to produce micrographs as they tend to be highly localised to the point of impact of the initial electron-beam on the sample surface, and so allow images to be collected with an extremely high resolution of ~ 5 nm (when using a W source, although it can be as low as ~ 1 nm in certain situations) [274]. Back-scattered electrons are those incident electrons which approach the atomic nucleus sufficiently closely to be scattered through a large angle and re-emerge from the sample surface. They come from deeper within the sample and so provide less resolution than the secondary electrons, although they can be used to gain information about the elemental distribution within the sample as elements of higher atomic mass produce points of higher contrast within the micrograph [274]. This, in addition to x-ray and Auger electron emission (both the result of ionisation of an electron from an atomic inner shell), can be used to gather complete information on the distribution and identity of the different elements present within the sample, respectively.

4. Experimental techniques

4.1 Abraded films

4.1.1 Manual abrasion

The general approach used to abrade thin films is shown in Figure 4.1.

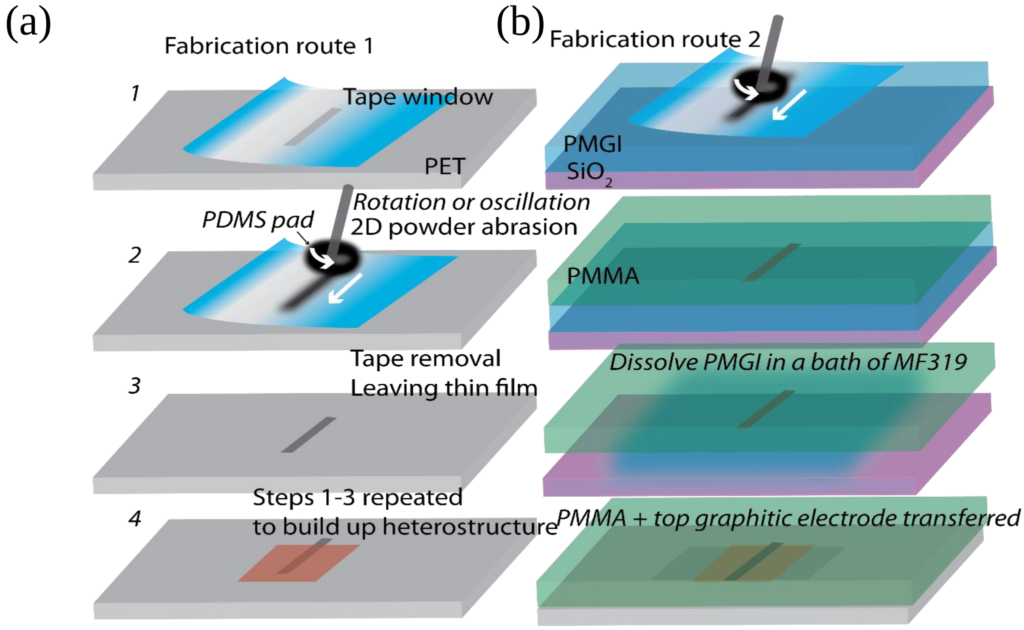

Figure 4.1: *Fabrication routes used to produce heterostructures through mechanical abrasion of vdW powders via a manual, direct write method.*

Essentially, I make use of a viscoelastic polymer, namely polydimethylsiloxane (PDMS), which is cut into 1 cm × 1 cm squares and then pressed into a bulk vdW material powder (graphite, TMDCs or hBN). This ensures full adhesion of the micron-sized powder particles to the PDMS surface and allows it to be used as a writing pad. All of the powders investigated during this study adhere equally well to the surface of the PDMS. The PDMS pad is then oscillated back and forth against the substrate with vdW materials embedded between it. The key parameters which govern the abrasion process on different substrates include the surface roughness, vdW material hardness (see Section 2.5.5) [275] and relative position on the triboelectric series [276] between the vdW material and the substrate (electrostatic charging). Subsequent deposition of material is then due to a friction-facilitated basal cleavage of micro-crystallites within the bulk material powder as it is rubbed against layers already adhered to the substrate, overall resulting in the deposition of a thin, abraded nanocrystalline film. The thickness of the deposited material is controlled by the rubbing time and force applied to the writing pad, as is discussed within Section 4.1.2.

To ensure that the vdW material is only written at selective locations, a tape mask (using Nikko cleanroom tape) can be applied to the substrate before writing (although this is not necessary with automated abrasion, unless < 5 mm pattern resolution is required). After the design has been written, the tape mask is removed leaving only the unmasked region coated in the vdW material, see Figure 4.1 (Steps 1-3). This process can then be repeated using different vdW powders to build up bespoke heterostructures, as is shown in Figure 4.1 (Step 4). An example of a set of vertical heterostructures produced in this manner is shown in Figure 4.2.

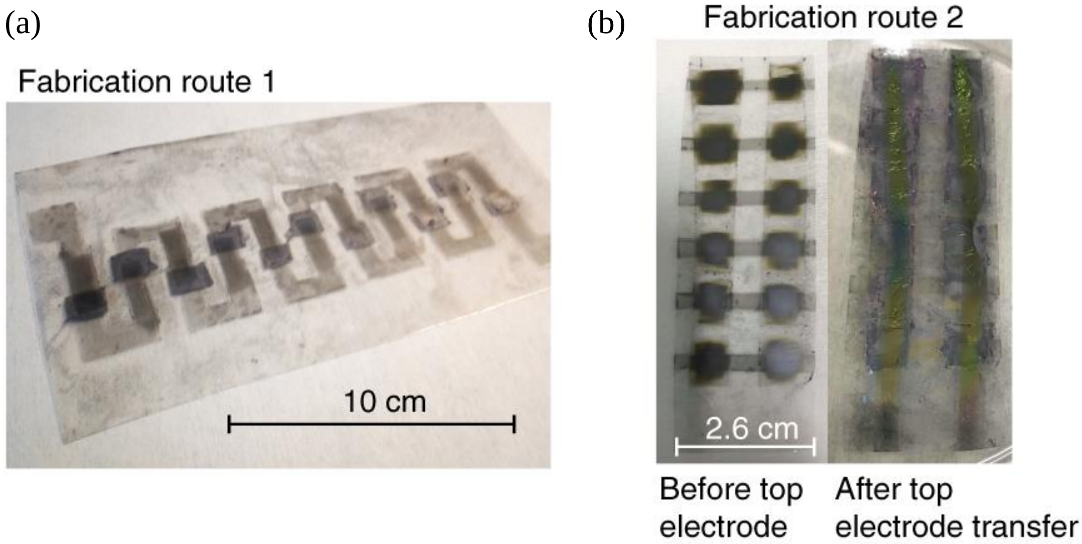

Figure 4.2: *(a) An example of multilayered vertical junction photodetectors based on a graphite/*WS_2*/graphite architecture produced through fabrication route 1. (b) The same architecture as (a) but this time produced through fabrication route 2, with the top graphite electrode transferred from PMGI, which leads to a higher device yield.*

A limiting factor on device yield when directly applying a top graphitic electrode layer was short circuiting, caused by deposition of the top graphitic electrode breaking the barrier material layer underneath (i.e. WS_2 for the devices in Figure 4.2). Moreover, it appears that direct abrasion of graphite onto TMDCs and hBN frequently damages the barrier material, likely due to the different materials' mechanical properties, while the reverse combination, e.g. TMDCs on graphite, are non-damaging. Recent calculations [275] predict that graphite is significantly harder than MoS_2, WS_2 and hBN, which may explain why the former so easily penetrates barrier layers made out of the latter. In order to overcome this, I developed a separate fabrication route (fabrication route 2 within Figure 4.1 (b)) allowing successful transfer of the final abraded graphite top electrode. This is achieved by first abrading the graphite onto a polydimethylglutarimide (PMGI) polymer layer, before spin-coating with 500 nm polymethyl methacrylate (PMMA). The sacrificial PMGI layer is then subsequently dissolved in a bath of MF319 developer leaving the graphitic film attached to the underside of the PMMA layer, which can then be transferred directly onto the target heterostructure.

After device fabrication, the films were characterised through a combination of optical and Raman spectroscopy, electron transport, AFM and SEM in order to indentify the surface roughness, film thicknesses and transport characteristics (see Section 5.1). The entire fabrication process was always performed under ambient conditions, although it could easily be reproduced in a controlled inert gas or high vacuum environment, widening the scope of compatible vdW materials. It should be noted that not all substrates are compatible with direct abrasion of graphite, although successful abrasion can be achieved on a wide variety of substrates including (but not limited to) polyethylene terephthalate (PET), polytetrafluoroethylene (PTFE), PMGI, PDMS (both purchased films (*Sigma Aldrich*) and sheets made in-house), polyethylene napthalate (PEN), PMMA, porous polyurethane (Tegaderm^{TM}, available from *3M*), aluminium, steel and paper. The approximate thickness (t) and average molecular weight ($\langle M_w \rangle$) of the polymers used are given in Table 4.1. The molecular weight of the Tegaderm^{TM} and PEN films are unknown as it is proprietary information.

Table 4.1: *Physical characteristics of the various polymer substrates used within this study.*

Polymer	t (**µm**)	$\langle M_w \rangle$
PET	100	31,000
PTFE	100	60,000
PDMS (purchased)	100	95,000
PDMS (in-house)	1000	95,000
PEN	125	N/A
PMMA	500	950,000
Tegaderm$^{\text{TM}}$	100	N/A

However, all other materials investigated in this study were compatible with SiO_2 as well. This is likely due to the surface chemistry and roughness of the different substrates, and particularly in how these parameters interact with the hardness of the material being deposited. It should also be noted that no prior treatment of the substrate is required for strong adhesion of the vdW material.

4.1.2 Automated abrasion

To better quantify the abrasion process, a CNC micro engraver system was modified to study the effect of force, feed rate and the sheet resistance as a function of the number of write passes. Figure 4.3 (a) shows the modified CNC 3018 Pro milling machine used.

The CNC drill bits were enveloped in a thin cap of PDMS covered in the vdW material of choice and then used to abrade onto a PET substrate in a pre-programmed pattern. To do this, PDMS was created in-house by mixing a 10:1 ratio of silicone elastomer base to reactive fluids, respectively. The mixture is left for one hour in order to degas. It can then be covered in several layers of Al foil through which the drill bits are pressed. The tension in the Al foil serves to keep the drill bits upright and suspended in the PDMS mixture during the curing process, see Figure 4.3 (b). The PDMS is then baked at 80 °C for three hours until cured. Afterwards, a scalpel is used to remove the drill bits and shape the PDMS cap (typically cut to be $\sim$ 2 mm thick on all sides), see Figure 4.3 (c). The PDMS cap is then covered in a vdW material (by pressing the PDMS into the bulk powder), as is shown in Figure 4.3 (d), and then used to write the pattern of choice. Subsequent layers of material can be

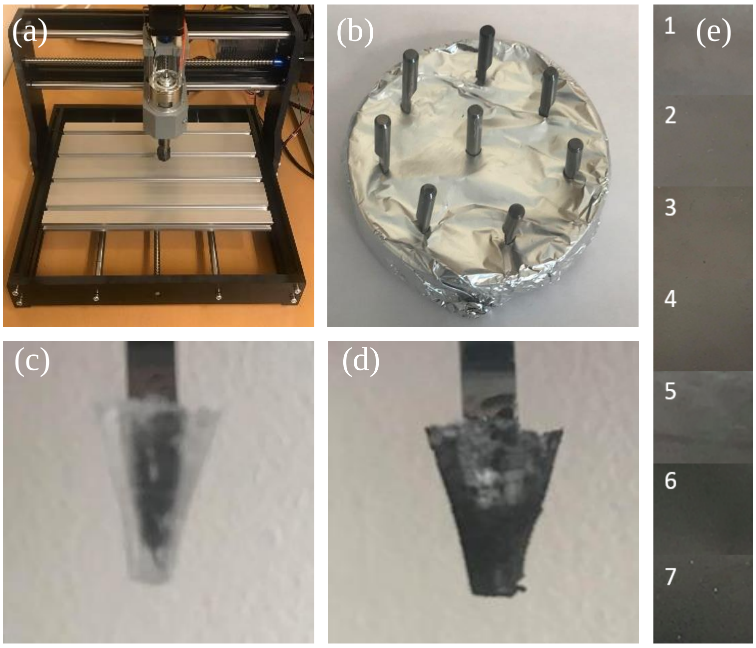

Figure 4.3: *(a) Modified CNC 3018 Pro milling machine. (b) Method used to produce a PDMS-capped drill bit. (c, d) PDMS-capped drill bit before (c) and after (d) covering with graphite powder. (e) Image showing the colour of the abraded graphite as the thickness increases (indicated by the number of write passes, 1-7).*

abraded by simply exchanging the PDMS-capped drill bit for another and repeating the process, allowing for the formation of a heterostructure. The drill was set to 100 rpm in the production of all devices. As in the manual abrasive method, the entire procedure was conducted in ambient conditions.

Calibration procedure: Figure 4.4 (a) illustrates the abraded graphite sheet resistance as a function of the "number of passes", N. This refers to the number of times that each abraded film was patterned in order to increase its thickness. As expected, the sheet resistance generally decreases as the thickness of the abraded graphite increases, to as low as 50 Ω/sq at 7 passes. However, it should be noted that a single pass alone is not enough to abrade a continuous graphitic film and thus no conduction is seen in these samples, similar to how the writing pad must be continually oscillated across the substrate for a prolonged period of time during the manual abrasion process. For both samples the sheet resistance spikes at 3 passes. This may be due to damage of the initial abraded film upon the second and third pass, which is then repaired as more graphite is added on subsequent passes. Figure 4.4 (b) illustrates sheet resistance as a function of force applied between the

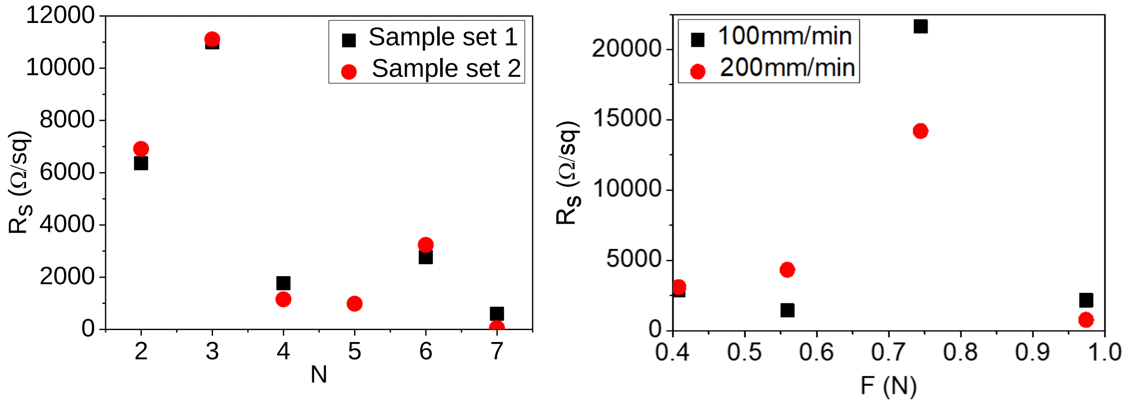

Figure 4.4: *(a) Sheet resistance, R_s, as a function of the number of write passes, N, used to abrade a set of graphite films. (b) Sheet resistance as a function of force applied by the PDMS-capped drill bit to the PET substrate and feed rate (in mm/min).*

PDMS-capped drill bit and the PET substrate, F, for two different feed rates. For each feed rate the sheet resistance spikes for an intermediate applied force of ~ 0.75 N. Application of forces larger than ~ 1 N consistently caused the underlying PET substrate to tear, and was particularly present for feed rates > 300 mm/min. Calibration of the automated abrasion process in this manner allowed for the production of complex device architectures without damage to the heterostructure, see Section 5.1.

4.2 Abraded device designs

4.2.1 Photodetectors

The photodetector device architectures investigated during this study are illustrated within Figure 4.5.

Figure 4.5 (a) shows a simple photodetector device made entirely from abraded vdW powders. It consists of a graphite channel abraded onto a PET substrate (which is optically transparent). The centre of this channel is then thinned down by back-peeling with specialist tape in order to increase the transparency in this

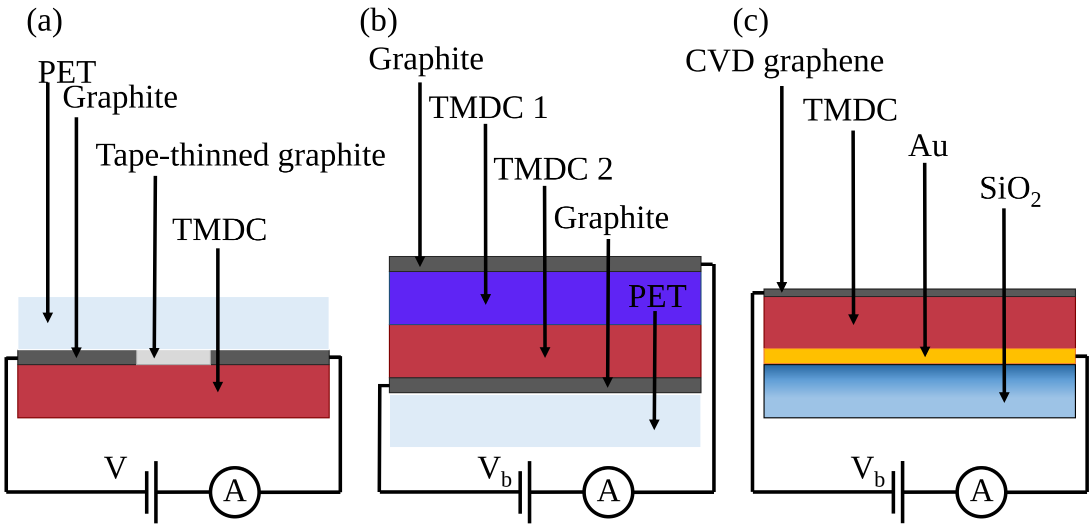

Figure 4.5: *(a) A simple double-layered photodetector consisting of a transparent graphitic channel overlaid with TMDC nanocrystals. (b) A complex multilayer heterostructure with a top graphite electrode produced via fabrication route 2. (c) A third device architecture, this time using a transferred, CVD-grown graphene layer as the transparent top electrode.*

region (to ~ 40 %) and allow light to reach the graphite/TMDC interface. A TMDC layer (MoS_2, $MoSe_2$ or WS_2) is then abraded on top of the graphite channel. Upon illumination, photoexcited carriers within the abraded TMDC layer transfer into the abraded graphite layer, resulting in a change of the free charge carrier density and thus a change in the electrical conductivity. Application of a voltage, V, between the ends of the electrode allow the current through the sheet to be measured, and thus the photoresponsivity of the entire device to be determined.

A more complex, multilayer heterostructure is shown in Figure 4.5 (b). Here, a second TMDC is abraded onto the first with a secondary top electrode transferred on top of the stack (via fabrication route 2) to produce a graphite/TMDC/TMDC/graphite heterostructure. Finally, a third architecure was utlised with the form Au/TMDC/graphene. By replacing the bottom and top electrodes with Au and transferred, highly transparent and conductive CVD-grown graphene, respectively, characterisation of the abraded TMDC alone can be achieved. The CVD grown graphene is monolayer, and purchased from *2D Semiconductors*. The fabrication was carried out as follows: PMMA was spin coated onto CVD graphene on copper, a tape window was then attached and the copper etched away in a 0.1 M aqueous solution of ammonium persulfate (APS), which nominally took 6 h. The CVD graphene was then transferred through two beakers of deionised (DI) water (>8 M Ohm cm) to remove excess APS. The graphene/PMMA membrane was then transferred onto the target device completing the heterostructure. The device along with CVD graphene/PMMA was baked for 1 h at 150 °C to improve the mechanical contact of the CVD graphene with the abraded nanocrystal films. In both of these architectures, the presence of a secondary electrode allows for the application of a back gate voltage, V_b, between the two. This can be used to modulate the charge transfer rate through the device and thus optimise the photoresponsivity.

The parameter of interest for these devices is the photoresponsivity, general measurement technique used is as follows: in order to characterise the photoresponsivity of these devices a fibre coupled white light source with an output power of 1.4 W at the fibre tip is used to excite the photoactive layers. The incident white light power density at the sample surface depends on the separation distance between the fibre tip and the surface, and is listed for each experiment in the relevant section of Chapter 5. Electron transport measurements both with and without white light excitation were carried out using a KE2400 source-metre which simultaneously applies a bias across the source and drain electrodes (and gate electrodes where relevant) whilst measuring the current. Photoexcitation of carriers within the active layer of the abraded photodetectors results in modulation of the charge carrier density (with the mechanism depending on device architecture, see Section 5.1.2) which in turn increases the current measured by the source-metre. The difference between the current both with and without white light excitation is known as the photocurrent, I_p, and, when used in conjunction with the known incident power, P, allows calculation of the device photoresponsivity, R, with

$$R = \frac{I_p}{P}. \tag{4.1}$$

4.2.2 Triboelectric nanogenerators

As discussed within Section 2.5.4, triboelectric nanogenerator (TENG) devices rely on the use of two materials at opposite ends of the triboelectric series [197]. Recently, it has been demonstrated that one strategy for enhancing the power output of a TENG relies on the use of multilayered structures. In the case of abraded films, this involves the introduction of charge trapping layers such as MoS_2 which increase the magnitude of the induced charge per unit area and thus enhance the power output [199, 201].

Figure 4.6 shows a schematic for the operation of a simple abraded TENG charging/discharging cycle. Here, the TENG electrode is comprised of a PET substrate and an abraded nanocrystal film or multilayer stack of abraded 2D materials. The entire TENG is then composed of an Al hammer (wrapped in PTFE tape) with a fluorinated PDMS polymer placed on top of the abraded vdW electrodes. PDMS and PET were chosen as the triboelectrically active layers due to their positions on the triboelectric series; fluorination of the underside of the PDMS was completed in order to increase its electronegativity and thus enhance the triboelectrically-induced surface charge density [199] (which was done using a reactive ion etcher (see Section 4.3.4) with CHF_3 as the active gas, at 30 mTorr gas pressure, 50 W rf level and a 6 minute etch time); the induction layer was being investigated and was chosen as any semiconducting abraded TMDC and abraded graphite was chosen as the electrode in order to keep the entire device as scalable as possible. Manual abrasion of graphite followed by the chosen TMDC layer was completed on a PET substrate. The graphite layer was then contacted using Ag epoxy and Cu adhesive tape to allow for measurement of TENG characteristics. A pre-made and fluorinated PDMS layer was then placed on top of the stack before the PTFE-coated hammer was brought into contact.

The operation of the device can be explained as follows: contact between the PTFE-coated hammer and the PDMS layer results in charge transfer via the triboelectric effect. Whilst they are in contact the system remains electrically neutral (Figure 4.6, process 1). Upon release and separation, the abraded electrode (a graphite/MoS_2

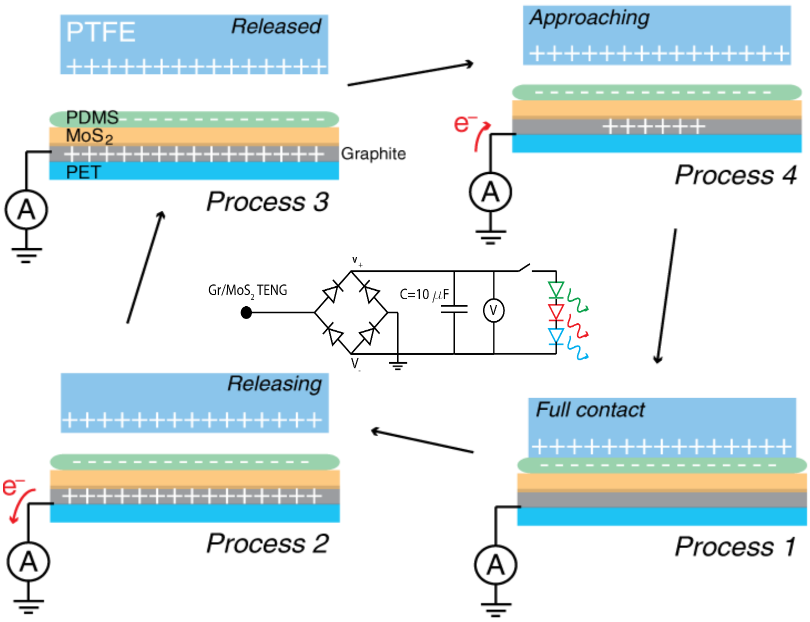

Figure 4.6: *Schematic showing the evolution of charge within an abraded triboelectric nanogenerator during a charging discharging cycle. Central inset: schematic of the circuitry used to measure the TENG power output.*

multilayer) is electrostatically induced by the negatively charged PDMS layer, and at this moment free electrons within the electrode move towards ground corresponding to a negative current (Figure 4.6, process 2). After a short while, when the PTFE-coated hammer has come to a standstill, electrostatic induction of the abraded electrode ceases and the current returns to zero (Figure 4.6, process 3). Finally, when the PTFE-coated hammer re-approaches the PDMS layer, electrons are drawn from the ground back into the TENG electrode and thus a positive current is observed (Figure 4.6, process 4), and so the cycle repeats. The abraded electrode can then be used to charge a capacitor placed in series and thus store energy, as is shown in the central inset of Figure 4.6.

4.2.3 Strain sensors

A thin, abraded graphite film consists of discrete micron-sized particles spread out across a substrate surface. In order to conduct electricity, there must be a continous conduction pathway from one end of the film to the other. This can generally be accomplished in one of two ways: (1) the abrasion process can continue until sufficient graphite has been deposited to form a continous film or (2) force the graphite crystals to make contact with each other by physically moving them. The latter can be accomplished by straining the system. If the unstrained film already has sufficient graphite to conduct then the application of compressive strain will open additional conduction pathways and thus enhance the conductivity of the film. Likewise, if tensile strain were to be applied instead, then the graphite crystals would be forced apart, removing conduction pathways and hence lowering the conductivity of the sheet.

Figure 4.7 (e, f) shows the bespoke bending rig set up (designed using SolidWorks, a computer assisted design and modelling software, see Appendix) which was used to apply uniaxial strain to the devices within this study.

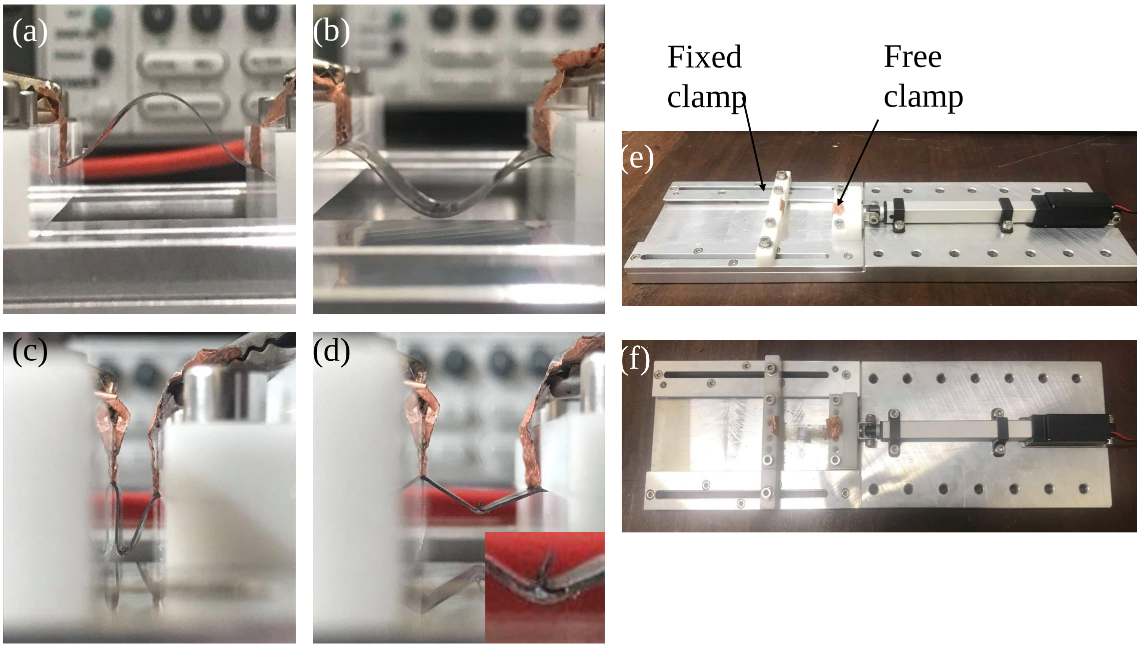

Figure 4.7: *(a) Image showing an abraded graphite/*MoS_2 *heterostructure on a PET substrate under tensile strain. (b) The same device as in (a) but under compressive strain. (c) An example of a device strained beyond the elastic limit and (d) the resultant plastic deformation. Inset: damage to the abraded heterostructure.*

These devices were typically a graphite/TMDC heterostructure adhered to a 0.5 mm thick, flexible PET substrate. They were held in place by two clamps, one of which is fixed in position to the underlying plate while the other is free to move. An Actuonix L16 Micro Linear Actuator is used to push the free clamp forwards in order to bend the sample and apply strain. Dovetail grooves are used to ensure the free clamp can only move parallel to the direction of the actuator arm. The actuator is driven by a

DC voltage pulse controlled by the VI software (LabVIEW) and the distance moved by the clamp can then be measured and used to calibrate the rig. The distance moved and therefore strain applied can the be accurately controlled by tailoring the duration of the voltage pulse applied to the actuator, with the direction moved also being controlled by the polarity of the applied potential. Conducting copper tape, pressed firmly onto the devices by the clamps, is used to provide electrical contact for two-terminal measurements. A KE2400 source-metre is used to apply a bias potential between the source and drain electrodes (with the magnitude applied given in the relevant results section) and measures the resultant current moving through the abraded channel. The strain applied to the channel is controlled whilst measuring said current, allowing the current-strain response to be measured for the device of interest.

4.2.4 Pressure sensor

Recently, there has been significant research effort into creating portable, lightweight and comfortable pressure sensors, with the primary goal being the creation of wearable heart rate monitors for the diagnosis of disease [277, 278, 279]. Many of these rely on the use of single crystal transistors [280], structured piezoresistive sensors [281] or commercially available carbon-based resistive rubber [282]. This study instead opts for capacitive pressure sensing via abraded graphite powder on Tegaderm$^{\text{TM}}$ film (a flexible polyurethane substrate, 0.1 mm thick), which can then be directly mounted onto a wrist in order to detect a pulse. A schematic of the abraded capacitor design is illustrated in Figure 4.8.

Bulk graphite powder was abraded onto two separate Tegaderm$^{\text{TM}}$ membranes using the automated abrasive method described in Section 4.1.2 to serve as the upper and lower electrodes of the capacitor. The graphite electrodes were then contacted using copper tape along with conductive silver epoxy to improve the electrical contact between the tape and the abraded graphite. The two individual Tegaderm$^{\text{TM}}$ films were then stacked with a separating dielectric barrier layer made from either a PDMS sheet (produced in house, see Section 4.1.2) or another Tegaderm$^{\text{TM}}$ membrane. A

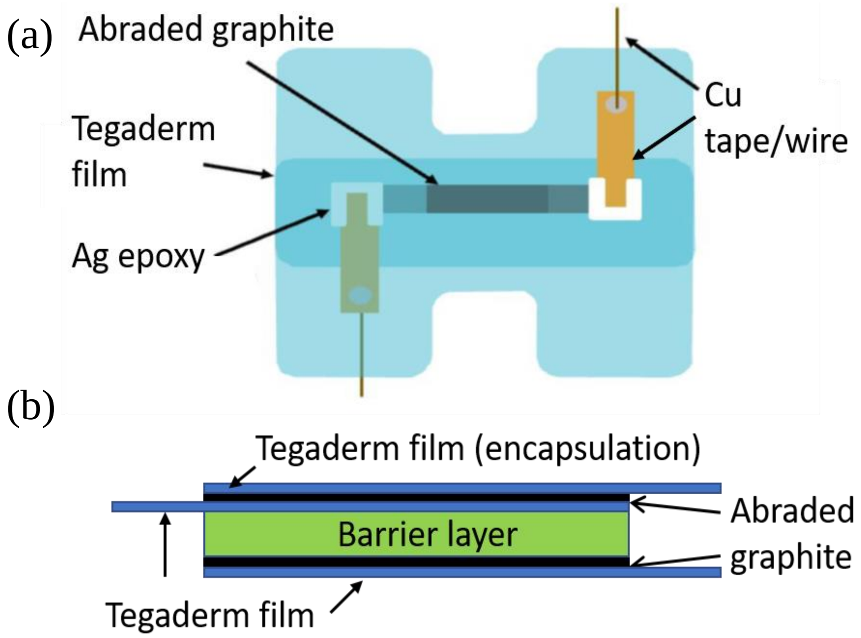

Figure 4.8: *(a) Illustration of a wearable, abraded capacitor. (b) Architecture of the capacitors, where the barrier layer was chosen as either a thin sheet of PDMS or another Tegaderm^{TM} film.*

final Tegaderm$^{\text{TM}}$ layer was then added to encapsulate the entire capacitor device and protect it from the environment. Capacitance spectroscopy was performed using a Rhode and Schwarz, Hameg HM8118 LCR Bridge. In order to measure the responsivity of the capacitors to external pressure, steel discs of mass $m = 3.56$ g and contact area $A = 12.56$ cm^2 were stacked onto surfaces of the capacitors whilst measuring the resulting change in capacitance.

4.2.5 Thermistors

Using the automated abrasion process it is possible to produce flexible, wearable thermistors as well. Bulk MoS_2 powder was mixed with graphite powder in varying concentrations, specifically MoS_2:graphite ratios of 10:90, 30:70, 50:50, 70:30 and 90:10. The composite powders were abraded into strips and contacted at either end using copper tape and conductive silver epoxy. Using a hotplate to control the temperature of the abraded film the current-voltage characteristics were measured at a number of different temperatures (ranging from $\sim 30 - 70$ °C). The temperature was monitored using an ADS1115 16-Bit ADC chip connected to a standard thermistor bonded to the samples using thermally conductive tape, whilst electrical measurements were carried out using a KE2400 source-meter. This data could then be used to extract the change in sheet resistance as a function of temperature It should be noted that the sample with a 90:10 ratio of MoS_2:graphite did not conduct within the applied bias range used throughout this study, and so the temperature response for this mixture was not taken.

The bulk MoS_2 powder used is an n-type semiconductor and thus provides a temperature dependant conductivity which can, with a graphite-facilitated reduction in channel resistance, easily be exploited to produce a significant temperature response within the abraded films. This is because transfer of charge carriers from the MoS_2 conduction band into the conduction band of graphite at the MoS_2/graphite flake interfaces within the abraded films serves to modulate the driven current as a function of temperature. Therefore, the addition of conductive graphite powder allows for an amplified temperature response at significantly lower bias voltages. For each mixture investigated, the channels were contacted using conductive Ag epoxy and adhesive Cu tape. This in turn allowed for application of a bias potential across the channel using a KE2400 source-metre whilst measuring the resulting current, allowing the thermistor devices to be electrically characterised. Temperature measurements were taken using an ADS1115 16-Bit ADC chip connected to a standard thermistor bonded to the samples using thermally conductive tape.

4.3 Exfoliated heterostructures

4.3.1 Mechanical exfoliation

The graphene, hBN, TMDC and talc samples used within this portion of the study were produced by mechanical exfoliation as this method consistently produces large, high-quality single-crystal flakes with length scales between 1-100 µm. To begin with, the substrate, which is usually a 0.5 mm thick Si base with a 300 nm thick SiO_2 oxide layer on the top and bottom surfaces, is cleaned first in acetone and then isopropyl alcohol (IPA) within a sonicator, for 10 minutes at each step, before drying with nitrogen gas. Acetone is required in order to remove unwanted hydrocarbons from the substrate surface, although if left to dry the solvent can leave hard-to-remove residue behind. This is why immediate transfer of the substrate into the IPA bath is required, to disperse the acetone and to ensure that after the second step of cleaning the substrate returns to its normal state. Once the substrate is dried it is immediately transferred into a reactive ion etching (RIE) machine which pre-treats the SiO_2 surface with an oxygen-argon plasma to remove any remaining contaminants. Afterwards the substrate is heated to 90 °C on a hot plate and, whilst this is happening, crystal fragments of the material of choice (graphite, hBN etc.) are cleaved away from the bulk material using two sheets of low-tack cleanroom tape. The tape is repeatedly pressed together and separated ($\sim$10 times) to disperse the material across a large area before being pressed down onto the substrate surface for one minute. Slow removal of the tape exfoliates the material onto the substrate ready for identification. The time between plasma treatment and exfoliation should be minimised in order to reduce the density of contaminants present on the substrate surface beneath the sample.

4.3.2 Flake identification

Suitable flakes are initially identified using an optical microscope. On a generic substrate identification of monolayer and few-layer samples would be difficult due to having a reduced optical contrast as a result of their thickness. This is why Si/SiO_2 substrates with a controlled oxide layer thickness are often used during the initial identification step, as the reflective Si and transparent SiO_2 creates thin film interference at visible wavelengths, resulting in constructive interference between light which reflects off of the flake and that which reflects from the underlying Si, see Figure 4.9 (e), increasing the contrast and allowing for approximate identification of flake thicknesses by eye [283, 284, 285]. However, the presence of contaminants can alter the separation distance and alter the contrast [6, 286], and so contrast measurements should not be used to conclusively determine sample thicknesses.

Figure 4.9 (a), (b) and (c) highlight the change in optical contrast with thickness for graphene, MoS_2 and WSe_2 on a Si/SiO_2 substrate with similar oxide thicknesses,

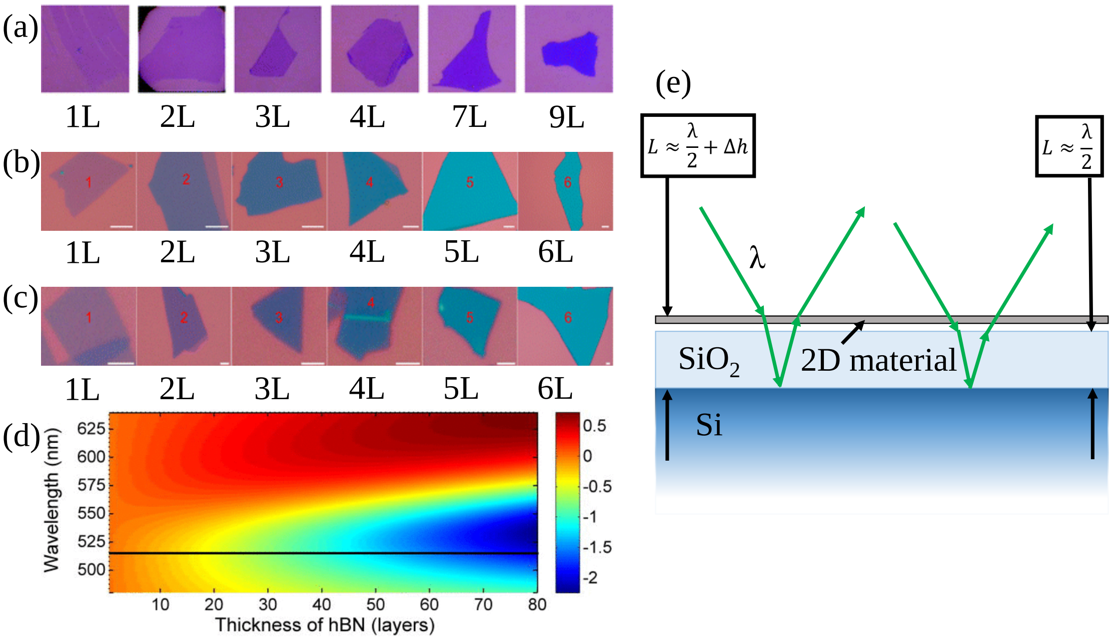

Figure 4.9: *Variation in optical contrast for 2D materials on Si/SiO$_2$ substrates. The number of layers present in each case is indicated below the image (monolayer being 1L, and so on). (a) Graphene of different thickness on a Si/SiO$_2$ substrate with a 285 nm thick oxide thickness. (b) MoS$_2$ of different thickness on a Si/SiO$_2$ substrate with a 300 nm thick oxide. (c) WSe$_2$ of different thickness on a Si/SiO$_2$ substrate with a 300 nm thick oxide thickness. (d) Calculated optical contrast as a function of the wavelength of the incident light and thickness of hBN for a 282 nm thick oxide layer. (e) Optical path length, L, and its difference, Δh, between light reflecting from the surface of an exfoliated 2D material and that which is reflected from the underlying Si. (a), (b, c) and (d) were adapated from [283], [285] and [284], respectively.*

respectively. Figure 4.9 (d) shows the calculated optical contrast as a function of incident wavelength and hBN thickness. In all four cases, as the exfoliated material becomes thicker the contrast increases, which can be enhanced further through an appropriate choice of wavelength for the incident light. Although initially the difference between mono- and bilayer materials, for example, is difficult to see, with experience the eye can be trained to quickly identify flake thicknesses by their contrast. This is useful as, due to the large number of flakes exfoliated and random distribution of thicknesses, characterising each flake precisely using methods such as Raman spectroscopy (see Section 3.1) or AFM (Section 3.3) becomes impractical. Optical contrast identification therefore allows one to quickly create a subset of potentially suitable flakes from the set of all exfoliated flakes, which can then be further reduced using the aforementioned, more precise, identification methods. In particular, Raman spectroscopy was carried out using 532 nm excitation at 1 mW laser power, which was focussed into a 1 µm diameter spot.

4.3.3 Transfer processes

In order to build high quality vertical heterostructures an all-dry transfer process was used [12]. Mechanical exfoliation of the bottom layer of the heterostructure onto an acceptor substrate is completed as discussed in the Section 4.3.1. Additional layers are built up by first exfoliating each individual material onto a transparent polymer layer, namely PDMS, which is in turn adhered onto a glass slide. The PDMS is a viscoelastic material, meaning that it behaves as an elastic solid when deformed over short timescales and can flow when deformed over long timescales. An optical microscope is used to identify appropriate flakes from their contrast, although this is more difficult due to the transparent nature of the PDMS. Once a suitable flake has been identified, the glass slide is mounted upside down onto a motorised stamping stage in order to allow sub-micrometre control of movement in the x-, y- and z-directions, along with that of lateral rotation. The acceptor substrate is then fixed in position on the stamping stage. A secondary optical microscope is used in conjunction with the motorised stage to align the flake adhered to the PDMS with that adhered to the acceptor substrate by looking through the transparent PDMS, and the two are carefully brought into contact. By slowly peeling off the PDMS from the surface, the viscoelastic material detaches and releases the secondary flake which preferentially adheres to the flake on the acceptor substrate. The entire dry-transfer technique is illustrated within Figure 4.10 (b). Repeating the transfer process allows for the creation of bespoke vertical heterostructures with atomic-layer thicknesses. As discussed in Section 2.5.1, self-cleaning along the interface ensures the production of high-quality devices, although the process is extremely time-consuming and cannot be scaled up. All transfer procedures during this study were completed in a cleanroom at 23 °C ± 1 °C with a humidity of 55 % ± 5 %. This stacking technique was chosen as wet-transfer methods often results in contamination and sample damage due to capillarily forces upon removal of the transfer polymer [12].

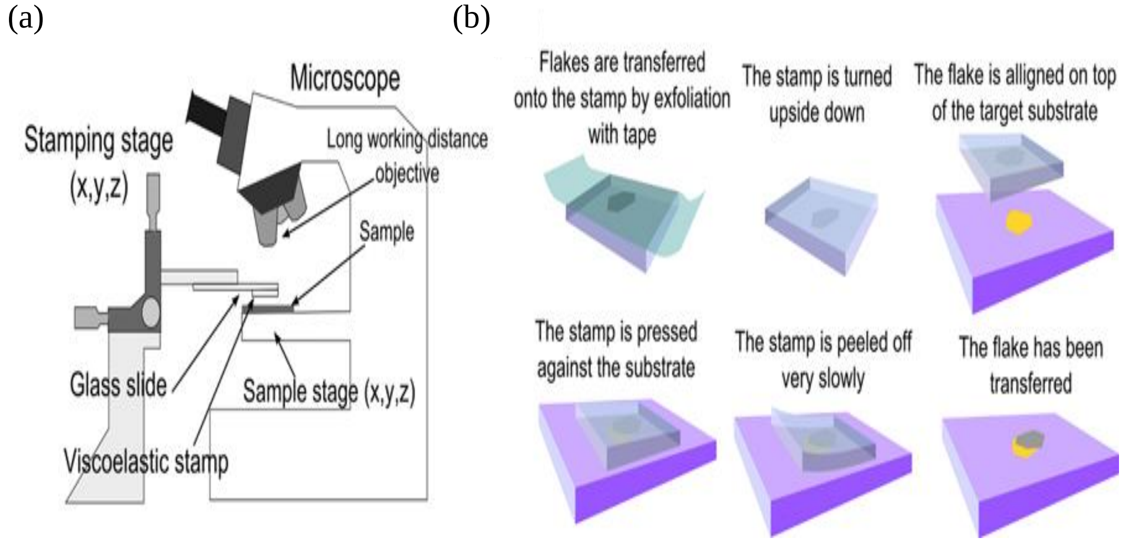

Figure 4.10: *Dry-transfer setup and process. (a) Schematic diagram of the experimental setup employed during the all-dry transfer process. (b) Diagram of the steps involved in the preparation of the viscoelastic stamp and the deterministic transfer of an atomically thin flake onto a user-defined location. Image taken from [12].*

4.3.4 Etching and contact deposition

Electrical contacting of the sample first requires spin-coating of $\sim$ 200 nm of PMMA (950K) across the substrate surface, sample included, which is then cured by heating to 130 °C for 10 minutes on a hot plate. PMMA resist is chosen as it allows for high ($\sim$ 1 nm) resolution patterning via electron beam lithography. A computer aided design software (AutoCAD) is used, in conjunction with optical micrographs collected during the identification and assembly stage, to create an electron beam writing pattern scaled to the substrate using Au calibration markers which are used to define the contact geometry, see Figure 4.10 (a). The contacts edges are designed to run parallel with each other as well as having at least 1 µm of overlap between the metal and material to ensure good electrical contact. The PMMA-coated sample is then placed in an electron beam lithography machine which accelerates electrons towards the surface (in the same manner as SEM, see Section 3.4) with an 80 kV potential and beam current of $\sim$ 10 nA through a vacuum. Bombardment by these high-energy electrons depolymerises the long-chain PMMA molecules in the regions specified by the writing pattern (as PMMA is a positive resist) and allows for the

PMMA here to be removed in a developer composed of IPA and methyl isobutyl ketone (MIBK) in a 15:1 ratio, leaving it exposed to the environment whilst the remainder of the substrate is covered in PMMA, as is shown in Figure 4.11 (b). To prevent overdevelopment the substrate is submerged in the developer for one minute before transferring into an IPA bath and then drying with nitrogen gas.

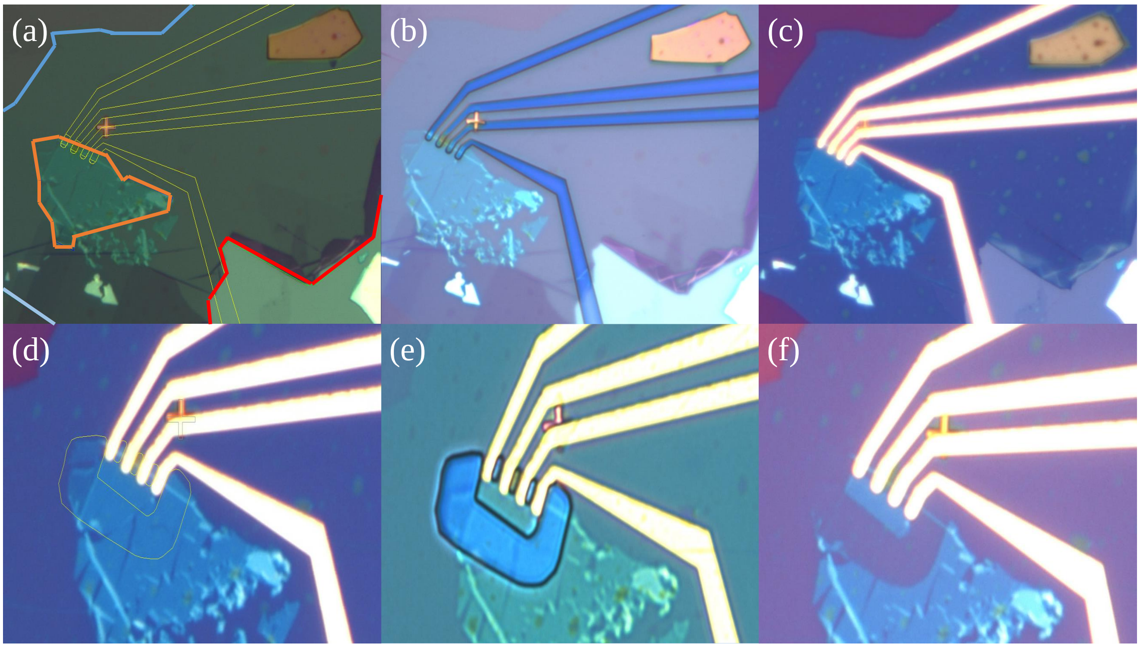

Figure 4.11: *Etching and contact deposition process for a graphite/talc/MoS_2 vertical heterostructure. (a) AutoCAD image of the device (taken under a green light filter), with graphite, talc and MoS_2 outlined in red, blue and orange, respectively. The writing pattern used to designate contact geometry is shown in yellow. (b) The device after electron beam lithography and removal of depolymerised PMMA in the contact regions. (c) After deposition of Cr/Au metal used to contact the MoS_2 layer, with the PMMA sacrificial layer removed. (d) AutoCAD image showing the designated region to be etched in yellow. (e) Exposed etch region after electron beam lithography. (f) After etching the MoS_2, with the sacrificial PMMA layer removed.*

Once the contact regions are exposed the sample is placed within a thermal evaporator. This machine is composed of a large vacuum chamber ($\sim 10^{-6}$ mbar is required in order to reduce evaporation temperatures, and to ensure ballistic travel towards the sample and thus even deposition), a crucible which holds the material to be evaporated and a quartz crystal microbalance (QCM). Current is passed through the crucible which Joule heats the contacting metal, causing it to evaporate and diffuse across the vacuum chamber towards the sample whereby it cools and forms a thin film. The rate of diffusion is controlled by the temperature and thus applied current, whilst the film thickness is monitored via the change in resonant frequency of the

QCM as the metal adheres to it. When the desired thickness is achieved a shutter is closed across the sample to prevent further deposition and the current applied to the crucible is slowly reduced to zero in order to prevent crucible damage through thermal shock.

Gold is both chemically inert and has high electrical conductivity, making it an ideal contacting metal. However, it is well known that it does not adhere well to SiO_2 and so a wetting layer, usually just a few nanometres thick, must be used as well. It is for this reason that Cr/Au contacts are used within this study with thicknesses of 5/50 nm. After deposition, the entire substrate is then submerged in acetone and left for $\sim$ 24 hours in order to dissolve the remaining PMMA and allow for the thin metallic film, which covers the entire substrate and not just the exposed regions, to be lifted off. As the contact metals adhere strongly to the substrate, the lift-off process does not remove material from the exposed regions. The final result is shown in Figure 4.11 (c).

To selectively etch away a region the process is repeated (see Figure 4.11 (d, e)), but after development of the PMMA the sample is placed within a reactive ion etcher (RIE) which uses a mixed plasma (typically composed of O_2 and Ar ions) to bombard the exposed flake. This causes the sample surface to sublimate, with the amount removed depending on the incident energy of the plasma (controlled via an accelerating electric field), the exposure time and the constituent ion species. This is shown in Figure 4.11 (f), where an area of MoS_2 monolayer has been etched away in order to isolate the active region. Additonal uses of RIE include removal of heavily contaminated areas and shaping of the sample to aid in future electrical characterisation (such as in resistivity measurements).

4.3.5 Device designs

Field-effect transistors

The field-effect transistor is the fundamental building block of modern integrated circuits in which they are used for information processing and storage [287]. FETs typically have at least three contact terminals designated as source, drain and gate, and in principle rely on controlling the current flow through a channel material by applying a potential to the gate electrode through a separating dielectric barrier in order to modulate the channel conductivity. As discussed within Section 2.3.2 and 2.4.2, respectively, the creation of the next generation of FETs requires optimisation of both the channel and dielectric barrier materials in order to improve electrical performance. It is for this reason that this study investigates the use of TMDC channel materials in conjunction with the promising alternate dielectric barrier material known as talc in order to characterise and compare their electrical performance against recent 2D FETs within the literature. The general FET structure used is illustrated within Figure 4.12.

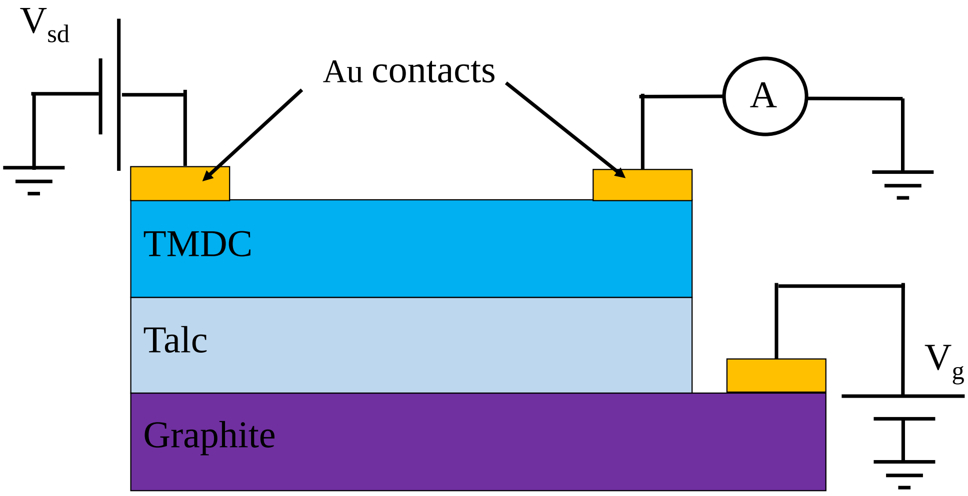

Figure 4.12: *Illustration of the back-gated FET structure used within]this study.*

It is a graphite/talc/TMDC vertical heterostructure assembled using the dry-transfer technique discussed within Section 4.3.3. The TMDC channel materials chosen were MoS_2 and $MoSe_2$ in order to measure both unipolar and ambipolar transport behaviour. In all cases a talc dielectric barrier layer is used in addition to a conductive graphite flake to allow for application of the potential between the channel and graphite layers. The TMDC channel and graphite layers were then contacted using the method described in Section 4.3.4. Electrical measurements were performed using two KE2400 sourcemeter in a two-terminal configuration in an inert He atmosphere, one to provide source-drain bias and another to bias the graphite gate electrode. In order to reduce noise within the measurement signal a 7265 DSP Lock-in amplifier (operating frequency of 1 kHz) was used.

Photoluminescence

In order to investigate the photoluminescence (PL) properties of talc, the PL emission spectra of TMDC/talc heterostructures were compared to that of exfoliated TMDC on a standard SiO_2/Si substrate. Micro-PL measurements were carried out at 300 K and 4 K using 532 nm laser excitation with varying laser power. The samples were placed within an Attocube positioner inside of a He flow cryostat, while the incident laser was focussed using a 50x Attocube objective lens within the cryostat resulting in a 4 µm diameter spot size at the sample surface. The incident laser would then result in the formation of excitons within the TMDC material, which then recombine and release PL emission. This PL emission is then collected and focussed onto a Spectra Pro 300i spectrometer coupled to a PyLon Princeton instruments Si CCD in order to build up the recorded spectrum, while reflected laser light is filtered out using a band pass filter.

4.4 Photodetector operating principles

The operating principle of the abraded photodector devices rely on either the photoconductive or photovoltaic effect, depending on the architecture of the device in question. The difference between the two is simple: photoconductive detectors use the increase in electrical conductivity resulting from increases in the number of free carriers generated when incident photons are absorbed; photovoltaic detectors use separation of photoexcited excitons in the vicinity of a p-n junction due to the inherent electric field at this location to modulate a current moving through the device.

Planar architecture: An example of a planar abraded photodetector is given in Figure 4.5 (a). Here, incident photons pass through the transparent PET substrate and thinned graphite channel and are absorbed in the TMDC layer, whereby an exciton is created and, in the presence of an applied potential, is in split into its constituent electron/hole and injected into the graphite/Ag epoxy, respectively. This is illustrated within Figure 4.13.

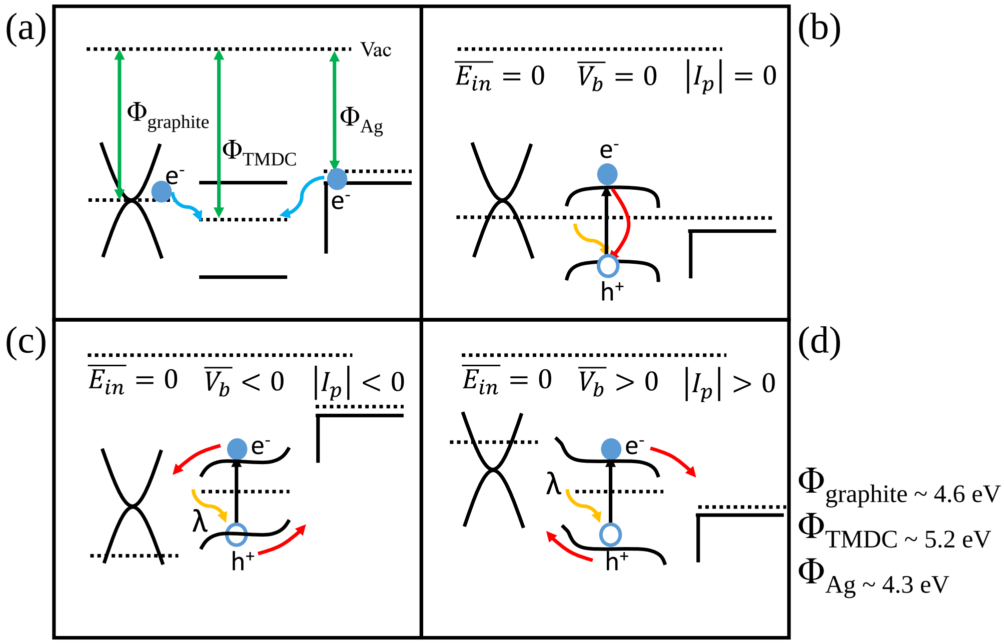

Figure 4.13: *Illustration photoconductivity-based detection of light using a planar abraded photodetector composed of graphite/TMDC and an Ag epoxy contact. (a) The band diagrams of the component layers before contact, (b) after contact with* $V_b = 0$*, (c) after contact with* $V_b < 0$ *and (d) after contact with* $V_b > 0$*.*

As can be seen, the inherent differences in work function for the component materials in this example lead to charge transfer into the TMDC at the interfaces with both the abraded graphite and the Ag epoxy. This leads to the formation of a p/n/n/p structure across the device, shown in (b), and thus there is no intrinsic electric field, $\bar{E}_{in}$, present across the TMDC. Therefore, absorption of an incident photon within the TMDC layer leads to the creation of an exciton as usual, but the lack of $\bar{E}_{in}$ prevents the electron-hole pair becoming separated in space and thus they quickly recombine and re-emit the light. If a negative bias is applied across the device, the TMDC band structure is re-aligned as shown in (c). In this situation the photoexcited electron-hole pair are separated by the external electric field which permeates the device and are injected into the graphite or Aq epoxy, respectively, leading to a negative photocurrent. Conversely, if a positive potential is applied then a positive photocurrent is obtained. As this modulation of photocurrent is due to a change of charge carrier density, it is a photocondutive effect which allows for the detection of light.

Vertical architecture: An example is a vertical photovoltaic device is shown in Figure 4.5 (c). In this device, photons pass through the CVD graphene and are absorbed in the abraded TMDC layer. As is shown in Figure 4.14, unlike in the previous example the inherent work function difference at each interface facilitates the creation of a intrinsic potential difference across the TMDC layer even when $V_b = 0$, as is shown in (b).

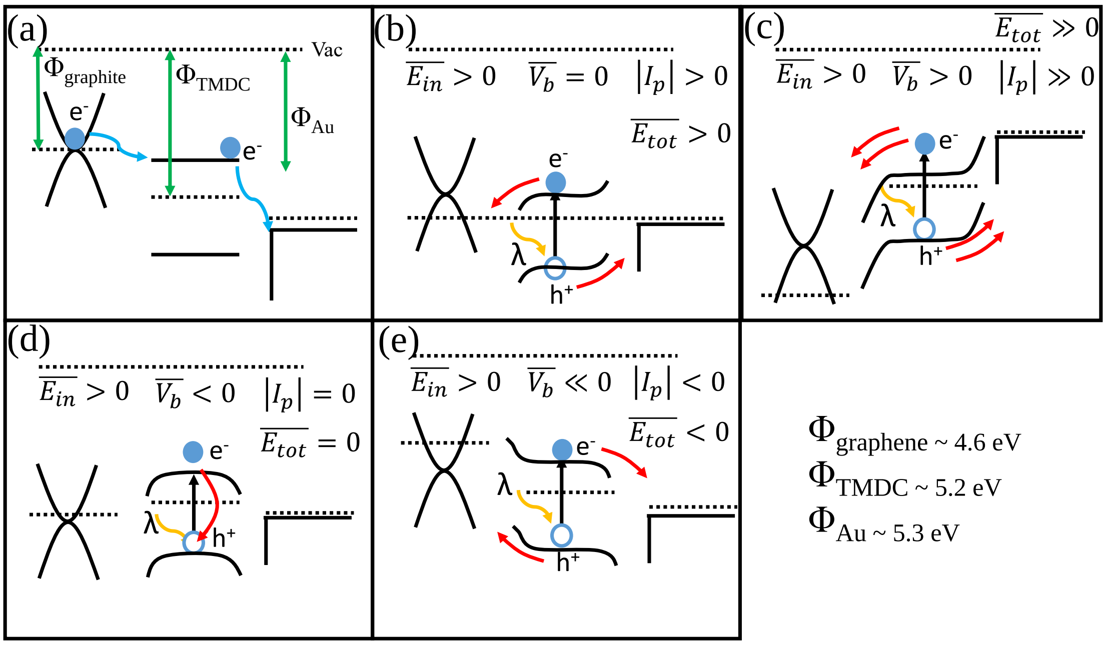

Figure 4.14: *Illustration photovoltaic-based detection of light using a vertical abraded photodetector composed of graphene/TMDCAu. (a) The band diagrams of the component layers before contact, (b) after contact with* $V_b = 0$*, (c) after contact with* $V_b > 0$*, (d) after contact with* $V_b < 0$ *and (e) after contact with* $V_b << 0$.

Therefore, a zero-bias photocurrent should be expected and is indicative that the device has an intrisic electric field present as a result of the p/n/p/n junctions, thus photoexcited excitons are separated upon creation and the component electrons/holes drift towards the graphene and Au, respectively.. If an external bias is applied parallel to this intrinsic field, then magnitude of the total electric field throughout the device, $\bar{E}_{tot}$, increases and thus the carrier velocities of these separated electrons and holes increases, meaning that a greater number of them reach the electrodes before recombination and a larger photocurrent is observed for a set amount of incident light power, see Figure 4.14 (c). Conversely, if the external bias is applied anti-parallel then $\bar{E_{tot}}$ decreases, eventually reaching zero when $\bar{E_{in}} = V_b$. This prevents separation of photoexcited carriers, resulting in the photocurrent and subsequent photoresponsivity dropping to zero, shown in (d). If the magnitude of the anti-parallel bias is increased beyond this point then the polarity of $\bar{E_{tot}}$ flips, meaning that exction separation once again occurs but with carriers moving in the opposite direction with electrons/holes injecting into the Au/graphene, respectively. Therefore the direction of the photocurrent is reversed, but the device once again becomes photoresponsive, see (e). Absorption of light in a photovoltaic serves to produce a photocurrent even in the absence of an applied bias, although application of such a bias can be used to modulate this current as per the definition given at the beginning of this section.

5. Results

5.1 Abraded heterostructures

5.1.1 Materials characterisation

Structural

In order to better understand the measured behaviour of the abraded films a full characterisation is needed. Information such as the distribution of film thicknesses and lateral sizes, their Raman behaviour and especially the configuration of crystallites at the interface of abraded heterostructures is crucial. Raman spectra were taken of six graphite, MoS_2, $MoSe_2$, WS_2 and hBN abraded films, see Figures 5.1-5.5, and used to calculate the average peak positions of the relevant modes for each material.

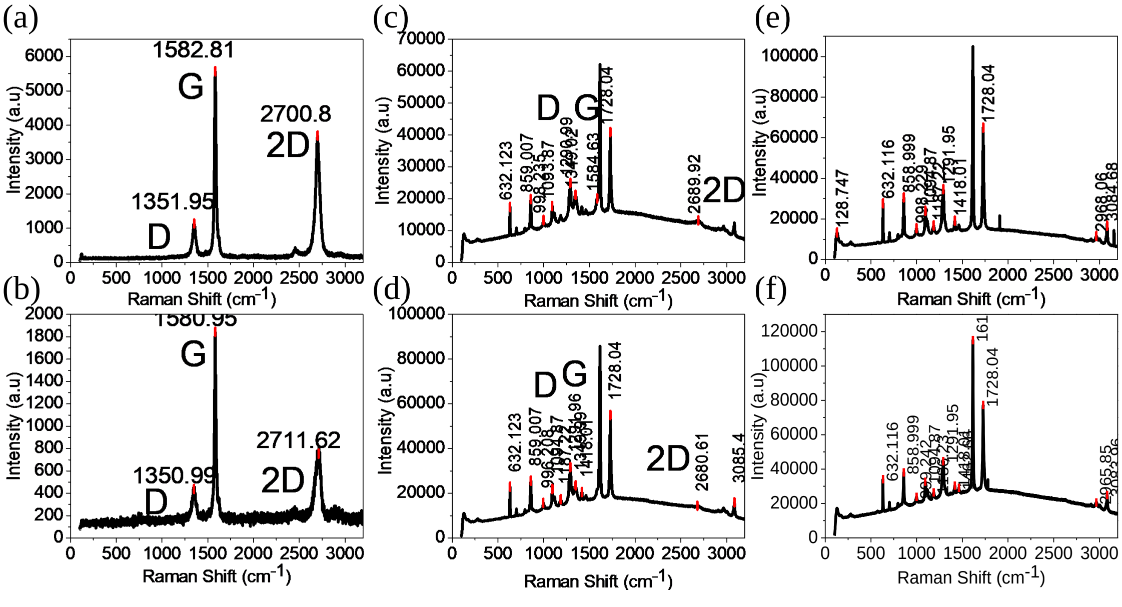

Figure 5.1: *Raman spectra for (a, b) graphite powder, (c, d) graphite abraded onto a PET substrate and (e, f) bare PET.*

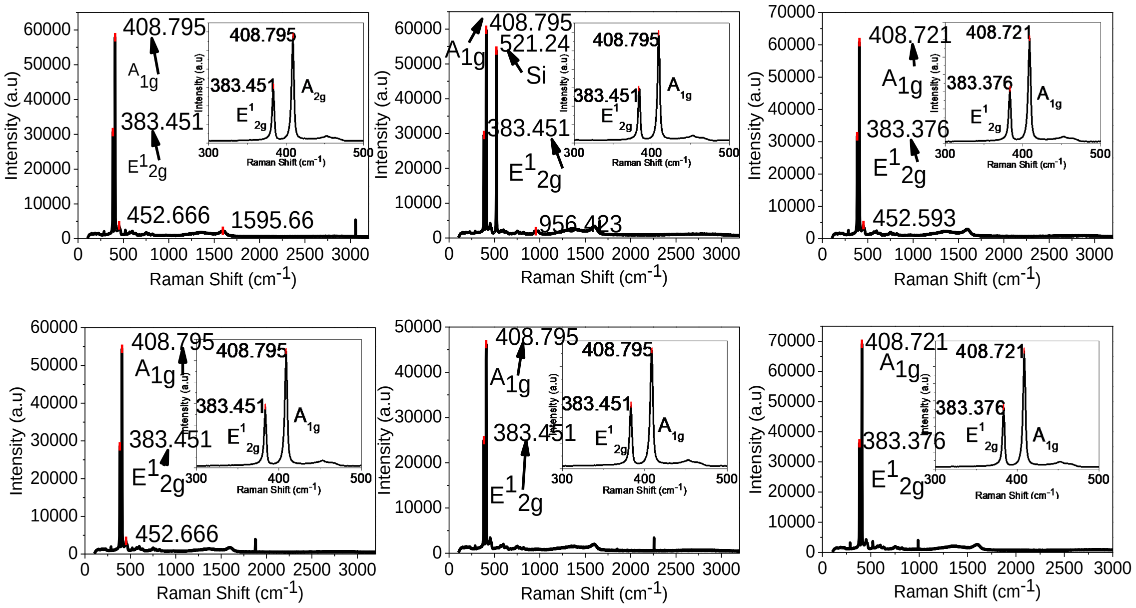

Figure 5.2: *Raman spectra for six* MoS_2 *samples abraded onto* SiO_2/Si *substrates.*

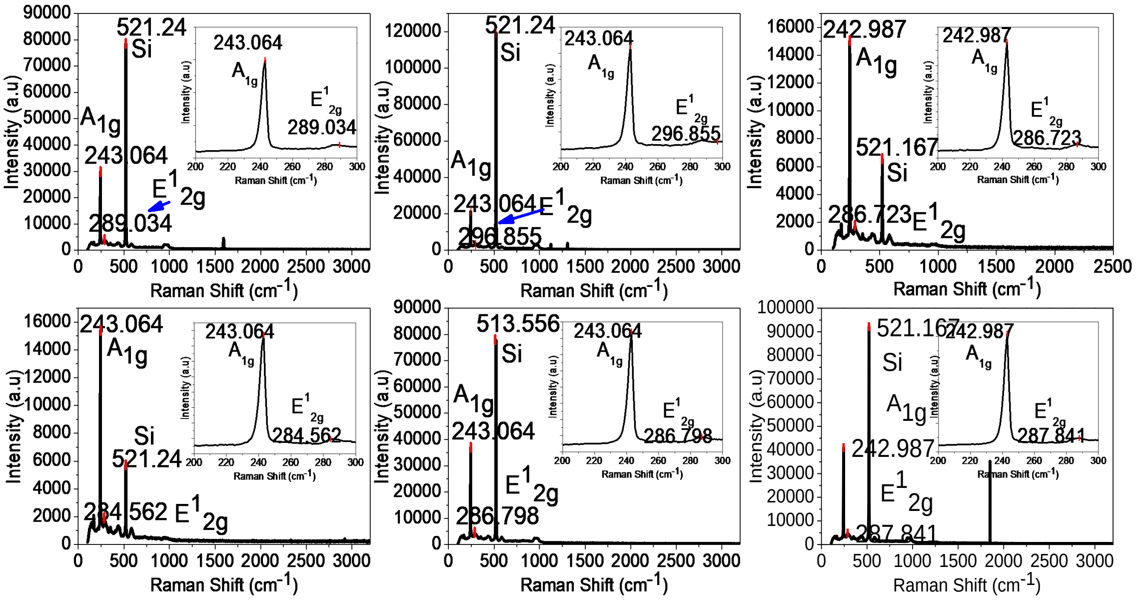

Figure 5.3: *Raman spectra for six* $MoSe_2$ *samples abraded onto* SiO_2/Si *substrates.*

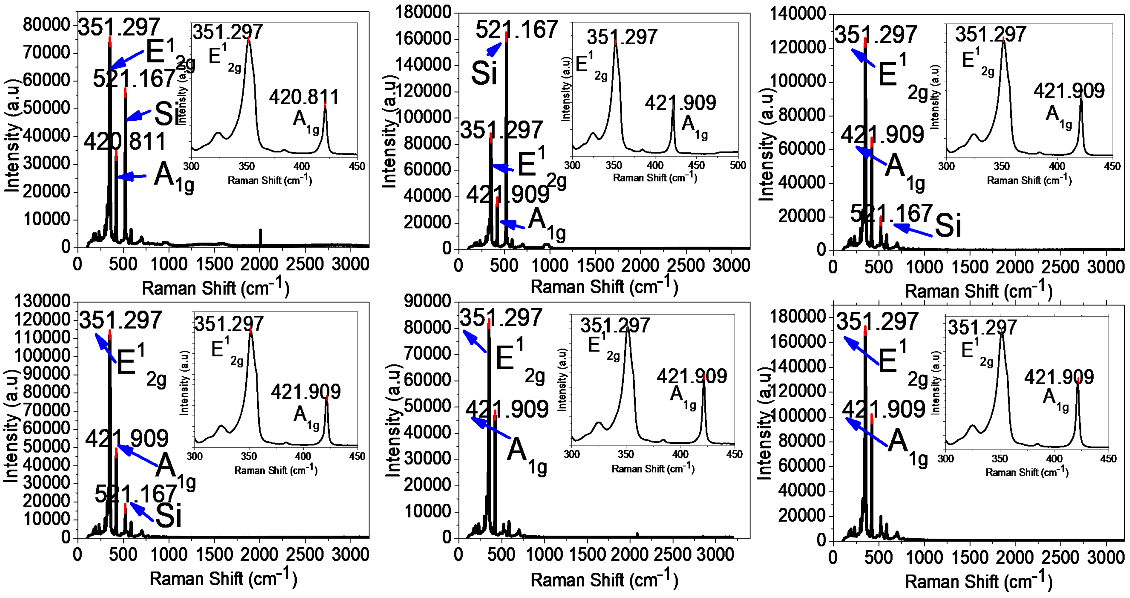

Figure 5.4: *Raman spectra for six* WS_2 *samples abraded onto* SiO_2/Si *substrates.*

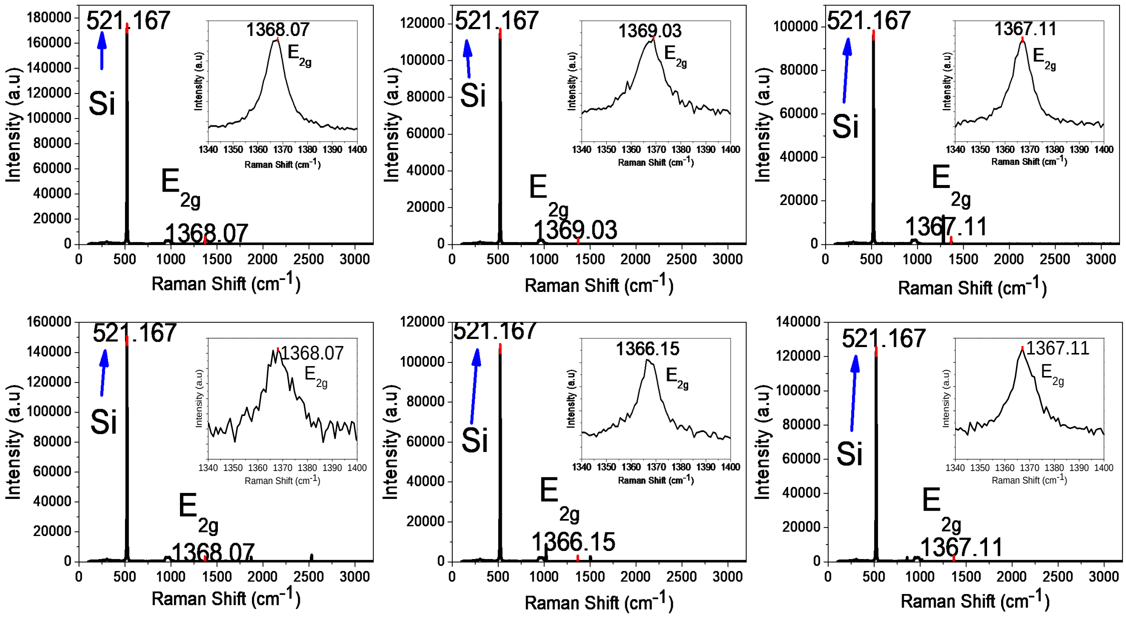

Figure 5.5: *Raman spectra for six hBN samples abraded onto* SiO_2/Si *substrates.*

Raman spectroscopy was carried out using 532 nm excitation at 1 mW laser power which was focussed into a 1 µm spot at the sample surface. Graphite was abraded onto PET whilst all other materials were abraded onto SiO_2. The normal Raman modes (see Section 3.1.1) are observed in graphite, with the $2D$, G and D peaks being found at ∼2711 cm^{-1}, ∼1581 cm^{-1} and ∼1350 cm^{-1}, respectively. It should be noted that the split peak seen in the G mode is an artefact of the removal of the PET background emission, which has very closely positioned Raman peaks to the graphite signal. The ratio of the intensity of the G peak (I_G) to the D peak (I_D), I_D/I_G, gives a measure of the disorder within the graphite sample. For graphite powder, $I_D/I_G = 0.2$ compared to $I_D/I_G = 1.43$ for the abraded film. The increase in disorder corresponds to a reduction in nanocrystallite size [288], which in the case of the abraded films may be due to basal cleavage of the material during the abrasion process. Specifically, I_D/I_G is related to the nanocrystallite size, L_a, with

$$\frac{I_D}{I_G} \propto \frac{1}{L_a} = \frac{C}{L_a}, \tag{5.1}$$

where C is a constant [288, 289]. The bulk graphite powder used within this study (graphite (282863), purchased from Sigma-Aldrich) has a maximum particulate size of $L_{a,powder} \leq 20$ µm, corresponding to a maximum abraded film nanocrystallite size of $L_{a,abraded} \approx 2.8$ µm. The Raman spectra for the abraded TMDC and hBN films were all found to be comparable to the literature values for the bulk crystals [6, 219, 290, 291]. The average Raman shift for the relevant modes within each material (excluding graphite) is available within Table 5.1.

Table 5.1: *Average Raman shift for the* E^1_{2g} *and* A_{1g} *modes for* MoS_2*,* $MoSe_2$*,* WS_2 *and hBN.*

Material	**$\langle E^1_{2g} \rangle$ (cm^{-1})**	**Error (cm^{-1})**	**$\langle A_{1g} \rangle$ (cm^{-1})**	**Error (cm^{-1})**
MoS_2	383.426	0.035	408.771	0.035
$MoSe_2$	288.638	3.912	243.038	0.036
WS_2	351.297	N/A	421.726	0.409
hBN	1367.590	0.919	N/A	N/A

The root mean square (RMS) roughness of each abraded film was estimated using AFM. For each material, six samples were produced by manually abrading onto a PET substrate. As graphite does not abrade onto SiO_2, PET substrates were used to allow for accurate comparison between the materials as it was assumed that the roughness of the final film would be influenced by the topography of the underlying substrate. AFM measurements were conducted using Nanosensors AFM tips with a radius of curvature < 10 nm, a spring constant of 42 Nm^{-1} and a nominal operating frequency of 330 kHz. Figures 5.6-5.10 show representative tapping mode AFM scans of each abraded material, clearly illustrating the change in surface roughness (height variations are shown on the z-axis) between each.

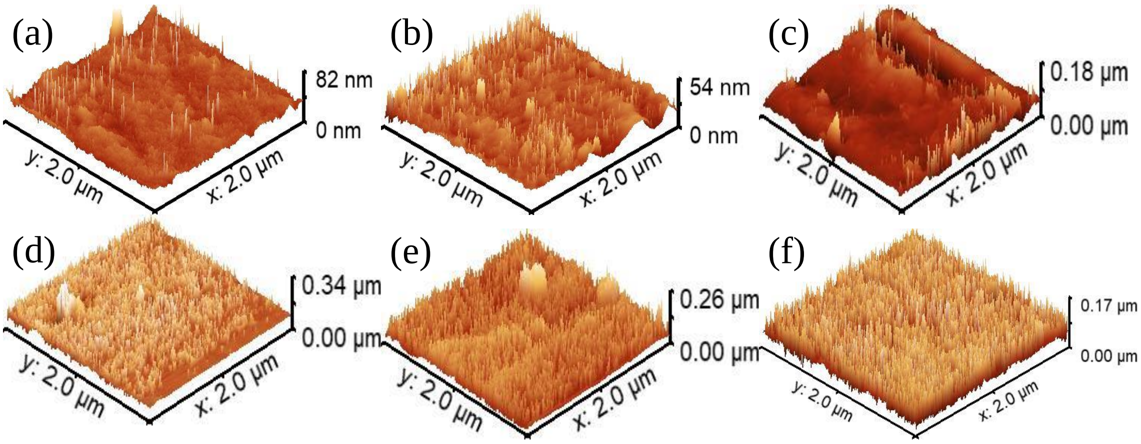

Figure 5.6: *(a-e) Tapping mode AFM scans for six graphite samples abraded onto PET substrates.*

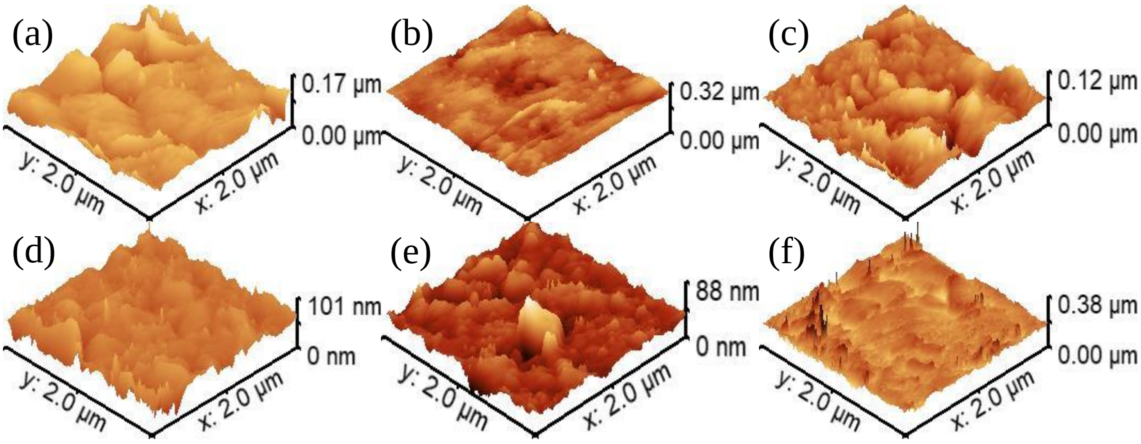

Figure 5.7: *(a-e) Tapping mode AFM scans for six* MoS_2 *samples abraded onto PET substrates.*

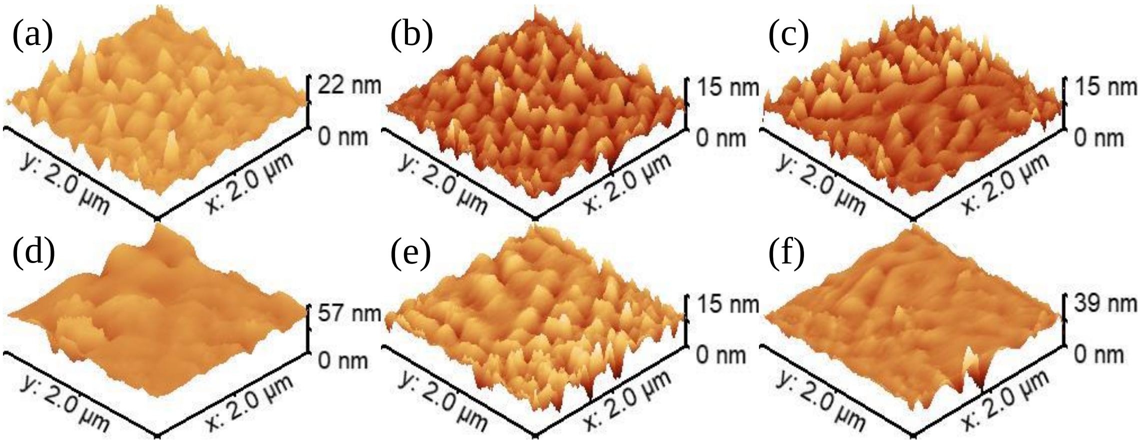

Figure 5.8: *(a-e) Tapping mode AFM scans for six* $MoSe_2$ *samples abraded onto PET substrates.*

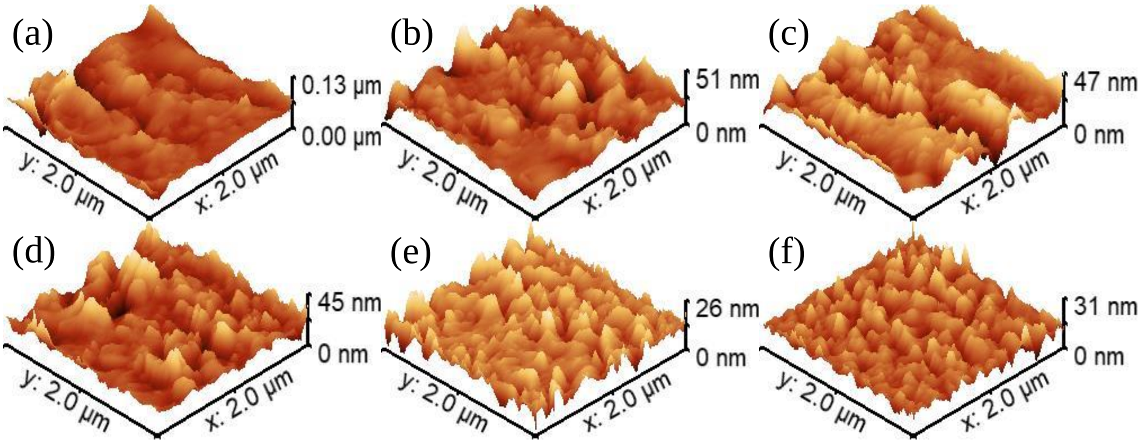

Figure 5.9: *(a-e) Tapping mode AFM scans for six* WS_2 *samples abraded onto PET substrates.*

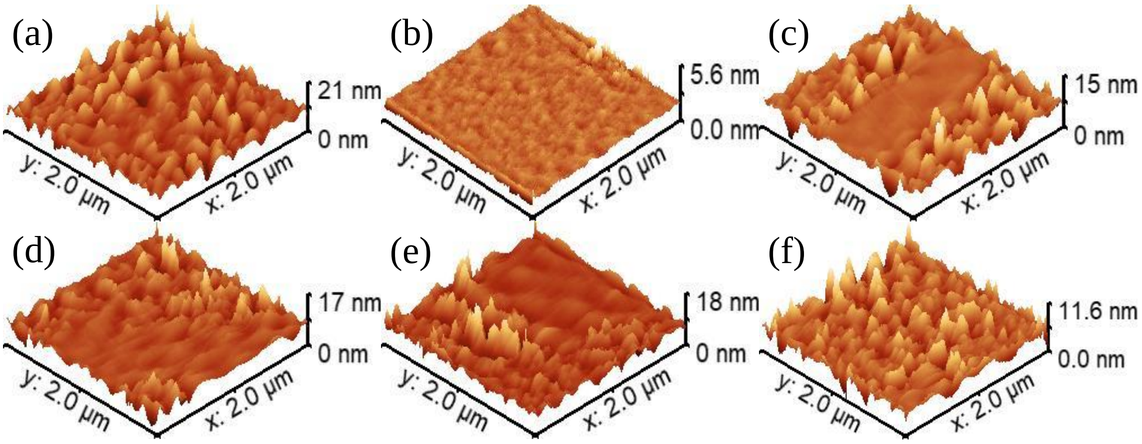

Figure 5.10: *(a-e) Tapping mode AFM scans for six hBN samples abraded onto PET substrates.*

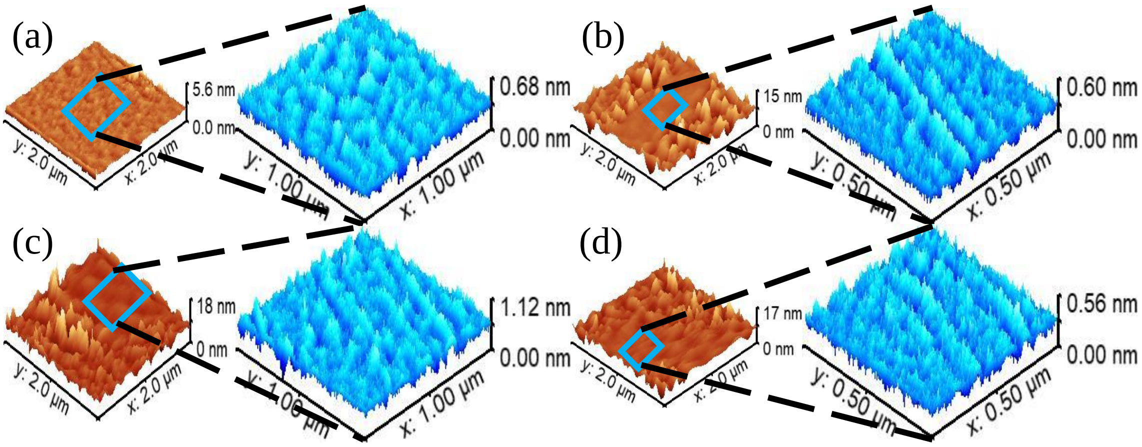

Figure 5.11: *(a-d) Tapping mode AFM scans of smooth regions of abraded hBN taken from (b-d) of Figure 5.10, respectively.*

Calculation of the RMS roughness was completed using Gwyddion analysis software [292] and allows for a quantitative comparison between materials. More precisely, the RMS roughness, ξ, was calculated using

$$\xi = \sqrt{\frac{1}{N}\sum_{n=1}^{N}(z_n - \bar{z})^2}, \tag{5.2}$$

where N is the total number of data points within a given line profile through the AFM data, z_n is the height of the nth data point and $\bar{z}$ is the average height of all the data points taken along the line. The results of these calculations can be found within Table 5.2, along with data present within the literature for inkjet printed materials. A general lack of comprehensive study on the surface topology of the latter prevents an accurate comparison.

Table 5.2: *Estimates of surface roughness and thickness of various manually abraded and inkjet printed films.*

Material	**ξ (nm)**	**Error (nm)**	**Thickness (nm)**	**Error (nm)**
Graphite	22.7	10	61	38
MoS_2	26.4	5	68	36
$MoSe_2$	4.2	2	52	40
WS_2	6.0	2	284	176
hBN	9.4 (rough)	3	152	118
hBN	0.019 (smooth)	0.004	–	–
Printed rGO [293]	$\sim$ 40	–	$\sim$ 450	–
Printed MoS_2 [294, 295]	$\sim$ 80	–	177	15
Printed $MoSe_2$ [296]	146	–	$\sim$ 810	–

There is very little information regarding the surface characteristics of inkjet printed WS_2 and WSe_2, but comparison with printed reduced graphene oxide (rGO), MoS_2 and $MoSe_2$ makes it apparent that abrasive deposition allows for the creation of functional nanocrystalline films whilst maintaining low thickness and surface roughness.

The variation in roughness between different abraded materials is likely due to how well the final film “conforms” to the underlying substrate. As these thin films are composed of discrete nanocrystallites rather than a continuous sheet (such as in graphene), they cannot be thought of as a membrane suspended across the substrate topography, but instead as particulates infilling the surface indentations until a continuous film is formed. As the material is deposited evenly across a large area of the substrate, this should in turn lead to a variation in surface height loosely correlated to the topography of the substrate, as is illustrated within Figure 5.12.

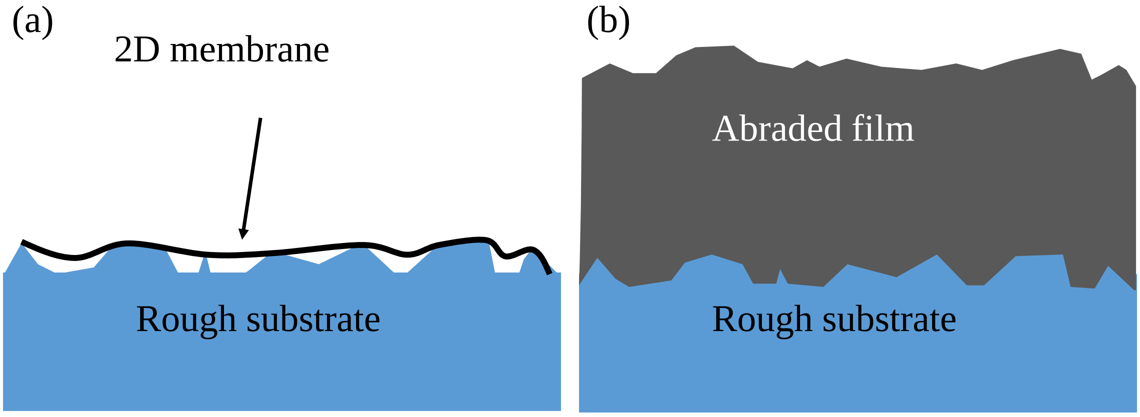

Figure 5.12: *Illustration of (a) conformation of a 2D membrane, such as graphene, and (b) an abraded film to a rough underlying substrate.*

The degree of conformation may therefore be a result of how well each material cleaves into smaller crystallites, with easy-to-cleave materials able to infill the substrate topography more closely which in turn corresponds to a reduced roughness manifesting at the surface, although a comprehensive investigation into exactly which variables control ξ is beyond the scope of this work. Furthermore, it appears that hBN has the tendency to abrade into regions of extremely low roughness (see Figure 5.10 (b-d) and Figure 5.11) surrounded by areas of relatively high roughness. Although hBN as a whole is far from the smoothest abraded film, as can be seen within Table 5.2, an investigation into the cause of these smooth regions would be of interest as, if it could be controlled, it would allow for the abrasion of extremely flat, large scale dielectrics which would be highly suitable for the formation of sharp heterointerfaces. However, atomically-flat, exfoliated hBN crystals have a surface roughness of $\xi \sim 0.4$ nm [80], an order of magnitude greater than for the smooth regions of these abraded films. Moreover, the roughness of these smooth regions is less than the diameter of a typical atom (~ 1 Å), and so it is likely that these regions are in fact simply errors within the AFM measurements of these samples.

In addition to the surface roughness, the typical thickness of the manually abraded films were also measured using an Alpha-Step D-100 Stylus Profiler, see Table 5.2 and Figure 5.13. Here, two samples were produced for each material which were then

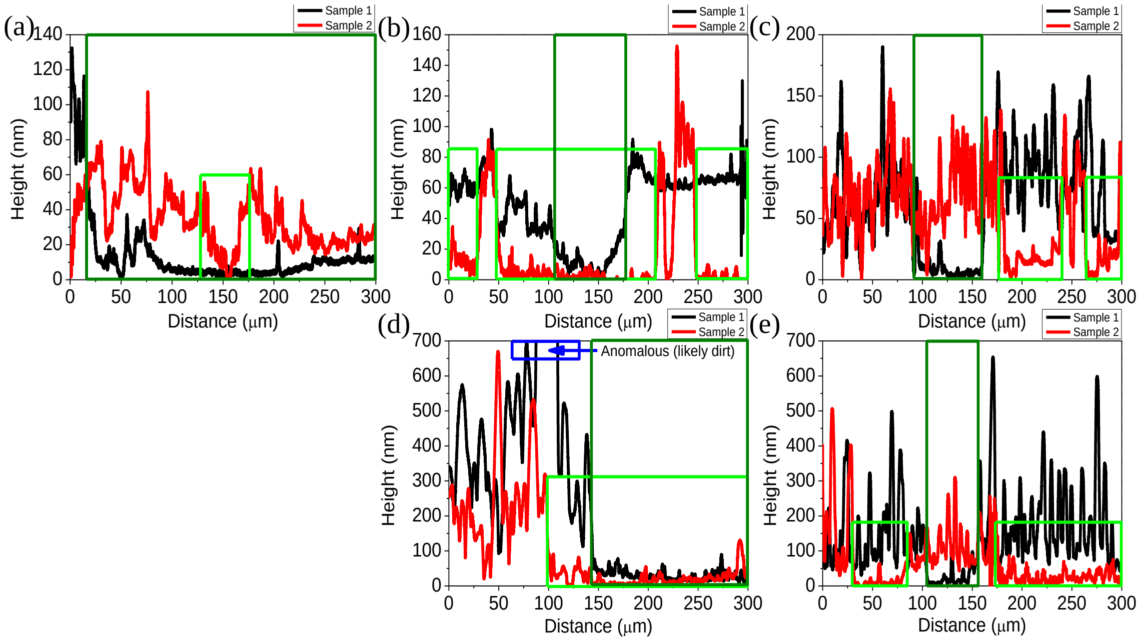

Figure 5.13: *Surface profile measurements of abraded (a) graphite, (b) MoS_2, (c) $MoSe_2$, (d) WS_2 and (e) hBN films on PET substrates. Scalpel marks associated with samples 1 and 2 are highlighted in the light and dark green boxes, respectively.*

scored using a scalpel. This creates a clean step between the substrate and the film surface which can easily be measured using the profiler. It should be noted that a surface profiler was required as the thicknesses of the abraded films exceeded the vertical movement range of the available AFM system. This, along with the fragile nature of the films with respect to the stylus tip and variation in film thickness across the substrate lead to significant uncertainty in these measurements. Regardless, these still provide general insight in that it is now known that the abraded films, regardless of material, have thicknesses in the 10^1-10^2 nm-regime. The large uncertainties in thickness given within Table 5.2 are a result of the significant variation in height when measured over large distances (hundreds of microns), see Figure 5.13.

To better quantify the distribution of individual nanocrystallite lengths and thicknesses, scanning transmission electron microscopy (STEM) was used to investigate abraded WS_2, graphite and hBN films, see Figure 5.14.

As can be seen, the dimensions of the mechanically abraded crystallites are similar regardless of which material is used (in agreement with the surface profiler measurements), with thicknesses of $\sim 10 - 40$ nm and lateral sizes of $\sim 10 - 600$ nm (well within the upper bound of $L_{a,abraded} \approx 2.8$ μm calculated using Raman spectroscopy

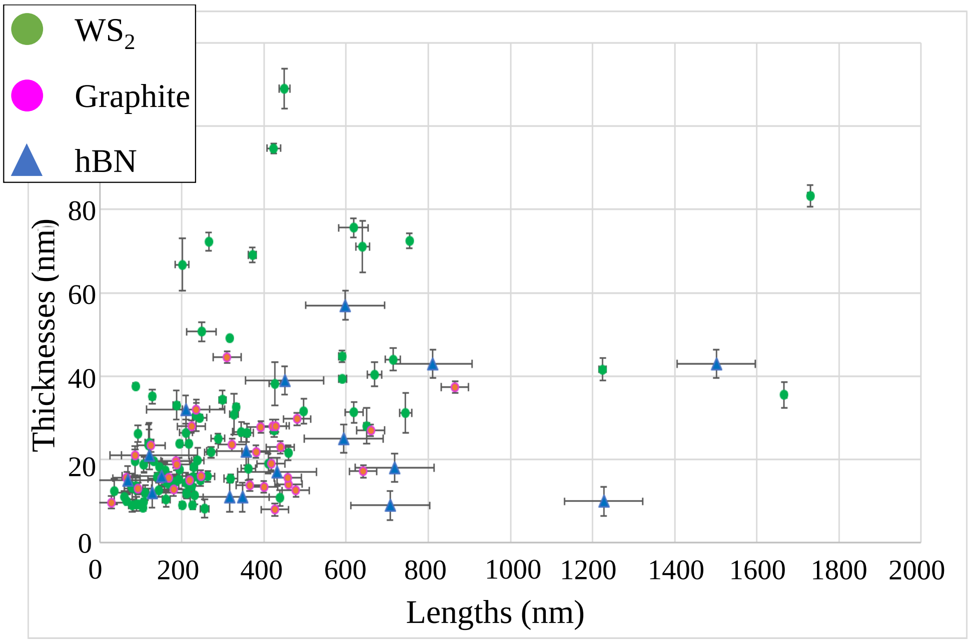

Figure 5.14: *Thickness and length distribution of* WS_2*, graphite and hBN nanocrystallites deposited through mechanical abrasion using STEM. This analysis is performed with a spatial resolution of* $\sim$*10 nm in order to sample a sufficiently large number of nanocrystallites, although higher magnification imaging reveals that many thinner flakes are also present in the deposited material. The error bars correspond to statistical variation observed within repeated manual measurements of each flake. Data collected by a collaborator, S. J. Haigh.*

of abraded graphite). Almost all of the measured crystallites have lateral sizes < 1 µm and so occupy the same inverse Hall-Petcher regime of material hardness. Therefore, penetration of the barrier layers of an abraded heterostructure produced via fabrication route 1 when applying a top graphitic electrode is a result of the intrinsic hardness of the materials themselves rather than due to a significant difference in crystallite sizes (e.g. nanocrystallites in different layers occupying different Hall-Petcher regimes), and thus this effect should be universal to all heterostructures produced this way and will not depend on the details of the initial bulk material powder. This bodes well for application of the abrasive method for future large scale device production as cheaper and more readily available sources of bulk powder are found, although a complete repeat of this study using different source materials (i.e. powders with different purities and particulate sizes) is needed in order to confirm this. The large variation in lateral dimension can clearly be seen within SEM images of the manually abraded films, such as those shown within Figure 5.15.

The SEM data was collected on a dual-beam xT Nova Nanolab 600 focussed ion beam (FIB) SEM system (10 kV accelerating voltage), whilst the STEM data was collected on a FEI Titan g2 80-200S/TEM system (200 kV accelerating voltage). Another important feature to be investigated is the type of interface present within abraded heterostructures - such as whether a sharp divide between adjacent layers is present or if there is a zone of intermixing between materials. Unlike in exfoliated heterostructures the answer to this is not intuitive, and so STEM energy dispersive X-ray spectroscopy (EDS) elemental maps were produced on a cross-sectional lamellar of a collection of abraded heterostructures, see Figures 5.16 - 5.18.

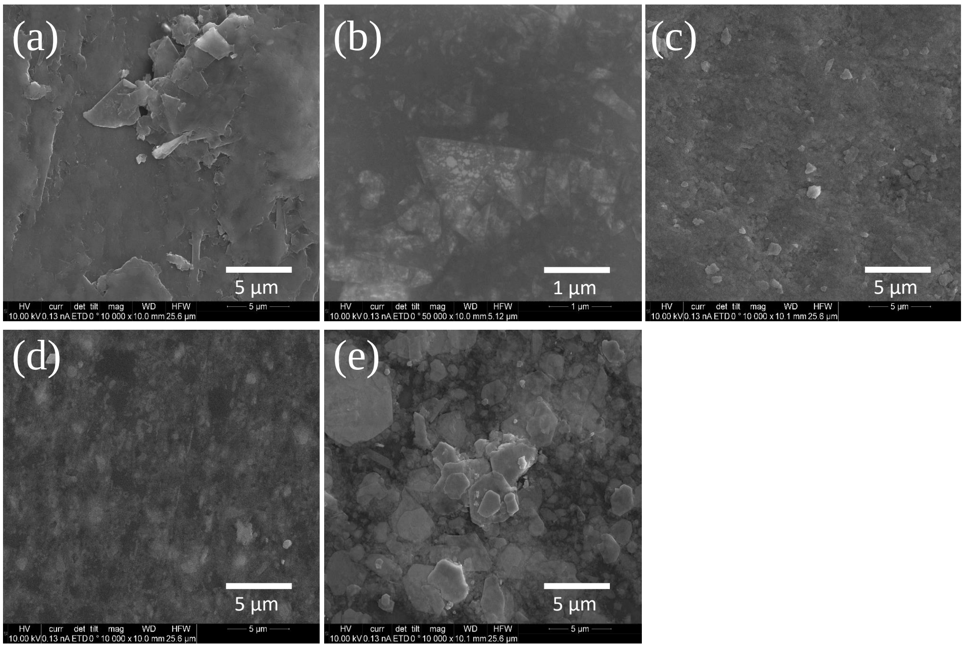

Figure 5.15: *SEM images of abraded (a) graphite (on a PET substrate) and (b) hBN, (c) MoS_2, $MoSe_2$ and WS_2 abraded films on SiO_2/Si substrates.*

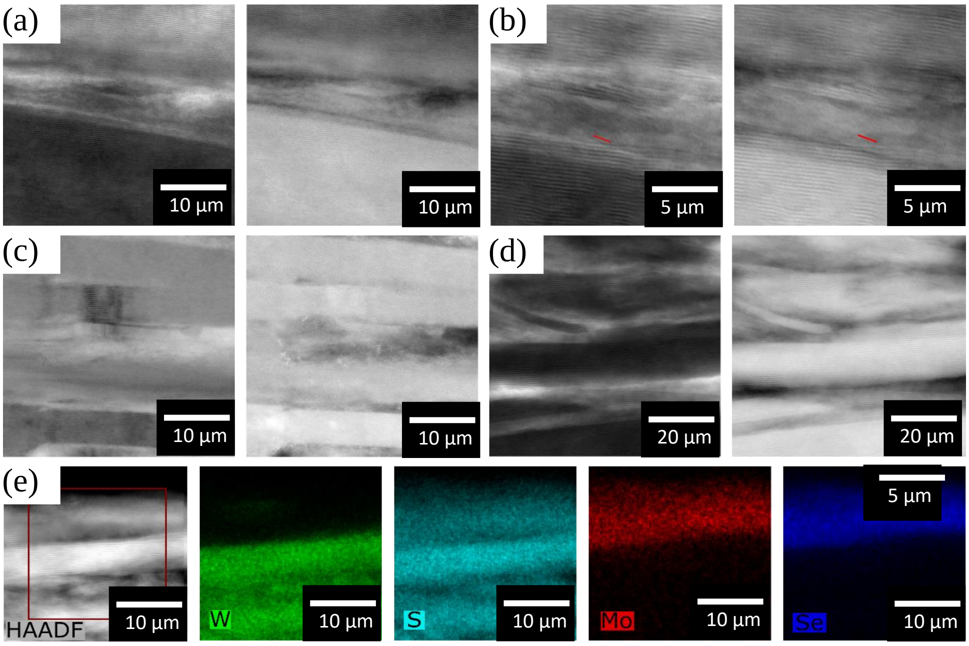

Figure 5.16: *STEM analysis of a hBN/graphite/WS_2/$MoSe_2$ manually abraded heterostructure on a SiO_2/Si substrate. (a, b, c, d) Cross-sectional bright field (left) and annular dark field (right) images displaying the (a, b) WS_2/$MoSe_2$ interface, (c) the graphite layer and (d) the hBN layer, respectively. (e) Annular dark field image and STEM-EDS elemental map of the WS_2/$MoSe_2$ interface region. Data collected by a collaborator, S. J. Haigh. Adapted from [297]*

Figures 5.16 and 5.17 show the STEM analysis for a pair of hBN/graphite/WS_2/$MoSe_2$ manually abraded heterostructures produced through fabrication route 1 on a SiO_2/Si

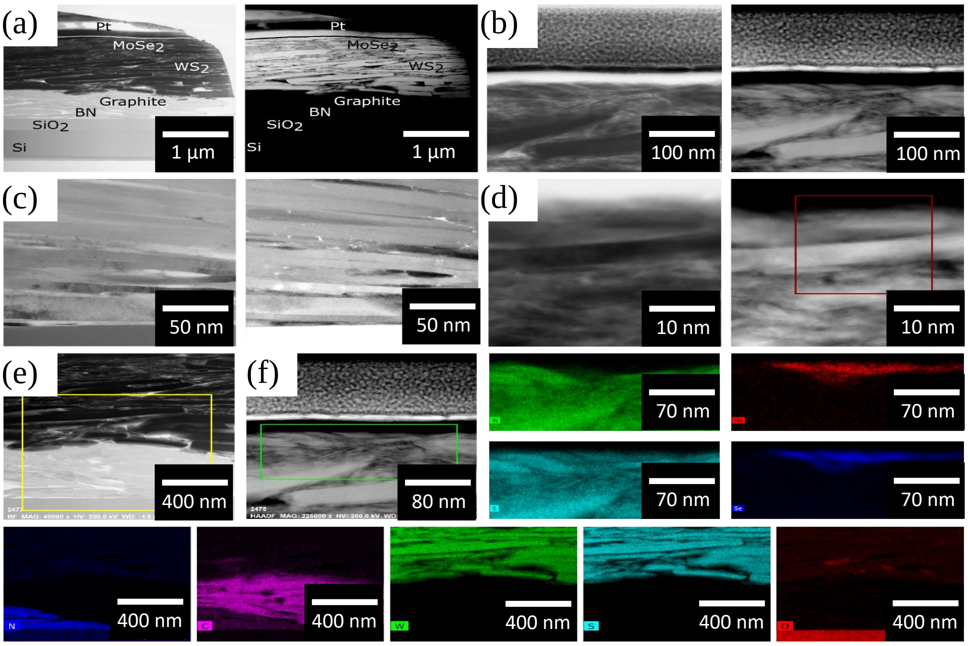

Figure 5.17: *STEM analysis of a second hBN/graphite/*WS_2*/*$MoSe_2$ *manually abraded heterostructure on a* SiO_2*/Si substrate. (a-d) Bright field (left) and annular dark field (right) STEM images. The different layers indicated within (a) were identified via elemental mapping. (e) STEM cross-sectional image of the hBN/graphite/*WS_2 *interface region, with elemental mapping shown in the bottom row of images. (f) STEM cross-sectional image of the* WS_2*/*$MoSe_2$ *interface region, with elemental mapping shown in the images adjacent to the right. Data collected by a collaborator, S. J. Haigh. Adapted from [297]*

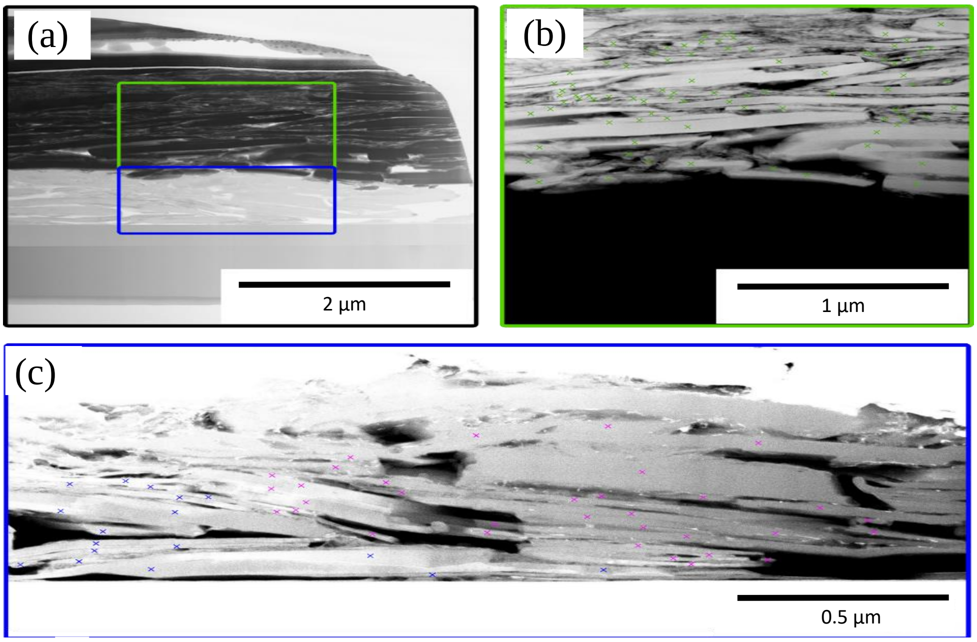

Figure 5.18: *STEM analysis of a hBN/graphite/*WS_2 *manually abraded heterostructure on a* SiO_2*/Si substrate. (a) Bright field STEM image of the full heterostructure, with (b, c) annular dark field STEM images for the rectangular regions indicated within (a). Data collected here was used to produce Figure 5.3. Data collected by a collaborator, S. J. Haigh. Adapted from [297]*

substrate. Figure 5.18 shows STEM analysis of a hBN/graphite/WS_2 manually abraded heterostructure. STEM-EDS elemental mapping of a cross-section through these structures reveal that, despite the number of layers, there is no material intermixing across the interfaces, allowing for the formation of sharp heterointerfaces. This enhances the charge transfer across the interface throughout the entire device by enhancing the potential difference between two contacted layers, as well as preventing short circuit during electrical measurements (e.g. in a graphite/TMDC/graphite heterostructure, material intermixing would short the two graphite layers). The latter of these effects serves to improve the performance of both photovoltaic and TENG devices investigated within this study.

Electrical

Important for use in potential applications are the electronic and dielectric properties of the abraded films, such as graphite and hBN, respectively.

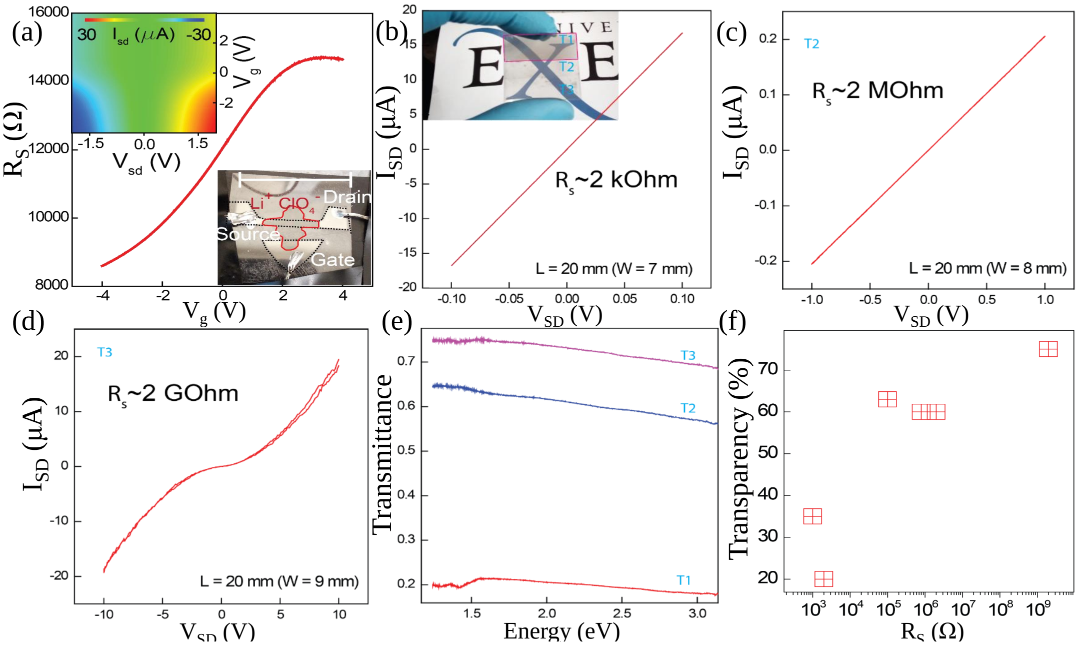

Figure 5.19: *(a) Gate dependance of a tape-thinned graphite channel using a* $LiClO_3$ *electrolyte (scale bar = 2.5 cm). Top left inset: Contour map of the* I_{SD}-V_{SD} *for different applied gate voltages. Bottom right inset: Optical image of the device. (b-d)* I_{SD}-V_{SD} *curves for graphitic films of different thicknesses achieved by back-peeling with specialist tape (b) one, (c) two or (d) three times. The number of peels is indicated by TX within the inset of (b). (e) Transparency of the films measured in (b-d). (f) Transparency vs sheet resistance for different abraded graphite samples.*

To begin with, the electrical characteristics of abraded graphite films were determined.

Figure 5.19 (a) shows the gate dependance of a tape-thinned graphite channel using an electrolyte ($LiClO_3$) gate drop-cast over the channel region. The source, drain and gate contacts were themselves made from thicker abraded graphite. An electrolyte dielectric was used in order to allow for super capacitive behaviour from the device and thus induce extreme charge carrier densities. At this point in the investigation it the thickness of the abraded films was not known. If the abraded films had thicknesses of only several atomic layers, then ambipolar behaviour would be observed in the I-V characteristics of the device due to direct tuning of the Fermi level between conduction and valence bands - which is not possible in bulk material due to electrostatic screening from surface charges. Therefore, observation of such behaviour would be indicative of the number of layers present in the films.

The electrolyte dielectric functions as follows: as the back gate voltage changes, the Fermi level is shifted into either the conduction or valence band of the material, resulting in *n*- and *p*-type doping, respectively. This charge draws oppositely charged ions from within the electrolyte towards the material surface but remain separated from the surface by the presence of a single layer of neutral electrolyte molecules, preventing charge transfer between the two. This region is highly polarised and screens the electric field between the two electrodes, and so the electrolyte acts as a normal dielectric material but of atomic thickness.

When the Fermi level passes through the point where the bands touch the material becomes electrically neutral (see Figure 2.6 (d)). Therefore, depending on the sign of back gate voltage required to reach the electroneutrality point, the type of doping already present can be inferred. As can be seen within the top-left inset of (a), the sheet resistance (calculated from I_{SD}) depends strongly on the applied gate voltage, with the electroneutrality region existing at large positive V_g. This indicates that graphite films abraded in an ambient atmosphere naturally become *p*-doped, likely the result of adsorption of water from the atmosphere [2, 298]. The presence of ambipolar behaviour in these measurements is indicative of film thicknesses of only several atomic layers. In order to investigate the exact film thickness, optical transmittance spectra were also taken.

The use of specialised tape to thin an abraded channel allows for control over both the sheet resistance and transmittance, T, as is shown in Figure 5.19 (b-f). A fibre coupled halogen white light source was used to pass light through the samples (which were abraded onto transparent PET) and onto a iDus 420 charged coupled device (CCD). The intensity of the transmitted light, I_{sample}, can then be compared between samples, along with the intensity through bare PET, I_{PET}, and in darkness, I_{dark}, to calculate the transmittance via

$$T = \frac{I_{sample} - I_{dark}}{I_{PET} - I_{dark}}. \tag{5.3}$$

For a particularly thick film ($T \sim 0\%$), the resistance can be as low as ~10 Ω. The resistance increases by approximately an order of magnitude per peel of the specialist tape, with the transparency increasing to as high as ~ 80 % after three peels, see Figure 5.19 (f). For comparison, we find the electrical and optical properties of our abraded graphite films are comparable to transparent electrodes produced through shear force exfoliation [299], which is an alternative graphene production method utilising graphite powder suspended within a liquid medium, which can then be used to exfoliate the graphite into graphene via turbulent shear forces (achieved by forcing flow between two closely separated surfaces) [300].

Next, an investigation into the transport quality of the abraded TMDC films was completed. Table 5.3 compares the resistivity of an abraded TMDC film (WS_2 in this case) to exfoliated, CVD and LPE TMDC systems.

Table 5.3: *Comparison of the bulk in-plane resistivity of our films compared to films produced through other methods.*

Device type and reference	**In-plane Resistivity at V_g = 1 V (Ωm)**
Abraded WS_2	17-50
Printed MoS_2[301]	4×10^6
Printed WS_2[302]	1×10^5
Printed graphene [303]	4×10^{-5}
Exfoliated graphene [304]	$\sim 10^{-2} - 10^{-5}$
Exfoliated WS_2 [117]	0.1-1
Exfoliated MoS_2 [305]	$\sim 0.01 - 0.1$
CVD grown WS_2 [306]	5-15

It should be noted that this comparison could be erroneous due to different conditions (e.g. charge carrier density, temperature, environment and so on). Despite this, effort has been made to compare only measurements taken under similar conditions and device type. Overall, the resistivity of the abraded TMDC film is found to be comparable to mechanically exfoliated [117] or CVD grown crystals [306], whilst at the same time showing significantly lower resistivity by a factor of $\sim 10^4$-10^5 compared to LPE films [301, 302]. This implies the formation of a continous layer of material within the abraded films, without significant boundaries or scattering centres within each nanocrystallite, and thus bodes well for the electronic quality of abraded TMDC devices.

Important for any integrated electronic application is the development of dielectric barriers. To investigate the suitability of the abrasive process for the production of large scale dielectrics, a hBN film was abraded over evaporated Au electrodes. In order to increase the film thickness the abrasion process was carried out for significantly longer than is required to create a continous layer, overall resulting in a film thickness, d, of 5 ± 2 µm. This was confirmed using a surface profiler as is shown within Figure 5.20 (a). Following the deposition of the hBN dielectric, a strip of CVD grown graphene was dry-transferred onto the hBN film subsequently followed by the deposition of two Au electrodes to act as the source and drain for the graphene channel, see inset of Figure 5.20 (b). CVD grown graphene was used as the capacitor top electrode (the underlying Au acts as the bottom electrode) to allow for electrostatic gating of the hBN, as these measurements were taken before the development of fabrication route 2 (Section 4.1.1) and so an all-abraded capacitor could not yet be investigated. The monolayer CVD grown graphene was purchased from *2D Semiconductors* and is transferred via the same technique introduced in Section 4.2.1. This also demonstrates that abraded films are compatible with CVD grown materials and their subsequent transfer. The device is now essentially a parallel plate capacitor, with a total capacitor area, A, of $\sim 2 \times 10^6$ m^2.

Figure 5.20 (b) shows the impedance spectrum recorded for this device using a Rhode and Schwarz, Hameg HM8118 LCR Bridge. The impedance spectrum can be well

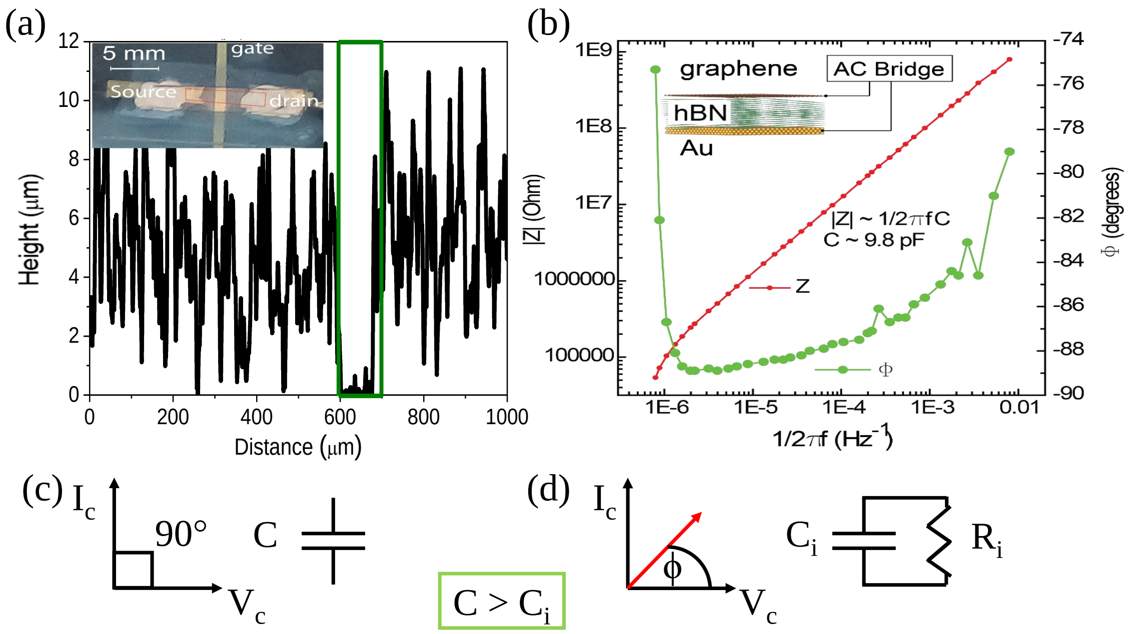

Figure 5.20: *(a) Profilometry of an extremely thick abraded hBN film. The scalpel mark used to create a groove within the film for measurement is highlighted in the dark green box. Top left inset: optical image of the hBN capacitor with the CVD graphene strip outlined in red. (b) Impedance spectroscopy for a hBN dielectric capacitor produced using the 5 µm thick hBN film. Top left inset: schematic of the capacitor device. (c, d) Phase diagram and equivalent circuits for an ideal (c) and lossy (d) capacitor.*

described by the capacitive contribution,

$$|Z_c| = \frac{1}{i\omega C} = \frac{1}{2\pi f C}, \tag{5.4}$$

at low frequencies. The right axis of Figure 5.20 (b) shows the phase angle between the charging current and the voltage across the capacitor. In an ideal capacitor this angle is always 90°, as is shown in (c), and so a measurement such as this not only allows one to monitor the capacitive behaviour of the device but also to identify the optimum frequency at which to operate it. The gradient to the linear fit for this portion of the curve gives $1/C$, yielding a capacitance of $C = 9.8$ pF. As the system is essentially a parallel plate capacitor, the capacitance is related to the dielectric constant of the hBN barrier layer, ϵ_r, through

$$C = \frac{\epsilon_r \epsilon_0 A}{d}, \tag{5.5}$$

where ϵ_0 is the permittivity of free space. This allows the dielectric constant of the abraded hBN film to be estimated as $\epsilon_r \approx 3 \pm 1$, with the error arising from uncertainty in film thickness. Previous reports have found widely varying values for the dielectric constant of nanocrystal hBN dielectrics ranging from $\sim$ 1.5 - 7.5 [307, 308], whilst single crystal hBN is known to possess a value of $\sim$ 4 [309]. The lower value for this abraded layer could be due to air voids within the film lowering the effective capacitance of the whole barrier.

Optical

The optical transmission spectra for each type of abraded material used within this study is shown in Figure 5.21. The spectra were recorded using an Andor Shamrock 500i spectrograph with 300 lines/mm grating resolution and an iDus 420 CCD. A fibre coupled halogen white light source was used to excite the photoactive samples which generates 1.4 W at the fibre tip. The white light is then collimated onto the sample surface to give a uniform excitation of 70-100 mWcm^{-2}.

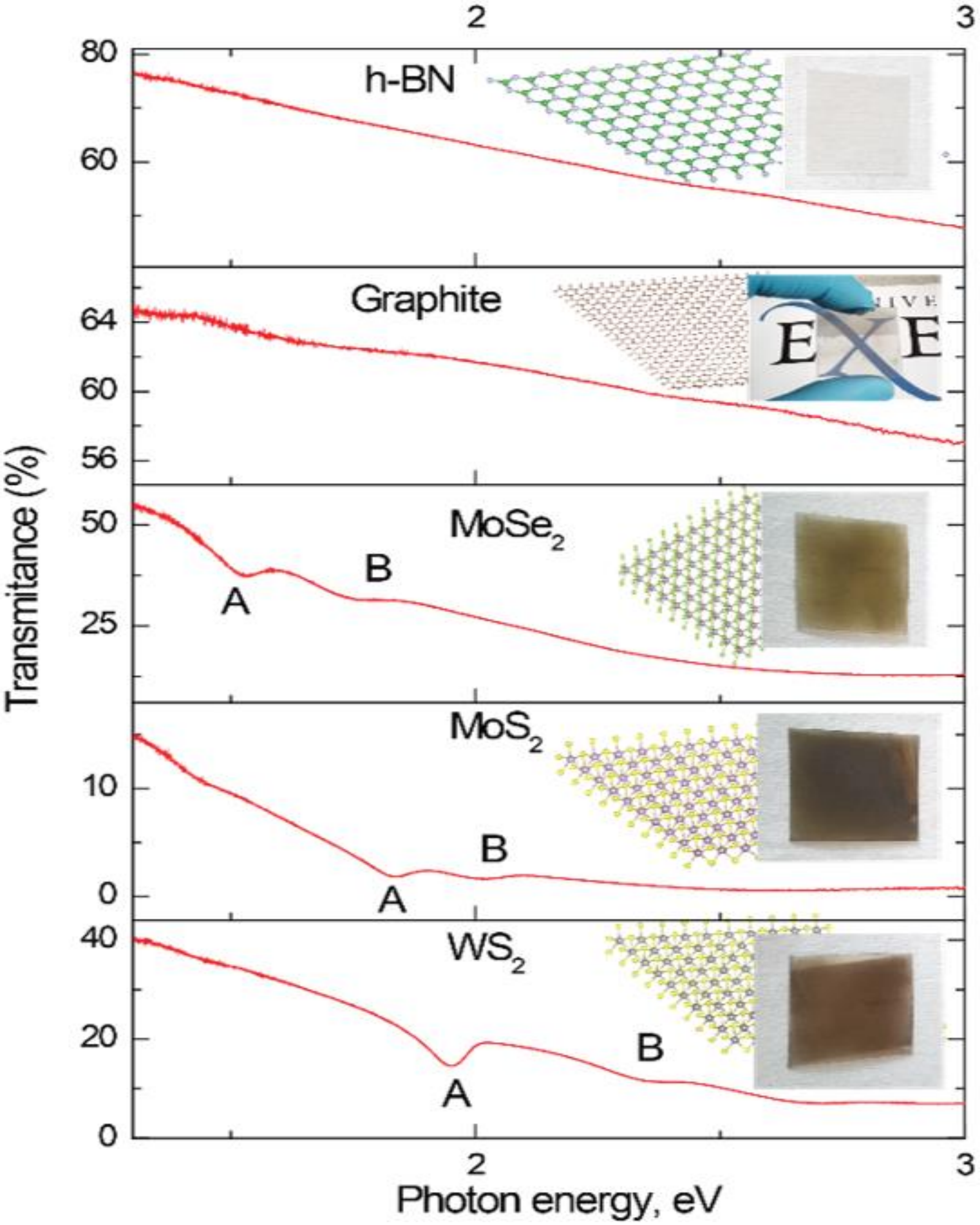

Figure 5.21: *Optical transmission spectra for abraded materials on PET substrates. Right insets: optical image of the respective abraded films, along with an illustration of their lattice structures.*

For the TMDCs, strong optical absorption associated with the A and B excitons are observed, indicating that the films retain their bulk optical properties [97, 107].

5.1.2 Photodetection devices

As discussed within Section 2.3, bulk TMDCs are indirect semiconducting materials and thus have some potential to be used within future flexible photovoltaic and photodetection applications. Such devices have already been created using atomically thin TMDC crystals [310, 311], although in this case the materials have a direct band gap and thus allow for enhanced photodetection via the absence of phonon-mediated transitions. The creation of photovoltaic heterostructures using bulk TMDC crystals, such as in those produced via LPE, typically display poor photoresponsivity in the order of 10-1000 μAW^{-1}, restricting their use in practical applications [32, 301, 302, 307, 312, 313].

The use of abraded TMDC materials for photodetection applications in a variety of device architectures, both planar and vertical, were therefore investigated. The simplest of these is depicted within Figure 4.4 (a), and consists of a tape-thinned graphite channel abraded onto a PET substrate, with a subsequent layer of TMDC material abraded on top. Upon illumination, photoexcited carriers within the semiconducting TMDC transfer into the graphite layer, resulting in a change of free charge carrier density leading to a subsequent change in electrical conductivity. These planar photodetectors use either MoS_2, $MoSe_2$ or WS_2 abraded onto an ~ 40 % transparent graphite channel. The same optical measurement set-up described previously was used, but this time the white light source was blocked using a mechanical shutter with a response time of 10 ms, allowing for the temporal response of the photocurrent to be measured. Additionally, the spectral dependance of the photocurrent was carried out using 10 nm band pass filters to filter the halogen white light source with the power at each wavelength measured using a Thorlabs photodiode S120C.

Figure 5.22 (a) shows the temporal response of the photocurrent for the three different heterostructures with a white light power density of 55 $mWcm^{-2}$ and a bias voltage of $V_b = 2$ V, with the optical excitation aimed through the transparent backside of the PET substrate (to enhance the light incident on the graphite/TMDC interface). Figure 5.22 (b) shows the I-V_b characteristics for the WS_2-based device within (a) both with and without optical excitation. This was recorded for each TMDC material which, for a given bias voltage, allows the photoresponsivity, R, of each device to be calculated using

$$R = \frac{I_p}{P}, \tag{5.6}$$

where I_p is the photocurrent and P is the incident power on the device from the white light source. The first devices were found to yield responsivities up to 24 mAW^{-1} for WS_2 (with an active area of ~ 0.5 cm^2), constituting more than a 10^2-10^3 improvement over comprable LPE photodetectors [301, 302, 312, 314]. Comparisons to LPE devices are made throughout this study as both the abrasive process and LPE offer a solution to the problem of how to produce high-quality, large-scale heterostructure devices.

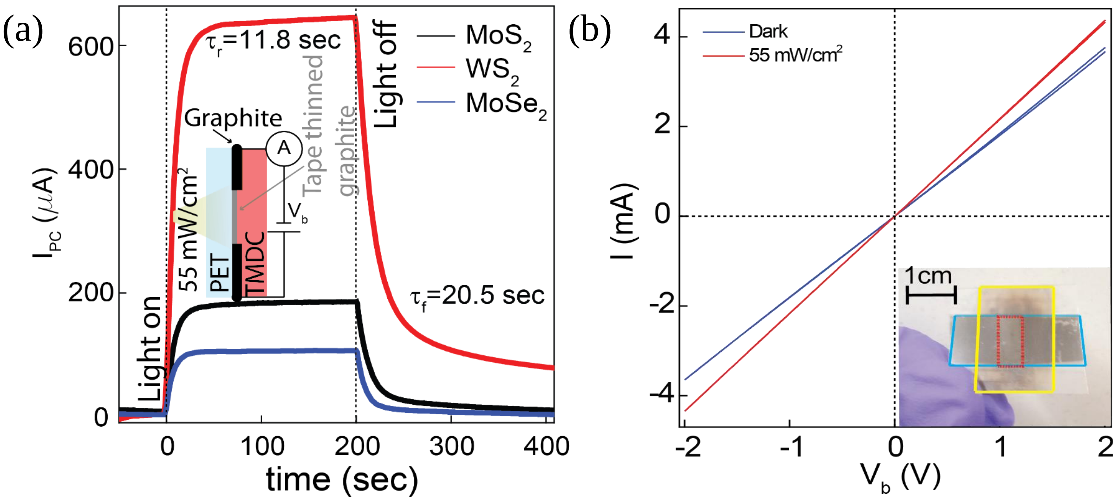

Figure 5.22: *(a) Temporal response for three planar photodetectors abraded onto PET substrates, consisting of graphite/MoS_2 (black), graphite/$MoSe_2$ (blue) and graphite/WS_2 (red). (b) I-V_b characteristics for the WS_2 planar photodetector device within (a) with (red curve) and whitout (blue curve) white light excitation. Inset: optical image of the device with the graphite, tape-thinned graphite and optically active TMDC layers highlighted in blue, red and yellow, respectively.*

The next device to be considered was a vertical heterostructure geometry consisting of an Au bottom electrode, a TMDC semiconducting barrier and a CVD-grown graphene top electrode, as is illustrated within Figure 4.4 (c). The I-V_b characteristic curve for this device (with WS_2 TMDC) without optical excitation is given in Figure 5.23 (a), while the same curve both with and without optical excitation is given in Figure 5.23 (b), indicating a peak response at a bias voltage of $V_b \sim -1$ V.

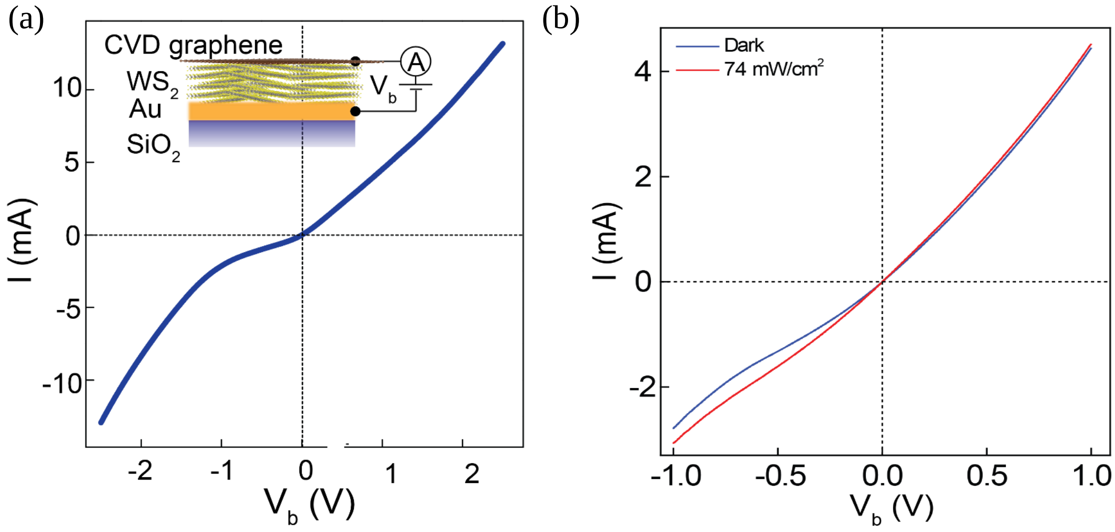

Figure 5.23: *(a) I-V_b for an Au/WS_2/CVD-grown graphene heterostructure with device area of 1 mm × 1mm and WS_2 film thickness of ∼ 300 nm. (b) I-V_b curve of the same device as in (a) with (red) and without (blue) optical excitation.*

The asymmetry in the I-V_b curves for this device is due to the difference in the work functions of the graphene layer (4.6-4.9 eV) [169] and Au (∼5.2 eV) [315] with the conduction band edge of WS_2 which is closely aligned with the neutrality point of graphene [316]. This means that at $V_b = 0$ V, the conductivity is high as charge transport occurs through the conduction band of the WS_2, whilst at negative bias voltages the energy difference between the chemical potential of graphene and the WS_2 conduction band increases [317], raising the potential barrier to transport between the two and reducing the conductivity - hence the nonlinear transport characteristics.

Figures 5.24 (a) and (b) shows the spectral dependance of the photoresponsivity on incident wavelength and power, respectively. The peak photoresponsivity (∼ 0.15 AW^{-1}) occurs at an incident photon energy of 2.0 eV and a bias voltage of V_b =

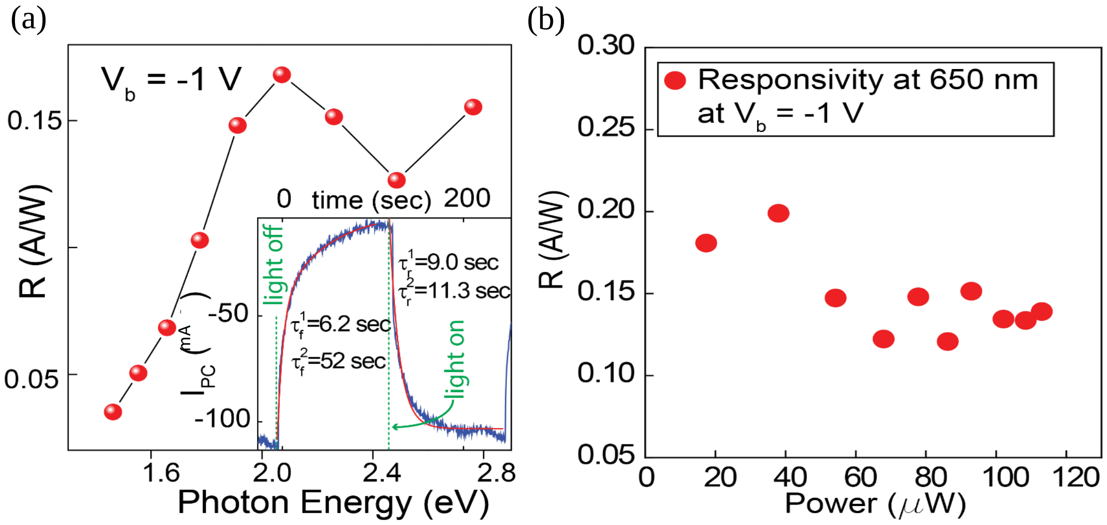

Figure 5.24: *(a) Spectral dependance of the photoresponsivity. Inset: the temporal response of the photocurrent with biexponential decay fitted (red curve). (b) Photoresponsivity measured using a 10 nm bandpass filter centred at 650 nm for increasing excitation power.*

-1 V, consistent with the peak in absorption associated with the formation of an A-exciton (see Figure 5.21 and Section 3.2.4). The peak photoresponsivity can be enhanced to as high as 0.2 AW^{-1} by modulating the incident power as is shown in Figure 5.24 (b). This once again constitutes a 10^2-10^4 improvement compared to LPE photodetectors [32, 307, 312]. The temporal response to incident white light is shown in the inset of Figure 5.24 (a), with peak photocurrent values of $\sim$ 100 mA at V_b = -1 V.

The enhanced photoresponsivity likely arises from using graphene as the top contact as the low carrier density of states near the Dirac point results in a tunable Schottky barrier which is extremely sensitive to external modulation, allowing for easy enhancement (and control) of the induced photocurrent. Furthermore, its high transparency ensures that most of the incident light reaches the graphene/TMDC interface, promoting exciton formation and thus photocurrent generation.

Similar architecture was used to produce photodetectors with n or p-type Si electrodes. To produce these devices, a 1 cm^2 region of SiO_2 was etched away in sodium bifluoride solution [318], leaving the exposed doped Si beneath. WS_2 was then abraded over n/p-type Si (labelled n-Si and p-Si, respectively) until no pinholes could be observed under a 50 × objective. CVD graphene was then transferred onto the abraded WS_2 film before baking at 100 °C for 30 minutes to ensure the remaining PMMA adheres well to the WS_2. During transport measurements this PMMA was left on which may have helped to bridge any pinholes within the WS_2 film, preventing short circuit between the doped Si and CVD graphene. The I-V transport characteristics of both *n* and *p*-doped Si/WS_2/CVD-graphene heterostructures are shown in Figure 5.25 (a, c), respectively. Improved performance was observed for *p*-Si based devices, due to the bulk WS_2 being *n*-type (determined via the same technique discussed in Figure 5.19 (a)), which facilitates charge transfer into the *p*-Si bottom electrode. However, overall this device architecture did not perform as well as the others investigated in this work due to the WS_2 being rather thick ($\sim 0.3 - 1$ µm), preventing incident light from reaching the WS_2/Si interface and resulting in $R_{pSi} \sim 3$ mA/W and $R_{nSi} \sim 1$ mA/W at V_b = -2 V.

Next, more complex multilayer vertical heterostructures formed through fabrication route 2 (see Section 4.1.1) where the entire device comprises abraded films were investigated, with particular focus being placed on graphite/WS_2/MoS_2/graphite heterostructures. Figure 5.26 (b) shows the I-V_b curves of three separate devices.

In total, 12 junctions were fabricated and measured, with 10 showing similar electron transport properties. The inset of Figure 5.26 (b) shows the I-V_b curves of the top and bottom abraded graphite electrodes, showing Ohmic behaviour with typical resistances of a few kOhms. Figure 5.25 (c) shows the I-V_b curve for device D2 within (b), with and without white light illumination with the inset showing the temporal response of the short circuit photocurrent at V_b = 0 V. These multilayered devices offer typically offered photoresponsivities between 4-10 mAW^{-1} at V_b = -1 V, lower than the first device architecture due to fabrication route 2 producing a thicker graphite top electrode. As the white light measurements were obtained when globally illuminating the device, it is important to rule out photocurrent generation from the contacts or elsewhere. To demonstrate this, photocurrent mapping measurements using a 405 nm laser beam focussed to a spot size of 5 µm were taken, see Figure 5.26. Here, the laser spot is scanned over the sample and the resultant photocurrent

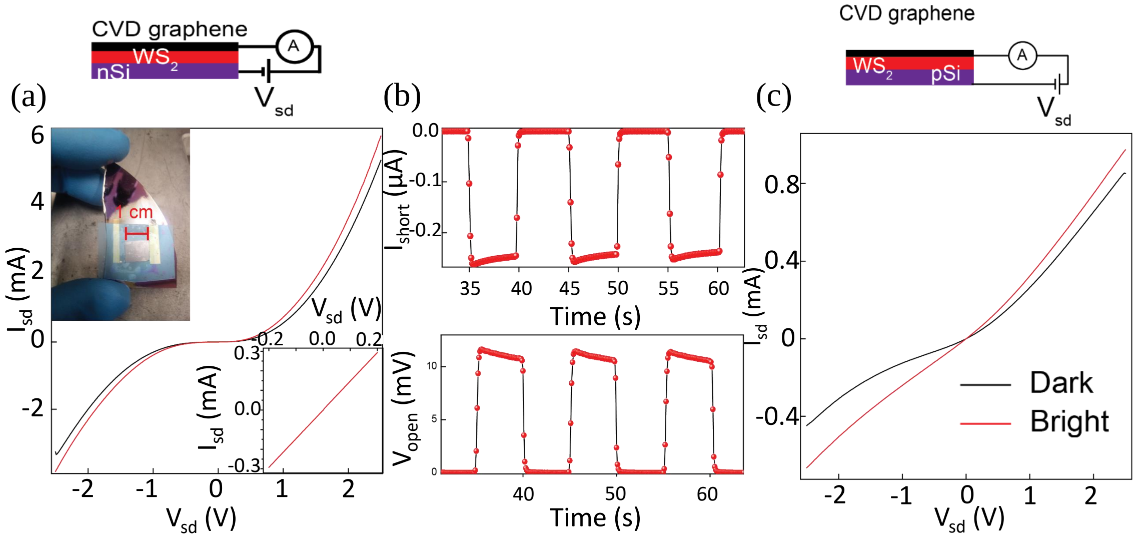

Figure 5.25: *(a) Vertical I-V_b curves for a n-Si/WS$_2$/CVD-grown graphene heterostructure. Inset: (bottom right) I-V_b curve of the CVD graphene top electrode, with a measured resistance of 650 Ω, (top left) optical image of the device and (top right) schematic of the measurement circuit. (b) Short circuit current and open circuit voltage for the device shown in (a). (c) Vertical I-V_b curves for an p-Si/WS$_2$/CVD-grown graphene heterostructure. Both (a) and (c) were taken with (red) and without (black) optical excitation.*

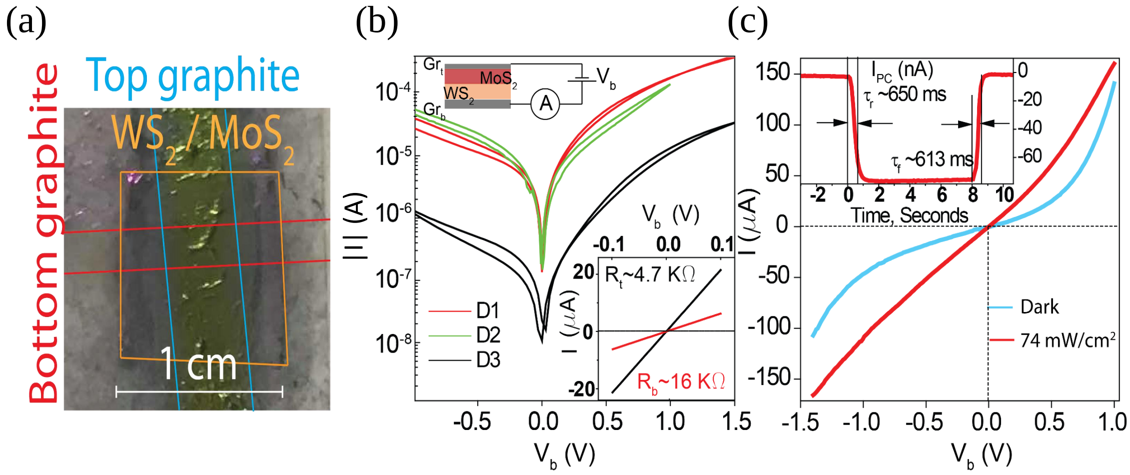

Figure 5.26: *(a) Optical image of a typical all-abraded, multilayer photodetector with the bottom graphite, top graphite and TMDC layers highlighted in red, blue and orange, respectively. (b) I-V_b curves for three representative graphite/WS$_2$/MoS$_2$/graphite devices, labelled D1, D2 and D3. Inset: (top) schematic of the measurement circuit and (bottom) I-V_b curves for the top and bottom graphitic electrodes. (c) I-V_b curves for the devices D2 shown within (b) with (red curve) and without (blue curve) white light excitation of 74 mWcm^{-2}. Inset: temporal response of the short circuit photocurrent at V_b = 0 V.*

is recorded as a function of laser spot position.

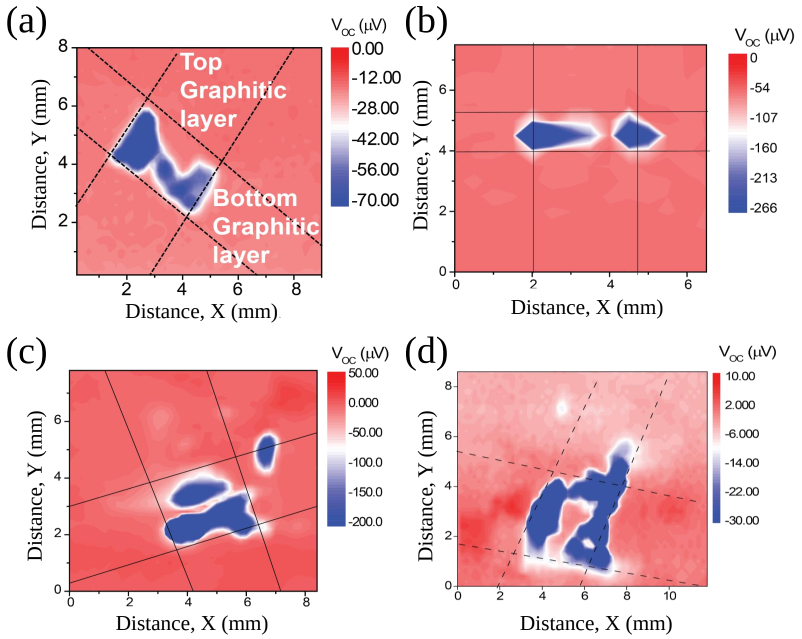

Figure 5.27: *(a-d) Photocurrent open voltage maps of several all-abraded, multilayer photodetectors measured using a focussed laser (E = 3.05 eV) with a power output of 0.5 mW and a spot size diameter of 5* µm.

A peak open circuit voltage, V_{oc}, is only ever observed in the region where all layers overlap, indicating vertical electron transport as the dominant mechanism in these devices. The inhomogeneity in the photovoltage maps arises due to variation in the contact quality between the top graphitic electrodes and the underlying TMDC layers (a result of fabrication route 2), which can be seen as “bubbles” within Figure 5.26 (a). The variation in contact quality also likely explains the reduction in photo current for device D3 within Figure 5.26 (b). The device within Figure 5.27 (a) was annealed to 150 °C for 60 minutes to allow for greater adhesion of the PMMA remaining on the top graphitic electrode, and thus consequently shows more uniform photovoltage over the entire device.

The planar devices shown in Figure 5.22 rely on charge injection into the graphite layer to enhance its conductivity, and is thus a photoconductive device. Those shown in Figures 5.23-5.27 rely on the separation of photoexcited charge carriers across a junction of two dissimilar materials via the in-built electric field here in order modulate the photocurrent, and hence are photovoltaic devices.

The stark difference in performance between vertical and planar architectures is directly related to the dimensions of the abraded nanocrystals. Consider the planar devices shown in Figure 5.22. Here, photoexcitation occurs at the surface of the TMDC layer and charges are generated which then propagate towards the graphite layer, whereby they quickly move towards the contacts due to the high conductivity of graphite. The majority of the distance travelled when moving to the contacts occurs laterally through the graphite - the direction in which the nanocrystallites are large - and thus relatively few hopping incidents are required for the carriers to move through nanocrysallite film to reach the contacts and thus the carrier mobility is enhanced. By comparison, for vertical architecture, photoexcited carriers must move vertically between contacts - the direction in which the nanocrystallite size is reduced - increasing the number of hopping incidents required to reach the contacts and hence lowering the carrier mobility. The two device architectures operate in two different mobility regimes which affect the efficiency with which photoexcited carriers can reach the contacts, and the vastly different photoresponsivities reflect this.

The variation in the performance of the vertical photovoltaic devices can be attributed to the ease with which incident light can reach the relevant active regions due to their distance from the device surface. For example, this is why the graphene/WS_2/Si and graphite/WS_2/MoS_2/graphite devices performed poorly, due to the thick TMDC layers in both inhibiting light penetration.

A comparison of the photoresponsivity of the highest performing all-abraded photodetector (the tape-thinned graphite/WS_2 heterostructure on a PET substrate, see Figure 4.4 (a)) to similar devices produced through LPE is available within Table 5.4.

Table 5.4: *Comparison of the photoresponsivity of abraded devices compared to those produced in the literature through LPE.*

Active material/ detector type/ method	**Key parameters: environment/ bias/ power**	**Photo-responsivity**	**Our like-for-like photo-responsivity**	**Abraded device enhancement factor**
WS_2/Vertical/ LPE [32]	Ambient/-0.5 V/2.76 mW (Laser)	36 µA/W	24 mA/W	667
WS_2/Vertical/ LPE [314]	Ambient/ -0.5 V/$\sim$ 334 mW/cm^2	$\sim$ 10 mA/W	5 mA/W	0.5
Graphite-WS_2-graphite/ Vertical/LPE (with exfoliated graphene and Au contacts, and a WS_2 thickness of 30 nm. Non-scalable production route) [307]	Ambient/-1 V/ 37 mW (Laser)	0.7 mA/W	0.15 A/W (The Au/WS_2/CVD-grown graphene device is used for comparison, as this has the thinnest WS_2 barrier of all the studied devices, as well as having monolayer graphene as the top electrode)	214
WS_2/Planar/ LPE [312]	Ambient/ -1 V/ < 800 mW/cm^2	0.1 µA/W	10 mA/W	1.0×10^5
WS_2/Planar/ LPE [302]	Ambient/-1 V/ 12.5 mW	0.56 µA/W	10mA/W	1.7×10^4

As previously mentioned, LPE offers a solution to the production of scalable vdW heterostructures. Clearly, devices produced via the abrasive method consistently offer enhanced photoresponsivities compared to LPE devices, and even outperform similar devices produced through non-scalable means (i.e. those which consist of mechanically exfoliated materials as well [307]). However, the responsivity of the abraded devices is still significantly lower than that which is observed in comparable devices entirely composed of mechanically exfoliated films [310], although the production of these devices cannot be scaled up and so have little chance of industrial uptake. It is expected that the performance of the all-abraded photodetectors can be improved by optimisation of post-fabrication annealing of the devices, which should improve the interfacial contact quality between the different nanocrystalline layers. Additionally, fabrication within an inert environment (e.g. by using a glovebox) should also limit the amount of contaminants present along the interfaces and thus improve device performance (see Section 2.5.1).

The importance of a sharp interface in the performance of abraded, multilayer photodetectors was investigated next. Previously, all device architectures utilised charge transfer between clearly defined layers (Figures 5.16-5.18) to enhance the conductivity of an electrode and thus detect incident light. Instead, a composite film composed of varying amounts of MoS_2 and graphite was abraded onto PET substrates (using the automated method, Section 4.1.2), contacted using Cu tape and Ag epoxy and then exposed to white light. I-V_b measurements were then taken with and without white light exposure and used to determine the photoresponsivity of the abraded composite films. The production of these devices follows the same method as described in Section 4.2.5 for the creation of abraded, wearable thermistors. In total, five devices were created with graphite:MoS_2 ratios of 10:90, 30:70, 50:50, 70:30 and 90:10. The I-V_b curves for these devices both with and without white light excitation are presented within Figure 5.28, while their temporal current response curves are shown in Figure 5.29.

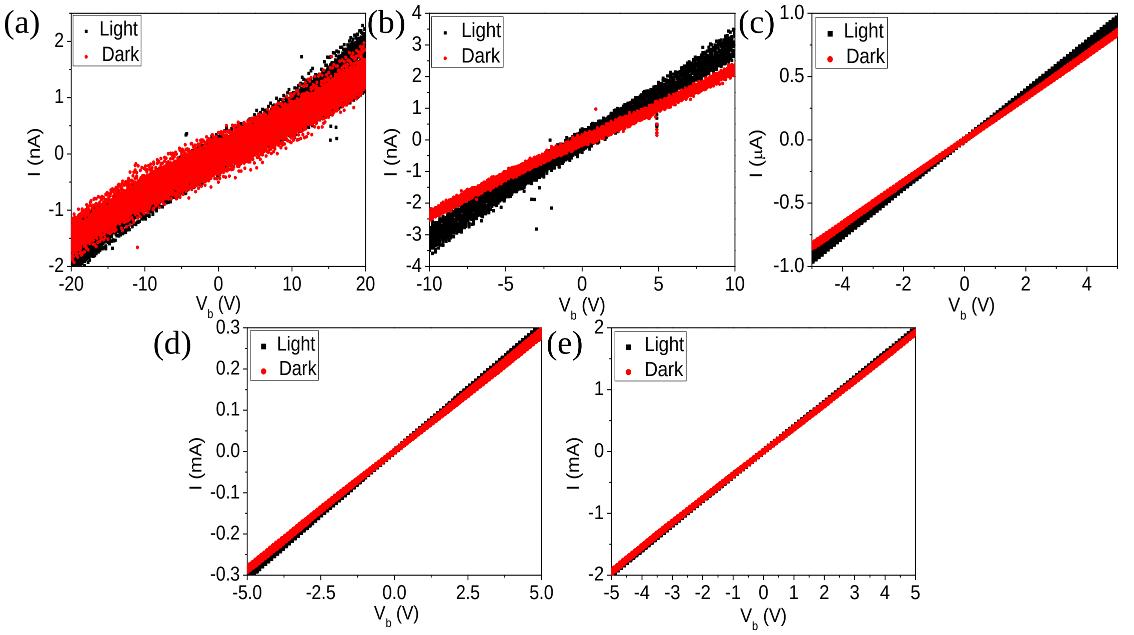

Figure 5.28: *I-*V_b *curves for abraded films with graphite:*MoS_2 *ratios of (a) 10:90, (b) 30:70, (c) 50:50, (d) 70:30 and (e) 90:10 both with (black) and without (red) white light excitation.*

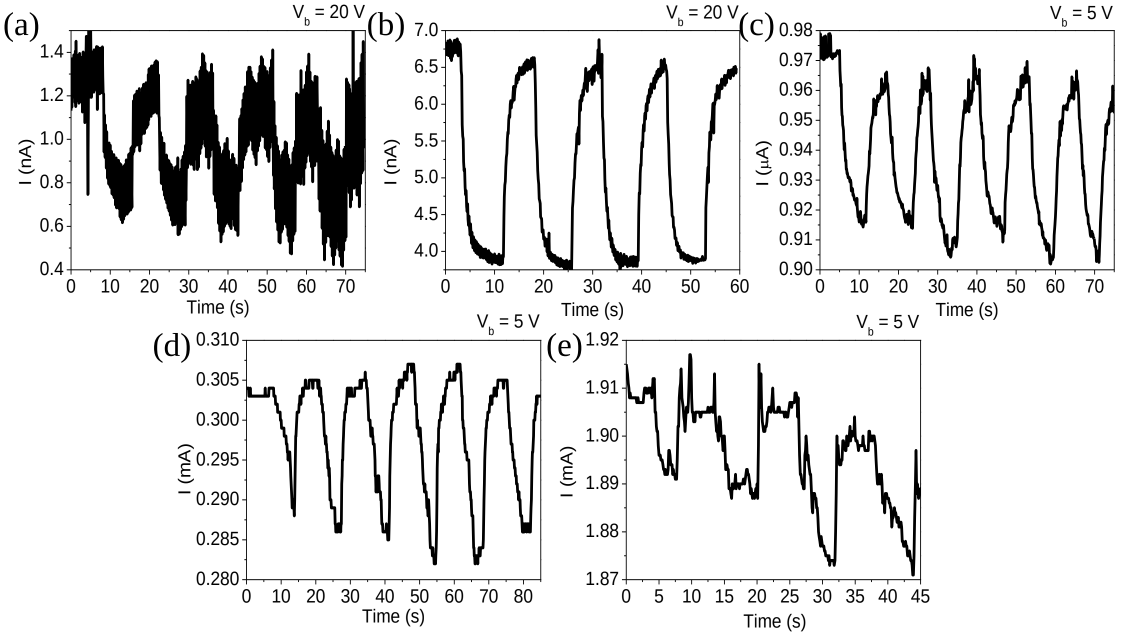

Figure 5.29: *Temporal current response curves for abraded films with graphite:*MoS_2 *ratios of (a) 10:90, (b) 30:70, (c) 50:50, (d) 70:30 and (e) 90:10 under white light excitation.* V_b *is indicated above the graph in each case.*

Naturally, as the graphite concentration within the abraded films increases so too does the conductivity, with resistance varying between $\sim$ 16 GΩ - 2.5 kΩ for films with graphite:MoS_2 ratios of 10:90 and 90:10, respectively, see Figure 5.30 (a). The white light power density incident on each device was once again 55 mWcm^{-2} and, using eqn. 5.6 with a spot size of diameter $\sim$ 1 cm, allows the photoresponsivity for each film to be determined as is shown in Figure 5.30 (c). A linear fit to the 10:90 I-V_b curve for small V_b (-1 V $< V_b <$ 1 V) was used in order to calculate the resistance of this film, while standard procedure was used for the other devices. The data collected for each device was smoothed using a 25-point moving average before fitting.

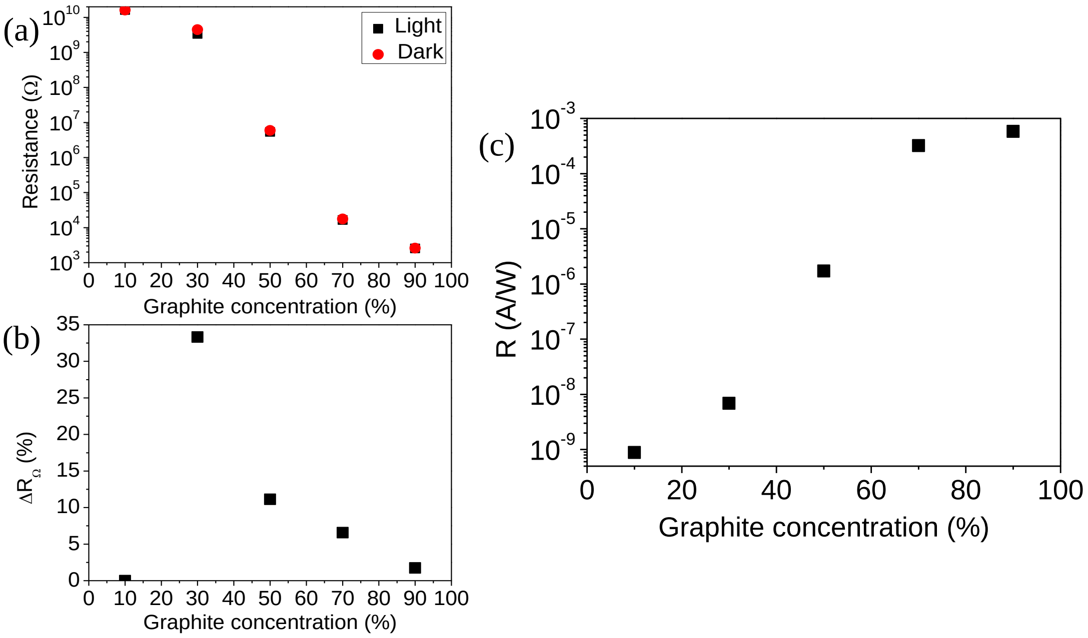

Figure 5.30: *(a) Resistance of the abraded composite films for varying graphite concentration. (b) Percentage change in resistance, ΔR_{Ω}, with and without white light excitation for varying graphite concentration. (c) Photoresponsivity of the abraded composite films for varying graphite concentration. All of the data displayed here corresponds to a bias voltage of V_b = 5 V.*

As the concentration of graphite within the composite films increases so does the photoresponsivity, see Figure 5.30 (c), with an approximate inverse proportionality to the resistance of the device. Although the percentage change in resistance, ΔR_{Ω}, with and without white light excitation peaks for a graphite:MoS_2 ratio of 30:70, this is not reflected in the photoresponsivity. Comparison between Figure 5.30 (a) and (c) indicates that the photoresponsivity is dominated by the resistance of the film, and that the effect of MoS_2 addition on the conductivity due to photoexcitation is obscured by the general reduction in resistance achieved by increasing the concentration of graphite, thus facilitating the detection of any incident light. Despite this, it would appear, from Figure 5.30 (b), that the greatest increase in photoresponsivity occurs for graphite concentrations of approximately 30%, although, as mentioned, this is dwarfed by devices with a larger inherent conductivity due to having a higher concentration of graphite. Overall, the highest photoresponsivity yielded by these composite films was 0.58 mA/W, an order of magnitude less than the worst performing abraded heterostructures (Figure 5.26). This highlights the importance of having a clear separation between the conducting graphite layer and the photosensitive TMDC layers, as in this case photoexcited carriers transition into the graphite (which always has a low resistance, unlike many of the composite films) and move towards the source and drain electrodes for detection. Furthermore, the presence of a large and unbroken TMDC layer allows for large scale exposure to incident light, whereas in the composite films only TMDC nanocrystallites at or near the exposed surface will contribute to the photoresponse due to the opacity of the film. Additionally, in the previous multilayered devices the transparency of the graphite layer can be reduced by back-peeling with specialist tape, increasing the amount of light incident on the interface with the TMDC layer. This is only possible because both the graphite and TMDC are confined to their respective planes, allowing one to focus light at a particular location to improve the photoresponsivity without severely hampering the conductivity of the graphite layer. This is not possible with a composite film, where both the graphite and TMDC are thoroughly mixed and thus prevent control over the light reaching the many graphite/TMDC interfaces laced throughout the film. Both of these effects lead to a significant reduction in the photoresponse of abraded composite films compared to their multilayed counterparts.

5.1.3 Triboelectric nanogenerators

The basic operating principle of a triboelectric nanogenerator (TENG) was discussed in Section 2.5.4, whilst an illustration of the evolution of charge within these devices was provided within Figure 2.23. Here, it was described how, although TENG devices typically rely on the use of two materials at the opposite end of the triboelectric series to induce charge separation, the output power could potentially be increased by the introduction of charge trapping layers such as MoS_2.

Therefore, to investigate the use of abraded films within TENGs, two device types were created. The devices consist of a fixed conductive electrode, made from either abraded graphite or an abraded graphite/n-type MoS_2 multilayer on a thin PET substrate, with a fluorinated PDMS polymer layer placed on top. An Al hammer is then wrapped in PTFE tape and repeatedly brought into contact with, and separated from, the electrode/PDMS stack, as is shown in Figure 4.5. The PDMS was created in-house using the method described in Section 4.1.2. PDMS was chosen due to its position on the triboelectric series relative to PTFE along with the ease with which it can be produced. The charge induction effect between the abraded graphitic electrodes and the PDMS is further accentuated by fluorination of one side of the PDMS (the side in contact with the electrode) using CHF_3 plasma within a RIE, see Section 4.2.2, which introduces extremely electronegative fluorine ions to the surface of the polymer and thus increases the charge induced per unit area upon contact with the electrodes.

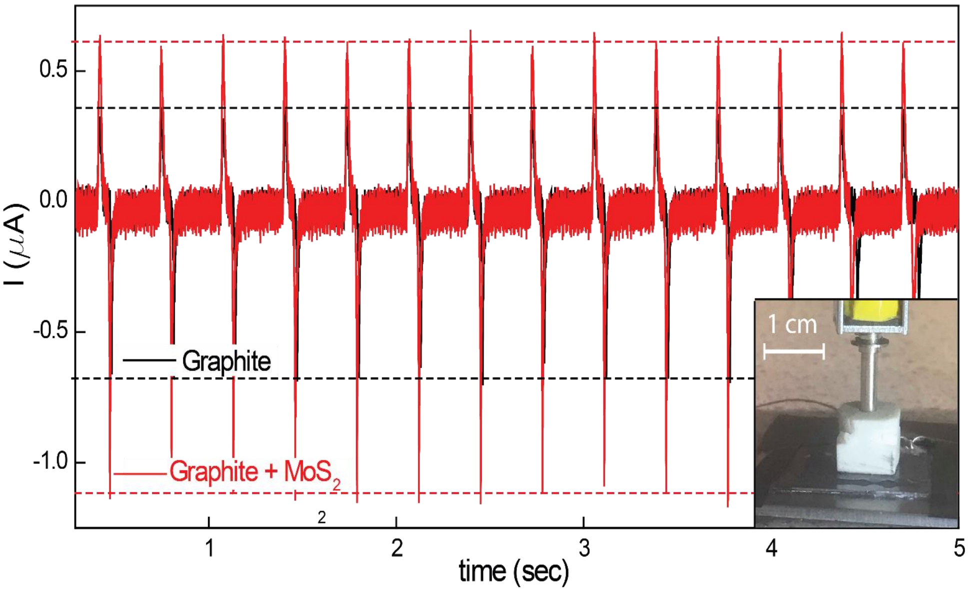

Figure 5.31: *Current response through a 1 MΩ resistor for an abraded graphite TENG electrode (black) compared with an abraded graphite/n-type* MoS_2 *TENG heterostructure electrode (red). Inset: PTFE hammer connected to a linear actuator used to generate the voltage pulses.*

The operation of the TENGs can be explained as follows: after several contacts between the PTFE-wrapped hammer and the PDMS pad, the hammer is completely released from the pad which is in turn attached to the graphitic electrodes. During the contact process, triboelectrification of the PTFE hammer and the PDMS pad occurs due to their relative positions within the triboelectric series. Upon separation, the negatively charged PDMS forces electrons from the adjacent graphitic electrode towards ground in order to electrically neutralise the stack, and a negative current is observed. As the PTFE hammer re-approaches the stack and makes contact with the PDMS, electrons are drawn back into the electrode for the same reason, and a positive current is observed. The direction of the observed current during each of these phases was used to infer the charging cycle presented within Figure 4.5.

To quantify any performance enhancement due to the addition of a MoS_2 charge trapping layer, the response of a simple graphitic electrode to the same electrode after abrasion of an additional MoS_2 layer was recorded (all other experimental parameters were kept constant). Figure 5.31 shows the current generated through a 1 MΩ resistor connected in series with the TENG electrodes, for the bare graphitic electrode (black) and the graphite/MoS_2 electrode (red) over several cycles. It was found that the introduction of an additional MoS_2 layer yields an enhancement of $\sim$ 50 % for the output current compared to the bare graphite electrode.

After confirming the enhancement due to charge trapping within the MoS_2 layer, incorporation of the abraded TENG into a practical device was considered. Figure 5.32 (a) displays the open circuit voltage and short circuit current for three cycles of a secondary, larger ($\sim$ 25 cm^2) device which yields an open circuit voltage in excess of V_{oc} =15 V and short circuit currents of I_{sc} = 0.38 µA, giving a peak power output, $P = I_{sc}V_{oc}$, of 5.7 µW, which is comparable to more complex LPE TENG electrodes [319, 320].

This larger electrode was then used to charge a 10 µF capacitor to 9 V, shown in Figure 5.32 (b). The inset shows the energy stored on the capacitor per cycle ($\Delta E \sim$ 10 nJ) when connected via a rectifying diode bridge. This is required as the current produced by the TENG is necessarily AC, and so must first be converted to DC in order to power a circuit. From the circuit schematic within Figure 5.32 (b), it can be seen that when the TENG output voltage is positive, diode D1 is forward biased and charge is pulled from the upper plate of the capacitor. Likewise,

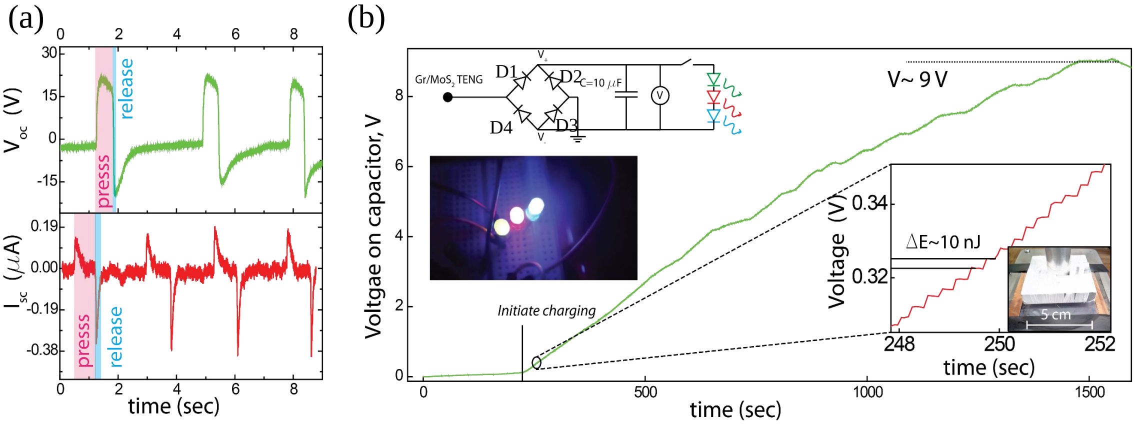

Figure 5.32: *(a) Top: temporal response of the open circuit voltage and bottom: temporal response of the short circuit current, for the graphite/n-type* MoS_2 *electrode. (b) Voltage accumulation on a capacitor vs time (hammer frequency* $\sim$ *3 Hz). Inset top: rectifying circuit used to charge the capacitor. Inset middle left: Three glowing LED's during capacitor discharge. Inset right: zoomed in region of the capacitor charging curve highlighting the energy stored on the capacitor per TENG discharge cycle.*

when the TENG output is negative, diode D4 becomes forward biased and charge is forced onto the lower plate of the capacitor. Over the course of one AC cycle, a net charge is therefore added to the capacitor. When discharge is required, the switch is closed and, as all four diodes are reverse biased against current backflow from the capacitor, and current flows through the LEDs instead. As the capacitance, C, is known, the energy stored per cycle, dE can be calculated (beginning with $E = CV^2/2 \rightarrow dE/dV = CV$) as

$$dE = CVdV = C\left(V_2^2 - V_1^2\right), \tag{5.7}$$

where V is the voltage on the capacitor. The discharge from this capacitor was then used to light three LED's, see the inset of Figure 5.32 (b).

5.1.4 Strain sensors

Electrical characterisation of abraded vdW heterostructures and films under strain was also performed. As discussed within Section 4.2.3, a bespoke bending rig was used to apply uniaxial strain to manually abraded MoS_2/WS_2 heterostructures with abraded graphite contacts adhered to a thin (0.5 mm) PET substrate. As the abraded films are adhered to the upper surface of the substrate, tensile or compressive strain can be applied by introducing positive or negative curvature to the PET, respectively, as is shown in Figure 5.32 (c). A LabView virtual interface was designed to pulse the voltage output from a ELC AL991S power supply which, in turn, allowed for accurate control of the actuator extension distance and thus the amount of strain applied to the abraded film. Between each extension step, a photograph of the device was taken and used to calculate the PET radius of curvature, R. In order to accurately determine R, the number of pixels between the bending rig clamps was measured using vector graphics software (Inkscape) and compared to the actual measured distance, L, allowing for a conversion between the pixels within the image and an actual physical distance. Next, a circle with curvature matching that of the PET was overlaid onto the image and used, with the aforementioned px → cm conversion, to determine the radius of curvature of the PET. This, in conjunction with the known PET thickness, d, allows the magnitude of the strain applied to the abraded films, β, to be approximated as

$$\beta = \frac{d}{2R}. \tag{5.8}$$

Figure 5.33 (a) shows an illustration of a PET substrate under strain, while (b) shows the process used to calculate the radius of curvature.

It should be noted that usually the thickness of any additional layer present on the substrate would need to be considered whilst calculating β. However, as determined within Section 5.1.1, the thickness of the abraded films are typically of the order of 50-500 nm. This is negligible compared to the thickness of the PET substrate, and so its effect on the calculation of strain can be ignored.

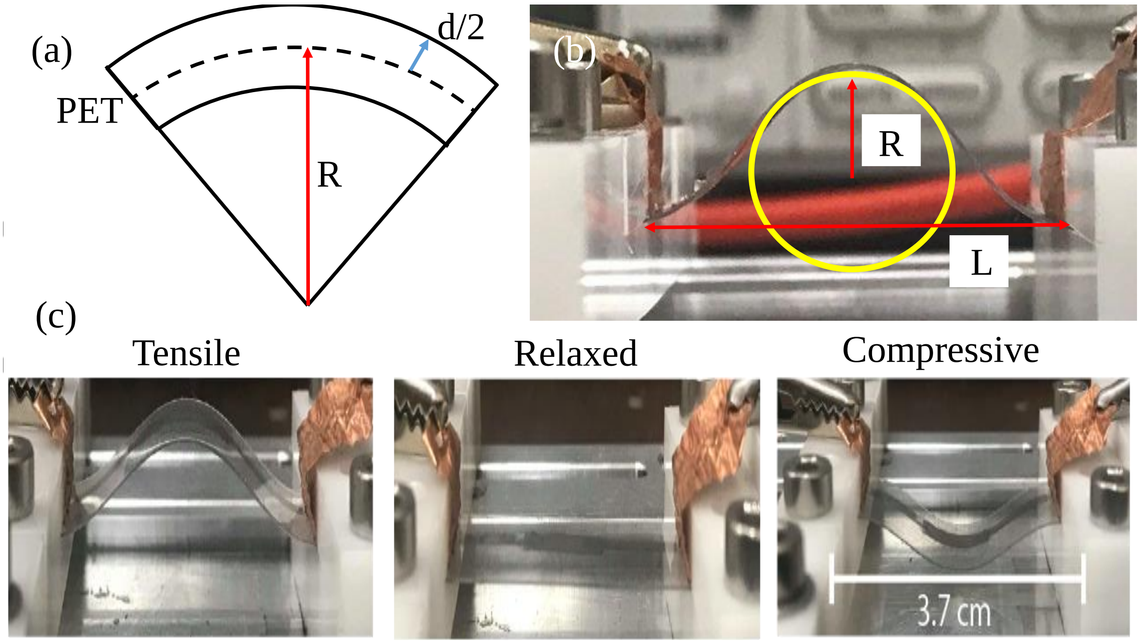

Figure 5.33: *(a) Illustration of a strained PET substrate, with the radius of curvature and thickness, R and d, respectively, indicated. (b) Optical image of a graphite/*MoS_2*/*WS_2 *heterostructure abraded onto a PET substrate under tensile strain. A circle with radius of curvature matching that of the substrate has been overlaid onto the image to indicate the process used to calculate R and thus the applied strain at each step during the strain cycle. (c) (left to right) Images of abraded films on a PET substrate under tensile, zero and compressive applied strain.*

Figure 5.34 shows typical I-V_b curves for these devices under increasing strain.

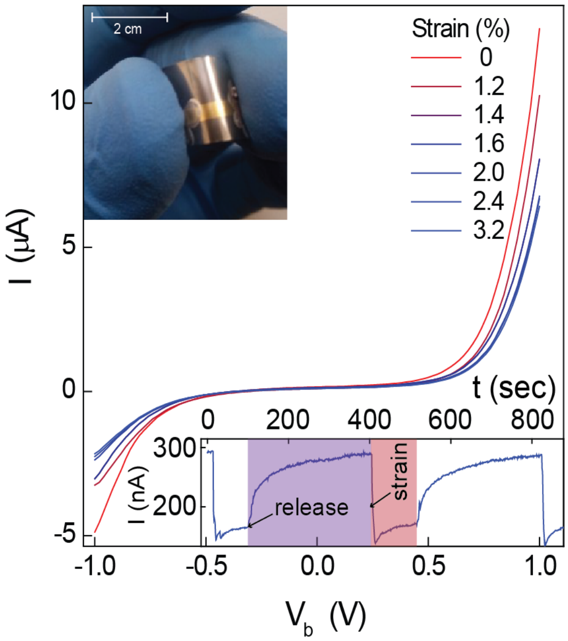

Figure 5.34: *Typical I-*V_b *curves for a manually abraded graphite/*MoS_2*/*WS_2 *heterostructure for different levels of applied uniaxial strain. Top inset: optical image of one such device on a flexible PET substrate. Bottom inset:* V_b *is held at 0.5 V and the device is subjugated to reversible uniaxial tensile strain, showing the evolution of I with time.*

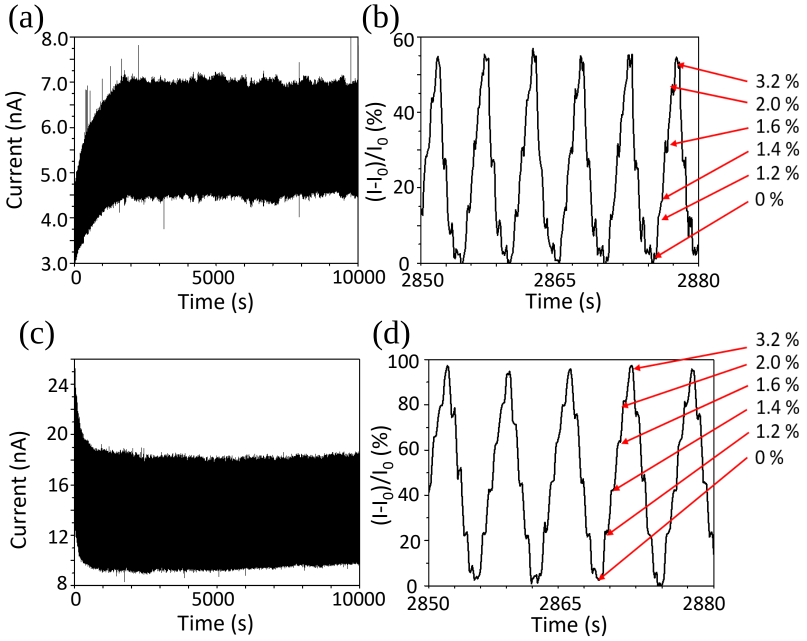

Figure 5.35: *(a) Change in current with tensile strain at $V_b = 5$ V. (b) The same data as (a), but zoomed in and modified to show the percentage change in current at each strain interval. At this scale, the individual strain cycles can be seen. (c) Change in current with compressive strain at $V_b = 5$ V. (d) The same data as (c), but zoomed in and modified to show the percentage change in current at each strain interval. The magnitude of applied strain at each point within the cycles are indicated by the red arrows.*

As tensile (compressive) strain is applied to the device the films constituent nanocrystals are forced further apart (closer together). This in turn reduces (increases) the number of available conduction pathways and thus raises (lowers) the film resistance. Figure 5.35 (a) and (c) show the change in current moving through the device (at $V_b = 5$ V) for tensile and compressive strains, respectively, over $\sim 10^3$ strain cycles. As can be seen, initial strain cycles lead to an irregular current response which eventually levels out and becomes highly reproducible. Figure 5.35 (b) and (d) show the percentage change in current moving through the device at each step within the strain cycle, where each step manifests as a shoulder in the current response curve. These graphs are a zoom-in of the data presented within (a, c), taken shortly after the current response stabilises, and once again highlights the potential for these abraded films to act as accurate and robust strain sensors.

Figure 5.36 shows a histogram of the current response to an applied tensile and compressive strain of 3.2 %. The data was collected in two phases. First, the device underwent $\sim 10^3$ compressive strain cycles (indicated by the blue and cyan data), followed by $\sim 10^3$ tensile strain cycles (orange and yellow data). In both cases, the histogram reveals that the current response to applied strain is highly reproducible. However, the slight increase in the range of the tensile response data compared to the compressive response may indicate that either the abraded film or PET substrate is damaged when the same sample transitions between tensile and compressive applied strains.

The current response of simple abraded graphite films on the same PET substrates to applied tensile and compressive strains were also recorded, as is shown in Figure 5.37. In all of the samples, the response to compressive strain was significantly greater than for tensile strain. This is also true for the abraded graphite/MoS_2/WS_2 heterostructures, as can be seen within Figure 5.35 (b, d), implying that the abraded films are more sensitive to compressive strains than tensile strains regardless of composition. This, in turn, implies that the process of separating the nanocrystallites within the films by a set amount has a weaker impact on the conductivity than the reverse process under compressive strain, although an explanation of why this asymmetrical behaviour occurs at all is beyond the scope of this study. Furthermore, this analysis relies on the assumption that strain applied to the PET directly translates to strain within the abraded films, although without a full investigation it is impossible to confirm this. For example, it may be that the abraded films undergo crumpling or similar deformations which serve to ease the strain throughout the film, reducing it compared to the strain measured for the PET substrate. However it is evident from Figures 5.35 and 5.36 that the abraded films provide a clear current response to the application of strain, regardless of what the exact magnitude of said strain is, and thus still have potential for use in future scalable and flexible strain sensors.

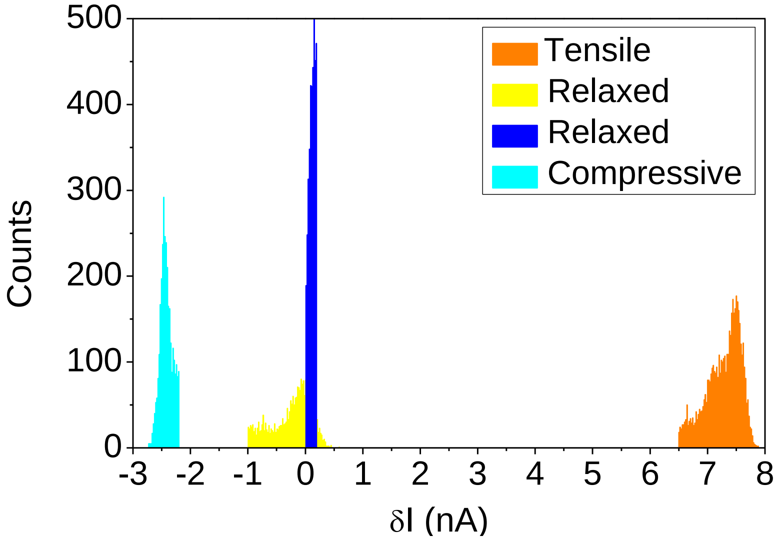

Figure 5.36: *Histogram of the compressive and tensile strain dependant changes in current (δI) through an abraded graphite/MoS_2/WS_2 heterostructure on a PET substrate for over 10^3 cycles at an applied strain of ϵ = 3.2 %.*

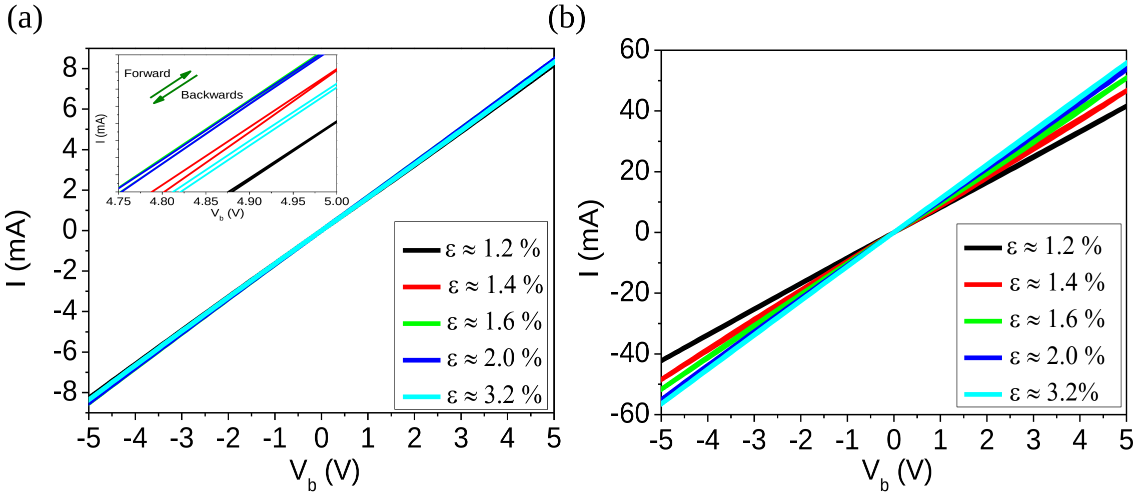

Figure 5.37: *Typical I-V_b curves for manually abraded graphite under different levels of applied (a) tensile and (b) compressive uniaxial strains. Inset of (a): zoom-in of data to highlight the effect of tensile strain on the I-V_b curves.*

5.1.5 Pressure sensors

The use of abraded films in the creation of wearable pressure sensors was discussed within Section 4.2.4. This study opts to use capacitive pressure sensing via abraded graphite powder on Tegaderm^{TM} film (using the automatic abrasion method, see

Section 4.1.2) to act as the upper and lower electrodes of the capacitor, whilst the dielectric barrier layer was chosen as either thin PDMS sheets produced in-house or simply another Tegaderm$^{\text{TM}}$ film. As the underside of each Tegaderm$^{\text{TM}}$ is adhesive, it allows for easy attachment to a wrist in order to act as a portable pressure sensor. In total, eight pressure sensors were fabricated, four of which used PDMS as the dielectric barrier whilst the others used a Tegaderm$^{\text{TM}}$ film. Current-voltage (I-V$_b$) measurements of the graphitic electrodes revealed an average film resistance of $\sim 5528 \pm 342$ kΩ. As discused within Section 4.2.4, steel discs were loaded onto the devices and the resultant change in capacitance, C and capacitive reactance, X_c, was recorded, see Figures 5.38 and 5.39. As the capacitor is being charged by an AC current, the rate of charging of each abraded graphite layer is determined by the frequency of said current. As the frequency, f, increases then the magnitude of the charge transfered between layers increases also, and the impedance of the circuit is reduced. As a result, both the capacitance and the capactitive reactance, which are related by $X_c = \frac{1}{2\pi f C}$, decrease as the supply frequency increases. Spectra such as these are important for device design as, depending on the choice of supply frequency, the device will exhibit behaviour which may not be desired.

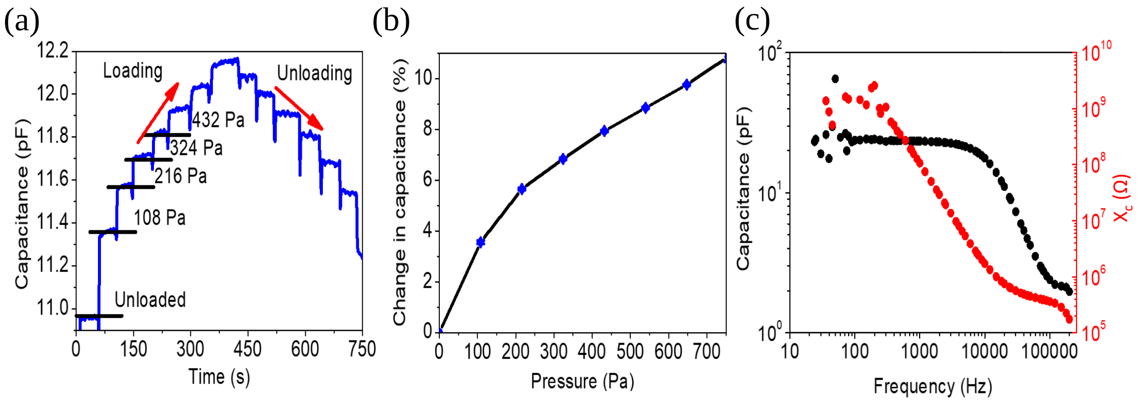

Figure 5.38: *Characterisation of an abraded graphite capacitor using a PDMS dielectric. (a) Capacitive response to applied pressure. (b) Percentage change in capacitance as a function of applied pressure. (c) C-X_c spectrum between 20-250,000 Hz.*

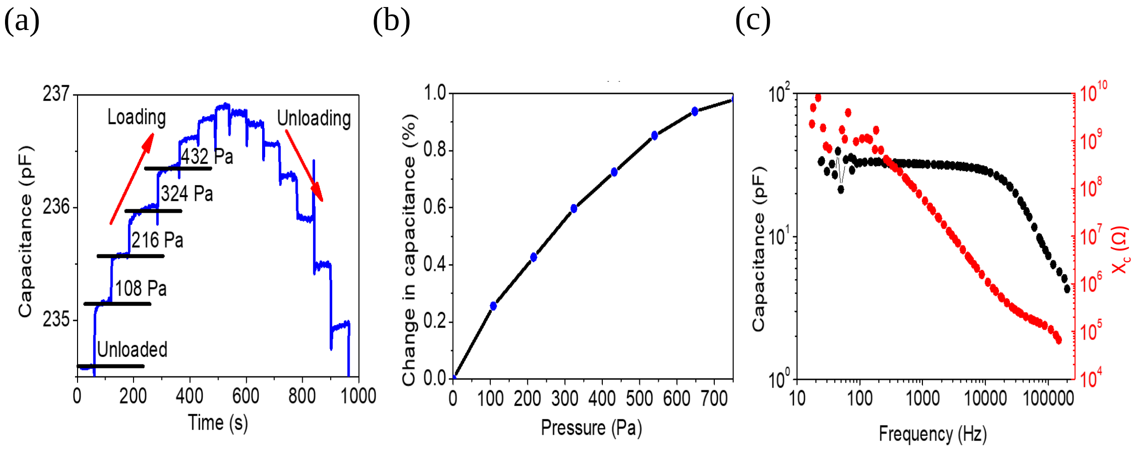

Figure 5.39: *Characterisation of an abraded graphite capacitor using a Tegaderm*^{TM} *dielectric. (a) Capacitive response to applied pressure. (b) Percentage change in capacitance as a function of applied pressure. (c)* C*-*X_c *spectrum between 20-250,000 Hz.*

The total pressure exerted by the addition of n discs, P_n, is given by

$$P_n = \frac{nmg}{A}, \tag{5.9}$$

where g is the acceleration due to gravity, 9.81 ms^{-2}. It should be noted that as the discs are stacked on top of one another the contact area remains constant throughout. Although the overall capacitance of the devices utilising Tegaderm$^{\mathrm{TM}}$ dielectrics is greater than those using PDMS (see Figures 5.38 and 5.39 (a)), which is simply a result of the decreased dielectric thickness ($\sim$ 0.1 mm compared to $\sim$ 1mm, respectively), the responsivity to external pressure of the PDMS-based capacitors exceeds that of the Tegaderm$^{\mathrm{TM}}$-based capacitors, as can be seen within Figure 5.38 and 5.39 (b). This is likely the result of the compression modulus of the PDMS ($\sim$ 187 MPa [321]) being less than that of Tegaderm$^{\mathrm{TM}}$ ($\sim$ 5 MPa - 2 GPa [322]). As a result, an equal applied pressure yields a greater compression of the PDMS dielectric than the Tegaderm$^{\mathrm{TM}}$ one, resulting in a greater percentage change in capacitance. This also provides insight into why the capacitors using PDMS dielectrics give a linear trend in capacitive response to applied pressure, whilst those using Tegaderm$^{\mathrm{TM}}$

dielectrics saturate at higher applied pressures – the thinner, stiffer Tegaderm barriers approach maximum compression within the range of pressure applied, leading to saturation within the response (see Figure 5.39 (a)). Furthermore, varying degrees of interface conformity between the dielectric and the electrodes may lead to the formation of micro-air pockets of varying number density at the electrode-dielectric interface, resulting in differing responsivity to applied pressure as said air pockets are displaced during compression.

Figures 5.38 and 5.39 (c) show the full spectrum of capacitance and resistance, R, as a function of supply frequency for the PDMS and Tegaderm$^{\text{TM}}$-based capacitors, respectively. The most ideal capacitive performance occurs between $\sim$ 0.1 - 7 kHz ($\sim$ 0.1 - 10 kHz) when a PDMS (Tegaderm$^{\text{TM}}$) dielectric barrier is used.

These abraded capacitors can easily detect pressures as low as 100 Pa, two orders of magnitude lower than other other wearable pressure sensors within the literature [277, 278, 280, 281, 323]. As discussed in Section 4.2.4, there has been significant research effort into creating portable, lightweight and comfortable pressure sensors, with the primary goal being the creation of wearable heart rate monitors for the diagnosis of disease. The pressure sensitivity offered by abraded films is far above the minimum threshold required to detect phenomena such as heat rate [278] and, due to the scalable nature of the automated abrasion process, these devices have significant potential for application within this field.

5.1.6 Thermistors

As discussed within Section 4.2.5, the use of abraded films within portable thermistors were also investigated. Bulk material powder (namely graphite and MoS_2) was mixed in varying concentrations (MoS_2:graphite ratios of 10:90, 30:70, 50:50, 70:30 and 90:10) and then abraded onto Tegaderm$^{\text{TM}}$ film using the automated abrasion process. In total, five devices were produced for each mixture, all of which showed similar behaviour to other devices within their set. Electrical characterisation of these composite films is available within Figure 5.40.

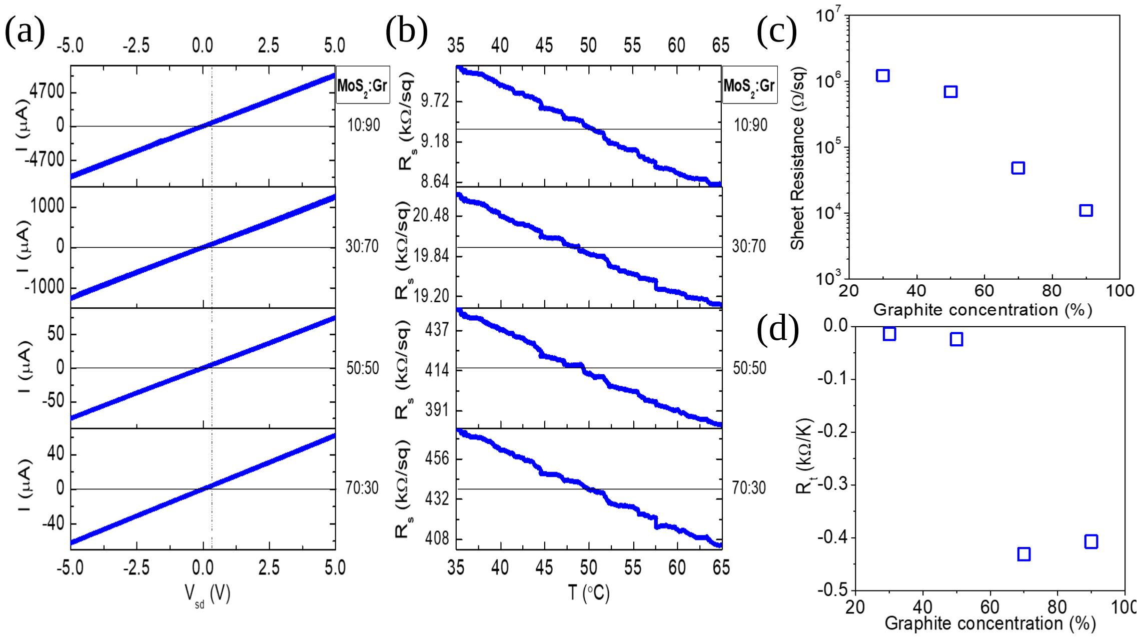

Figure 5.40: *(a) I-V_b curves for the abraded thermistor devices. (b) Change in thermistor sheet resistance, R_s, as a function of temperature at V_b = 0.5 V. In (a, b) the ratio of* MoS_2*:graphite (Gr) associated with each measurement is indicated to the right of the curves. (c) Thermistor sheet resistance as a function of graphite concentration. (d) Rate of change of sheet resistance, R_t, with temperature as a function of graphite concentration.*

Figure 5.40 (a) shows a set of typical I-V_b curves for abraded thermistors of varying composition. As the concentration of conductive graphite within the films increases the resistance decreases, likely a result of additional graphitic conduction pathways becoming available within the films. This is summarised within Figure 5.40 (c), which shows an approximately exponential decrease in sheet resistance with increasing graphite concentration.

The temperature response of the thermistors were recorded by continually monitoring the I-V_b characteristics of each device as they were heated on a hot plate. The temperature was monitored using an ADS1115 16-Bit ADC chip connected to a standard thermistor bonded to the samples using thermally conductive tape, whilst electrical measurements were carried out using a KE2400 source-meter. This data could then be used to extract the change in sheet resistance as a function of temperature, as is shown in Figure 5.40 (b). The rate of change in sheet resistance with temperature, R_t, increases in the abraded thermistors with greater concentrations of MoS_2. Overall, the thermistors have a negative temperature coefficient of resistance between -0.3 - 0.5 $\%K^{-1}$, an order of magnitude lower than other composite-film thermistors within the literature [324, 325, 326]. At 90 % graphite concentration R_t saturates, which is most probably the result of the low MoS_2 concentration inhibiting the temperature response of the film. In the case of composite films such as this, one would expect a negative temperature coefficient of resistance as a result of either (a) charge injection from the semi-conducting MoS_2 or (b) by modulation of hopping conduction through the graphite nanocrystals [327, 328]. The latter of these mechanisms arise from the formation of a Schottky barrier at the interface between the conductive graphite and semiconductive MoS_2. Electrons within the conduction band of MoS_2 here will tunnel into the graphite conduction band provided the width and height of the Schottky barrier is not too great. As the temperature increases, these electrons gain energy and the tunneling probability increases, leading to an increase in charge injection and thus a subsequent increase in current. The I-V characteristics of this transport method is known to be non-linear [329], and therefore the absence of non-linearity within Figure 5.40 (a) is indicative of direct charge injection rather than modulation of the tunneling probability.

5.2 Exfoliated heterostructures

5.2.1 Field-effect transistors

State of the art FETs have been scaled down to the nanometre regime and are now approaching their fundamental size limitations [330]. Moore's law has shown an exponential increase in FET number density with time and, in turn, requires that the length scales associated with the device decrease accordingly. Furthermore, as discussed within Sections 2.3.2 and 2.4.2, future FETs need to show continual improvement in their electrical performance which may be addressed by optimising both the channel and dielectric barrier materials within the device, such as through the incorporation of TMDCs and atomically flat dielectrics, respectively. Previous TMDC-based FETs have already been shown to have competitive switching behaviour [15, 16, 17] and sub-threshold swings [18, 19, 20] compared to the theoretical limit of traditional Si-based FETs [331, 332]. Despite this, they consistently underperform when compared to their maximum theoretical potential [15, 21], a direct result of both extrinsic (adsorbents, lattice vacancies, etc) and intrinsic (channel and channel-dielectric interfacial phonon) scattering, both of which lower the channel carrier mobility and reduce FET performance [22]. As a result, the choice of dielectric material is a crucial component in reducing the gap between the real and theoretical maximum performance of these devices.

It is for this reason that the secondary focus of this study investigates the use of talc as a dielectric in mechanically exfoliated TMDC-based FETs, in order to compare device performance against those using conventional 2D dielectrics such as hBN and Al_2O_3. Figure 4.11 shows an illustration of the back-gated FET architecture used within this study, with the TMDC chosen as either MoS_2 or $MoSe_2$. The TMDCs, talc and graphite were mechanically exfoliated from their corresponding bulk crystals and transferred onto SiO_2/Si substrates with an oxide thickness of 270 nm. Once suitable flakes had been identified by optical contrast measurements (see Section 4.3.2), the FET heterostructures were then fabricated using the PDMS-based dry transfer technique (Section 4.3.3) along with standard lithography and metallisation procedures (Section 4.3.4). Optical micrographs of both device types are shown in Figure 5.41.

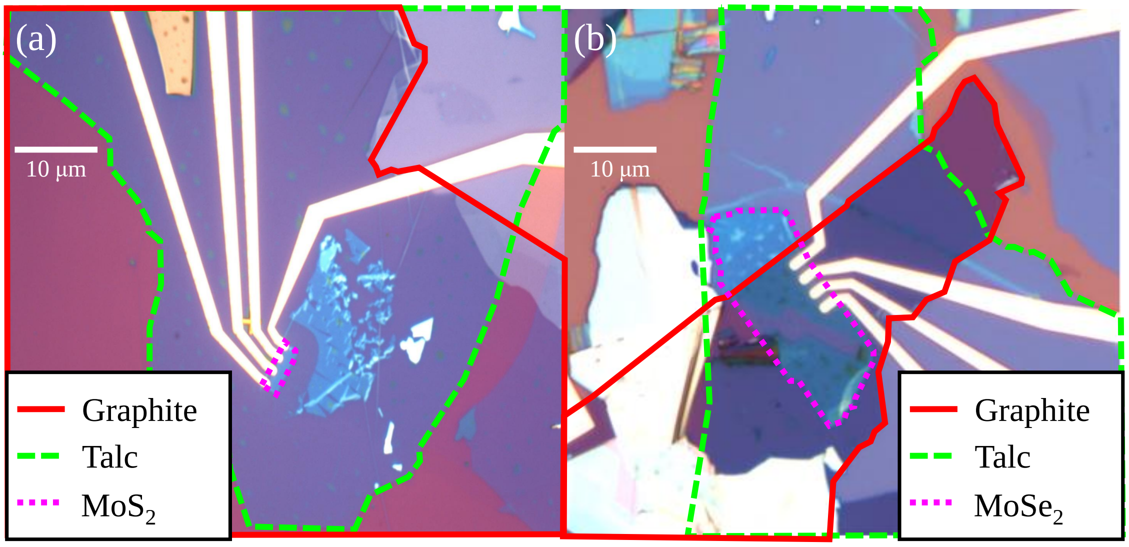

Figure 5.41: *Optical micrographs of two representative talc-based FETs using (a) MoS_2 and (b) $MoSe_2$ as the channel materials. The graphite, talc and TMDC layers are highlighted in red, green and pink, respectively. The scale bars (white) in each represent 10* µm*.*

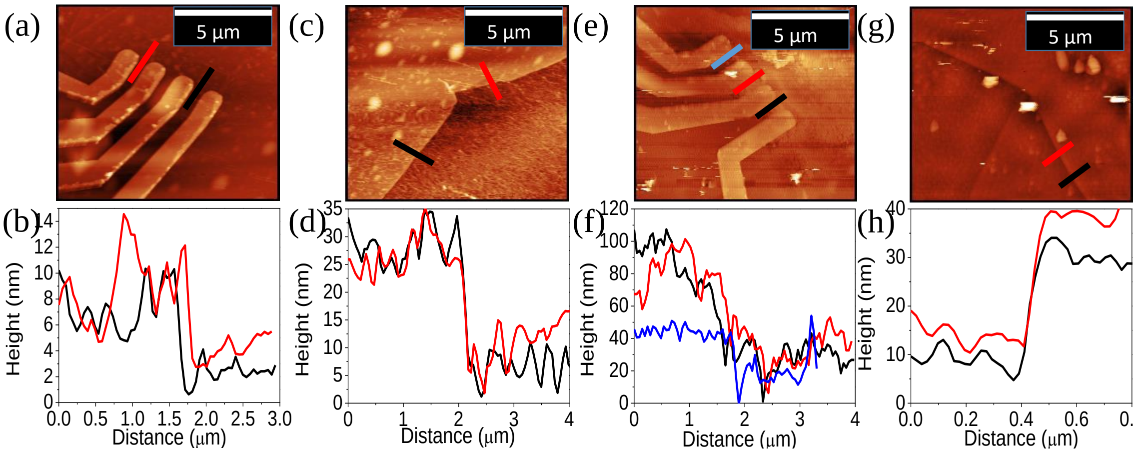

Figure 5.42: *AFM topographic images of TMDC/talc/graphite FET heterostructures. (a, b) and (c, d) are the AFM images and line profiles of the MoS_2 channel material and talc dielectric within the MoS_2/talc FET, respectively. (e, f) and (g, h) are the AFM images and line profiles of the $MoSe_2$ channel material and talc dielectric within the $MoSe_2$/talc FET, respectively.*

In order to understand the following FET electrical transport measurements, it is necessary to measure the physical dimensions of the individual layers of the heterostructure, in particular that of the talc dielectric as this is needed to calculate the field-effect mobility, µ, for each device type. AFM was used to determine the talc thicknesses, see Figure 5.42, which were measured for two devices, $d_{talc} = 18.4 \pm 1.9$ nm and 29.4 ± 3.3 nm in the MoS_2 and $MoSe_2$-based FETs, respectively, with an average roughness of $\xi_{talc} = 0.76 \pm 0.18$ nm, comparable to mono- and few-layer hBN [79]. The AFM images and line profiles presented within Figure 5.40 were computed using Gwyddion analysis software [292]. In addition to this, AFM was also used in conjunction with Raman microscopy to determine the thickness [231, 233] of the MoS_2 and $MoSe_2$ channels, which were measured using AFM to be 4.5 ±0.3 nm and 40.1 ±6.9 nm, respectively. The large uncertainty in the thickness of the $MoSe_2$ channel material is a result of inhomogeneous channel thickness across its length, as is shown by the blue line profile within Figure 5.42 (f). Raman spectroscopy of these channels are available within Figure 5.43.

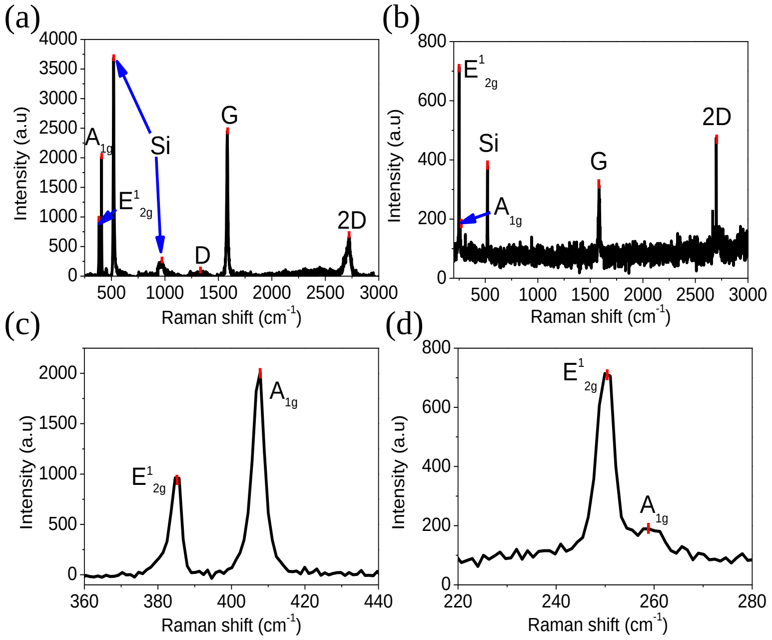

Figure 5.43: *Raman characterisation of TMDC/talc FET heterostructures. (a, b) Full Raman spectra of the MoS_2/talc and $MoSe_2$/talc FETs, respectively. (c) The same Raman spectrum as (a) between 360 cm^{-1} and 440 cm^{-1}, highlighting the characteristic Raman emission of MoS_2. (d) The same Raman spectrum as (b) between 220 cm^{-1} and 280 cm^{-1}, highlighting the characteristic Raman emission of $MoSe_2$.*

The Raman spectra indicate that both channels are present in the bulk, as was confirmed using AFM. The peaks at $\sim$ 520 cm^{-1} and $\sim$ 960 cm^{-1} correspond to the Si substrate, whilst those present at $\sim$ 1350 cm^{-1}, $\sim$ 1580 cm^{-1} and $\sim$ 2710 cm^{-1} are the D, G and 2D Raman mode emissions, respectively, from the underlying graphite contact layer. Only the intense Si peak at $\sim$ 520 cm^{-1} is present in the MoSe$_2$ spectra due to the thickness of the material obfuscating the underlying substrate, along with the noise present in the spectrum obscuring lower intensity peaks. This is also why the D peak of the underlying graphite is missing. .

Figure 5.44 (a, b, d, e) shows, for both channel materials, the typical I-V$_b$ sweeps taken at different values of back gate voltage, V$_g$, in each device, whilst (c, f) shows I-V$_g$ curves at a bias voltage of V$_b$ = 0.03 V. The MoS$_2$ and MoSe$_2$ FETs show unipolar and ambipolar behaviour, respectively, as is shown in (b, d). All data was recorded at room temperature.

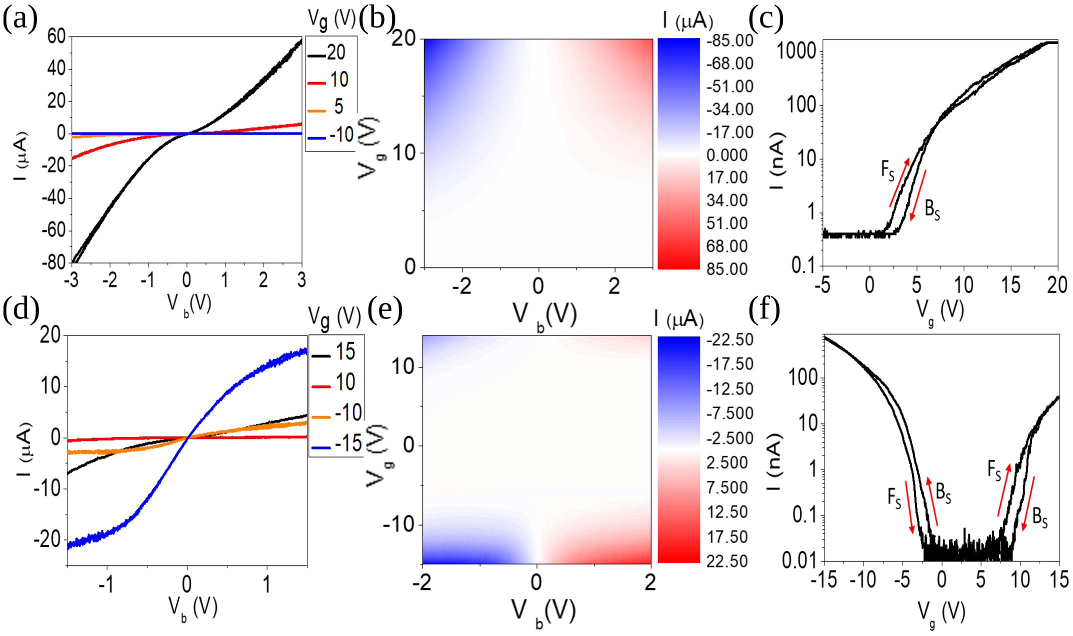

Figure 5.44: *(a, b, c) Electronic transport measurements on the MoS$_2$/talc FET. (d, e, f) Electronic transport measurements on the MoSe$_2$ device. (a, d) I-V$_b$ sweeps for select values of V$_g$, with complete contour plots shown in (b, e), highlighting ambipolar behaviour within the MoSe$_2$ channel. (c, f) Representative I-V$_g$ with V$_b$ = 0.03 V, where F$_s$ and B$_s$ represent the forwards and backwards sweep directions, respectively.*

Hysteresis can be seen within Figure 5.44 (c, f), likely the result of defects at the channel-dielectric interface charging as V$_g$ is swept [333] which then act as scattering centres for carriers within the channel material, altering the transport characteristics.

This is in turn a consequence of both surface adsorbates and natural impurities within the composition of our talc crystals (expected to be Fe and Al [334]) as the material was not artificially synthesised but rather taken from a mine in the Ouro Preto region of Brazil. The magnitude of the hysteresis width (the difference between forward and backward-sweep threshold voltages, ΔV_{th}) can be controlled by the back gate sweep rate, and shows a small increase above ~ 0.5 Vs^{-1} in both MoS_2 and $MoSe_2$ FETs. ΔV_{th} is approximately constant for both device types for sweep rates less than this, see Figure 5.45, and $\Delta V_{th,e} \sim 2$ V for electron conduction in both FET types and $\Delta V_{th,h} \sim 0.75$ V for hole conduction within the $MoSe_2$ FET for sweep rates > 0.5 Vs^{-1}.

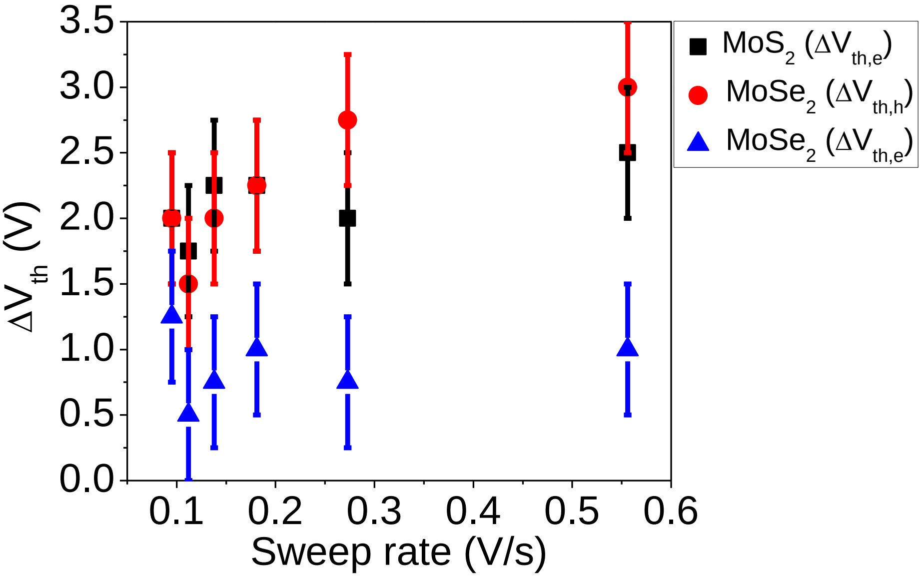

Figure 5.45: *The change in threshold voltage between forwards and backwards sweeps in* V_g*,* ΔV_{th}*, for electron conduction in the* MoS_2 *FET and both electron and hole conduction within the* $MoSe_2$ *FET as a function of* V_g *sweep rate.*

There is a wide range of hysteresis widths reported in the literature for both MoS_2 and $MoSe_2$ FETs utilizing either SiO_2 or hBN as a dielectric, a result of several factors such as the measurement conditions, dielectric material used and whether or not the devices were encapsulated [24, 29, 86, 335]. Table 5.5 presents the hysteresis widths of comparable devices within the literature and contrasts them to our talc-based devices. The lack of available data within the literature prevents a like-for-like comparison, and thus Table 5.5 serves only as an approximate guide into the performance of talc compared to other commonly used dieletrics.

Table 5.5: *Comparison of hysteresis widths for a number of* MoS_2 *and* $MoSe_2$*-based FETs using different dielectrics within the literature.*

FET architecture	**Key parameters: environment/ production/ encapsulation/ annealing/ sweep rate (Vs^{-1})**	**Hysteresis width (V)**	**Talc diminution factor ($\Delta V_{th,x}$/ $\Delta V_{th,talc}$)**	**Comments**
$MoS_2/SiO_2/Si$ [28]	Ambient/exfoliated/ none/none/0.5	15	6.67	
$MoS_2/SiO_2/Si$ [24]	Vacuum/exfoliated/ none/thermal/0.1	~ 0.5	~ 0.29	Annealed at 85 °C for 12 hours.
MoS_2/hBN/Si [24]	Vacuum/exfoliated/ none/thermal/0.1	~ 0.5	~ 0.29	Annealed at 85 °C for 12 hours.
hBN/MoS_2/ hBN/SiO_2/Si [86]	Ambient/exfoliated/ yes/none/2	~ 7.5	~ 4.3	ΔV_{th} increases for decreasing sweep rate [24, 28, 29, 86, 336], and so the talc diminution factor at comparable sweep rates to those presented within Figure 5.29 would be even higher
hBN/MoS_2/ SiO_2/Si [86]	Ambient/exfoliated/ yes/none/2	~ 22.5	~ 12.9	ΔV_{th} increases for decreasing sweep rate [24, 28, 29, 86, 336], and so the talc diminution factor at comparable sweep rates to those presented within Figure 5.29 would be even higher
$MoSe_2/SiO_2/Si$ [29]	Vacuum/exfoliated/ none/none/0.1	~ 1.5	~ 2	

All of these factors determine the concentration of adsorbates both on the surface of the channel material and at the channel dielectric interface [24, 287] which can become charged and introduce hysteretic effects into the measurements.

The MoS_2 FET is unipolar across -5 V $\leq V_g \leq$ 20 V with a forward sweep threshold voltage, $V_{th,f} \sim 3$ V at room temperature. At a bias voltage of $V_b = 0.03$ V, the MoS_2 FET had an on/off ratio of 4 x 10^3 for electron conduction at $V_g = 20$ V, an off-state current, $I_{off} < 100$ pA, a sub-threshold swing, SS = 1.60 ± 0.07 Vdec^{-1} and, using $\epsilon = 3$ as the permittivity of talc, an electron mobility of ~ 0.81 $\mathrm{cm}^2\mathrm{V}^{-1}\mathrm{s}^{-1}$. This electron mobility is less than reported for MoS_2/hBN and MoS_2/Al_2O_3 FETs [23, 25], and is comparable to MoS_2/SiO_2 FETs [25]. The low mobility is well known to be due to the presence of Schottky barriers at the interface between the TMDC channel and the Cr/Au contacts [182], see Section 2.5.3. These manifest as an increase in the contact resistance present at each electrode, although without four-terminal measurements it is impossible to unequivocally explain the reduced field effect mobility. The large value of sub-threshold swing is a result of the thickness of the talc dielectric used, because as the dielectric becomes thicker its ability to screen incident electric fields increases. Therefore, a greater bias potential is required to modulate the channel carrier density by a given amount for a thick dielectric than for a thin dielectric of the same material, which manifests as an increased sub-threshold swing for the FET.

The $MoSe_2$ FET shows typical ambipolar behaviour [337, 338] across -15 V $\leq V_g \leq$ 15 V with a forward sweep threshold voltage, $V_{th,f} \sim -2.5$ V (7 V) and a backwards sweep threshold voltage of $V_{th,b} \sim -0.5$ V (8 V) for hole (electron) conduction at room temperature. At a bias voltage of $V_b = 0.03$ V, the $MoSe_2$ FET had an on/off current ratio of 1 x 10^5 (5 x 10^3) for hole (electron) conduction at $V_g = -15$ V (15 V), an off state current $I_{off} < 10$ pA, sub-threshold swing SS = 1.39 ± 0.12 Vdec^{-1} (1.17 ± 0.15 Vdec^{-1}) and, with $\epsilon = 3$, a carrier mobility of ~ 5.1 $\mathrm{cm}^2\mathrm{V}^{-1}\mathrm{s}^{-1}$ (~ 3.3 $\mathrm{cm}^2\mathrm{V}^{-1}\mathrm{s}^{-1}$). Similar to the MoS_2 FET, the carrier mobilities in this device are lower than those reported for $MoSe_2$/hBN and even $MoSe_2/SiO_2$-based FETs [339].

In both devices the SS was calculated using

$$SS = \left(\frac{d\left(log_{10}\left(I\right)\right)}{dV_g}\right)^{-1} \tag{5.10}$$

by taking data from the linear region of the $log_{10}\left(I\right)$-V$_g$ curves. Similarly, the field-effect mobility, μ_{FE}, is given by

$$\mu_{FE} = \frac{dI}{dV_g}\frac{L}{WC_iV_b}, \tag{5.11}$$

where L and W are then channel lengths and widths, respectively, C_i is the area-normalised capacitance of the particular talc crystal within a device and V_b is the applied bias voltage.

The ability of talc to act as a barrier material between the channel and back gate was also investigated. The barrier material must be sufficient to prevent leakage current between these two elements so that the channel can be effectively modulated by the back gate. Therefore, the current moving between the channel and graphite electrode was measured for various back gate sweep rates and magnitudes, see Figure 5.46.

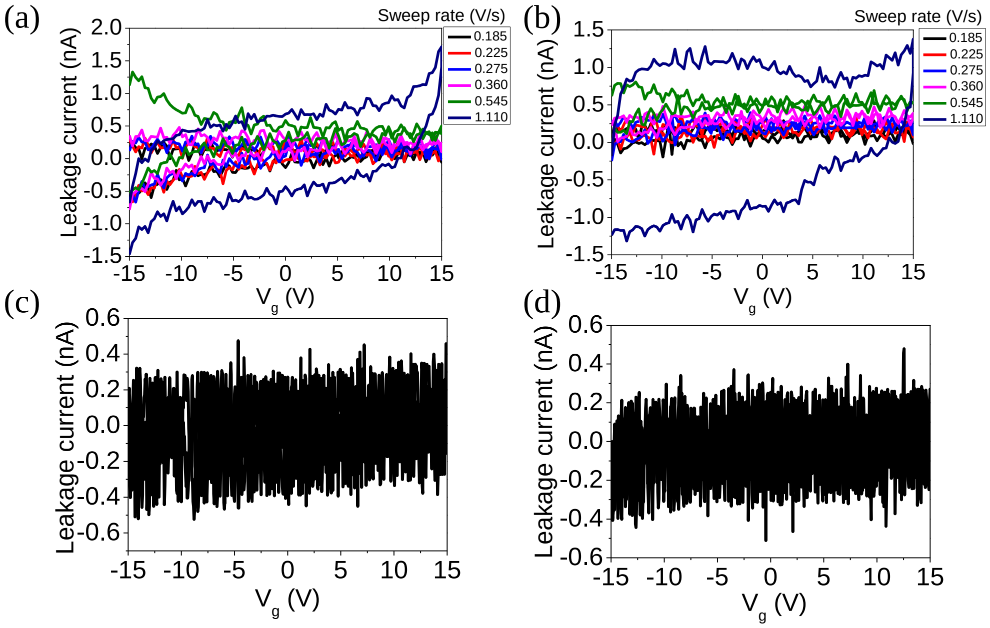

Figure 5.46: *Data presented in (a, c) and (b, d) were collected from the* MoS_2 *and* $MoSe_2$ *FETs, respectively. (a, b) Gate leakage current vs* V_g *at various back gate sweep rates. (c, d) Representative leakage current vs* V_g *during electrical measurements, where the sweep rate was* $\ll 0.1\ Vs^{-1}$.

Figure 5.46 (a, b) shows hysteretic behaviour within the leakage current for sufficient back gate sweep rates (> 0.5 Vs^{-1}), while (c, d) illustrates typical leakage current values which would be present during device characterisation measurements. Additional electrical characterisation of these FET devices were completed at various temperatures ranging from $\sim$ 300 K - 4 K, as is shown within Figure 5.47.

Figure 5.47 (a, b) shows the current moving through the FET channel as a function of V$_g$ for a range of temperatures, with $V_{sd} = 30$ mV. Freeze-out of the charge carriers can clearly be seen in both devices by the reduction in current magnitude and the drift of the activation voltages, as is also illustrated within (c, d).

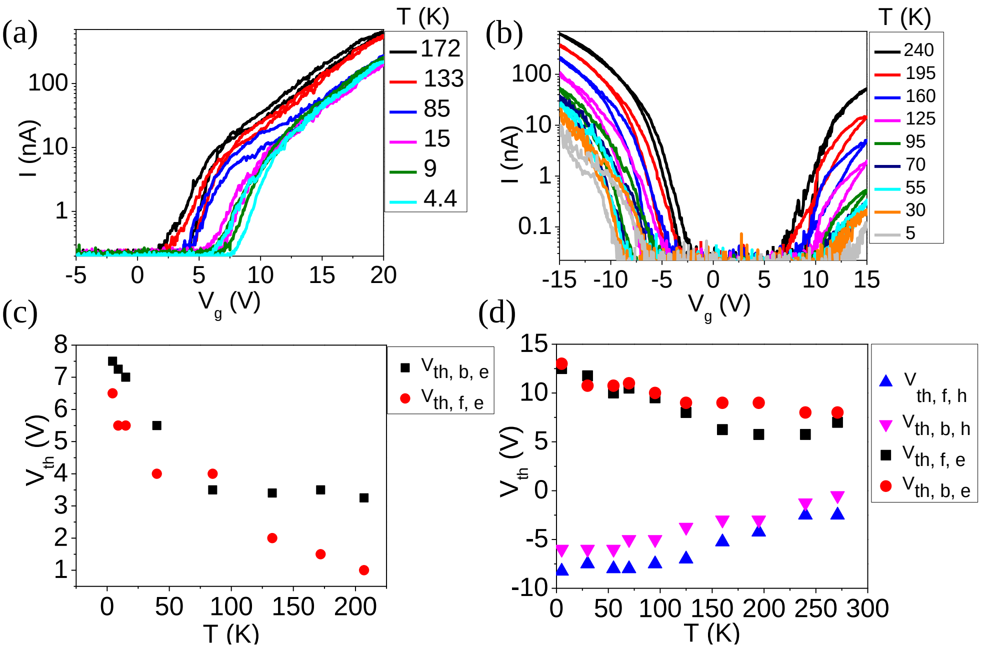

Figure 5.47: *Data presented in (a, c) and (b, d) were collected from the* MoS_2 *and* $MoSe_2$ *FETs, respectively. (a, b) I-*V_g *curves for the two device types at various temperatures. (c, d) Temperature dependance of the threshold voltage where* $V_{th,f,e}$ $(V_{th,b,e})$ *and* $V_{th,f,h}$ $(V_{th,b,h})$ *are the threshold voltages corresponding to electron and hole conduction during the forwards (backwards) sweeps of the gate voltage, respectively.*

5.2.2 Photoluminescence

Attention is now placed on the optical performance of TMDCs placed on talc dielectrics. Similar to the talc used within the FETs, these have an average roughness of $\xi_{talc} = 0.65 \pm 0.16$ nm, comparable to mono- and few-layer hBN [79]. Monolayer TMDC thickness was required in order to enhance the photoluminescence quantum yield as discussed in Section 3.2.4. The fabrication procedure for these devices is much the same as before, beginning with mechanical exfoliation from bulk crystals onto a SiO_2/Si substrate followed by optical identification and subsequent dry-stacking into heterostructures. Monolayer WS_2 was initially investigated due to it having increased chemical stability compared to other TMDCs as it was unknown how the talc substrate might affect the PL properties [310].

WS_2 photoluminescence: Figure 5.46 (a) shows an optical micrograph of the monolayer WS_2/talc heterostructure investigated within this study. Figure 5.46 (b) shows a typical PL spectrum of a WS_2 monolayer at room temperature, whilst (c) shows PL spectra taken at 4 K for various laser power excitations.

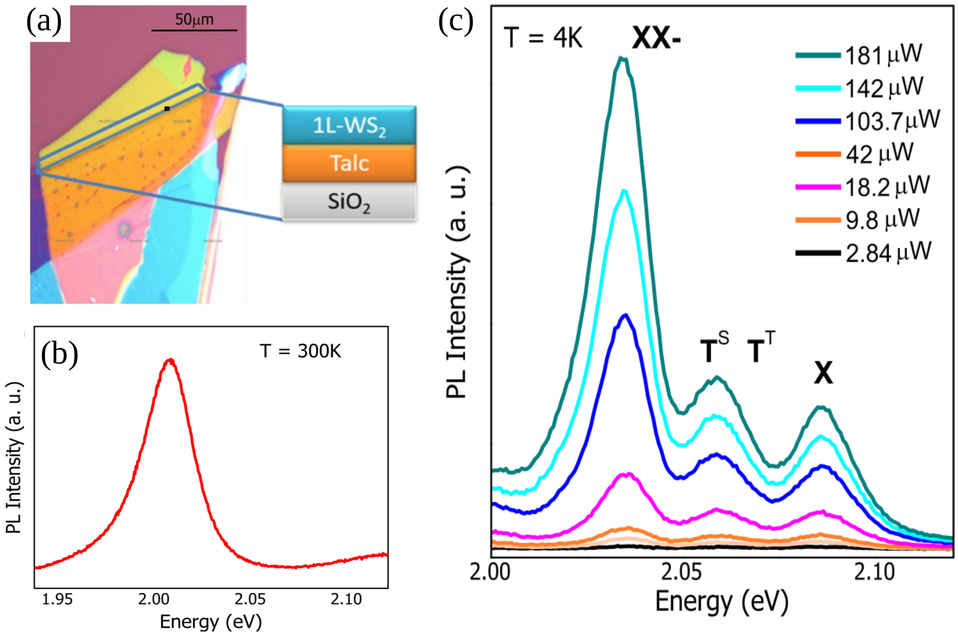

Figure 5.48: *(a) Optical micrograph of a monolayer (1L) WS_2/talc heterostructure. (b) Typical PL spectrum of a WS_2 monolayer on talc at 300 K. (c) PL spectra at 4 K for different incident laser powers. Data collected by collaborators, G. Prando and Y. Galvão.*

In (b), a PL peak is observed at 2.008 eV. This is blue-shifted from the value of $\sim$ 1.84 eV given in Table 3.2, which is often seen in monolayers which have been transferred from one substrate to another due to a reduction in the magnitude of strain acting on the lattice [340], with similar PL spectra to ours being observed for monolayer WS_2 on other analogous dielectrics such as hBN [341]. Furthermore, this room-temperature emission has a FWHM of $\sim$ 30 meV, approximately $\sim$ 5 meV less than comparable samples on SiO_2/Si substrates [340]. This is reduced further as the sample is cooled, with the typical FWHM of the neutral exciton emission peak reaching as low as $\sim$ 10 meV. This could be reduced further by using standard thermal annealing techniques already used in TMDC/hBN stacks [342]. The observed small FWHM and strong PL intensity suggests that talc can serve as an effective material for isolating TMDC monolayers from SiO_2 and consequently preserve the intrinsic properties of the TMDC.

Both the neutral exciton (X) and charged trion (T^T, T^S) emission peaks are observed within Figure 5.46 (c) at 2.086 eV and 2.056 eV, respectively. Moreover, it can be seen that the trion peak presents a clear asymmetry which is associated with unresolved PL emission from different trion states (see Figure 3.13 and Section 3.2.1). Therefore, the trion peak was deconvolved into two separate peaks, one at 2.053 eV and the other at 2.060 eV which are associated to singlet (T^S) and triplet (T^T) states formed via the Coloumb exchange interaction [341]. As with the neutral exciton emission, the charged trion peaks are also blue shifted relative to that found in comparable works within the literature [341], although unlike the former this is likely due to the effect of having talc as a substrate, whereas comparable works utilise hBN. In addition to these, another strong PL peak at 2.034 eV was observed, which, by measuring the energy shift with incident laser power (Figure 5.46 (c)), was determined to be due to emission from biexcitons (XX^-) [343, 344], which is a four-particle state composed of a pair of excitons, via the superlinear relationship between incident laser power and peak position [341, 343], see Figure 5.47. In order to further analyse these peaks, the PL spectra were fitted with Voigt functions. This was necessary as each peak undergoes homogeneous (e.g. due to finite lifetimes of occupied excited states) and inhomogeneous (e.g. due to local defects) broadening, which produce Lorentzian and Gaussian profiles, respectively. A Voigt function is a convolution between these two functions, and so is ideal for fitting PL emissions such as these. Figure 5.47 shows the PL intensity, I, of each peak as a function of incident laser power, P. This dependancy can be expressed as $I \propto P^{\alpha}$, yielding $\alpha = 1$ for the neutral exciton emission, $\alpha = 1.19$ and $\alpha = 1.02$ for the T^T and T^S states, respectively, and $\alpha = 1.30$ for the biexciton emission, as is shown within Figure 5.47. As the the neutral and biexcitons are known to exhibit a linear and superlinear relationship to incident laser power [341, 343], respectively, fitting the peaks in this manner allows the various peaks within the PL spectra to be identified. With these values in mind, the observed laser power dependencies for all emission peaks are consistent to previous interpretations of the PL spectra measured from WS_2 monolayers reported in the literature which use hBN as an isolating substrate

[341, 343, 344]. The identity of the charged trion peaks are further confirmed by their relative increase in intensity to the neutral exciton emission as a function of increasing laser power, see Figure 5.46 (c). This is because a higher incident laser power results in an increased amount of laser-induced doping present within the TMDC [344], in turn encouraging the formation of charged trions via combination of a neutral exciton with an excited charge carrier.

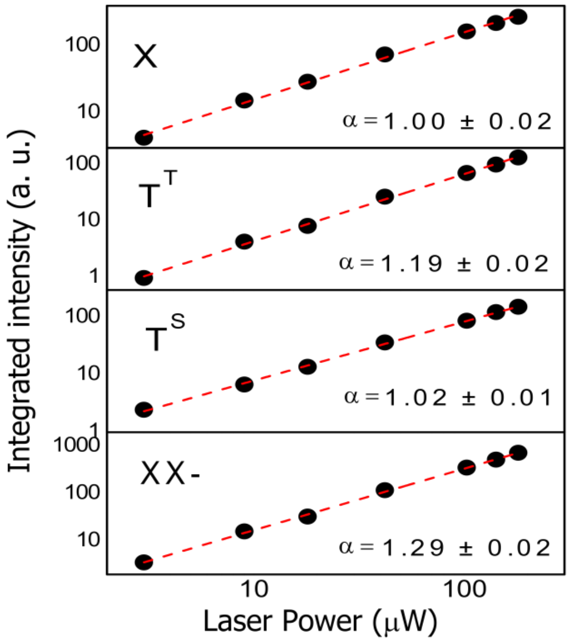

Figure 5.49: *Double logarithmic representation of integrated PL intensity as a function of laser power. Data collected by collaborators, G. Prando and Y. Galvão.*

MoS_2 and $MoSe_2$ photoluminescence: Figure 5.48 shows optical micrographs of two more talc-based photoluminescent devices with MoS_2 and $MoSe_2$ active layers. Unlike the previous WS_2-based device, these have an underlying layer of graphene to facilitate the application of a back gate voltage and thus allow for investigation into the formation of trions within these materials.

These were fabricated with the same procedure as used for the WS_2 device, detailed within Section 4.3, although additional gold pins were necessary (see Figure 5.48) in order to pin the heterostructure to the substrate during the lift-off step. PL spectra were recorded using the set up described previously, with the application of a back gate voltage provided by a Keithley 2400 sourcemeter. This data is presented within Figure 5.49.

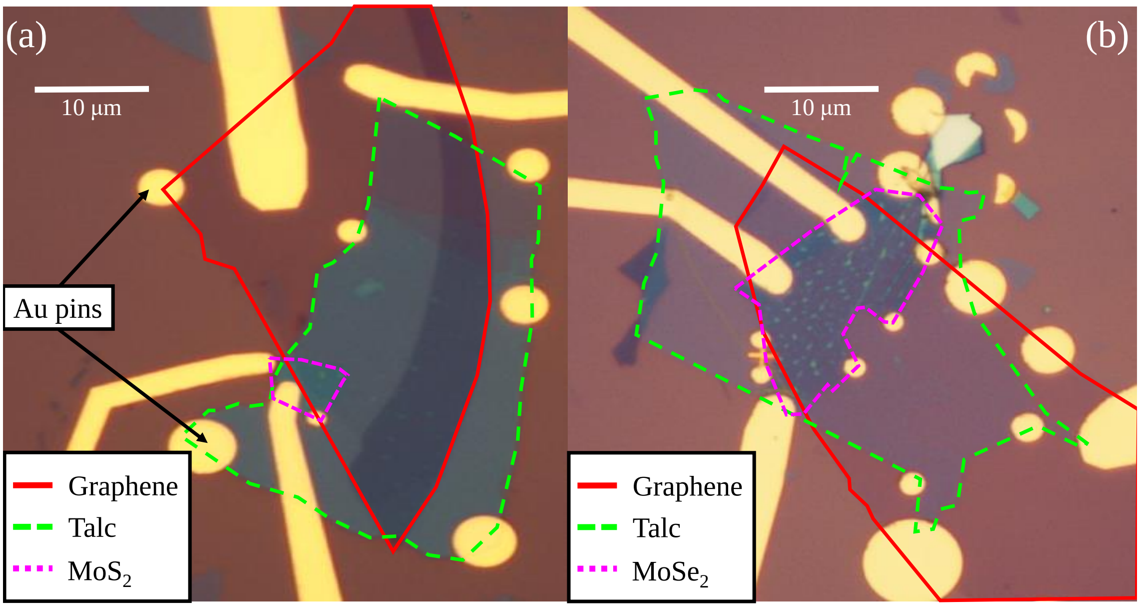

Figure 5.50: *Optical micrographs of two talc-based PL devices using (a) MoS_2 and (b) $MoSe_2$ as the active materials. The graphene, talc and TMDC layers are highlighted in red, green and pink, respectively. The scale bars (white) in each represent 10* µm.

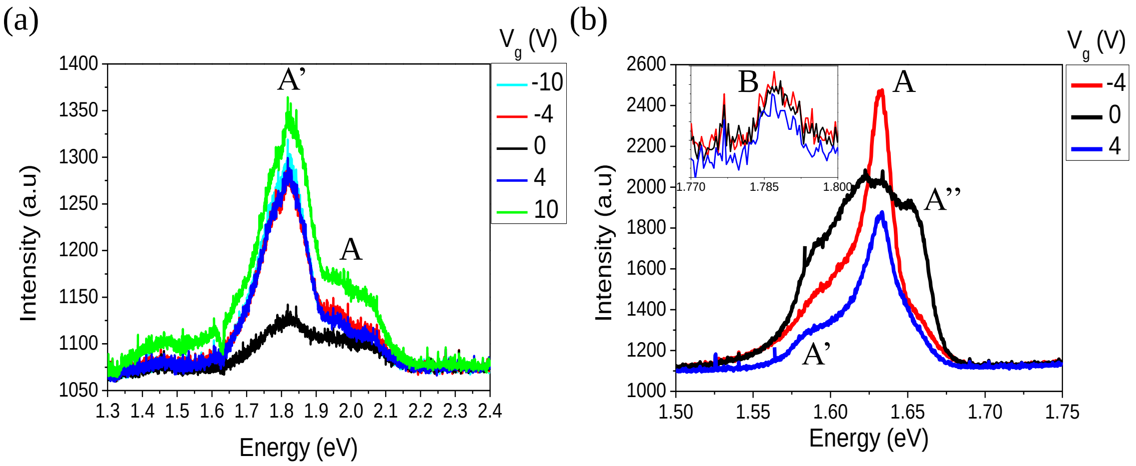

Figure 5.51: *PL spectra of monolayer (a) MoS_2 and (b) $MoSe_2$ on talc under application of a back gate voltage, V_g. Inset: zoom-in of data highlighting the presence of B-exciton emission. Measurements taken at 300 K.*

As can be seen, both materials exhibit a single prominent peak along with adjacent shoulder peaks. In order to identify the physical processes associated with the formation of each, an external back gate potential was applied to the MoS_2 and $MoSe_2$ active layers between -10 V $\leq V_g \leq$ 10 V and -4 V $\leq V_g \leq$ 4 V, respectively.

The smaller range of V_g applied to the $MoSe_2$ was chosen in order to prevent dielectric breakdown of the thinner talc used within this device.

In bulk TMDC materials, trions typically have a lower binding energy than their neutral exciton counterparts as a result of their greater orbital radius leading to increased dielectric screening from the surrounding medium [345]. Therefore it would seem that the low-energy shoulders within the PL spectra of MoS_2 and $MoSe_2$ are the result of trion recombination whilst the remaining peak corresponds to neutral exciton recombination (from either A- or B-excitons, which will be determined later). As discussed in Section 3.2.1, excitons within 2D materials behave very differently, with excitons of larger orbital radius showing an increase in binding energy due to a reduction in dielectric screening associated with the 2D nature of the crystal [193, 345]. This is also true of trions within these materials, and so the low energy shoulders are still attributed to trion emission at first glance [346, 347].

In order to confirm this, PL spectra were recorded throughout the applied back gate range and then deconvoluted to gain information on the individual features. Details of the deconvolution process are given in the Appendix. Application of V_g in this manner will lead to an increased dopant concentration throughout the TMDC active layers which in turn facilitates the formation of trions. Therefore, by increasing V_g, the trion formation rate (and subsequent recombination rate) will increase accordingly, enhancing the intensity of the corresponding peak within the PL spectra and allow for its identification. Figure 5.50 (a, b) shows the ratio of peak intensities as a function of V_g.

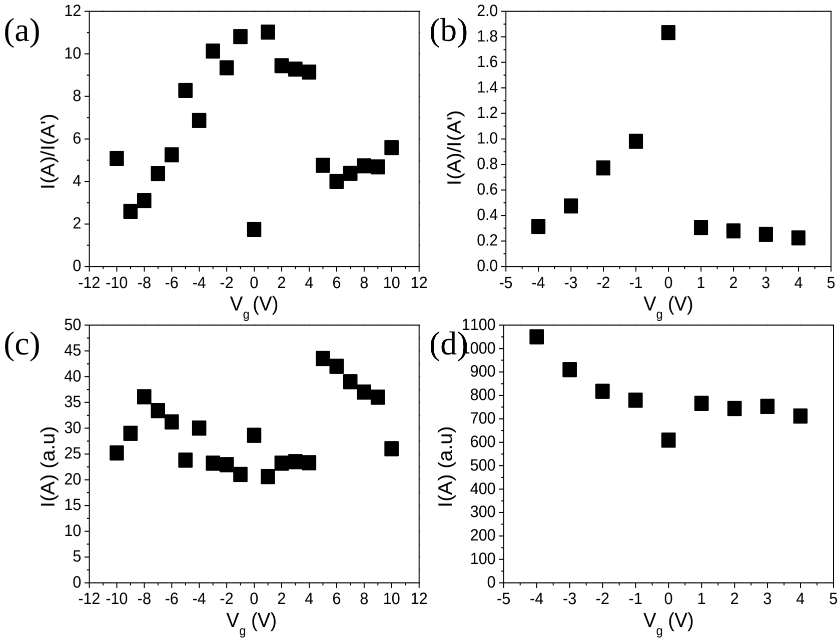

Figure 5.52: *(a, b) Ratio of PL peak intensities for* MoS_2 *and* $MoSe_2$*, respectively, as a function of* V_g*. (c, d) Intensity of the A-peak as a function of* V_g *for* MoS_2 *and* $MoSe_2$*, respectively.*

Barring the anomalous point for $V_g = 0$ V in Figure 5.50 (a), both devices show a clear inverse proportionality in the peak intensity ratio as a function of V_g, indicating that the intensity of the peak used within the denominator increases with increasing V_g. In both devices, this peak is labelled A' within Figure 5.49 and, as both lie at lower energies than the remaining features, likely correspond to trion recombination within the devices. The identity of this peak can be further confirmed by plotting the intensity of the other feature, labelled A in Figure 5.49, as a function of V_g as is shown within Figure 5.50 (c, d). As can be seen, the A-peak intensity shows little variation with V_g and thus indicates that it does not originate from trion recombination.

The PL spectra of $MoSe_2$ presents an additional feature, labelled A" within Figure 5.49 (b), whose behaviour shows no clear correlation with increasing back gate potential. The cause of this is unknown and would require further study to elucidate, although it is likely due to significant disorder within this device. Both MoS_2 and $MoSe_2$ devices lack encapsulation and thus a significant amount of doping by adsorbants should be expected, and is observed here through the low I(A)/I(A') ratios even in the absence of an applied back gate potential which in turn indicates a high initial doping concentration. This is most prevelant in the $MoSe_2$ device and so a high dopant concentration may explain the anomalous feature. Additional sources may include other factors such as strain, damage to the TMDC crystal lattice during device manufacture or PL emission from adsorbants. In fact, a clear difference in the quality of the interfaces of the two devices can be seen by examination of Figure 5.48, with the $MoSe_2$-based device having a high density of bubbles, likely filled with hydrocarbons, present across the $MoSe_2$/talc interface. It could be this additional material, or the strain that this induces within the $MoSe_2$ lattice, which produces the A" feature within the $MoSe_2$ PL spectra.

Following identification of the peaks within the PL spectra, a comparison of their positions to devices within the literature utlising alternate dielectrics can be completed. The positions of these peaks are given in Table 5.6.

Table 5.6: *Peak positions within the PL spectra of MoS_2 and $MoSe_2$ on talc.*

Material	**A (eV)**	**± (eV)**	**A' (eV)**	**± (eV)**	**A" (eV)**	**± (eV)**
MoS_2	2.026	0.003	1.812	0.019	N/A	N/A
$MoSe_2$	1.631	0.002	1.599	0.005	1.659	0.005

The peak position of the A-exciton emission of the MoS_2 and $MoSe_2$ are blue-shifted by approximately 0.1 eV and 0.08 eV [264, 348], respectively, when using talc substrates compared to when using SiO_2/Si substrates. Likewise, the MoS_2 and $MoSe_2$ A-peak positions are blue-shifted by approximately 0.07 eV and 0.06 eV [346, 347], respectively, compared to devices using hBN substrates.

Photoluminescent spectra of both MoS_2 and $MoSe_2$ are known to exhibit secondary peaks due to B-exciton emission (see Section 3.2.4) which are usually $\sim$ 0.1-0.15 eV [252] and $\sim$ 0.15-0.2 eV higher in energy than the materials corresponding A-peak positions [252, 348], respectively, due to originating in the lower split valence band at the K-point of the Brillouin zone. The peak corresponding to B-exciton emission should therefore be present at higher energies than this, although no feature could be found within the data for the MoS_2-based device. The absence of a B-peak often occurs within the literature and an explanation for this is given within Section 3.2.4. For $MoSe_2$ on talc, a small feature is observed which is centered at $\sim$ 1.79 eV, 0.16

eV higher in energy than the A-exciton emission, and is therefore identified as being due to B-exciton emission (see Figure 5.49 (b) inset).

The dependancy of the FWHM of the PL peaks as a function of the back gate potential was also investigated, as is shown within Figure 5.51.

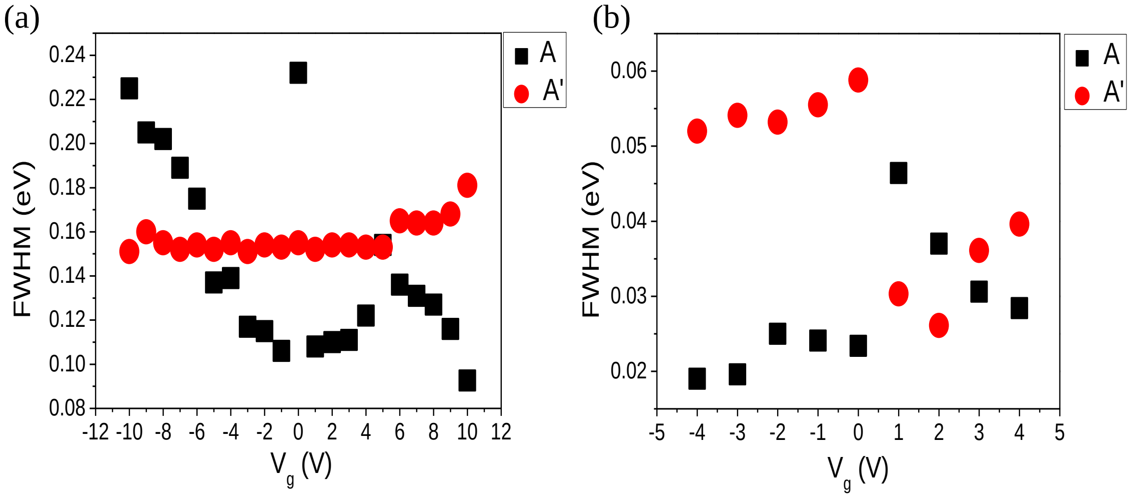

Figure 5.53: *(a, b) FWHM of the A and A-peaks within the PL spectra of* MoS_2 *and* $MoSe_2$*, respectively.*

Once again barring the anomalous data point at $V_g = 0$ within Figure 5.51 (a), the MoS_2 A-peak FWHM shows a weak correlation with the applied back gate potential, whilst the same peak within the $MoSe_2$ spectrum does not. The A'-peaks of both PL spectra do not seem to depend upon V_g. As the A'-peaks within the spectra of both TMDCs arise from trion recombination, one would assume that they would exhibit similar responses to external stimuli. The lack of this once again indicates that an external differing factor between the two devices, as opposed to a difference in fundamental physics, is obscuring the inherent PL behaviour of the devices. Despite this, the FWHM of both peaks within the individual PL spectra are clearly separated into two groups – with those belonging to MoS_2 having FWHM in the range of ~90-250 meV, whilst the $MoSe_2$ peaks have FWHM of ~20-60 meV. These values of FWHM for MoS_2 are significantly larger than for comparable devices using both SiO_2/Si [264] and hBN [349] substrates. This is likely due to both a lack of talc encapsulation as well as interfacial contamination, both of which introduce charge scattering centres and thus reduce the excitonic lifetimes. It is expected that these two factors could be mitigated via the use of encapsulation and thermal annealing, respectively. Surprisingly, despite the disorder apparent within the PL spectra of the $MoSe_2$-based device, it yields low FWHM values less than those found in comparable devices using SiO_2/Si substrates by ~ 60 meV [348], but still greater than is found in devices using hBN substrates [347]. The variation in the FWHM of these spectral features when compared to devices within the literature suggest that, with further optimisation of production techniques, talc substrates have the potential to greatly outperform conventional SiO_2/Si substrates, and potentially compete with hBN, with regards to preserving the intrinsic PL properties of TMDC monolayers.

6. Conclusions

The results presented within this thesis demonstrate a novel approach to the production of scalable vdW heterostructures utilising graphite, TMDC and hBN bulk powders as the source material. An abrasion-based procedure was developed to allow for the creation of sharp interfaces between layers as well as the deposition of abraded graphite top electrodes via a PMGI sacrificial layer. Since the first isolation of graphene and its analogues there has been significant research into production methods which allowed for the creation of scalable, multilayered devices. These have included CVD growth, which allowed for atomic layer thicknesses within the heterostructure and could be scaled over many square centimetres, but are typically limited in terms of electronic performance due to the presence of domain boundaries, and LPE, which produces robust and scalable heterostructure devices at the cost of leaving monolayer thicknesses, and the associated phenomena, behind, in addition to generally having sub-par electronic performance. The abrasive method represents the next step in the evolution of the latter, as it offers a means to produce robust, scalable heterostructures whilst maintaining electrical performance comparable to many LPE/exfoliated and strictly exfoliated devices.

This was demonstrated through the creation of a plethora of device types including photovoltaics, TENGs, strain sensors, capacitive pressure sensors and thermistors, all through the use of abraded vdW powders. To summarise: abraded photovoltaic devices displayed responsivities far exceeding comparable LPE devices; the TENG devices had a power output comparable to equivalent LPE devices, although, given the wide variety of 2D material combinations, it should be expected that further work could easily be completed to optimise the architecture and improve performance beyond this; abraded strain sensors proved to be extremely robust, showing a consistent response to external strain over thousands of cycles without the need for prior substrate treatment, and offered additional sensitivity to compressive strain compared to tensile strain; the capacitive pressure sensors offered sensitivities far greater than the threshold needed to detect a human heart beat, opening avenues for the creation of future wearable, flexible and robust heart rate monitors; and finally the abraded thermistors were able to easily detect external changes in temperature, and may allow for the creation of flexible and robust thermometers, although they displayed temperature coefficients roughly an order of magnitude lower than other composite-film devices within the literature.

Overall, abraded films and devices offer superior performance to LPE whilst maintaining robustness and scalability, all while using a simple and easy production technique. In fact, the abrasive method is simple enough to be almost entirely automated, as was done to produce the capacitive pressure sensors and thermistors, requiring only the bare minimum of human interference. This not only increases repeatability for future experiments by removing human error and providing an accurate control over the dimensions of the abraded film (through knowledge of applied pressure, drill bit RPM, feed rate and the number of passes), but would also allow for the creation of devices using exotic and volatile materials, as the entire procedure could be completed in a clean and inert environment whilst controlled from afar. Moreover, abrasive deposition of the investigated materials is compatible with a large number of substrates including (but not limited to) SiO_2, PET, PTFE, PMGI, PDMS, polyethylene napthalate, polyurethane, Al, steel and paper, further extending the possibilities for future device design.

In addition to this, investigation into the use of mechanically exfoliated talc as a dielectric barrier material within TMDC-channel FETs was completed. This was to explore the entire dielectric parameter space in the hopes of yielding improved FET performance, as heavy attention is already given to optimisation of channel materials in exfoliated FET heterostructures. Despite the lack of encapsulation within the talc-based devices they offer comparable hysteresis widths to devices using hBN as a dielectric. As hBN is already well established as a near-ideal barrier material due to having an atomically flat surface and providing a clean interface, this would suggest that future devices utilising talc could be optimised to one day outperform hBN - at least in terms of interfacial cleanliness. Furthermore, the magnitude of the leakage current was consistently < 0.5 nA throughout the back gate potential range applied, showing that talc of sufficient thickness is suitable as a barrier material due to its high dielectric constant. However, both talc-based architectures displayed significantly reduced field-effect mobilities and thus a severe reduction in electronic performance, such as having increased sub-threshold swings and reduced current on/off ratios when compared to hBN-based FETs within the literature, although these may stem from the aforementioned lack of encapsulation and the resultant presence of impurities on the surface of the channel material. Therefore, future devices utilising encapsulated channel materials along with a reduction in dielectric thickness (preferably down to mono- or few-layer) would be needed in order to thoroughly compare talc to other established materials such as hBN, Al_2O_3 and SiO_2.

Finally, the photoluminescent properties of TMDCs using talc as a substrate was investigated. The high intensity of the PL peaks within the emission spectra of these devices, along with having a narrow FWHM, suggests that talc can be used as an isolating substrate to preserve the intrinsic PL properties of monolayer TMDC materials in the same manner as hBN. This is also evidenced by the formation of biexcitons within our WS_2/talc heterostructure, typically only seen in clean and/or hBN-encapsulated systems. This was achieved without encapsulation by either talc or hBN, and so it should be expected that doing so within future experiments would yield PL behaviour even closer to that of the intrinsic TMDC. Furthermore, the spontaneous doping properties of talc when used as a substrate allowed for room-temperature observation of trion emission in all of the PL devices measured, opening up new avenues of research into high carrier density optoelectronics without the need for the application of a back gate potential.

Bibliography

[1] Philip Richard Wallace. The band theory of graphite. *Physical review*, 71(9):622, 1947.

[2] Kostya S Novoselov, Andre K Geim, Sergei V Morozov, De-eng Jiang, Yanshui Zhang, Sergey V Dubonos, Irina V Grigorieva, and Alexandr A Firsov. Electric field effect in atomically thin carbon films. *Science*, 306(5696):666–669, 2004.

[3] Chul Chung, Young-Kwan Kim, Dolly Shin, Soo-Ryoon Ryoo, Byung Hee Hong, and Dal-Hee Min. Biomedical applications of graphene and graphene oxide. *Accounts of Chemical Research*, 46(10):2211–2224, 2013.

[4] François Perreault, Andreia Fonseca De Faria, and Menachem Elimelech. Environmental applications of graphene-based nanomaterials. *Chemical Society Reviews*, 44(16):5861–5896, 2015.

[5] Andrea Splendiani, Liang Sun, Yuanbo Zhang, Tianshu Li, Jonghwan Kim, Chi-Yung Chim, Giulia Galli, and Feng Wang. Emerging photoluminescence in monolayer MoS_2. *Nano Letters*, 10(4):1271–1275, 2010.

[6] Roman V Gorbachev, Ibtsam Riaz, Rahul R Nair, Rashid Jalil, Liam Britnell, Branson D Belle, Ernie W Hill, Kostya S Novoselov, Kenji Watanabe, Takashi Taniguchi, et al. Hunting for monolayer boron nitride: optical and Raman signatures. *Small*, 7(4):465–468, 2011.

[7] Han Liu, Adam T Neal, Zhen Zhu, Zhe Luo, Xianfan Xu, David Tománek, and Peide D Ye. Phosphorene: an unexplored 2D semiconductor with a high hole mobility. *ACS Nano*, 8(4):4033–4041, 2014.

[8] Boubekeur Lalmi, Hamid Oughaddou, Hanna Enriquez, Abdelkader Kara, Sébastien Vizzini, Bénidicte Ealet, and Bernard Aufray. Epitaxial growth of a silicene sheet. *Applied Physics Letters*, 97(22):223109, 2010.

[9] ME Dávila, Lede Xian, Seymur Cahangirov, Angel Rubio, and Guy Le Lay. Germanene: a novel two-dimensional germanium allotrope akin to graphene and silicene. *New Journal of Physics*, 16(9):095002, 2014.

[10] Ananias B Alencar, Ana Paula M Barboza, Bráulio S Archanjo, Helio Chacham, and Bernardo RA Neves. Experimental and theoretical investigations of monolayer and few-layer talc. *2D Materials*, 2(1):015004, 2015.

[11] Can Ataca, Hasan Sahin, and Salim Ciraci. Stable, single-layer MX_2 transition-metal oxides and dichalcogenides in a honeycomb-like structure. *The Journal of Physical Chemistry C*, 116(16):8983–8999, 2012.

[12] Andres Castellanos-Gomez, Michele Buscema, Rianda Molenaar, Vibhor Singh, Laurens Janssen, Herre SJ Van Der Zant, and Gary A Steele. Deterministic transfer of two-dimensional materials by all-dry viscoelastic stamping. *2D Materials*, 1(1):011002, 2014.

[13] Andre K Geim and Irina V Grigorieva. Van der Waals heterostructures. *Nature*, 499(7459):419–425, 2013.

[14] Konstantin Novoselov, Artem Mishchenko, Alexandra Carvalho, and Antonio H. Castro Neto. 2D materials and van der Waals heterostructures. *Science*, 353(6298), 2016.

[15] Leitao Liu, S Bala Kumar, Yijian Ouyang, and Jing Guo. Performance limits of monolayer transition metal dichalcogenide transistors. *IEEE Transactions on Electron Devices*, 58(9):3042–3047, 2011.

[16] Yury Yu Illarionov, Kirby KH Smithe, Michael Waltl, Theresia Knobloch, Eric Pop, and Tibor Grasser. Improved hysteresis and reliability of MoS_2 transistors with high-quality CVD growth and Al_2O_3 encapsulation. *IEEE Electron Device Letters*, 38(12):1763–1766, 2017.

[17] Yu Yu Illarionov, Kirby KH Smithe, Michael Waltl, RW Grady, S Deshmukh, Eric Pop, and Tibor Grasser. Annealing and Encapsulation of CVD-MoS_2 FETs with 10^{10} On/Off Current Ratio. In *2018 76th Device Research Conference (DRC)*, pages 1–2. IEEE, 2018.

[18] Prateek Kumar, Maneesha Gupta, and Kunwar Singh. Performance evaluation of transition metal dichalcogenides based steep subthreshold slope tunnel field effect transistor. *Silicon*, pages 1–8, 2019.

[19] Bin Peng, Wei Zheng, Jiantao Qin, and Wanli Zhang. Two-dimensional MX_2 semiconductors for sub-5 nm junctionless field effect transistors. *Materials*, 11(3):430, 2018.

[20] Pavel Bolshakov, Peng Zhao, Angelica Azcatl, Paul K Hurley, Robert M Wallace, and Chadwin D Young. Improvement in top-gate MoS_2 transistor performance due to high quality backside Al_2O_3 layer. *Applied Physics Letters*, 111(3):032110, 2017.

[21] Youngki Yoon, Kartik Ganapathi, and Sayeef Salahuddin. How good can monolayer MoS_2 transistors be? *Nano letters*, 11(9):3768–3773, 2011.

[22] Zhihao Yu, Zhun-Yong Ong, Songlin Li, Jian-Bin Xu, Gang Zhang, Yong-Wei Zhang, Yi Shi, and Xinran Wang. Analyzing the Carrier Mobility in Transition-Metal Dichalcogenide MoS_2 Field-Effect Transistors. *Advanced Functional Materials*, 27(19):1604093, 2017.

[23] Branimir Radisavljevic, Aleksandra Radenovic, Jacopo Brivio, Valentina Giacometti, and Andras Kis. Single-layer MoS_2 transistors. *Nature Nanotechnology*, 6(3):147–150, 2011.

[24] Yury Yu Illarionov, Gerhard Rzepa, Michael Waltl, Theresia Knobloch, Alexander Grill, Marco M Furchi, Thomas Mueller, and Tibor Grasser. The role of charge trapping in MoS_2/SiO_2 and MoS_2/hBN field-effect transistors. *2D Materials*, 3(3):035004, 2016.

[25] Gwan-Hyoung Lee, Young-Jun Yu, Xu Cui, Nicholas Petrone, Chul-Ho Lee, Min Sup Choi, Dae-Yeong Lee, Changgu Lee, Won Jong Yoo, Kenji Watanabe, et al. Flexible and transparent MoS_2 field-effect transistors on hexagonal boron nitride-graphene heterostructures. *ACS Nano*, 7(9):7931–7936, 2013.

[26] Robert M Wallace. High-K Dielectrics: A Perspective on Applications from Silicon to 2D Materials. *ECS Transactions*, 80(1):17, 2017.

[27] Namphung Peimyoo, Matthew D. Barnes, Jake D. Mehew, Adolfo De Sanctis, Iddo Amit, Janire Escolar, Konstantinos Anastasiou, Aiden. P Rooney, Sarah J. Haigh, Saverio Russo, et al. Laser-writable high-k dielectric for van der Waals nanoelectronics. *Science Advances*, 5(1):eaau0906, 2019.

[28] Dattatray Late, Bin Liu, Ramakrishna Matte, Vinayak Dravid, and Chen Rao. Hysteresis in single-layer MoS_2 field effect transistors. *ACS Nano*, 6(6):5635–5641, 2012.

[29] Yury Yu Illarionov, Aday J Molina-Mendoza, Michael Waltl, Theresia Knobloch, Marco M Furchi, T Mueller, and Tibor Grasser. Reliability of next-generation field-effect transistors with transition metal dichalcogenides. In *2018 IEEE International Reliability Physics Symposium (IRPS)*, pages 5A–5. IEEE, 2018.

[30] Edrian Mania, Ananias B. Alencar, Alisson R. Cadore, Bruno R. Carvalho, Kenji Watanabe, Takashi Taniguchi, Bernardo R. A. Neves, Helio Chacham, and Leonardo C. Campos. Spontaneous doping on high quality talc-graphene-hBN van der Waals heterostructures. *2D Materials*, 4(3):031008, 2017.

[31] Zhengyang Cai, Bilu Liu, Xiaolong Zou, and Hui-Ming Cheng. Chemical vapor deposition growth and applications of two-dimensional materials and their heterostructures. *Chemical Reviews*, 118(13):6091–6133, 2018.

[32] Daryl McManus, Sandra Vranic, Freddie Withers, Veronica Sanchez-Romaguera, Massimo Macucci, Huafeng Yang, Roberto Sorrentino, Khaled Parvez, Seok-Kyun Son, Giuseppe Iannaccone, et al. Water-based and bio-

compatible 2D crystal inks for all-inkjet-printed heterostructures. *Nature Nanotechnology*, 12(4):343–350, 2017.

[33] Valeria Nicolosi, Manish Chhowalla, Mercouri G Kanatzidis, Michael S Strano, and Jonathan N Coleman. Liquid exfoliation of layered materials. *Science*, 340(6139), 2013.

[34] Jonathan N Coleman, Mustafa Lotya, Arlene O'Neill, Shane D Bergin, Paul J King, Umar Khan, Karen Young, Alexandre Gaucher, Sukanta De, Ronan J Smith, et al. Two-dimensional nanosheets produced by liquid exfoliation of layered materials. *Science*, 331(6017):568–571, 2011.

[35] Felice Torrisi and Tian Carey. Graphene, related two-dimensional crystals and hybrid systems for printed and wearable electronics. *Nano Today*, 23:73–96, 2018.

[36] Mark O. Goerbig. Electronic properties of graphene in a strong magnetic field. *Reviews of Modern Physics*, 83(4):1193, 2011.

[37] Samuel David Littlejohn. *Electrical properties of graphite nanoparticles in silicone: Flexible oscillators and electromechanical sensing.* Springer Science & Business Media, 2013.

[38] Antonio H. Castro Neto, Francisco Guinea, Nuno MR Peres, Kostya S Novoselov, and Andre K Geim. The electronic properties of graphene. *Reviews of Modern Physics*, 81(1):109, 2009.

[39] Marcos Henrique Diniz Guimaraes. Spin and charge transport in graphene devices in the classical and quantum regimes. *Nature Physics*, 7:616–20, 2011.

[40] John C Slater and George F Koster. Simplified LCAO method for the periodic potential problem. *Physical Review*, 94(6):1498, 1954.

[41] Javier Munárriz Arrieta. *Modelling of plasmonic and graphene nanodevices.* Springer, 2014.

[42] David J Griffiths and Darrell F Schroeter. *Introduction to quantum mechanics*. Cambridge University Press, 2018.

[43] Malte Rösner. *Electronic Structure of Novel Two-dimensional Materials and Graphene Heterostructures*. PhD thesis, Universität Bremen, 2016.

[44] Vitor M Pereira and AH Castro Neto. Strain engineering of graphene's electronic structure. *Physical Review Letters*, 103(4):046801, 2009.

[45] Monica F. Craciun, Saverio Russo, Masahiro Yamamoto, and Seigo Tarucha. Tuneable electronic properties in graphene. *Nano Today*, 6(1):42–60, 2011.

[46] Mikhail I. Katsnelson, Konstantin S. Novoselov, and Andre K. Geim. Chiral tunnelling and the Klein paradox in graphene. *Nature Physics*, 2(9):620–625, 2006.

[47] Konstantin S Novoselov, Z Jiang, Y Zhang, SV Morozov, Horst L Stormer, U Zeitler, JC Maan, GS Boebinger, Philip Kim, and Andre K Geim. Room-temperature quantum Hall effect in graphene. *Science*, 315(5817):1379–1379, 2007.

[48] Yuanbo Zhang, Yan-Wen Tan, Horst L Stormer, and Philip Kim. Experimental observation of the quantum Hall effect and Berry's phase in graphene. *Nature*, 438(7065):201–204, 2005.

[49] Andrey Kretinin, Geliang Yu, Rashid Jalil, Yuan Cao, Freddie Withers, Artem Mishchenko, Mikhail Katsnelson, Konstantin Novoselov, Andre Geim, and Fransisco Guinea. Quantum capacitance measurements of electron-hole asymmetry and next-nearest-neighbor hopping in graphene. *Physical Review B*, 88(16):165427, 2013.

[50] In Edwin Abbott's. Graphene: exploring carbon flatland. *Physics Today*, 60(8):35, 2007.

[51] Jingang Wang, Fengcai Ma, and Mengtao Sun. Graphene, hexagonal boron

nitride, and their heterostructures: properties and applications. *RSC Advances*, 7(27):16801–16822, 2017.

[52] Pooja Rani and VK Jindal. Designing band gap of graphene by B and N dopant atoms. *RSC Advances*, 3(3):802–812, 2013.

[53] Arlenciu Celis, MN Nair, Amina Taleb-Ibrahimi, EH Conrad, Claire Berger, WA De Heer, and Antonio Tejeda. Graphene nanoribbons: fabrication, properties and devices. *Journal of Physics D: Applied Physics*, 49(14):143001, 2016.

[54] Young-Woo Son, Marvin L Cohen, and Steven G Louie. Energy gaps in graphene nanoribbons. *Physical Review Letters*, 97(21):216803, 2006.

[55] Francisco Guinea, MI Katsnelson, and AK Geim. Energy gaps and a zero-field quantum Hall effect in graphene by strain engineering. *Nature Physics*, 6(1):30–33, 2010.

[56] Oskar Klein. The reflection of electrons at a potential jump according to dirac's relativistic dynamics. In *The Oskar Klein Memorial Lectures: (Volume 2)*, pages 131–139. World Scientific, 1994.

[57] Pierre E Allain and Jean-Noel Fuchs. Klein tunneling in graphene: optics with massless electrons. *The European Physical Journal B*, 83(3):301, 2011.

[58] Vadim V Cheianov and Vladimir I Fal'ko. Selective transmission of Dirac electrons and ballistic magnetoresistance of n- p junctions in graphene. *Physical Review B*, 74(4):041403, 2006.

[59] Andrea F Young and Philip Kim. Quantum interference and Klein tunnelling in graphene heterojunctions. *Nature Physics*, 5(3):222–226, 2009.

[60] Kirill I Bolotin, K J Sikes, Zd Jiang, M Klima, G Fudenberg, J Hone, Ph Kim, and HL Stormer. Ultrahigh electron mobility in suspended graphene. *Solid State Communications*, 146(9-10):351–355, 2008.

[61] Changgu Lee, Xiaoding Wei, Jeffrey W Kysar, and James Hone. Measurement of the elastic properties and intrinsic strength of monolayer graphene. *Science*, 321(5887):385–388, 2008.

[62] Ezzatollah Shamsaei, Felipe Basquiroto de Souza, Xupei Yao, Emad Benhelal, Abozar Akbari, and Wenhui Duan. Graphene-based nanosheets for stronger and more durable concrete: A review. *Construction and Building Materials*, 183:642–660, 2018.

[63] J Scott Bunch, Arend M Van Der Zande, Scott S Verbridge, Ian W Frank, David M Tanenbaum, Jeevak M Parpia, Harold G Craighead, and Paul L McEuen. Electromechanical resonators from graphene sheets. *Science*, 315(5811):490–493, 2007.

[64] Xinxin Li, Takahito Ono, Yuelin Wang, and Masayoshi Esashi. Ultrathin single-crystalline-silicon cantilever resonators: fabrication technology and significant specimen size effect on Young's modulus. *Applied Physics Letters*, 83(15):3081–3083, 2003.

[65] Robert Ilic, Harold G. Craighead, Sergey Krylov, Wageesha Senaratne, Curtis Ober, and Pavel J. Neuzil. Attogram detection using nanoelectromechanical oscillators. *Journal of Applied Physics*, 95(7):3694–3703, 2004.

[66] Rahul Raveendran Nair, Peter Blake, Alexander N Grigorenko, Konstantin S Novoselov, Tim J Booth, Tobias Stauber, Nuno MR Peres, and Andre K Geim. Fine structure constant defines visual transparency of graphene. *Science*, 320(5881):1308–1308, 2008.

[67] Keun Soo Kim, Yue Zhao, Houk Jang, Sang Yoon Lee, Jong Min Kim, Kwang S Kim, Jong-Hyun Ahn, Philip Kim, Jae-Young Choi, and Byung Hee Hong. Large-scale pattern growth of graphene films for stretchable transparent electrodes. *Nature*, 457(7230):706–710, 2009.

[68] Seongsu Kim, Manoj Kumar Gupta, Keun Young Lee, Ahrum Sohn, Tae Yun Kim, Kyung-Sik Shin, Dohwan Kim, Sung Kyun Kim, Kang Hyuck Lee, Hyeon-

Jin Shin, et al. Transparent flexible graphene triboelectric nanogenerators. *Advanced materials*, 26(23):3918–3925, 2014.

[69] Zhong Yan, Denis L Nika, and Alexander A Balandin. Thermal properties of graphene and few-layer graphene: applications in electronics. *IET Circuits, Devices & Systems*, 9(1):4–12, 2015.

[70] Nadejda D. Zincenco, Denis L. Nika, Evghenii P. Pokatilov, and Alexander A. Balandin. Acoustic phonon engineering of thermal properties of silicon-based nanostructures. In *Journal of Physics: Conference Series*, volume 92, page 012086. IOP Publishing, 2007.

[71] Eric Pop, Vikas Varshney, and Ajit K Roy. Thermal properties of graphene: Fundamentals and applications. *MRS bulletin*, 37(12):1273–1281, 2012.

[72] Dhriti S. Ghosh, Irene Calizo, Desalegne Teweldebrhan, Evghenii P. Pokatilov, Denis L. Nika, Alexander A. Balandin, Wenzhong Bao, Feng Miao, and C. Ning Lau. Extremely high thermal conductivity of graphene: Prospects for thermal management applications in nanoelectronic circuits. *Applied Physics Letters*, 92(15):151911, 2008.

[73] Alexander A Balandin, Suchismita Ghosh, Wenzhong Bao, Irene Calizo, Desalegne Teweldebrhan, Feng Miao, and Chun Ning Lau. Superior thermal conductivity of single-layer graphene. *Nano Letters*, 8(3):902–907, 2008.

[74] Zhong Yan, Guanxiong Liu, Javed M Khan, and Alexander A Balandin. Graphene quilts for thermal management of high-power GaN transistors. *Nature Communications*, 3(1):1–8, 2012.

[75] Bart Partoens and FM Peeters. From graphene to graphite: Electronic structure around the K point. *Physical Review B*, 74(7):075404, 2006.

[76] F Guinea, AH Castro Neto, and NMR Peres. Electronic states and Landau levels in graphene stacks. *Physical Review B*, 73(24):245426, 2006.

[77] Yuanbo Zhang, Tsung-Ta Tang, Caglar Girit, Zhao Hao, Michael C Martin, Alex Zettl, Michael F Crommie, Y Ron Shen, and Feng Wang. Direct observation of a widely tunable bandgap in bilayer graphene. *Nature*, 459(7248):820–823, 2009.

[78] Michael V Mirkin and Shigeru Amemiya. *Nanoelectrochemistry.* CRC Press, 2015.

[79] Cory R Dean, Andrea F Young, Inanc Meric, Chris Lee, Lei Wang, Sebastian Sorgenfrei, Kenji Watanabe, Takashi Taniguchi, Phillip Kim, Kenneth L Shepard, et al. Boron nitride substrates for high-quality graphene electronics. *Nature Nanotechnology*, 5(10):722–726, 2010.

[80] Kailiang Zhang, Yulin Feng, Fang Wang, Zhengchun Yang, and John Wang. Two dimensional hexagonal boron nitride (2D-hBN): synthesis, properties and applications. *Journal of Materials Chemistry C*, 5(46):11992–12022, 2017.

[81] Wei-Qiang Han, Lijun Wu, Yimei Zhu, Kenji Watanabe, and Takashi Taniguchi. Structure of chemically derived mono-and few-atomic-layer boron nitride sheets. *Applied Physics Letters*, 93(22):223103, 2008.

[82] Ricardo M. Ribeiro and Nuno M. R. Peres. Stability of boron nitride bilayers: Ground-state energies, interlayer distances, and tight-binding description. *Physical Review B*, 83(23):235312, 2011.

[83] Joanna Sławińska, Ilona Zasada, and Zbigniew Klusek. Energy gap tuning in graphene on hexagonal boron nitride bilayer system. *Physical Review B*, 81(15):155433, 2010.

[84] Gwan-Hyoung Lee, Young-Jun Yu, Changgu Lee, Cory Dean, Kenneth L Shepard, Philip Kim, and James Hone. Electron tunneling through atomically flat and ultrathin hexagonal boron nitride. *Applied Physics Letters*, 99(24):243114, 2011.

[85] Lu Hua Li and Ying Chen. Atomically thin boron nitride: unique properties and applications. *Advanced Functional Materials*, 26(16):2594–2608, 2016.

[86] Changhee Lee, Servin Rathi, Muhammad Atif Khan, Dongsuk Lim, Yunseob Kim, Sun Jin Yun, Doo-Hyeb Youn, Kenji Watanabe, Takashi Taniguchi, and Gil-Ho Kim. Comparison of trapped charges and hysteresis behavior in hBN encapsulated single MoS_2 flake based field effect transistors on SiO_2 and hBN substrates. *Nanotechnology*, 29(33):335202, 2018.

[87] Wugang Liao, Wei Wei, Yu Tong, Wai Kin Chim, and Chunxiang Zhu. Electrical performance and low frequency noise in hexagonal boron nitride encapsulated $MoSe_2$ dual-gated field effect transistors. *Applied Physics Letters*, 111(8):082105, 2017.

[88] Yusuke Hoshi, Takashi Kuroda, Mitsuhiro Okada, Rai Moriya, Satoru Masubuchi, Kenji Watanabe, Takashi Taniguchi, Ryo Kitaura, and Tomoki Machida. Suppression of exciton-exciton annihilation in tungsten disulfide monolayers encapsulated by hexagonal boron nitrides. *Physical Review B*, 95(24):241403, 2017.

[89] Régis Decker, Yang Wang, Victor W Brar, William Regan, Hsin-Zon Tsai, Qiong Wu, William Gannett, Alex Zettl, and Michael F Crommie. Local electronic properties of graphene on a BN substrate via scanning tunneling microscopy. *Nano Letters*, 11(6):2291–2295, 2011.

[90] Nicholas Petrone, Tarun Chari, Inanc Meric, Lei Wang, Kenneth L Shepard, and James Hone. Flexible graphene field-effect transistors encapsulated in hexagonal boron nitride. *ACS Nano*, 9(9):8953–8959, 2015.

[91] Joachim Dahl Thomsen, Tue Gunst, Søren Schou Gregersen, Lene Gammelgaard, Bjarke Sørensen Jessen, David MA Mackenzie, Kenji Watanabe, Takashi Taniguchi, Peter Bøggild, and Timothy J Booth. Suppression of intrinsic roughness in encapsulated graphene. *Physical Review B*, 96(1):014101, 2017.

[92] Lu Hua Li, Jiri Cervenka, Kenji Watanabe, Takashi Taniguchi, and Ying Chen. Strong oxidation resistance of atomically thin boron nitride nanosheets. *ACS Nano*, 8(2):1457–1462, 2014.

[93] Li Liu, Sunmin Ryu, Michelle R Tomasik, Elena Stolyarova, Naeyoung Jung, Mark S Hybertsen, Michael L Steigerwald, Louis E Brus, and George W Flynn. Graphene oxidation: thickness-dependent etching and strong chemical doping. *Nano Letters*, 8(7):1965–1970, 2008.

[94] Haiqing Zhou, Jixin Zhu, Zheng Liu, Zheng Yan, Xiujun Fan, Jian Lin, Gunuk Wang, Qingyu Yan, Ting Yu, Pulickel M Ajayan, et al. High thermal conductivity of suspended few-layer hexagonal boron nitride sheets. *Nano Research*, 7(8):1232–1240, 2014.

[95] Aleksey Falin, Qiran Cai, Elton JG Santos, Declan Scullion, Dong Qian, Rui Zhang, Zhi Yang, Shaoming Huang, Kenji Watanabe, Takashi Taniguchi, et al. Mechanical properties of atomically thin boron nitride and the role of interlayer interactions. *Nature Communications*, 8(1):1–9, 2017.

[96] Hennrik Schmidt, Francesco Giustiniano, and Goki Eda. Electronic transport properties of transition metal dichalcogenide field-effect devices: surface and interface effects. *Chemical Society Reviews*, 44(21):7715–7736, 2015.

[97] Rafael Roldán, Jose A Silva-Guillén, M Pilar López-Sancho, Francisco Guinea, Emmanuele Cappelluti, and Pablo Ordejón. Electronic properties of single-layer and multilayer transition metal dichalcogenides MX_2 (M= Mo, W and X= S, Se). *Annalen der Physik*, 526(9-10):347–357, 2014.

[98] Kostya S Novoselov, Andre K Geim, Sergei Vladimirovich Morozov, Da Jiang, Michail I Katsnelson, IV Grigorieva, and SV Dubonos. Two-dimensional gas of massless Dirac fermions in graphene. *Nature*, 438(7065):197–200, 2005.

[99] Yi-Hsien Lee, Xin-Quan Zhang, Wenjing Zhang, Mu-Tung Chang, Cheng-Te Lin, Kai-Di Chang, Ya-Chu Yu, Jacob Tse-Wei Wang, Chia-Seng Chang, Lain-Jong Li, et al. Synthesis of large-area MoS_2 atomic layers with chemical vapor deposition. *Advanced Materials*, 24(17):2320–2325, 2012.

[100] Allan Bromley, Ray B. Murray, and Abe D. Yoffe. The band structures of some

transition metal dichalcogenides. III. Group VIA: trigonal prism materials. *Journal of Physics C: Solid State Physics*, 5(7):759, 1972.

[101] Ray B. Murray, Allan Bromley, and Abe D. Yoffe. The band structures of some transition metal dichalcogenides. II. Group IVA; octahedral coordination. *Journal of Physics C: Solid State Physics*, 5(7):746, 1972.

[102] Wonbong Choi, Nitin Choudhary, Gang Hee Han, Juhong Park, Deji Akinwande, and Young Hee Lee. Recent development of two-dimensional transition metal dichalcogenides and their applications. *Materials Today*, 20(3):116–130, 2017.

[103] Rajesh Kappera, Damien Voiry, Sibel Ebru Yalcin, Brittany Branch, Gautam Gupta, Aditya D Mohite, and Manish Chhowalla. Phase-engineered low-resistance contacts for ultrathin MoS_2 transistors. *Nature Materials*, 13(12):1128–1134, 2014.

[104] Yung-Chang Lin, Dumitru O Dumcenco, Ying-Sheng Huang, and Kazu Suenaga. Atomic mechanism of the semiconducting-to-metallic phase transition in single-layered MoS_2. *Nature Nanotechnology*, 9(5):391–396, 2014.

[105] Chithra H. Sharma, Ananthu P. Surendran, Abin Varghese, and Madhu Thalakulam. Stable and scalable 1t mos 2 with low temperature-coefficient of resistance. *Scientific reports*, 8(1):1–9, 2018.

[106] E Cappelluti, Rafael Roldán, JA Silva-Guillén, Pablo Ordejón, and F Guinea. Tight-binding model and direct-gap/indirect-gap transition in single-layer and multilayer MoS_2. *Physical Review B*, 88(7):075409, 2013.

[107] Kin Fai Mak, Changgu Lee, James Hone, Jie Shan, and Tony F Heinz. Atomically thin MoS_2: a new direct-gap semiconductor. *Physical Review Letters*, 105(13):136805, 2010.

[108] Weijie Zhao, Zohreh Ghorannevis, Leiqiang Chu, Minglin Toh, Christian Kloc, Ping-Heng Tan, and Goki Eda. Evolution of electronic structure in atomically thin sheets of WS_2 and WSe_2. *ACS Nano*, 7(1):791–797, 2013.

[109] Agnieszka Kuc, Thomas Heine, and Andras Kis. Electronic properties of transition-metal dichalcogenides. *MRS Bulletin*, 40(ARTICLE):577–584, 2015.

[110] Ignacio Gutiérrez Lezama, Ashish Arora, Alberto Ubaldini, Céline Barreteau, Enrico Giannini, Marek Potemski, and Alberto F Morpurgo. Indirect-to-direct band gap crossover in few-layer $MoTe_2$. *Nano Letters*, 15(4):2336–2342, 2015.

[111] Agnieszka Kuc, Nourdine Zibouche, and Thomas Heine. Influence of quantum confinement on the electronic structure of the transition metal sulfide TS_2. *Physical Review B*, 83(24):245213, 2011.

[112] Zhiyong Y Zhu, Yingchun C Cheng, and Udo Schwingenschlögl. Giant spin-orbit-induced spin splitting in two-dimensional transition-metal dichalcogenide semiconductors. *Physical Review B*, 84(15):153402, 2011.

[113] JA Reyes-Retana and F Cervantes-Sodi. Spin-orbital effects in metal-dichalcogenide semiconducting monolayers. *Scientific Reports*, 6(1):1–10, 2016.

[114] Jesús A Del Alamo. Nanometre-scale electronics with III–V compound semiconductors. *Nature*, 479(7373):317–323, 2011.

[115] Wenzhong Bao, Xinghan Cai, Dohun Kim, Karthik Sridhara, and Michael S Fuhrer. High mobility ambipolar MoS_2 field-effect transistors: Substrate and dielectric effects. *Applied Physics Letters*, 102(4):042104, 2013.

[116] Stefano Larentis, Babak Fallahazad, and Emanuel Tutuc. Field-effect transistors and intrinsic mobility in ultra-thin $MoSe_2$ layers. *Applied Physics Letters*, 101(22):223104, 2012.

[117] Dmitry Ovchinnikov, Adrien Allain, Ying-Sheng Huang, Dumitru Dumcenco, and Andras Kis. Electrical transport properties of single-layer WS_2. *ACS nano*, 8(8):8174–8181, 2014.

[118] Hyun Goo Ji, Pablo Solís-Fernández, Daisuke Yoshimura, Mina Maruyama, Takahiko Endo, Yasumitsu Miyata, Susumu Okada, and Hiroki Ago. Chemically

Tuned p-and n-Type WSe_2 Monolayers with High Carrier Mobility for Advanced Electronics. *Advanced Materials*, 31(42):1903613, 2019.

[119] K Nagashio, Tadahiro Yamashita, T Nishimura, K Kita, and A Toriumi. Electrical transport properties of graphene on SiO_2 with specific surface structures. *Journal of Applied Physics*, 110(2):024513, 2011.

[120] Melinda Y Han, Barbaros Özyilmaz, Yuanbo Zhang, and Philip Kim. Energy band-gap engineering of graphene nanoribbons. *Physical Review Letters*, 98(20):206805, 2007.

[121] Zhengtang Luo, Patrick M Vora, Eugene J Mele, AT Charlie Johnson, and James M Kikkawa. Photoluminescence and band gap modulation in graphene oxide. *Applied Physics Letters*, 94(11):111909, 2009.

[122] Kristen Kaasbjerg, Kristian S Thygesen, and Karsten W Jacobsen. Phonon-limited mobility in n-type single-layer MoS_2 from first principles. *Physical Review B*, 85(11):115317, 2012.

[123] Hennrik Schmidt, Shunfeng Wang, Leiqiang Chu, Minglin Toh, Rajeev Kumar, Weijie Zhao, AH Castro Neto, Jens Martin, Shaffique Adam, Barbaros Ozyilmaz, et al. Transport properties of monolayer MoS_2 grown by chemical vapor deposition. *Nano Letters*, 14(4):1909–1913, 2014.

[124] Mahdi Ghorbani-Asl, Stefano Borini, Agnieszka Kuc, and Thomas Heine. Strain-dependent modulation of conductivity in single-layer transition-metal dichalcogenides. *Physical Review B*, 87(23):235434, 2013.

[125] Peng Lu, Xiaojun Wu, Wanlin Guo, and Xiao Cheng Zeng. Strain-dependent electronic and magnetic properties of MoS_2 monolayer, bilayer, nanoribbons and nanotubes. *Physical Chemistry Chemical Physics*, 14(37):13035–13040, 2012.

[126] Liliana Hromadova, Roman Martoňák, and Erio Tosatti. Structure change, layer sliding, and metallization in high-pressure MoS_2. *Physical Review B*, 87(14):144105, 2013.

[127] Swastibrata Bhattacharyya and Abhishek K Singh. Semiconductor-metal transition in semiconducting bilayer sheets of transition-metal dichalcogenides. *Physical Review B*, 86(7):075454, 2012.

[128] Kouji Taniguchi, Akiyo Matsumoto, Hidekazu Shimotani, and Hidenori Takagi. Erratum:"Electric-field-induced superconductivity at 9.4 K in a layered transition metal disulphide MoS_2"[Appl. Phys. Lett. 101, 042603 (2012)]. *Applied Physics Letters*, 101(10):109902, 2012.

[129] JT Ye, Yj J Zhang, R Akashi, Ms S Bahramy, R Arita, and Y Iwasa. Superconducting dome in a gate-tuned band insulator. *Science*, 338(6111):1193–1196, 2012.

[130] Jaesung Lee, Zenghui Wang, Keliang He, Rui Yang, Jie Shan, and Philip X-L Feng. Electrically tunable single-and few-layer MoS_2 nanoelectromechanical systems with broad dynamic range. *Science advances*, 4(3):eaao6653, 2018.

[131] Riccardo Frisenda, Matthias Drüppel, Robert Schmidt, Steffen Michaelis de Vasconcellos, David Perez de Lara, Rudolf Bratschitsch, Michael Rohlfing, and Andres Castellanos-Gomez. Biaxial strain tuning of the optical properties of single-layer transition metal dichalcogenides. *npj 2D Materials and Applications*, 1(1):1–7, 2017.

[132] Feifan Yu, Qianwen Liu, Xin Gan, Mingxiang Hu, Tianyi Zhang, Cheng Li, Feiyu Kang, Mauricio Terrones, and Ruitao Lv. Ultrasensitive pressure detection of few-layer MoS_2. *Advanced Materials*, 29(4):1603266, 2017.

[133] Dattatray J Late, Thomas Doneux, and Moussa Bougouma. Single-layer $MoSe_2$ based NH_3 gas sensor. *Applied Physics Letters*, 105(23):233103, 2014.

[134] Simone Bertolazzi, Jacopo Brivio, and Andras Kis. Stretching and breaking of ultrathin MoS_2. *ACS Nano*, 5(12):9703–9709, 2011.

[135] Zeng Fan, Zhang Wei-Bing, and Tang Bi-Yu. Electronic structures and elastic properties of monolayer and bilayer transition metal dichalcogenides MX_2 (M

= Mo, W; X = O, S, Se, Te): a comparative first-principles study. *Chinese Physics B*, 24(9):097103, 2015.

[136] Andres Castellanos-Gomez, Ronald van Leeuwen, Michele Buscema, Herre SJ van der Zant, Gary A Steele, and Warner J Venstra. Single-layer MoS_2 mechanical resonators. *Advanced Materials*, 25(46):6719–6723, 2013.

[137] Chhanda Samanta, Patel R. Yasasvi Gangavarapu, and Akshay K. Naik. Nonlinear mode coupling and internal resonances in MoS_2 nanoelectromechanical system. *Applied physics letters*, 107(17):173110, 2015.

[138] Jaesung Lee, Zenghui Wang, Keliang He, Jie Shan, and Philip X-L Feng. High frequency MoS_2 nanomechanical resonators. *ACS Nano*, 7(7):6086–6091, 2013.

[139] Nicolas Morell, Antoine Reserbat-Plantey, Ioannis Tsioutsios, Kevin G Schadler, Francois Dubin, Frank HL Koppens, and Adrian Bachtold. High quality factor mechanical resonators based on WSe_2 monolayers. *Nano Letters*, 16(8):5102–5108, 2016.

[140] Rusen Yan, Jeffrey R Simpson, Simone Bertolazzi, Jacopo Brivio, Michael Watson, Xufei Wu, Andras Kis, Tengfei Luo, Angela R Hight Walker, and Huili Grace Xing. Thermal conductivity of monolayer molybdenum disulfide obtained from temperature-dependent Raman spectroscopy. *ACS Nano*, 8(1):986–993, 2014.

[141] Xian Zhang, Dezheng Sun, Yilei Li, Gwan-Hyoung Lee, Xu Cui, Daniel Chenet, Yumeng You, Tony F Heinz, and James C Hone. Measurement of lateral and interfacial thermal conductivity of single-and bilayer MoS_2 and $MoSe_2$ using refined optothermal Raman technique. *ACS Applied Materials & Interfaces*, 7(46):25923–25929, 2015.

[142] Namphung Peimyoo, Jingzhi Shang, Weihuang Yang, Yanlong Wang, Chunxiao Cong, and Ting Yu. Thermal conductivity determination of suspended mono- and bilayer WS_2 by Raman spectroscopy. *Nano Research*, 8(4):1210–1221, 2015.

[143] Catalin Chiritescu, David G Cahill, Ngoc Nguyen, David Johnson, Arun Bodapati, Pawel Keblinski, and Paul Zschack. Ultralow thermal conductivity in disordered, layered WSe_2 crystals. *Science*, 315(5810):351–353, 2007.

[144] Michele Buscema, Maria Barkelid, Val Zwiller, Herre SJ van der Zant, Gary A Steele, and Andres Castellanos-Gomez. Large and tunable photothermoelectric effect in single-layer MoS_2. *Nano Letters*, 13(2):358–363, 2013.

[145] Wu-Xing Zhou and Ke-Qiu Chen. First-principles determination of ultralow thermal conductivity of monolayer WSe_2. *Scientific Reports*, 5:15070, 2015.

[146] Akira Yoneda, Mitsuhide Yonehara, and Masahiro Osako. Anisotropic thermal properties of talc under high temperature and pressure. *Physics of the Earth and Planetary Interiors*, 190:10–14, 2012.

[147] William Ward and James M Phillips. Calculated lamellar binding: I. Van der Waals bonding in talc and pyrophyllite. *Surface Science*, 25(2):379–384, 1971.

[148] Ingrid D Barcelos, Alisson R Cadore, Ananias B Alencar, Francisco CB Maia, Edrian Mania, Rafael F Oliveira, Carlos CB Bufon, Angelo Malachias, Raul O Freitas, Roberto L Moreira, et al. Infrared Fingerprints of Natural 2D Talc and Plasmon–Phonon Coupling in Graphene–Talc Heterostructures. *ACS Photonics*, 5(5):1912–1918, 2018.

[149] E Ozsoy, UMUT Onen, and TAHSİN Boyraz. Microstructural characterization and thermal properties of aluminium titanate/talc ceramic matrix composites. *Acta Physica Polonica A*, 127(4):1136–1138, 2015.

[150] William F. Deacon and Jonathon F. Goodman. Lubrication by lamellar solids. *Proceedings of the Royal Society of London. Series A. Mathematical and Physical Sciences*, 243(1235):464–482, 1958.

[151] Kirill I Bolotin, Fereshte Ghahari, Michael D Shulman, Horst L Stormer, and Philip Kim. Observation of the fractional quantum Hall effect in graphene. *Nature*, 462(7270):196–199, 2009.

[152] Rahul Nandkishore, Leonid S. Levitov, and Andrey V Chubukov. Chiral superconductivity from repulsive interactions in doped graphene. *Nature Physics*, 8(2):158, 2012.

[153] Min Sup Choi, Deshun Qu, Daeyeong Lee, Xiaochi Liu, Kenji Watanabe, Takashi Taniguchi, and Won Jong Yoo. Lateral MoS_2 p–n junction formed by chemical doping for use in high-performance optoelectronics. *ACS Nano*, 8(9):9332–9340, 2014.

[154] Eri Uesugi, Hidenori Goto, Ritsuko Eguchi, Akihiko Fujiwara, and Yoshihiro Kubozono. Electric double-layer capacitance between an ionic liquid and few-layer graphene. *Scientific Reports*, 3:1595, 2013.

[155] Sarah J. Haigh, Ali Gholinia, Rashid Jalil, Roger Romani, Liam Britnell, Doron C. Elias, Konstantin S. Novoselov, Leonid A. Ponomarenko, Andre K. Geim, and Roman Gorbachev. Cross-sectional imaging of individual layers and buried interfaces of graphene-based heterostructures and superlattices. *Nature Materials*, 11(9):764–767, 2012.

[156] Andrey V. Kretinin, Yuan Cao, Jhih-Sian Tu, Geliang Yu, Rashid Jalil, Konstantin S. Novoselov, Sarah J. Haigh, Ali Gholinia, Artem Mishchenko, Marcelo Lozada, et al. Electronic properties of graphene encapsulated with different two-dimensional atomic crystals. *Nano Letters*, 14(6):3270–3276, 2014.

[157] Stefan Wakolbinger, Fabian R Geisenhof, Felix Winterer, Samuel Palmer, Juri G Crimmann, Kenji Watanabe, Takashi Taniguchi, Frank Trixler, and R Thomas Weitz. Locally-triggered hydrophobic collapse induces global interface self-cleaning in van-der-Waals heterostructures at room-temperature. *2D Materials*, 7(3):035002, 2020.

[158] Richard C Remsing, Erte Xi, Srivathsan Vembanur, Sumit Sharma, Pablo G Debenedetti, Shekhar Garde, and Amish J Patel. Pathways to dewetting in hydrophobic confinement. *Proceedings of the National Academy of Sciences*, 112(27):8181–8186, 2015.

[159] Matthew R Rosenberger, Hsun-Jen Chuang, Kathleen M McCreary, Aubrey T Hanbicki, Saujan V Sivaram, and Berend T Jonker. Nano-“squeegee” for the creation of clean 2D material interfaces. *ACS Applied Materials & Interfaces*, 10(12):10379–10387, 2018.

[160] Masa Ishigami, Jyong-Hao Chen, William G. Cullen, Michael S. Fuhrer, and Ellen D. Williams. Atomic structure of graphene on SiO_2. *Nano Letters*, 7(6):1643–1648, 2007.

[161] Mikhail I. Katsnelson and Andre K. Geim. Electron scattering on microscopic corrugations in graphene. *Philosophical Transactions of the Royal Society A: Mathematical, Physical and Engineering Sciences*, 366(1863):195–204, 2008.

[162] Jorge Quereda, Andres Castellanos-Gomez, Nicolás Agraït, and Gabino Rubio-Bollinger. Single-layer MoS_2 roughness and sliding friction quenching by interaction with atomically flat substrates. *Applied Physics Letters*, 105(5):053111, 2014.

[163] Fan Zhang, Zhixing Lu, Yichul Choi, Haining Liu, Husong Zheng, Liming Xie, Kyungwha Park, Liying Jiao, and Chenggang Tao. Atomically Resolved Observation of Continuous Interfaces between an As-Grown MoS_2 Monolayer and a WS_2/MoS_2 Heterobilayer on SiO_2. *ACS Applied Nano Materials*, 1(5):2041–2048, 2018.

[164] Bong Gyu Shin, Gang Hee Han, Seok Joon Yun, Hye Min Oh, Jung Jun Bae, Young Jae Song, Chong-Yun Park, and Young Hee Lee. Indirect bandgap puddles in monolayer MoS_2 by substrate-induced local strain. *Advanced Materials*, 28(42):9378–9384, 2016.

[165] Jiamin Xue, Javier Sanchez-Yamagishi, Danny Bulmash, Philippe Jacquod, Aparna Deshpande, K Watanabe, T Taniguchi, Pablo Jarillo-Herrero, and Brian J LeRoy. Scanning tunnelling microscopy and spectroscopy of ultra-flat graphene on hexagonal boron nitride. *Nature Materials*, 10(4):282–285, 2011.

[166] Eun-Ah Kim and AH Castro Neto. Graphene as an electronic membrane. *EPL (Europhysics Letters)*, 84(5):57007, 2008.

[167] N Levy, SA Burke, KL Meaker, M Panlasigui, A Zettl, F Guinea, AH Castro Neto, and Michael F Crommie. Strain-induced pseudo–magnetic fields greater than 300 tesla in graphene nanobubbles. *Science*, 329(5991):544–547, 2010.

[168] Gakpa Giovannetti, Petr A Khomyakov, Geert Brocks, VM vd Karpan, Jeroen van den Brink, and Paul J Kelly. Doping graphene with metal contacts. *Physical Review Letters*, 101(2):026803, 2008.

[169] Seung Min Song, Jong Kyung Park, One Jae Sul, and Byung Jin Cho. Determination of work function of graphene under a metal electrode and its role in contact resistance. *Nano Letters*, 12(8):3887–3892, 2012.

[170] Antonio Di Bartolomeo. Graphene schottky diodes: An experimental review of the rectifying graphene/semiconductor heterojunction. *Physics Reports*, 606:1–58, 2016.

[171] Eduardo JH Lee, Kannan Balasubramanian, Ralf Thomas Weitz, Marko Burghard, and Klaus Kern. Contact and edge effects in graphene devices. *Nature Nanotechnology*, 3(8):486–490, 2008.

[172] Jens Martin, N Akerman, G Ulbricht, T Lohmann, JH v Smet, K Von Klitzing, and Amir Yacoby. Observation of electron–hole puddles in graphene using a scanning single-electron transistor. *Nature Physics*, 4(2):144–148, 2008.

[173] Yuanbo Zhang, Victor W Brar, Caglar Girit, Alex Zettl, and Michael F Crommie. Origin of spatial charge inhomogeneity in graphene. *Nature Physics*, 5(10):722–726, 2009.

[174] RH Miwa, Tome M Schmidt, WL Scopel, and A Fazzio. Doping of graphene adsorbed on the a-SiO_2 surface. *Applied Physics Letters*, 99(16):163108, 2011.

[175] Lingmei Kong, Cameron Bjelkevig, Sneha Gaddam, Mi Zhou, Young Hee Lee, Gang Hee Han, Hae Kyung Jeong, Ning Wu, Zhengzheng Zhang, Jie Xiao, et al.

Graphene/substrate charge transfer characterized by inverse photoelectron spectroscopy. *The Journal of Physical Chemistry C*, 114(49):21618–21624, 2010.

[176] Rui Wang, Shengnan Wang, Dongdong Zhang, Zhongjun Li, Ying Fang, and Xiaohui Qiu. Control of carrier type and density in exfoliated graphene by interface engineering. *ACS Nano*, 5(1):408–412, 2011.

[177] Long Yuan, Ting-Fung Chung, Agnieszka Kuc, Yan Wan, Yang Xu, Yong P Chen, Thomas Heine, and Libai Huang. Photocarrier generation from interlayer charge-transfer transitions in WS_2-graphene heterostructures. *Science Advances*, 4(2):e1700324, 2018.

[178] Horacio Coy Diaz, Rafik Addou, and Matthias Batzill. Interface properties of CVD grown graphene transferred onto MoS_2 (0001). *Nanoscale*, 6(2):1071–1078, 2014.

[179] Lili Yu, Yi-Hsien Lee, Xi Ling, Elton JG Santos, Yong Cheol Shin, Yuxuan Lin, Madan Dubey, Efthimios Kaxiras, Jing Kong, Han Wang, et al. Graphene/MoS_2 hybrid technology for large-scale two-dimensional electronics. *Nano Letters*, 14(6):3055–3063, 2014.

[180] Yandong Ma, Ying Dai, Meng Guo, Chengwang Niu, and Baibiao Huang. Graphene adhesion on MoS_2 monolayer: an ab initio study. *Nanoscale*, 3(9):3883–3887, 2011.

[181] Raymond T Tung. The physics and chemistry of the Schottky barrier height. *Applied Physics Reviews*, 1(1):011304, 2014.

[182] Daniel S Schulman, Andrew J Arnold, and Saptarshi Das. Contact engineering for 2D materials and devices. *Chemical Society Reviews*, 47(9):3037–3058, 2018.

[183] Hui Fang, Mahmut Tosun, Gyungseon Seol, Ting Chia Chang, Kuniharu Takei, Jing Guo, and Ali Javey. Degenerate n-doping of few-layer transition metal dichalcogenides by potassium. *Nano Letters*, 13(5):1991–1995, 2013.

[184] Hui Fang, Steven Chuang, Ting Chia Chang, Kuniharu Takei, Toshitake Takahashi, and Ali Javey. High-performance single layered WSe_2 p-FETs with chemically doped contacts. *Nano Letters*, 12(7):3788–3792, 2012.

[185] Sungjin Wi, Hyunsoo Kim, Mikai Chen, Hongsuk Nam, L Jay Guo, Edgar Meyhofer, and Xiaogan Liang. Enhancement of photovoltaic response in multilayer MoS_2 induced by plasma doping. *ACS Nano*, 8(5):5270–5281, 2014.

[186] Saptarshi Das, Hong-Yan Chen, Ashish Verma Penumatcha, and Joerg Appenzeller. High performance multilayer MoS_2 transistors with scandium contacts. *Nano Letters*, 13(1):100–105, 2013.

[187] Changsik Kim, Inyong Moon, Daeyeong Lee, Min Sup Choi, Faisal Ahmed, Seunggeol Nam, Yeonchoo Cho, Hyeon-Jin Shin, Seongjun Park, and Won Jong Yoo. Fermi level pinning at electrical metal contacts of monolayer molybdenum dichalcogenides. *ACS Nano*, 11(2):1588–1596, 2017.

[188] Thomas Mueller and Ermin Malic. Exciton physics and device application of two-dimensional transition metal dichalcogenide semiconductors. *npj 2D Materials and Applications*, 2(1):1–12, 2018.

[189] Michael KL Man, Skylar Deckoff-Jones, Andrew Winchester, Guangsha Shi, Gautam Gupta, Aditya D Mohite, Swastik Kar, Emmanouil Kioupakis, Saikat Talapatra, and Keshav M Dani. Protecting the properties of monolayer MoS_2 on silicon based substrates with an atomically thin buffer. *Scientific Reports*, 6:20890, 2016.

[190] Yuanyuan Li, Zeming Qi, Miao Liu, Yuyin Wang, Xuerui Cheng, Guobin Zhang, and Liusi Sheng. Photoluminescence of monolayer MoS_2 on $LaAlO_3$ and $SrTiO_3$ substrates. *Nanoscale*, 6(24):15248–15254, 2014.

[191] Michele Buscema, Gary A Steele, Herre SJ van der Zant, and Andres Castellanos-Gomez. The effect of the substrate on the Raman and photoluminescence emission of single-layer MoS_2. *Nano Research*, 7(4):561–571, 2014.

[192] Archana Raja, Andrey Chaves, Jaeeun Yu, Ghidewon Arefe, Heather M Hill, Albert F Rigosi, Timothy C Berkelbach, Philipp Nagler, Christian Schüller, Tobias Korn, et al. Coulomb engineering of the bandgap and excitons in two-dimensional materials. *Nature Communications*, 8(1):1–7, 2017.

[193] Alexey Chernikov, Timothy C Berkelbach, Heather M Hill, Albert Rigosi, Yilei Li, Ozgur Burak Aslan, David R Reichman, Mark S Hybertsen, and Tony F Heinz. Exciton binding energy and nonhydrogenic Rydberg series in monolayer WS_2. *Physical Review Letters*, 113(7):076802, 2014.

[194] Jun Kang, Sefaattin Tongay, Jian Zhou, Jingbo Li, and Junqiao Wu. Band offsets and heterostructures of two-dimensional semiconductors. *Applied Physics Letters*, 102(1):012111, 2013.

[195] Dmitrii Unuchek, Alberto Ciarrocchi, Ahmet Avsar, Kenji Watanabe, Takashi Taniguchi, and Andras Kis. Room-temperature electrical control of exciton flux in a van der Waals heterostructure. *Nature*, 560(7718):340–344, 2018.

[196] Maurizia Palummo, Marco Bernardi, and Jeffrey C Grossman. Exciton radiative lifetimes in two-dimensional transition metal dichalcogenides. *Nano Letters*, 15(5):2794–2800, 2015.

[197] Haiyang Zou, Ying Zhang, Litong Guo, Peihong Wang, Xu He, Guozhang Dai, Haiwu Zheng, Chaoyu Chen, Aurelia Chi Wang, Cheng Xu, et al. Quantifying the triboelectric series. *Nature Communications*, 10(1):1–9, 2019.

[198] Patricia F O'grady. *Thales of Miletus: the beginnings of western science and philosophy.* Taylor & Francis, 2017.

[199] Jeong Min Baik and Jin Pyo Lee. Strategies for ultrahigh outputs generation in triboelectric energy harvesting technologies: from fundamentals to devices. *Science and Technology of Advanced Materials*, 20(1):927–936, 2019.

[200] Cheng Xu, Yunlong Zi, Aurelia Chi Wang, Haiyang Zou, Yejing Dai, Xu He, Peihong Wang, Yi-Cheng Wang, Peizhong Feng, Dawei Li, et al. On the

electron-transfer mechanism in the contact-electrification effect. *Advanced Materials*, 30(15):1706790, 2018.

[201] Hyun-Woo Park, Nghia Dinh Huynh, Wook Kim, Choongyeop Lee, Youngsuk Nam, Sangmin Lee, Kwun-Bum Chung, and Dukhyun Choi. Electron blocking layer-based interfacial design for highly-enhanced triboelectric nanogenerators. *Nano Energy*, 50:9–15, 2018.

[202] Edward O. Hall. The deformation and ageing of mild steel: III discussion of results. *Proceedings of the Physical Society. Section B*, 64(9):747, 1951.

[203] Sneha N Naik and Stephen M Walley. The Hall–Petch and inverse Hall–Petch relations and the hardness of nanocrystalline metals. *Journal of Materials Science*, 55(7):2661–2681, 2020.

[204] Wangqing Yuan, Suraj K. Panigrahi, and Rajiv S. Mishra. Influence of grain size and texture on Hall–Petch relationship for a magnesium alloy. *Scripta Materialia*, 65(11):994–997, 2011.

[205] John D. Eshelby, Frederick C. Frank, and Frank R. N. Nabarro. XLI. the equilibrium of linear arrays of dislocations. *The London, Edinburgh, and Dublin Philosophical Magazine and Journal of Science*, 42(327):351–364, 1951.

[206] Ronald W Armstrong. 60 years of Hall-Petch: past to present nano-scale connections. *Materials Transactions*, 55(1):2–12, 2014.

[207] Atul H. Chokshi and Herbert Gleiter. On the validity of the Hall-Petch relationship in nanocrystalline materials. *Scripta Metallurgica*, 23(10):1679–1684, 1989.

[208] Hans Conrad and Jagdish Narayan. On the grain size softening in nanocrystalline materials. *Scripta Materialia*, 42(11):1025–1030, 2000.

[209] Terence G Langdon. Grain boundary sliding revisited: Developments in sliding over four decades. *Journal of Materials Science*, 41(3):597–609, 2006.

[210] John R Ferraro. *Introductory raman spectroscopy*. Elsevier, 2003.

[211] Derek Albert Long and DA Long. The Raman effect: a unified treatment of the theory of Raman scattering by molecules. 2002.

[212] Stewart O Williams and Dan G Imre. Raman spectroscopy: time-dependent pictures. *The Journal of Physical Chemistry*, 92(12):3363–3374, 1988.

[213] Martin Schmitt and Jurgen Popp. Raman spectroscopy at the beginning of the twenty-first century. *Journal of Raman Spectroscopy: An International Journal for Original Work in all Aspects of Raman Spectroscopy, Including Higher Order Processes, and also Brillouin and Rayleigh Scattering*, 37(1-3):20–28, 2006.

[214] Neil W Ashcroft, N David Mermin, et al. Solid state physics [by] Neil W. Ashcroft [and] N. David Mermin., 1976.

[215] Stevo K Jaćimovski, Maša Bukurov, Jovan P Šetrajčić, and Dejan I Raković. Phonon thermal conductivity of graphene. *Superlattices and microstructures*, 88:330–337, 2015.

[216] PL De Andres, F Guinea, and MI Katsnelson. Bending modes, anharmonic effects, and thermal expansion coefficient in single-layer and multilayer graphene. *Physical Review B*, 86(14):144103, 2012.

[217] Michele Lazzeri, Claudio Attaccalite, Ludger Wirtz, and Francesco Mauri. Impact of the electron-electron correlation on phonon dispersion: Failure of LDA and GGA DFT functionals in graphene and graphite. *Physical Review B*, 78(8):081406, 2008.

[218] LM Malard, Marcos Assunção Pimenta, Gene Dresselhaus, and MS Dresselhaus. Raman spectroscopy in graphene. *Physics Reports*, 473(5-6):51–87, 2009.

[219] Andrea C Ferrari. Raman spectroscopy of graphene and graphite: Disorder, electron–phonon coupling, doping and nonadiabatic effects. *Solid State Communications*, 143(1-2):47–57, 2007.

[220] Otakar Frank, Marcel Mohr, Janina Maultzsch, Christian Thomsen, Ibtsam Riaz, Rashid Jalil, Kostya S Novoselov, Georgia Tsoukleri, John Parthenios, Konstantinos Papagelis, et al. Raman 2D-band splitting in graphene: theory and experiment. *ACS Nano*, 5(3):2231–2239, 2011.

[221] Georgia Tsoukleri, John Parthenios, Konstantinos Papagelis, Rashid Jalil, Andrea C Ferrari, Andre K Geim, Kostya S Novoselov, and Costas Galiotis. Subjecting a graphene monolayer to tension and compression. *small*, 5(21):2397–2402, 2009.

[222] Ji Eun Lee, Gwanghyun Ahn, Jihye Shim, Young Sik Lee, and Sunmin Ryu. Optical separation of mechanical strain from charge doping in graphene. *Nature Communications*, 3(1):1–8, 2012.

[223] Irene Calizo, Alexander A. Balandin, Feng Miao, and Chun-Ning Lau. Temperature dependence of the raman spectra of graphene and graphene multilayers. *Nano Letters*, 7(9):2645–2649, 2007.

[224] Anindya Das, Simone Pisana, Biswanath Chakraborty, Stefano Piscanec, Srijan K Saha, Umesh V Waghmare, Konstantin S Novoselov, Hulikal R Krishnamurthy, Andre K Geim, Andrea C Ferrari, et al. Monitoring dopants by raman scattering in an electrochemically top-gated graphene transistor. *Nature Nanotechnology*, 3(4):210–215, 2008.

[225] S Jiménez Sandoval, D Yang, RF Frindt, and JC Irwin. Raman study and lattice dynamics of single molecular layers of MoS_2. *Physical Review B*, 44(8):3955, 1991.

[226] Andrea C Ferrari and Denis M Basko. Raman spectroscopy as a versatile tool for studying the properties of graphene. *Nature Nanotechnology*, 8(4):235–246, 2013.

[227] YY Wang, ZH Ni, ZX Shen, HM Wang, and YH Wu. Interference enhancement of Raman signal of graphene. *Applied Physics Letters*, 92(4):043121, 2008.

[228] SJ Kim, SJ Park, HY Kim, GS Jang, DJ Park, Ji-Yong Park, Soonil Lee, and YH Ahn. Characterization of chemical doping of graphene by in-situ Raman spectroscopy. *Applied Physics Letters*, 108(20):203111, 2016.

[229] R Geick, CH Perry, and G Rupprecht. Normal modes in hexagonal boron nitride. *Physical Review*, 146(2):543, 1966.

[230] S Reich, AC Ferrari, R Arenal, A Loiseau, I Bello, and J Robertson. Resonant Raman scattering in cubic and hexagonal boron nitride. *Physical Review B*, 71(20):205201, 2005.

[231] Philipp Tonndorf, Robert Schmidt, Philipp Böttger, Xiao Zhang, Janna Börner, Andreas Liebig, Manfred Albrecht, Christian Kloc, Ovidiu Gordan, Dietrich RT Zahn, et al. Photoluminescence emission and Raman response of monolayer MoS_2, $MoSe_2$, and WSe_2. *Optics Xxpress*, 21(4):4908–4916, 2013.

[232] Gitti L Frey, Reshef Tenne, Manyalibo J Matthews, MS Dresselhaus, and G Dresselhaus. Raman and resonance Raman investigation of MoS_2 nanoparticles. *Physical Review B*, 60(4):2883, 1999.

[233] Hong Li, Qing Zhang, Chin Chong Ray Yap, Beng Kang Tay, Teo Hang Tong Edwin, Aurelien Olivier, and Dominique Baillargeat. From bulk to monolayer MoS_2: evolution of Raman scattering. *Advanced Functional Materials*, 22(7):1385–1390, 2012.

[234] Fang Wang, Ian A Kinloch, Daniel Wolverson, Reshef Tenne, Alla Zak, Eoghan O'Connell, Ursel Bangert, and Robert J Young. Strain-induced phonon shifts in tungsten disulfide nanoplatelets and nanotubes. *2D Materials*, 4(1):015007, 2016.

[235] Hai Li, Gang Lu, Yanlong Wang, Zongyou Yin, Chunxiao Cong, Qiyuan He, Lu Wang, Feng Ding, Ting Yu, and Hua Zhang. Mechanical exfoliation and characterization of single-and few-layer nanosheets of WSe_2, TaS_2, and $TaSe_2$. *Small*, 9(11):1974–1981, 2013.

[236] Ayse Berkdemir, Humberto R Gutiérrez, Andrés R Botello-Méndez, Néstor Perea-López, Ana Laura Elías, Chen-Ing Chia, Bei Wang, Vincent H Crespi, Florentino López-Urías, Jean-Christophe Charlier, et al. Identification of individual and few layers of WS_2 using Raman Spectroscopy. *Scientific Reports*, 3(1):1–8, 2013.

[237] Weijie Zhao, Zohreh Ghorannevis, Kiran Kumar Amara, Jing Ren Pang, Minglin Toh, Xin Zhang, Christian Kloc, Ping Heng Tan, and Goki Eda. Lattice dynamics in mono-and few-layer sheets of WS_2 and WSe_2. *Nanoscale*, 5(20):9677–9683, 2013.

[238] Changgu Lee, Hugen Yan, Louis E Brus, Tony F Heinz, James Hone, and Sunmin Ryu. Anomalous lattice vibrations of single-and few-layer MoS_2. *ACS Nano*, 4(5):2695–2700, 2010.

[239] Andreij de Carvalho Gadelha. Unraveling Optoelectronic Properties of 2D Materials. 2019.

[240] Hongyan Shi, Rusen Yan, Simone Bertolazzi, Jacopo Brivio, Bo Gao, Andras Kis, Debdeep Jena, Huili Grace Xing, and Libai Huang. Exciton dynamics in suspended monolayer and few-layer MoS_2 2D crystals. *ACS Nano*, 7(2):1072–1080, 2013.

[241] Charles Kittel, Paul McEuen, and Paul McEuen. *Introduction to solid state physics*, volume 8. Wiley New York, 1996.

[242] U Finardi. Nanotechnology: Concepts, methodologies, tools, and applications, 2014.

[243] Claus F Klingshirn. *Semiconductor optics*. Springer Science & Business Media, 2012.

[244] Hartmut Haug and Stephan W Koch. *Quantum theory of the optical and electronic properties of semiconductors: fifth edition*. World Scientific Publishing Company, 2009.

[245] Alex A. High, Aeron T. Hammack, Leonid V. Butov, and Arthur C. Gossard. Exciton optoelectronic transistor. *Optics Letters*, 32(17):2466–2468, 2007.

[246] Chun Hung Lui, Kin Fai Mak, Jie Shan, Tony F Heinz, et al. Ultrafast photoluminescence from graphene. *Physical Review Letters*, 105(12):127404, 2010.

[247] LI Cao, Mohammed J Meziani, Sushant Sahu, and Ya-Ping Sun. Photoluminescence properties of graphene versus other carbon nanomaterials. *Accounts of Chemical Research*, 46(1):171–180, 2013.

[248] Kenji Watanabe, Takashi Taniguchi, and Hisao Kanda. Direct-bandgap properties and evidence for ultraviolet lasing of hexagonal boron nitride single crystal. *Nature Materials*, 3(6):404–409, 2004.

[249] Périne Jaffrennou, Julien Barjon, J-S Lauret, Brigitte Attal-Trétout, François Ducastelle, and Annick Loiseau. Origin of the excitonic recombinations in hexagonal boron nitride by spatially resolved cathodoluminescence spectroscopy, 2007.

[250] Christine Elias, Pierre Valvin, Thomas Pelini, A Summerfield, CJ Mellor, TS Cheng, L Eaves, CT Foxon, PH Beton, SV Novikov, et al. Direct bandgap crossover in epitaxial monolayer boron nitride. *Nature Communications*, 10(1):1–7, 2019.

[251] Fulvio Paleari, Thomas Galvani, Hakim Amara, François Ducastelle, Alejandro Molina-Sánchez, and Ludger Wirtz. Excitons in few-layer hexagonal boron nitride: Davydov splitting and surface localization. *2D Materials*, 5(4):045017, 2018.

[252] Kathleen M McCreary, Aubrey T Hanbicki, Saujan V Sivaram, and Berend T Jonker. A-and B-exciton photoluminescence intensity ratio as a measure of sample quality for transition metal dichalcogenide monolayers. *APL Materials*, 6(11):111106, 2018.

[253] Heather M Hill, Albert F Rigosi, Cyrielle Roquelet, Alexey Chernikov, Timothy C Berkelbach, David R Reichman, Mark S Hybertsen, Louis E Brus, and Tony F Heinz. Observation of excitonic Rydberg states in monolayer MoS_2 and WS_2 by photoluminescence excitation spectroscopy. *Nano Letters*, 15(5):2992–2997, 2015.

[254] Humberto R Gutiérrez, Nestor Perea-López, Ana Laura Elías, Ayse Berkdemir, Bei Wang, Ruitao Lv, Florentino López-Urías, Vincent H Crespi, Humberto Terrones, and Mauricio Terrones. Extraordinary room-temperature photoluminescence in triangular WS_2 monolayers. *Nano Letters*, 13(8):3447–3454, 2013.

[255] Qingqing Ji, Yanfeng Zhang, Teng Gao, Yu Zhang, Donglin Ma, Mengxi Liu, Yubin Chen, Xiaofen Qiao, Ping-Heng Tan, Min Kan, et al. Epitaxial monolayer MoS_2 on mica with novel photoluminescence. *Nano Letters*, 13(8):3870–3877, 2013.

[256] Tengfei Yan, Xiaofen Qiao, Xiaona Liu, Pingheng Tan, and Xinhui Zhang. Photoluminescence properties and exciton dynamics in monolayer WSe_2. *Applied Physics Letters*, 105(10):101901, 2014.

[257] Chunxiao Cong, Jingzhi Shang, Xing Wu, Bingchen Cao, Namphung Peimyoo, Caiyu Qiu, Litao Sun, and Ting Yu. Synthesis and optical properties of large-area single-crystalline 2D semiconductor WS_2 monolayer from chemical vapor deposition. *Advanced Optical Materials*, 2(2):131–136, 2014.

[258] Long Yuan and Libai Huang. Exciton dynamics and annihilation in WS_2 2D semiconductors. *Nanoscale*, 7(16):7402–7408, 2015.

[259] Ashwin Ramasubramaniam. Large excitonic effects in monolayers of molybdenum and tungsten dichalcogenides. *Physical Review B*, 86(11):115409, 2012.

[260] Yuxuan Lin, Xi Ling, Lili Yu, Shengxi Huang, Allen L Hsu, Yi-Hsien Lee, Jing Kong, Mildred S Dresselhaus, and Tomás Palacios. Dielectric screening

of excitons and trions in single-layer MoS_2. *Nano Letters*, 14(10):5569–5576, 2014.

[261] Hannu-Pekka Komsa and Arkady V Krasheninnikov. Effects of confinement and environment on the electronic structure and exciton binding energy of MoS_2 from first principles. *Physical Review B*, 86(24):241201, 2012.

[262] Jason S Ross, Sanfeng Wu, Hongyi Yu, Nirmal J Ghimire, Aaron M Jones, Grant Aivazian, Jiaqiang Yan, David G Mandrus, Di Xiao, Wang Yao, et al. Electrical control of neutral and charged excitons in a monolayer semiconductor. *Nature Communications*, 4(1):1–6, 2013.

[263] Hiram J Conley, Bin Wang, Jed I Ziegler, Richard F Haglund Jr, Sokrates T Pantelides, and Kirill I Bolotin. Bandgap engineering of strained monolayer and bilayer MoS_2. *Nano Letters*, 13(8):3626–3630, 2013.

[264] Kin Fai Mak, Keliang He, Changgu Lee, Gwan Hyoung Lee, James Hone, Tony F Heinz, and Jie Shan. Tightly bound trions in monolayer MoS_2. *Nature Materials*, 12(3):207–211, 2013.

[265] Kevin P. O'donnell and Xie Chen. Temperature dependence of semiconductor band gaps. *Applied physics letters*, 58(25):2924–2926, 1991.

[266] Gerd Binnig, Calvin F Quate, and Ch Gerber. Atomic force microscope. *Physical Review Letters*, 56(9):930, 1986.

[267] Nicholas A Geisse. AFM and combined optical techniques. *Materials Today*, 12(7-8):40–45, 2009.

[268] Oscar Custance, Ruben Perez, and Seizo Morita. Atomic force microscopy as a tool for atom manipulation. *Nature Nanotechnology*, 4(12):803–810, 2009.

[269] Yoshiaki Sugimoto, Masayuki Abe, Shinji Hirayama, Noriaki Oyabu, Óscar Custance, and Seizo Morita. Atom inlays performed at room temperature using atomic force microscopy. *Nature materials*, 4(2):156–159, 2005.

[270] Qi Zhong, Kris Kjoller, and Virgil B. Elings. Fractured polymer/silica fiber surface studied by tapping mode atomic force microscopy. *Surface Science*, 290(1-2):L688–L692, 1993.

[271] Yves Martin, Clayton C Williams, and H Kumar Wickramasinghe. Atomic force microscope–force mapping and profiling on a sub 100-$\AA$ scale. *Journal of Applied Physics*, 61(10):4723–4729, 1987.

[272] Louis De Broglie. *Recherches sur la théorie des quanta*. PhD thesis, Migration-université en cours d'affectation, 1924.

[273] Michael Walock. *Nanocomposite coatings based on quaternary metalnitrogen*. PhD thesis, Paris, ENSAM, 2012.

[274] KD Vernon-Parry. Scanning electron microscopy: an introduction. *III-Vs Review*, 13(4):40–44, 2000.

[275] Mircea I. Petrescu. Theoretical hardness calculated from crystallo-chemical data for MoS_2 and WS_2 crystals and nanostructures. *Acta Crystallographica Section B: Structural Science*, 68(5):501–510, 2012.

[276] Minsu Seol, Seongsu Kim, Yeonchoo Cho, Kyung-Eun Byun, Haeryong Kim, Jihye Kim, Sung Kyun Kim, Sang-Woo Kim, Hyeon-Jin Shin, and Seongjun Park. Triboelectric series of 2D layered materials. *Advanced Materials*, 30(39):1801210, 2018.

[277] Gregor Schwartz, Benjamin C-K Tee, Jianguo Mei, Anthony L Appleton, Do Hwan Kim, Huiliang Wang, and Zhenan Bao. Flexible polymer transistors with high pressure sensitivity for application in electronic skin and health monitoring. *Nature Communications*, 4:1859, 2013.

[278] Yi Shu, Cheng Li, Zhe Wang, Wentian Mi, Yuxing Li, and Tian-Ling Ren. A pressure sensing system for heart rate monitoring with polymer-based pressure sensors and an anti-interference post processing circuit. *Sensors*, 15(2):3224–3235, 2015.

[279] Changhyun Pang, Gil-Yong Lee, Tae-il Kim, Sang Moon Kim, Hong Nam Kim, Sung-Hoon Ahn, and Kahp-Yang Suh. A flexible and highly sensitive strain-gauge sensor using reversible interlocking of nanofibres. *Nature Materials*, 11(9):795–801, 2012.

[280] Stefan CB Mannsfeld, Benjamin CK Tee, Randall M Stoltenberg, Christopher V HH Chen, Soumendra Barman, Beinn VO Muir, Anatoliy N Sokolov, Colin Reese, and Zhenan Bao. Highly sensitive flexible pressure sensors with microstructured rubber dielectric layers. *Nature Materials*, 9(10):859–864, 2010.

[281] Ikjin Lee and Hyung Jin Sung. Development of an array of pressure sensors with PVDF film. *Experiments in Fluids*, 26(1-2):27–35, 1999.

[282] Takao Someya, Tsuyoshi Sekitani, Shingo Iba, Yusaku Kato, Hiroshi Kawaguchi, and Takayasu Sakurai. A large-area, flexible pressure sensor matrix with organic field-effect transistors for artificial skin applications. *Proceedings of the National Academy of Sciences*, 101(27):9966–9970, 2004.

[283] ZH Ni, HM Wang, Johnson Kasim, HM Fan, Tongxi Yu, Yong Hua Wu, YP Feng, and ZX Shen. Graphene thickness determination using reflection and contrast spectroscopy. *Nano Letters*, 7(9):2758–2763, 2007.

[284] Dheeraj Golla, Kanokporn Chattrakun, Kenji Watanabe, Takashi Taniguchi, Brian J LeRoy, and Arvinder Sandhu. Optical thickness determination of hexagonal boron nitride flakes. *Applied Physics Letters*, 102(16):161906, 2013.

[285] Hai Li, Jumiati Wu, Xiao Huang, Gang Lu, Jian Yang, Xin Lu, Qihua Xiong, and Hua Zhang. Rapid and reliable thickness identification of two-dimensional nanosheets using optical microscopy. *ACS Nano*, 7(11):10344–10353, 2013.

[286] Matteo Bruna and Stefano Borini. Assessment of graphene quality by quantitative optical contrast analysis. *Journal of Physics D: Applied Physics*, 42(17):175307, 2009.

[287] Frank Schwierz, Jörg Pezoldt, and Ralf Granzner. Two-dimensional materials and their prospects in transistor electronics. *Nanoscale*, 7(18):8261–8283, 2015.

[288] F Tuinstra and J Lo Koenig. Raman spectrum of graphite. *The Journal of chemical physics*, 53(3):1126–1130, 1970.

[289] Andrea C Ferrari and John Robertson. Interpretation of Raman spectra of disordered and amorphous carbon. *Physical Review B*, 61(20):14095, 2000.

[290] Andrea C Ferrari, Jannik C. Meyer, Vittorio Scardaci, Cinzia Casiraghi, Michele Lazzeri, Francesco Mauri, Stefano Piscanec, Da Jiang, Konstantin S. Novoselov, Stefan Roth, et al. Raman spectrum of graphene and graphene layers. *Physical Review Letters*, 97(18):187401, 2006.

[291] Xin Zhang, Qing-Hai Tan, Jiang-Bin Wu, Wei Shi, and Ping-Heng Tan. Review on the Raman spectroscopy of different types of layered materials. *Nanoscale*, 8(12):6435–6450, 2016.

[292] David Nečas and Petr Klapetek. Gwyddion: an open-source software for SPM data analysis. *Open Physics*, 10(1):181–188, 2012.

[293] Pei He. *Inkjet Printing of Two Dimensional Materials.* PhD thesis, University of Manchester, 2016.

[294] Jung-Woo Ted Seo, Jian Zhu, Vinod K Sangwan, Ethan B Secor, Shay G Wallace, and Mark C Hersam. Fully inkjet-printed, mechanically flexible mos2 nanosheet photodetectors. *ACS applied materials & interfaces*, 11(6):5675–5681, 2019.

[295] Tian Carey, Adrees Arbab, Luca Anzi, Helen Bristow, Fei Hui, Sivasambu Bohm, Gwenhivir Wyatt-Moon, Andrew Flewitt, Andrew Wadsworth, Nicola Gasparini, et al. Inkjet printed circuits with 2d semiconductor inks for high-performance electronics. *Advanced Electronic Materials*, page 2100112, 2021.

[296] Muhammad Awais, Muhammad Umair Khan, Arshad Hassan, Jinho Bae, and Tahseen Elahi Chattha. Printable highly stable and superfast humidity sensor based on two dimensional molybdenum diselenide. *Scientific reports*, 10(1):1–13, 2020.

[297] Darren Nutting, Jorlandio F Felix, Evan Tillotson, Dong-Wook Shin, Adolfo De Sanctis, Hong Chang, Nick Cole, Saverio Russo, Adam Woodgate, Ioannis Leontis, et al. Heterostructures formed through abraded van der waals materials. *Nature Communications*, 11(1):1–10, 2020.

[298] Dong-Wook Shin, Hyun Myoung Lee, Seong Man Yu, Kwang-Soo Lim, Jae Hoon Jung, Min-Kyu Kim, Sang-Woo Kim, Jae-Hee Han, Rodney S Ruoff, and Ji-Beom Yoo. A facile route to recover intrinsic graphene over large scale. *ACS Nano*, 6(9):7781–7788, 2012.

[299] Dong-Wook Shin, Matthew D Barnes, Kieran Walsh, Dimitar Dimov, Peng Tian, Ana IS Neves, C David Wright, Seong Man Yu, Ji-Beom Yoo, Saverio Russo, et al. A new facile route to flexible and semi-transparent electrodes based on water exfoliated graphene and their single-electrode triboelectric nanogenerator. *Advanced Materials*, 30(39):1802953, 2018.

[300] Keith R Paton, Eswaraiah Varrla, Claudia Backes, Ronan J Smith, Umar Khan, Arlene O'Neill, Conor Boland, Mustafa Lotya, Oana M Istrate, Paul King, et al. Scalable production of large quantities of defect-free few-layer graphene by shear exfoliation in liquids. *Nature Materials*, 13(6):624–630, 2014.

[301] David J Finn, Mustafa Lotya, Graeme Cunningham, Ronan J Smith, David McCloskey, John F Donegan, and Jonathan N Coleman. Inkjet deposition of liquid-exfoliated graphene and MoS_2 nanosheets for printed device applications. *Journal of Materials Chemistry C*, 2(5):925–932, 2014.

[302] Graeme Cunningham, Damien Hanlon, Niall McEvoy, Georg S Duesberg, and Jonathan N Coleman. Large variations in both dark-and photoconductivity in nanosheet networks as nanomaterial is varied from MoS_2 to WTe_2. *Nanoscale*, 7(1):198–208, 2015.

[303] Ethan B Secor, Pradyumna L Prabhumirashi, Kanan Puntambekar, Michael L Geier, and Mark C Hersam. Inkjet printing of high conductivity, flexible

graphene patterns. *The journal of physical chemistry letters*, 4(8):1347–1351, 2013.

[304] Azhar A Pirzado, Guillaume Dalmas, Lam Nguyen-Dinh, Ivan Komissarov, Francois Le Normand, and Izabela Janowska. The electrical property of large few layer graphene flakes obtained by microwaves assisted exfoliation of expanded graphite. *Current Microwave Chemistry*, 3(2):139–144, 2016.

[305] Goki Eda, Hisato Yamaguchi, Damien Voiry, Takeshi Fujita, Mingwei Chen, and Manish Chhowalla. Photoluminescence from chemically exfoliated mos2. *Nano letters*, 11(12):5111–5116, 2011.

[306] Tongxin Chen, Yuewen Sheng, Yingqiu Zhou, Ren-jie Chang, Xiaochen Wang, Hefu Huang, Qianyang Zhang, Linlin Hou, and Jamie H Warner. High photoresponsivity in ultrathin 2D lateral graphene: WS_2: graphene photodetectors using direct CVD growth. *ACS Applied Materials & Interfaces*, 11(6):6421–6430, 2019.

[307] Freddie Withers, Huafeng Yang, Liam Britnell, Aiden P. Rooney, Edward Lewis, Alexandre Felten, Colin R. Woods, Veronica Sanchez Romaguera, Thanasis Georgiou, Axel Eckmann, et al. Heterostructures produced from nanosheet-based inks. *Nano Letters*, 14(7):3987–3992, 2014.

[308] Robyn Worsley, Lorenzo Pimpolari, Daryl McManus, Ning Ge, Robert Ionescu, Jarrid A Wittkopf, Adriana Alieva, Giovanni Basso, Massimo Macucci, Giuseppe Iannaccone, et al. All-2D material inkjet-printed capacitors: toward fully printed integrated circuits. *ACS Nano*, 13(1):54–60, 2018.

[309] Ki Kang Kim, Allen Hsu, Xiaoting Jia, Soo Min Kim, Yumeng Shi, Mildred Dresselhaus, Tomas Palacios, and Jing Kong. Synthesis and characterization of hexagonal boron nitride film as a dielectric layer for graphene devices. *ACS nano*, 6(10):8583–8590, 2012.

[310] Liam Britnell, RM Ribeiro, A Eckmann, R Jalil, BD Belle, A Mishchenko, Y-J Kim, RV Gorbachev, T Georgiou, SV Morozov, et al. Strong light-matter in-

teractions in heterostructures of atomically thin films. *Science*, 340(6138):1311–1314, 2013.

[311] Deep Jariwala, Artur R Davoyan, Joeson Wong, and Harry A Atwater. Van der Waals materials for atomically-thin photovoltaics: Promise and outlook. *ACS Photonics*, 4(12):2962–2970, 2017.

[312] D McManus, ANDREA Dal Santo, PB Selvasundaram, R Krupke, A LiBassi, and C Casiraghi. Photocurrent study of all-printed photodetectors on paper made of different transition metal dichalcogenide nanosheets. *Flexible and Printed Electronics*, 3(3):034005, 2018.

[313] Roberto S Aga, Jack P Lombardi, Carrie M Bartsch, and Emily M Heckman. Performance of a printed photodetector on a paper substrate. *IEEE Photonics Technology Letters*, 26(3):305–308, 2013.

[314] Ting Leng, Khaled Parvez, Kewen Pan, Junaid Ali, Daryl McManus, Kostya S Novoselov, Cinzia Casiraghi, and Zhirun Hu. Printed graphene/WS_2 battery-free wireless photosensor on papers. *2D Materials*, 7(2):024004, 2020.

[315] Wolfgang M. H. Sachtler. The work function of gold. *Surface Science*, 5(2):221–229, 1966.

[316] Young-Jun Yu, Yue Zhao, Sunmin Ryu, Louis E Brus, Kwang S Kim, and Philip Kim. Tuning the graphene work function by electric field effect. *Nano letters*, 9(10):3430–3434, 2009.

[317] Thanasis Georgiou, Rashid Jalil, Branson D Belle, Liam Britnell, Roman V Gorbachev, Sergey V Morozov, Yong-Jin Kim, Ali Gholinia, Sarah J Haigh, Oleg Makarovsky, et al. Vertical field-effect transistor based on graphene–WS_2 heterostructures for flexible and transparent electronics. *Nature Nanotechnology*, 8(2):100, 2013.

[318] Yue Niu, Riccardo Frisenda, Eduardo Flores, Jose R Ares, Weicheng Jiao, David Perez de Lara, Carlos Sánchez, Rongguo Wang, Isabel J Ferrer, and Andres

Castellanos-Gomez. Polarization-Sensitive and Broadband Photodetection Based on a Mixed-Dimensionality TiS_3/Si p–n Junction. *Advanced Optical Materials*, 6(19):1800351, 2018.

[319] Daewoong Hong, Young-Man Choi, Yunseok Jang, and Jaehwa Jeong. A multilayer thin-film screen-printed triboelectric nanogenerator. *International Journal of Energy Research*, 42(11):3688–3695, 2018.

[320] Myeong-Lok Seol, Jin-Woo Han, Dong-Il Moon, Kyung Jean Yoon, Cheol Seong Hwang, and MJNE Meyyappan. All-printed triboelectric nanogenerator. *Nano Energy*, 44:82–88, 2018.

[321] Ian D. Johnston, Daniel K. McCluskey, Christabel K. L. Tan, and Monica C. Tracey. Mechanical characterization of bulk Sylgard 184 for microfluidics and microengineering. *Journal of Micromechanics and Microengineering*, 24(3):035017, 2014.

[322] Innovadex LLC. Polyurethane (PUR) Typical Properties Generic PUR, Unspecified, 2020.

[323] Tomohito Sekine, Ryo Sugano, Tomoya Tashiro, Kenjiro Fukuda, Daisuke Kumaki, Fabrice Domingues Dos Santos, Atsushi Miyabo, and Shizuo Tokito. Fully printed and flexible ferroelectric capacitors based on a ferroelectric polymer for pressure detection. *Japanese Journal of Applied Physics*, 55(10S):10TA18, 2016.

[324] Junshi Soeda, Yoshinori Ikeda, and Takashi Shiro. Solution-processing of flexible thin-film negative-temperature-coefficient silicon thermistors using silicon nanoparticles. *Japanese Journal of Applied Physics*, 56(7):070310, 2017.

[325] Yasser Khan, Mohit Garg, Qiong Gui, Mark Schadt, Abhinav Gaikwad, Donggeon Han, Natasha AD Yamamoto, Paul Hart, Robert Welte, William Wilson, et al. Flexible hybrid electronics: Direct interfacing of soft and hard electronics for wearable health monitoring. *Advanced Functional Materials*, 26(47):8764–8775, 2016.

[326] Pandiyan Murugaraj, David Mainwaring, and Nelson Mora-Huertas. Thermistor behaviour in a semiconducting polymer–nanoparticle composite film. *Journal of Physics D: Applied Physics*, 39(10):2072, 2006.

[327] Anett Király and Ferenc Ronkay. Temperature dependence of electrical properties in conductive polymer composites. *Polymer Testing*, 43:154–162, 2015.

[328] Qian-ying Chen, Jing Gao, Kun Dai, Huan Pang, Jia-zhuang Xu, Jian-hua Tang, and Zhong-ming Li. Nonlinear current-voltage characteristics of conductive polyethylene composites with carbon black filled pet microfibrils. *Chinese Journal of Polymer Science*, 31(2):211–217, 2013.

[329] Yang Yuan, Zhaoming Qu, Qingguo Wang, Xiaoning Sun, and Erwei Cheng. Reversible nonlinear iv behavior of zno-decorated graphene nanoplatelets/epoxy resin composites. *Polymers*, 12(4):951, 2020.

[330] Gordon E Moore. No exponential is forever: but" forever" can be delayed![semiconductor industry]. In *2003 IEEE International Solid-State Circuits Conference, 2003. Digest of Technical Papers. ISSCC.*, pages 20–23. IEEE, 2003.

[331] Qiang Chen, Bhavna Agrawal, and James D Meindl. A comprehensive analytical subthreshold swing (s) model for double-gate mosfets. *IEEE Transactions on Electron Devices*, 49(6):1086–1090, 2002.

[332] Gen Pei, Jakub Kedzierski, Phil Oldiges, Meikei Ieong, and EC-C Kan. FinFET design considerations based on 3-D simulation and analytical modeling. *IEEE Transactions on Electron Devices*, 49(8):1411–1419, 2002.

[333] Antonio Di Bartolomeo, Luca Genovese, Filippo Giubileo, Laura Iemmo, Giuseppe Luongo, Tobias Foller, and Marika Schleberger. Hysteresis in the transfer characteristics of MoS_2 transistors. *2D Materials*, 5(1):015014, 2017.

[334] Michael Leonardo Marques Rodrigues and Rosa Malena Fernandes Lima. Cleaner production of soapstone in the Ouro Preto region of Brazil: a case study. *Journal of Cleaner Production*, 32:149–156, 2012.

[335] Dattatray Late, Bin Liu, Ramakrishna Matte, Vinayak Dravid, and Chen Rao. Hysteresis in single-layer MoS_2 field effect transistors. *ACS Nano*, 6(6):5635–5641, 2012.

[336] Theresia Knobloch, Gerhard Rzepa, Yury Yu Illarionov, Michael Waltl, Franz Schanovsky, Bernhard Stampfer, Marco M Furchi, Thomas Mueller, and Tibor Grasser. A physical model for the hysteresis in MoS_2 transistors. *IEEE Journal of the Electron Devices Society*, 6:972–978, 2018.

[337] Nihar R Pradhan, Daniel Rhodes, Yan Xin, Shahriar Memaran, Lakshmi Bhaskaran, Muhandis Siddiq, Stephen Hill, Pulickel M Ajayan, and Luis Balicas. Ambipolar molybdenum diselenide field-effect transistors: field-effect and hall mobilities. *ACS Nano*, 8(8):7923–7929, 2014.

[338] Deliris N Ortiz, Idalia Ramos, Nicholas J Pinto, Meng-Qiang Zhao, Vinayak Kumar, and AT Charlie Johnson. Ambipolar transport in CVD grown $MoSe_2$ monolayer using an ionic liquid gel gate dielectric. *AIP Advances*, 8(3):035014, 2018.

[339] Bhim Chamlagain, Qing Li, Nirmal Jeevi Ghimire, Hsun-Jen Chuang, Meeghage Madusanka Perera, Honggen Tu, Yong Xu, Minghu Pan, Di Xaio, Jiaqiang Yan, et al. Mobility improvement and temperature dependence in $MoSe_2$ field-effect transistors on parylene-c substrate. *ACS Nano*, 8(5):5079–5088, 2014.

[340] Kathleen M McCreary, Aubrey T Hanbicki, Simranjeet Singh, Roland K Kawakami, Glenn G Jernigan, Masa Ishigami, Amy Ng, Todd H Brintlinger, Rhonda M Stroud, and Berend T Jonker. The effect of preparation conditions on Raman and photoluminescence of monolayer WS_2. *Scientific Reports*, 6:35154, 2016.

[341] Philipp Nagler, Mariana V Ballottin, Anatolie A Mitioglu, Mikhail V Durnev, Takashi Taniguchi, Kenji Watanabe, Alexey Chernikov, Christian Schüller, Mikhail M Glazov, Peter CM Christianen, et al. Zeeman splitting and inverted

polarization of biexciton emission in monolayer WS_2. *Physical Review Letters*, 121(5):057402, 2018.

[342] Shunya Hayashida, Risa Saitoh, Kenji Watanabe, Takashi Taniguchi, Kentarou Sawano, and Yusuke Hoshi. Reduced Inhomogeneous Broadening in Hexagonal Boron Nitride-Encapsulated $MoTe_2$ Monolayers by Thermal Treatment. *ACS Applied Electronic Materials*, 2020.

[343] Matteo Barbone, Alejandro R-P Montblanch, Dhiren M Kara, Carmen Palacios-Berraquero, Alisson R Cadore, Domenico De Fazio, Benjamin Pingault, Elaheh Mostaani, Han Li, Bin Chen, et al. Charge-tuneable biexciton complexes in monolayer WSe_2. *Nature Communications*, 9(1):1–6, 2018.

[344] V Orsi Gordo, MAG Balanta, Y Galvão Gobato, FS Covre, HVA Galeti, F Iikawa, ODD Couto, F Qu, M Henini, DW Hewak, et al. Revealing the nature of low-temperature photoluminescence peaks by laser treatment in van der Waals epitaxially grown WS_2 monolayers. *Nanoscale*, 10(10):4807–4815, 2018.

[345] Igor Filikhin, Roman Ya Kezerashvili, and Branislav Vlahovic. On binding energy of trions in bulk materials. *Physics Letters A*, 382(11):787–791, 2018.

[346] Joanna Jadczak, Joanna Kutrowska-Girzycka, Maciej Bieniek, Tomasz Kazimierczuk, Piotr Kossacki, Janina J. Schindler, Jörg Debus, Kenji Watanabe, Takashi Taniguchi, Ching-Hwa Ho, et al. Probing negatively charged and neutral excitons in mos2/hbn and hbn/mos2/hbn van der waals heterostructures. *Nanotechnology*, 32(14):145717, 2021.

[347] Emmanuel Courtade, Bo Han, Cédric Robert, Xavier Marie, Pierre Renucci, Takashi Taniguchi, Kenji Watanabe, Joao M. J. Lopes, et al. Spectrally narrow exciton luminescence from monolayer mos2 and mose2 exfoliated onto epitaxially grown hexagonal bn. *Applied Physics Letters*, 113(3):032106, 2018.

[348] Xin Lu, M Iqbal Bakti Utama, Junhao Lin, Xue Gong, Jun Zhang, Yanyuan Zhao, Sokrates T Pantelides, Jingxian Wang, Zhili Dong, Zheng Liu, et al.

Large-area synthesis of monolayer and few-layer mose2 films on sio2 substrates. *Nano Letters*, 14(5):2419–2425, 2014.

[349] Yosuke Uchiyama, Alex Kutana, Kenji Watanabe, Takashi Taniguchi, Kana Kojima, Takahiko Endo, Yasumitsu Miyata, Hisanori Shinohara, and Ryo Kitaura. Momentum-forbidden dark excitons in hbn-encapsulated monolayer mos 2. *npj 2D Materials and Applications*, 3(1):1–6, 2019.

SolidWorks design for bespoke bending rig

The SolidWorks design used to create the bespoke bending rig is shown below within Figure 1.

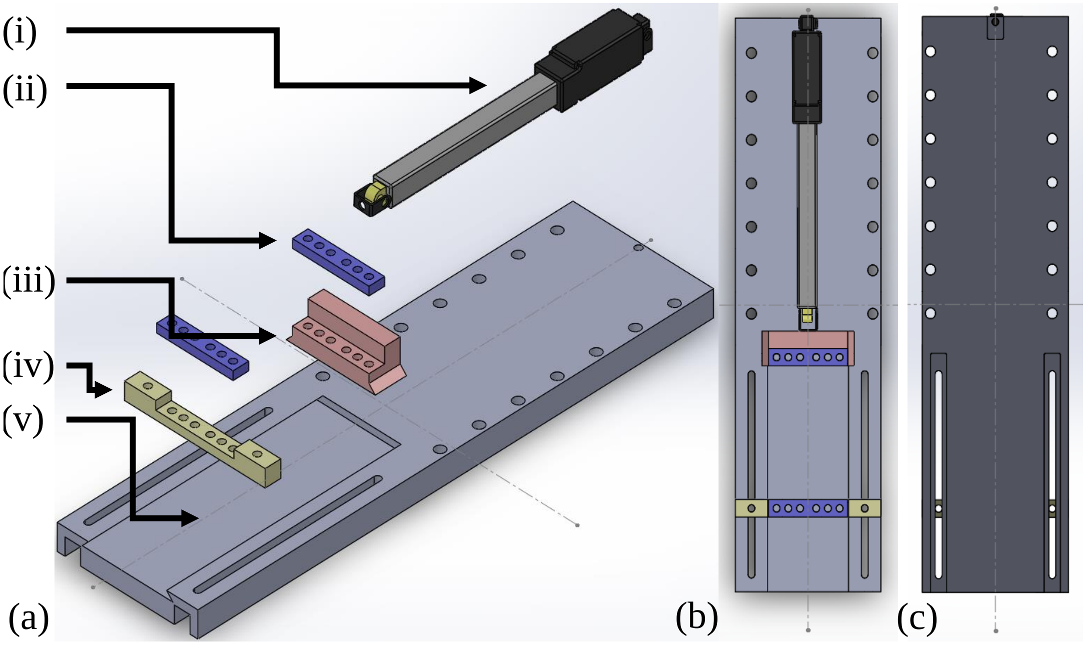

Figure 1: *SolidWorks design of the bespoke bending rig. (a) Exploded schematic of the rig showing the (i) linear actuator, (ii) clamps to hold the flexible substrate in place (purple), (iii) movable clamp, (iv) fixed clamp and (v) the base plate, which can be securely fixed to a tabletop. (b) Image of the schematic from above. (c) Image of the schematic from below.*

Spectral deconvolution

An example of a deconvolved photoluminescent spectrum is given below within Figure 2. The data, shown in black, clearly contains two overlapping features which can be deconvolved using QtiPlot analysis software. By first selecting the number of peaks required to fit the spectra and then approximating the peak positions, this software can easily be used to derive the positions and form of the A and A'-peaks within this spectrum. Each spectra is fitted by an appropriate number of Lorentzian curves to identify the obscured features, as is detailed within [252].

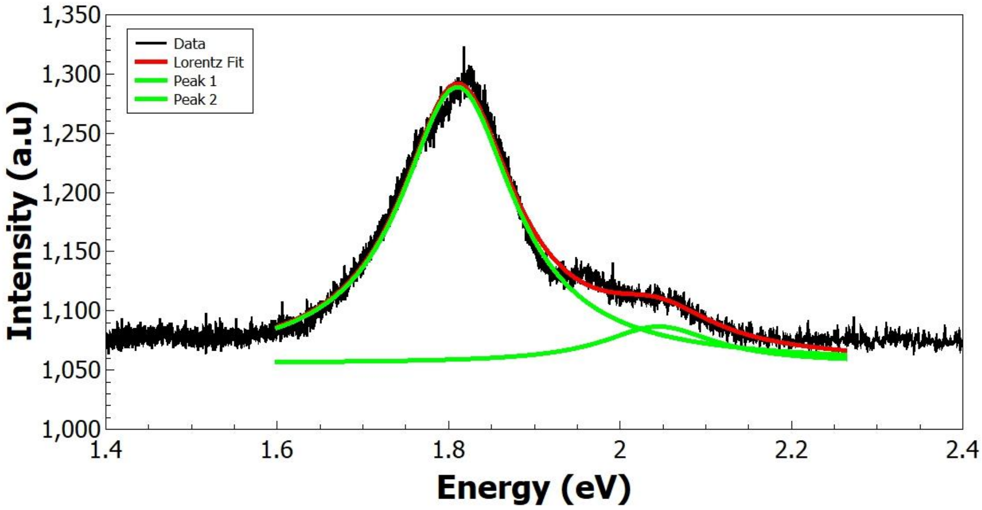

Figure 2: *The PL spectrum for monolayer* MoS_2 *on talc. The data is shown in black whilst the total Lorentz fit along with its component peaks are shown in red and green, respectively.*